X-ray Studies of the Innermost Regions of Black Hole Accretion

Jiachen Jiang

Supervisor: Andrew C. Fabian

Wolfson College
University of Cambridge

This dissertation is submitted for the degree of
Doctor of Philosophy

Institute of Astronomy

May 2019

I would like to dedicate this thesis to all my friends in Cambridge.

Declaration

I hereby declare that the contents of this dissertation are original and have not been submitted in whole or in part for consideration for any other degree or qualification in this, or any other university. This dissertation is my own work and contains nothing which is the outcome of work done in collaboration with others, except as specified in the text and Acknowledgements. This dissertation contains fewer than 60,000 words including abstract, appendices, footnotes, tables and equations.

Chapters of this thesis based on published are as follows:

- Chapter 2

  Jiang, J., Fabian, A. C., Wang, J., Walton, D. J., García, J. A., Parker, M. L., Steiner, J. F., and Tomsick, J. A. (2019). High-density reflection spectroscopy: I. A case study of GX 339-4. MNRAS, 484:1972–1982.

- Chapter 4

  Jiang, J., Parker, M. L., Fabian, A. C., Alston, W. N., Buisson, D. J. K., Cackett, E. M., Chiang, C.-Y., Dauser, T., Gallo, L. C., García, J. A., Harrison, F. A., Lohfink, A. M., De Marco, B., Kara, E., Miller, J. M., Miniutti, G., Pinto, C., Walton, D. J., and Wilkins, D. R. (2018). The 1.5 Ms Observing Campaign on IRAS 13224-3809: X-ray Spectral Analysis I. MNRAS, 477:3711–3726.

- Chapter 5

  Jiang, J., Walton, D. J., Fabian, A. C., and Parker, M. L. (2019). A relativistic disc reflection model for 1H0419-577: Multi-epoch spectral analysis with XMM-Newton and NuSTAR. MNRAS, 483:2958–2967.

Jiachen Jiang
May 2019

Abstract

Title: X-ray Studies of the Innermost Regions of Black Hole Accretion
Name: Jiachen Jiang

In this thesis, I present the results of my research on the X-ray spectra of accreting black holes. The content of this thesis can be broadly separated into two parts: Chapter 2-3 for stellar-mass black holes in X-ray binaries (XRBs) and Chapter 4-6 for supermassive black holes in active galactic nuclei (AGN).

This work mainly focuses on the X-ray spectral shape and the spectral variability of these accreting black hole systems. By studying the broad band spectra of XRBs and AGN, we are able to extract some information about the innermost regions of the discs from their X-ray observations. For example, we are able to 1) constrain the size of the coronal region that illuminates the disc; 2) estimate some properties of the discs, such as the density in the disc surface; 3) measure the spin parameters of the accreting black holes. In the meantime, I also study the variability of the innermost regions by comparing different observations or different flux states of individual sources. For example, Chapter 2-3 compare different accretion states of black hole XRBs. Chapter 4 discusses the extreme and fast flux variability on a timescale less than one kilo-second in the narrow-line Seyfert 1 galaxy IRAS 13224−3809. Chapter 5 studies the long-term spectral variability of the Seyfert 1 galaxy 1H0419−577.

The main spirit of this thesis is to test for high density discs. A disc reflection model with a variable disc density parameter is used for each source in this work. In the last chapter, I apply the same model to a large sample of Seyfert 1 galaxies in order to compare the disc densities at different black hole mass scales and different accretion rates.

Acknowledgements

My deepest gratitude goes to my supervisors, colleagues, and advisors for unending support for my research. There are so many people I want to thank that I can not mention all of them in an one-page acknowledgement. Below are some of those names I can still remember.

Firstly, I would like to thank Andy Fabian for spending an enormous amount of time teaching me black holes and correcting articles in my papers with great patience. Special thanks are due to Dom Walton and Michael Parker for never being bored by my endless stupid questions or scared by my knocks on their office doors. I have also been helped by other members of the X-ray group in Cambridge as well: Chris Reynolds, George Lansbury, and Will Alston. Anne Lohfink, Ciro Pinto and Helen Russell were here as well. Thanks to Douglas Buisson and Peter Kosec for being the most amazing office mates who I can share office gossip with. Special thanks must be reserved for Roderick Johnstone who taught me how to switch on my desktop and always backed up my files when I broke my computer.

Secondly, I would like to acknowledge support by the Cambridge Trust and the Chinese Scholarship Council Joint Scholarship Programme. Without them, I would not even be able to get on that flight from China to UK on my first day. I am also grateful to Wolfson College for providing travel grant for me to travel to several conferences.

Thirdly, thanks are due to Cosimo Bambi for teaching me how to speak 'black hole' in English in the beginning and convincing my parents that a scientist is no worse than a businessman except for much less money. I am also very grateful to Jack Steiner and Matteo Guainazzi for fully supporting me to apply for PhD in Cambridge.

Last but not least, I am most thankful to my friends in Cambridge: Alfonso Timoneda Monfort, Eric Swanson, Marios Christodoulides, and all the other dancing queens. Without you I would have felt like being trapped in a black hole in the last two years and would probably have graduated one year earlier.

Jiachen Jiang

Cambridge, April 2019

Table of contents

List of figures

List of tables

Chapter 1

Introduction

"If the semidiameter of a sphere of the same density with the sun were to exceed that of the sun in the proportion of 500 to 1, a body falling from an infinite height towards it, would have acquired at its surface a greater velocity than that of light."

– John Michell (1784)

1.1 Black Holes in Our Universe

The existence of black holes (BHs) was first predicted by John Michell in 1784 [181]. They were referred to as 'dark stars' at that time as no light can escape from them by definition. However the work of John Michell was ignored due to the lack of a gravity theory to understand the light path in a strong gravitational field. Schwarzschild [273] first calculated the radius of a BH in the Schwarzschild metric, the first solution of the Einstein field equations in General Relativity [57]. Since the prediction of BHs, a lot of progress has been made in both theoretical and observational studies. Right now, we are already able to obtain an image of the shadow of a nearby BH in the radio band over 100 years after the publication of Einstein's theory of General Relativity [60].

In astronomy, BHs are simply classified by their masses and spins. In this section, I present a short introduction of supermassive black holes (SMBHs) in active galactic nuclei (AGN) and stellar-mass BHs in X-ray binaries (XRBs).

1.1.1 Active Galactic Nuclei

A Brief History of SMBHs in AGN

The discovery of SMBHs in AGN started with the radio source 3C 273 in the early 1960s. In 1962, Hazard et al. [109] was able to obtain an accurate position for 3C 273 based on the observations taken by the 210-foot antenna at the Parkes Station in Australia. Schmidt [270] found that the hydrogen emission lines presented in the spectrum of 3C 273 were redshifted by the same factor (z=0.16), indicating that the emitting gas was moving away from us. Oke [217] confirmed this idea by identifying another redshifted emission line in the infrared band. By adopting the cosmological redshift, Greenstein and Schmidt [94] were able to obtain a spherical Hβ emission region of 1.2 pc for 3C 273. Combining the size measurement of the emitting region and the observed optical variability, Smith and Hoffleit [280] was able to derive a mass of $10^9 M_\odot$ for the central object in 3C 273.

Hoyle and Fowler [115] suggested that a relativistic collapse of a supermassive star with a mass of $\approx 10^8 M_\odot$ might be able to energize the observed high luminosities from radio sources like 3C 273. Zel'dovich and Poduret [336] proposed that the accretion process onto massive objects is able to power these quasars. In the meantime, a mass of $10^8 M_\odot$ is required to balance the radiation pressure according to the observed luminosities. Lynden-Bell [161] later described the accretion process onto a $10^{7-9} M_\odot$ 'Schwarzchild throat' (supermassive black hole in later terminology) in the form of a disc. In order to power these quasars, a mass accretion process of about one solar mass per year has to occur in them. Such an accretion

process might slow down later on but the BHs still remain in the centres of ordinary galaxies without AGN, such as our own Galaxy, which was predicted by Lynden-Bell and Rees [162]. Later, a compact radio source with synchroton emission was found in Sgr A* at the centre of the Milky Way by Balick and Brown [11] using the Green Bank Interferometer. By studying the motion of a nearby star, Schödel et al. [272] were able to strengthen the evidence for a SMBH with three million solar masses in Sgr A*.

The Unified Model of Seyfert Galaxies

Seyfert [275] was the first one who systematically studied a number of AGN, which led to the classification of Seyfert galaxies based on the presence and absence of broad permitted emission lines in the optical band. For example, the top left panel of Fig. 1.1 presents the UK Schmidt Telescope (UKST) spectra of two AGN, Ark 120 and MCG -01−24−012. Ark 120 shows broad Hβ and Hα emission lines and a narrow forbidden [O III] line in the UKST spectrum. Sources that show similar broad permitted emission lines (1000–20,000 km s^{-1}) are called Seyfert 1 galaxies (Sy1). By contrast, sources that show narrow permitted emission lines (300–1000 km s^{-1}) are called Seyfert 2 galaxies (Sy2), such as MCG -01−24−012.

One of the most popular unified models of Seyfert galaxies is based on the idea that different AGN are fundamentally similar, but viewed at different orientations [e.g. 7, 305]. Here are the basic components in this unified model:

- A sub-pc accretion disc around the SMBH: the disc can be optically thin or optically thick, depending on the accretion state of the disc.
- The broad line region: high-density and dust-free gas clouds moving at Keplerian velocities at a distance of 0.01–1 pc from the SMBH.
- The 'torus': an axisymmetric dusty structure at a distance of 0.1–10 pc from the SMBH.
- The radio jet: an outflowing jet in the general direction of the disc.
- The narrow line region: low-density, low-velocity and ionised gas extending to 100–1000 pc.

Fig. 1.1 shows a schematic picture of AGN in the unified model. The accretion disc and the broad line region cannot be observed directly by an edge-on observer close to the middle plane of the torus. However the narrow line region can still be seen as it is more extended. These sources correspond to the Sy2 galaxies. The obscuration of the torus explains the lack of broad permitted emission lines from the broad line region in the optical spectrum.

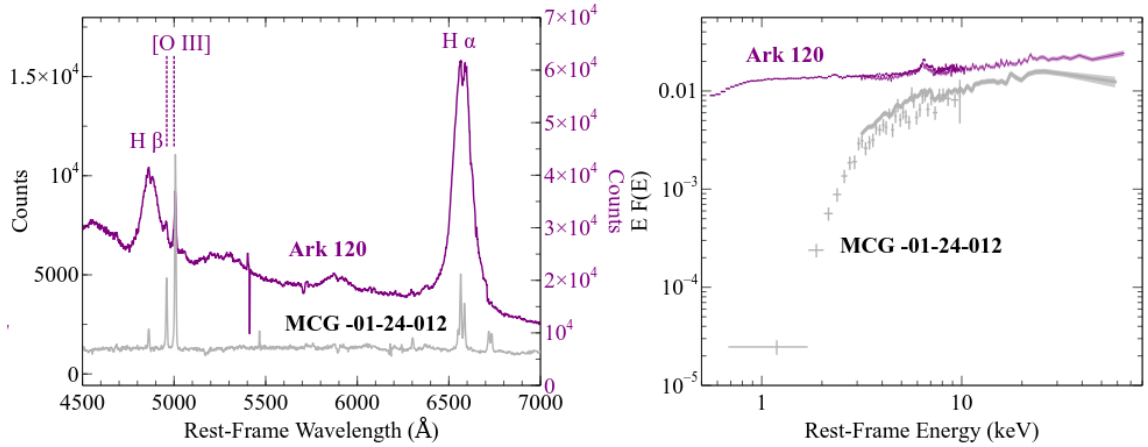

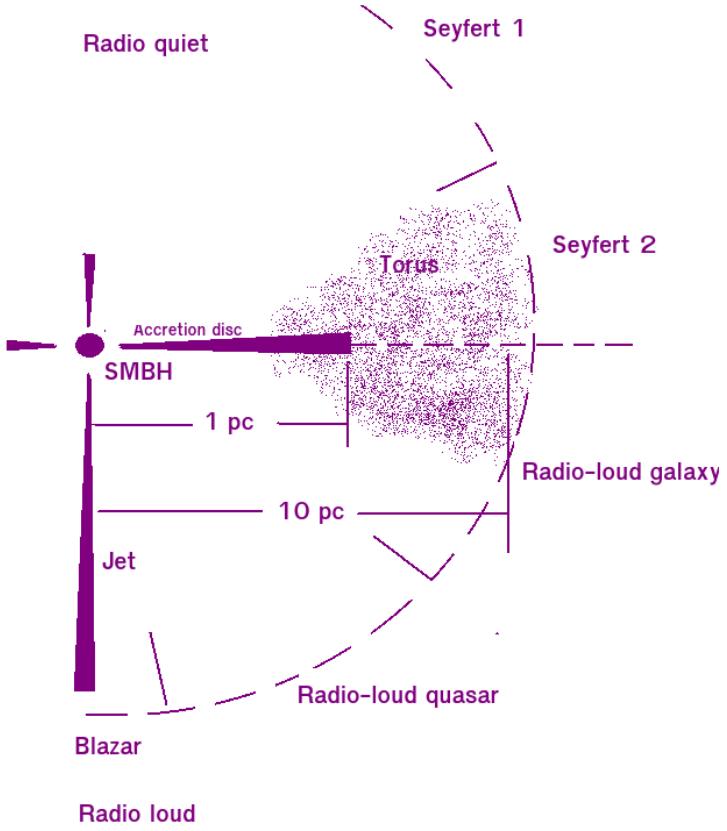

Fig. 1.1 Top: the optical spectra and X-ray spectra of Ark 120 (Sy1) and MCG -01−24−012 (Sy2). The optical spectra are from the UK Schmidt Telescope and the X-ray spectra are from *XMM-Newton* and *NuSTAR* observatories. Bottom: a schematic picture of AGN in the orientation-based unified model.

An observer closer to the torus axis can see into the nuclear region of the AGN without obscuration in the line of sight. These sources correspond to Sy1 galaxies. The presence of broad emission lines in the polarised optical spectra of many Sy2 galaxies are consistent with the idea that Sy1 and Sy2 are fundamentally similar [e.g. 194]. The broad polarised emission lines are due to the reflection of the gas and dust of the torus, indicating a hidden broad line region in Sy2 galaxies.

In the X-ray band, the Sy1 Ark 120 shows little obscuration while the Sy2 MCG -01—24—012 shows evidence for photoelectric absorption by neutral material along our line of sight to the X-ray source. In the unified model, the X-ray obscuration is due to the torus. See the top right panel of Fig. 1.1 for *NuSTAR* and *XMM-Newton* spectra of these two sources. The spectra are unfolded through a constant model to remove the effects of the effective area of the detectors. Systematic studies have shown that most Sy2 galaxies indeed show heavier obscuration in the X-ray band than Sy1 galaxies [e.g. 259]. In this thesis, I present my studies of radio-quiet Sy1 galaxies in the X-ray band. Radio-loud AGN are similar to radio-quiet ones in this model but with additional emission from the jet.

The orientation-based unified model successfully explains the spectral diversity of most AGN. However it is being challenged by some recent observations. One of the challenges is the discoveries of unobscured Sy2 AGN [e.g. 224, 223]. These sources show only narrow emission lines in the optical band and little or no obscuration in the X-ray band ($N_{\rm H} < 10^{22}$ cm^{-2}). Although some of them are shown to be 'true Sy2' where no broad polarised emission lines are found and the broad line region is thought to be naturally missing, many still show disagreement between the X-ray and optical bands [e.g. 279, 299]. Another challenge comes from the infrared observations of AGN. Recent interferometry observations in the mid-infrared band of Sy1 galaxies shows that most infrared emission originates from the dust in the polar region instead of in the disc plane, suggesting a different shape of torus [e.g. 114].

1.1.2 Black Hole X-ray Binaries

A Brief History of BH XRBs

X-ray binaries (XRBs) are binary systems that are powered by accretion processes and are luminous in X-rays. They are usually identified in the X-ray band. The BHs in BH XRBs usually have a mass of $4 - 20 M_{\odot}$ and are formed by the gravitational collapse of stars. For example, Cyg X-1 is one of the first X-ray sources identified in the sky. It was first discovered by the *Aerobee* surveys in 1965 [29]. Shortly after the discovery of the X-ray emission from Cyg X-1, Braes and Miley [31], Hjellming and Wade [112] discovered radio emission from

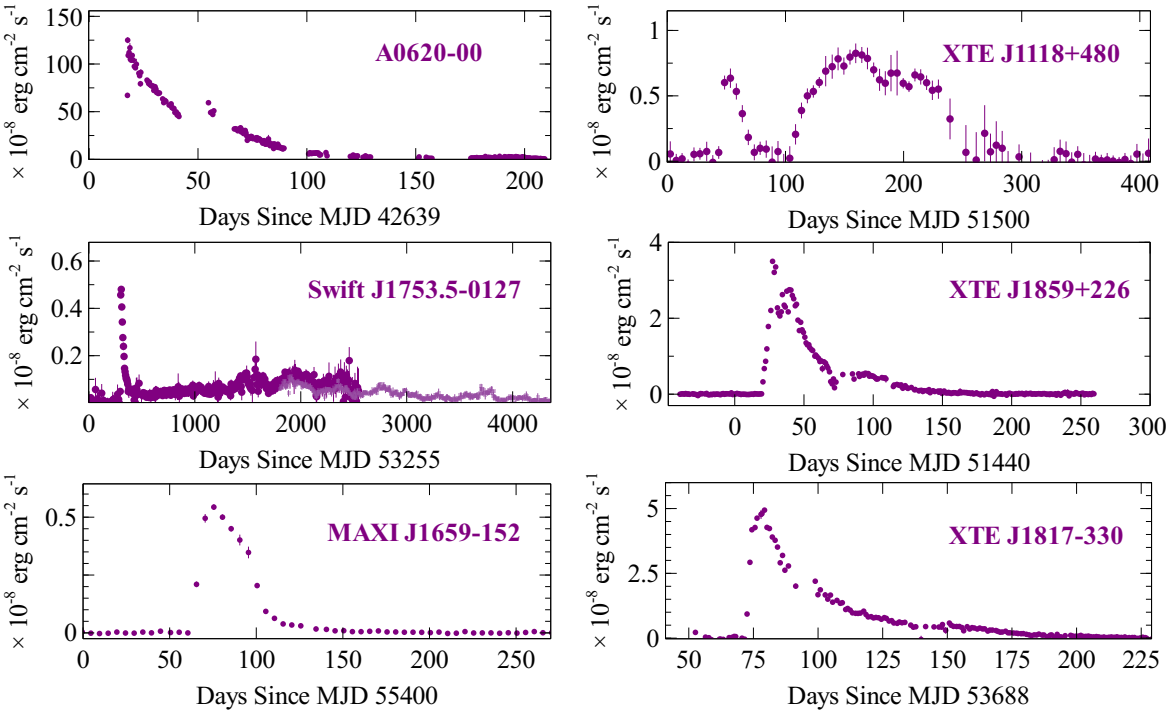

Fig. 1.2 Long term 2–10 keV flux light curves for A0620−00 (*Ariel-V*) in 1975, XTE J1118+480 (*RXTE*) in 2000, Swift J1753.5−0127 (purple: *RXTE*; faint purple: *MAXI*) in 2004–2014, MAXI J1659−152 (*MAXI*) in 1999, XTE J1859+226 (*RXTE*) in 2010, and XTE J1817−330 (*RXTE*) in 2005.

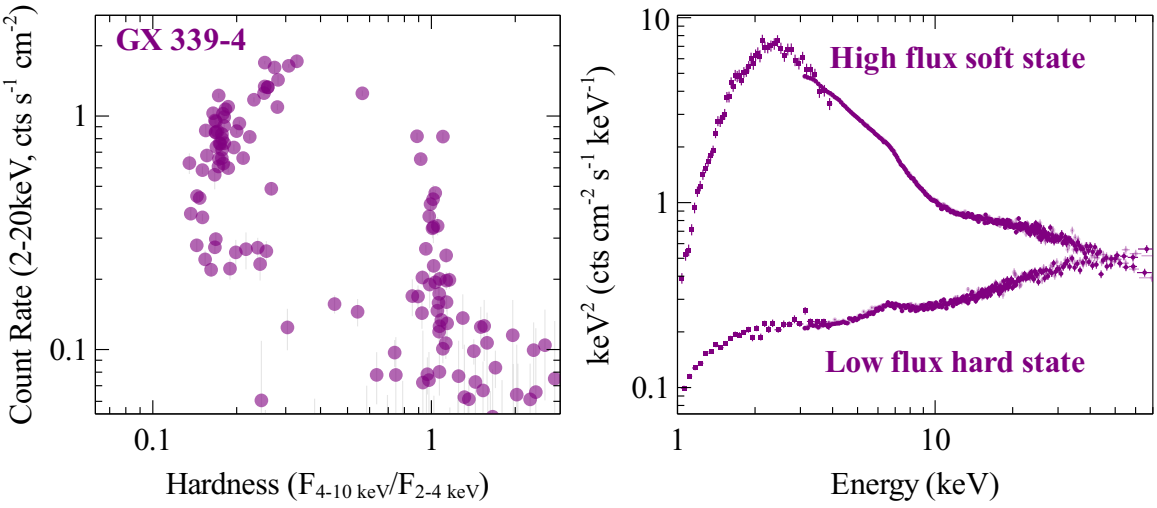

Fig. 1.3 Left: the weekly *MAXI* hardness-intensity diagram (HID) for the 2009-2018 period of GX 339−4. Right: The *NuSTAR* and *Swift* spectra of GX 339−4 during a very high flux soft state and a low flux hard state in 2015.

the same source that is associated with a supergiant star. However the star itself is not able to produce such strong X-ray emission [149]. In 1971, Bolton [28], Webster and Murdin [321] identified Cyg X-1 as a binary system where the central object has to be a BH with a high predicted mass by analysing the spectra of the moving companion star. The most recent study of Cyg X-1 shows that the central BH has a mass of $M_{\rm BH}/M_\odot = m_{\rm BH} = 14.8 \pm 1.0$ [218]. Ever since the discovery of Cyg X-1, more stellar-mass BHs have been found in our Galaxy [e.g. GX 339−4, 30] and in nearby galaxies [e.g. M33 X-7, 219].

Black Hole Transients

Many BH XRBs show transient events that are characterised by outbursts in the X-ray band. Some outbursts last for only few weeks [e.g. MAXI J1659−152, 199] while some last for years before they return to the quiescent state [e.g. Swift J1753.5−0127, 281]. See Fig. 1.2 for X-ray light curves of some BH XRBs during their historical outbursts.

The existence of two different accretion states in BH XRBs was first realized in the X-ray emission of Cyg X-1 [215]. Its X-ray spectrum can change from a soft spectrum characterized by a disc thermal component to a hard spectrum characterized by a power-law continuum. Such a transition is commonly seen during an outburst. Many BH XRBs show a 'Q'-shaped pattern in the hardness-intensity diagram (HID) during their outbursts. For example, the left panel of Fig. 1.3 shows the HID for the 2009-2018 period of GX 339−4 from *MAXI*. The hardness in this figure is defined by the flux ratio between the 4–10 keV and 2–4 keV bands. An outburst usually starts from the low flux hard state (bottom right) in the HID diagram.

As the flux rises, the spectrum turns softer and reaches the high flux soft state (top left) in the HID diagram. The right panel of Fig. 1.3 shows the spectra of GX 339−4 in the hard and soft states correspondingly. In some cases, some BH transients approach the soft state but never reach the canonical soft state where they are supposed to show a high X-ray flux and the spectra are dominated by the disc thermal component [e.g. GRS 1716−249 in 2016–2017, 19]. These outbursts are often referred to as 'failed' outbursts.

In Chapter 2, I present a detailed analysis of the spectra of GX 339−4 in the low flux hard and high flux soft states; in Chapter 3, I analyse the spectra of GRS 1716−249 in the hard and intermediate states.

1.2 X-ray Missions

High energy X-rays are the primary tool for studying the innermost environment of AGN and BH XRBs as they are produced from the area closest to the central BHs and able to penetrate the absorbing materials in the line of sight easily. In this section, I first introduce the most commonly used mirror and detector designs for X-ray observatories. Second, I will introduce the X-ray observatories where spectra considered in my work are collected from – *XMM-Newton*, *NuSTAR*, and *Swift*.

1.2.1 X-ray Mirrors and Detectors

X-ray mirrors are designed to make sure all the reflections occur at grazing incidence based on the idea of the total external reflection. The most common design is called *Wolter type-I* where a paraboloid and a hyperboloid are used to focus the X-rays onto the detector. *Wolter type-I* has been used on several historical X-ray observatories, such as *ROSAT* and *ASCA*.

Two types of detectors are commonly used in X-ray observatories: proportional counters and solid state detectors. A proportional counter is based on the principle of electron cascade, where the incoming X-rays cause photo-ionisation in the filling gas (mainly neon or argon). The energetic photo-electrons ionise nearby atoms and produce a certain number of primary electrons, requiring an energy of 25 eV for each electron-ion pair. The detector counts the number of these primary electrons by counting the number of secondary electrons in the wire anode, the number of which are proportional to the number and energy of the primary electrons. For example, a 10 keV incoming photon produces 400 primary electrons. Considering a Poisson distribution, the uncertainty of the number of the primary electrons is 20, yielding a moderate spectral energy resolution of 0.5 keV at 10 keV. Such a technology has been used on several X-ray observatories. For example, the Gas Slit Camera (GSC) on the Monitor of All-sky X-ray Image [*MAXI*, 172] is equipped with a proportional counter and is able to provide light curves between 2–20 keV on time intervals ranging from a day to a few months. In Chapter 2 and 3, *MAXI* light curves are used to show long-term X-ray variability of BH XRBs. A solid state charge-coupled device (CCD) detector is similar to a proportional counter but has a much higher spectral resolution due to lower energy threshold to generate pairs in a semiconductor. Such a technology has been commonly used on more recent X-ray missions, such as *Chandra*, *XMM-Newton*, and *Suzaku*.

Name	Launch Date	Name	Energy Resolution	Effective Area
XMM-Newton	10 December, 1999	EPIC-pn	0.15 keV	1200 cm^2@ 2 keV
		EPIC-MOS	0.15 keV	500cm^2 @ 2 keV
NuSTAR	13 June, 2012	FPM	0.4 keV	400 cm^2@ 10 keV
Swift	20 November, 2004	XRT	0.2 keV	120 cm^2@ 1.2 keV

Table 1.1 A summary of X-ray missions where the X-ray spectra considered in this work are from. The unit of the effective area is cm^2. The fourth column shows the energy resolutions at 6 keV.

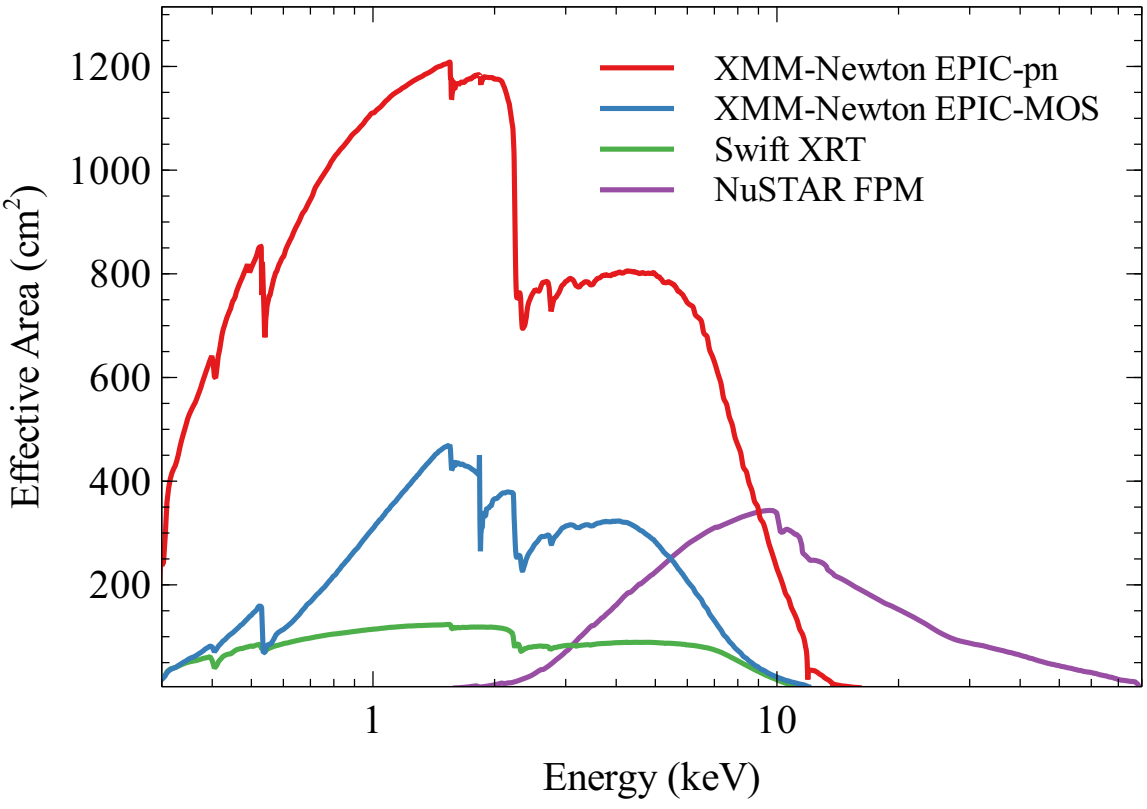

Fig. 1.4 The on-axis effective area of the X-ray detectors used in this work. Note that *XMM-Newton* has two EPIC-MOS cameras and *NuSTAR* has two FPM cameras.

1.2.2 X-ray Observatories in the Moderate (CCD) Resolution Era

XMM-Newton

The *XMM-Newton* observatory [121] was launched in 1999 by the European Space Agency (ESA) aiming to provide a large effective area in the 0.5–10 keV band. *XMM-Newton* carries three CCD cameras. The EPIC-pn CCD camera [285] reaches an on-axis effective area of 1200 cm^2 around 2 keV and the two EPIC-MOS [metal oxide semiconductor, 301] cameras reach a combined on-axis effective area of 1000 cm^2 in the same energy band. In total, the three EPIC CCD cameras are able to reach a total effective area of 2200 cm^2 around 2 keV, making it the X-ray observatory with the highest effective area [1]. See Fig. 1.4 for comparison of effective area of different detectors. Each CCD camera is equipped with 58 nested thin coaxial *Walter type-I* mirrors. The width of the point spread function (PSF) is about 4–6 arcsecond FWHM at 1.5 keV.

In addition to the three main imaging cameras, two of the *Wolter type-I* telescopes for EPIC-MOS cameras are also equipped with reflection grating arrays (RGS). The RGS instruments focus more on the soft X-ray band (0.3–2.5 keV) and have 10 times smaller effective area than EPIC. However, they have a much higher energy resolution (e.g. 1700 km s^{-1} at 17 Å for the first orders). An optical/UV monitor (OM) is co-aligned with the X-ray telescopes on *XMM-Newton*. The OM covers 6 energy bands from 180 to 600 nm. Thanks to OM, *XMM-Newton* is able to provide strictly simultaneous optical/UV–X-ray data.

NuSTAR

The *NuSTAR* observatory [108] was launched by the National Aeronautics and Space Administration (NASA) in 2012, focusing on the hard X-ray energy band (3–78 keV). *NuSTAR* is the very first X-ray telescope which is able to providing hard X-ray focusing images. The two focal plane modules (FPMs) of *NuSTAR* are equipped with a conical-approximation mirror of the *Wolter type-I* design, consisting of 133 concentric mirrors coated with Pt/SiC and W/Si multilayers. Two FPM cameras are able to reach an effective area of 800 cm^2 in total at 10 keV. The energy resolution of FPM is around 0.4 keV FWHM at 6 keV. FPMs have a triggered readout, which is similar to proportional counters. Therefore, one of the advantages of *NuSTAR* is that there are no pile-up effects in most observations [2].

[1] The X-ray telescope *NICER* on the International Space Station has an effective area of 2000 cm^2, making it the individual instrument with the highest effective area.

[2] Pile-up effects are due to the limited readout frequency of the detectors. When the brightness of the source exceeds the pile-up threshold, multiple photons may hit the same pixel between two readouts. The signal will be mistaken as one single higher energy photon.

Swift

The *Swift* X-ray observatory was launched by NASA dedicated for the study of Gamma-ray Bursts (GRBs) in 2004. The Burst Alert Telescope [BAT, 18] covers a large fraction of the sky at a time and is able to detect new GRBs in the 15–150 keV band. Follow-up observations can be taken in the soft energy band (0.5–8 keV) with the X-ray Telescope [XRT, 36] and in the UV/optical band with the UV/Optical Telescope [UVOT, 261]. The other major science of *Swift* is to monitor and detector new X-ray sources by conducting long-term all sky surveys [e.g. 216]. *Swift* works in collaboration with *NuSTAR* by providing 2–3 ks snapshot observations for most of the *NuSTAR* observations. This work will mainly use the data from XRT to back up the *NuSTAR* observations in the soft X-ray band.

1.3 An Overview of Accretion Disc Models

In this section, I present a brief introduction of some classical theories based on the standard α-disc model. These disc models will help us to better understand the measurements of some of the disc properties in later work (e.g. the density of the inner disc).

1.3.1 Relativistic Standard Accretion Disc Model

The classical disc model for the description of a geometrically thin and optically thick [3] relativistic accretion disc is the Novikov-Throne model [214, 221], which is a relativistic extension of the standard Shakura-Sunyaev disc model [277] in the Kerr geometry [141]. In Kerr metric, only two parameters describe the spacetime around a BH – BH mass $M_{\rm BH}$ and the dimensionless BH spin parameter $a_* = J/M_{\rm BH}^2 c$, where J is the angular momentum of the BH and c is the velocity of light. The other two fundamental parameters in the Novikov-Throne model are the BH mass accretion rate $\dot{M}$ and the viscosity parameter α, similar as in Shakura and Sunyaev [277].

In the Novikov-Throne model, the matter in the disc is accreting towards the centre due to viscous stress and the angular momentum is transported outwards. The stress is a fraction of the pressure inside the disc. The radiation pressure dominates over the gas pressure inside the disc when $\dot{M}/\dot{M}_{\rm Edd} \gtrapprox 0.01$, where $\dot{M}_{\rm Edd}$ is the mass accretion rate at the Eddington limit [4]. Then the disc thickness is regulated by the vertical radiation flux. Assuming each annulus of the disc is optically thick and radiates a black-body spectrum ($F \propto T^4$), one will get the maximum surface temperature of $T \approx 10^5$ K for AGN and $T \approx 10^7$ K for BH XRBs. The major success of the standard thin disc model is the predicted temperatures do match the observed UV emission in AGN and the X-ray emission in the soft state of BH XRBs.

However, the standard thin disc model is based on several fundamental assumptions:

- The spacetime is stationary, axisymmetric, and mirror-symmetric with respect to the midplane of the disc.
- The self-gravity of the disc is ignored.

[3] A geometrically thin disc requires $h/r \ll 1$, where h is the semi-thickness of the disc at a radius r. An optically thick disc requires $l = 1/(\sigma n) \ll h$, where l is the photon mean free path, σ is the cross section, and n is the number density of scattering particles.

[4] The Eddington limit $L_{\rm Edd}$ is the maximum luminosity of an object where the radiation force and the gravitational force are equal. For pure ionised hydrogen, $L_{\rm Edd} = \frac{4\pi G M m_p c}{\sigma_T}$, where M is the mass of the central object, $m_{\rm p}$ is the mass of a proton, and σ_T is the Thomson scattering cross section for an electron. The mass accretion rate at Eddington limit is $\dot{M}_{\rm Edd} c^2 = L_{\rm Edd}/\epsilon$, where ϵ is the accretion efficiency.

- The inner edge of the disc is at the innermost stable circular orbit (ISCO). The ISCO is the smallest circular orbit where a particle can orbit stably around a massive object in General Relativity. The matters inside the ISCO are plunged into the BH with no further radiation.
- The solution is time-averaged over a timescale t that is long enough to neglect the inhomogeneities in the system.
- Radial heat transport is ignored. The energy is radiated only from the disc surface locally.
- Magnetic fields are ignored.
- Returning radiation to the disc due to the light-bending effects is not considered.
- A uniform density is considered in the vertical direction of the disc.

Some of these fundamental assumptions are only appropriate for certain circumstances. More physics are required by observations or some assumptions need to be relaxed. For example, 1) it is not necessary that the inner edge of the accretion disc is at ISCO. The inner disc radius of a BH XRB in the hard state ($L_{\rm X}/L_{\rm Edd} < 1\%$) can vary between 1–100 $r_{\rm ISCO}$ [e.g. 90]. 2) There is increasing evidence for ultra-fast outflows in sources that are accreting around or likely above the Eddington limit [236], which provides a way for the apparent accretion rate to exceed the Eddington limit and releases the energy of the disc in the form of outflows. Therefore the disc model needs to be extended to the super-critical accretion region by taking outflows into consideration. 3) In the standard models, the energy released through viscosity is radiated away locally. However, a radiatively-inefficient disc needs to be considered too for objects that have a very low accretion rate. One model for a radiatively-inefficient disc is an optically-thin advection-dominated accretion flow [e.g. 207]. This model successfully explains the X-ray emission from Sgr A*, where the high energy emission is underestimated by the standard low-accretion disc model [208]. 4) MHD simulations show that the properties of the disc can have distributions instead of being uniform in the vertical direction [e.g. 302]. 5) One of the biggest problems is the neglected coronal region in the model. This will be discussed in section 1.3.2.

1.3.2 Accretion Disc Corona

It has been realized for a very long time that the spectra of both Seyfert galaxies and BH XRBs can not be simply described by only the disc thermal component [156, 103, 104, 201].

This additional component shows a power-law shape with a high energy exponential cutoff and is believed to be from the corona above the accretion disc. This spectral shape can be explained by the Comptonisation process of disc seed photons in the hot coronal regions. However the physics of the corona is very complex. One of the difficulties is the exchange of energy between the corona and the disc. The magnetic field of the disc may play a vital role in the energy transfer and the origin of the corona [e.g. 140]. In this model, the magnetic disc corona is expected to be rapidly variable as well.

Haardt and Maraschi [103] shows that a significant fraction of disc energy has to be dissipated in the corona in order to account for the typical spectral energy distribution (SED) of a Sy1 galaxy. This fraction parameter is called f hereafter. The co-existence of the disc thermal component and the coronal power-law component not only successfully explains the shape of the UV–X-ray SED of AGN and the X-ray spectra of BH XRBs but also provides possibilities for the existence of the reprocess emission ('reflection') from 'cold' materials predicted by Guilbert and Rees [102]. The reflection spectra in AGN and XRBs were later found by Fabian et al. [67] and Tanaka et al. [291]. More introduction about reflection spectra from the discs can be found in Section 1.4.1. Svensson and Zdziarski [288] carefully re-calculated the solutions of the standard thin disc model by introducing the factor f. A non-zero f will result in a colder and denser disc with larger optical depths compared to the Shakura and Sunyaev [277] thin disc model. More details can be found in the discussion section of Chapter 2.

1.4 Relativistic Disc Reflection Spectra

Relativistic studies of the innermost accretion on BHs started with the discovery of the broad Fe Kα emission lines from the discs of accreting BHs [67, 291]. These features are the reprocessed emission of the hot coronal emission from the disc surfaces. The modelling of disc reflection spectra are being carried out in two aspects at the same time: 1) the calculation of relativistic effects; 2) the modelling of ionised disc reflection spectra in the disc frame. They will be introduced separately in section 1.4.1. Reflection-based studies of the BH-corona-disc system will be introduced in section 1.4.2, 1.4.3, and 1.4.4 respectively. Note that I do not emphasize the difference between the reflection spectra from BH XRBs and AGN as they show very similar spectral features despite their very different BH masses. Miller [183], Fabian [61] and Dauser et al. [48] provided very good reviews of relativistic disc reflection spectra from both theoretical and observational points of view.

1.4.1 Relativistic Disc Reflection Spectroscopy

Relativistic Modelling of the Broad Fe Kα Emission Lines

The broad Fe Kα emission line in an AGN was first identified in the *ASCA* spectrum of the Seyfert 1.2 galaxy MCG-6−30−15 [291]. The broad band spectra of MCG-6−30−15 extracted from recent simultaneous *XMM-Newton* and *NuSTAR* observations are shown in Fig. 1.5. The iron band [5] of both *XMM-Newton* and *NuSTAR* spectra show a very complex emission feature. The peak of the emission feature is at 6.4 keV in the rest frame of the source, corresponding to the Fe Kα [6] emission line in a low ionisation state [$\xi = 10\,\mathrm{erg\,cm\,s^{-1}}$, 165]. The red wing of the broad emission component extends to 3 keV and the blue wing extends to 7 keV. In addition to the broad emission component, the spectra of MCG-6−30−15 shows evidence for a narrow core in the Fe K emission profile, indicating a cold distant reflector [328, 165].

Ever since the first discovery of the broad Fe Kα emission line in MCG-6−30−15, a lot of effort has been made to look for other similar sources. Some astronomers work on detailed reflection spectral analysis for individual AGN, such as 1H0707−495 [e.g. 65, 70], Mrk 335 [e.g. 151, 79, 314, 231], NGC 3783 [e.g. 33, 248], NGC 1365 [e.g. 258, 318], IRAS 00521−7054 [e.g. 290, 257, 315], and Swift J2127.4+5654 [e.g. 192, 165]. Some work on systematic search in the archive [e.g. 203] or the global picture by stacking the spectra of Seyfert galaxies in the source frame [e.g. 40]. Broad Fe Kα emission line is not only found in AGN but also in

[5] The 4–10 keV band is referred to as the iron band in this thesis.

[6] K means K-shell. Kα (Kβ) represents the emission line corresponding to the 2p-1s (3p-1s) transition.

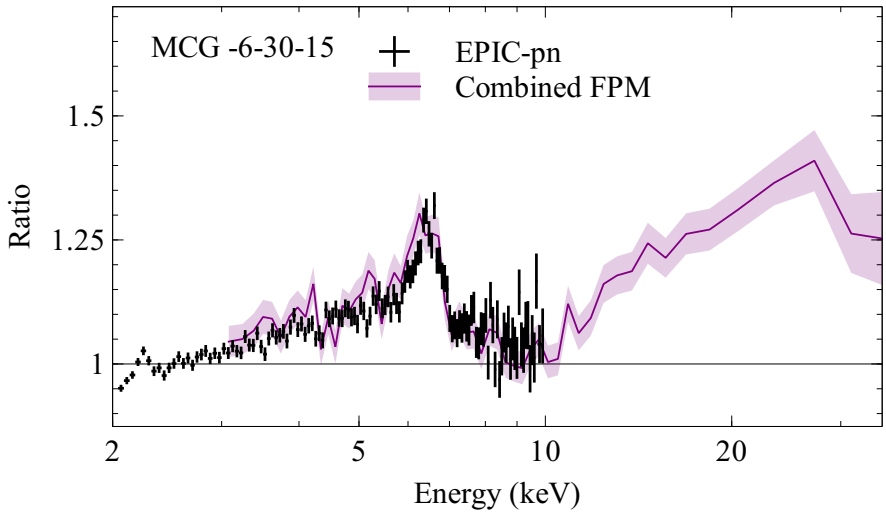

Fig. 1.5 A ratio plot of the *NuSTAR* and *XMM-Newton* spectra of MCG-6−30−15 fit with a Galactic absorbed power-law model. The *NuSTAR* and the *XMM-Newton* observations are taken simultaneously in 2013.

BH XRBs [e.g. 17, 67, 14, 168, 185, 191, 267, 182, 184, 283], indicating a similar physics in the accretion discs of stellar-mass BHs and SMBHs despite their very different BH masses.

The explanation for the broadening of the iron emission lines is the relativistic effects in the vicinity of a BH [e.g. 67]. Fig. 1.6 presents the emission lines from different regions of the disc. The rest-frame energy of the Fe Kα emission line is 6.4 keV in a neutral accretion disc, marked by the gray dashed line in the figure. The dashed emission line model shows the emission from 100$r_{\rm g}$ of the disc and has a double-peak line profile due to Doppler effects. The blue wing corresponds to the approaching side of the orbiting disc and the red wing corresponds to the receding side. The blue wing has a higher intensity than the red wing because of the relativistic beaming effect. The solid line model shows the emission from the innermost region of the disc (2–10$r_{\rm g}$). The line profile is redshifted due to stronger gravitational redshift compared to that from the regions farther away from the BH. By combining the emission from different regions of the disc, one will obtain a very broad emission line, as seen in Fig. 1.5. The position of the red wing depends on the inner radius of the disc and the position of the blue wing depends on the inclination angle of the disc. See Laor [150] and Dauser et al. [50] for more detailed calculations of the relativistic effects in the disc.

Rest-Frame Ionised Disc Reflection Spectral Modelling

The other important aspect of the relativistic disc reflection spectral modelling is to calculate the reflection spectrum of an ionised disc in the disc frame. A lot of effort has been made in this topic [e.g. 268, 211, 12, 56, 265, 84, 85]. Among them, the work of Ross et al. [266] was distilled into the `reflionx` code [262–264], which was widely used in data analysis. More recently, a more updated version of the reflection model `xillver` written by García and Kallman [84] becomes available. The `xillver` model uses more updated atomic physics for absorption, excitation and emission processes in Kallman and Bautista [131], and allows more chemical elements and angle dependency compared with previous models. I will mainly introduce the rest-frame disc reflection spectra by presenting the `xillver` [85] models in this section.

All of these ionised disc reflection spectral models assume a constant-density slab parallel to the thin disc plane under hydro-static equilibrium. One side of the slab is illuminated by incoming photons with a certain spectral shape (e.g. a power law with a high energy exponential cutoff or a thermal Comptonisation model). These models calculate the reflected spectra by considering both absorption and emission processes. For example, Fig. 1.7 presents some rest-frame disc reflection spectra for different ionisation states of the disc calculated by `xillver`. The ionisation parameter increases from bottom to top. A simple power law-shaped input spectrum of $\Gamma = 2$ is considered [7]. Below 10 keV, the opacity of the slab is dominated by the photo-electric opacity. Therefore there is a mixture of absorption and emission features. The ions in the slab are excited by the incoming photons. The energy is released by emitting a photon or an Auger electron. The probability of emitting a photon over an Auger electron is proportional to Z^4, where Z is the number of the nuclear charge. This process makes the Fe K lines the strongest lines in the reflection spectrum. However, the cross section of photon-electric absorption is proportional to E^{-3} while the cross section of electron scattering is roughly constant with energy. Therefore, the electron scattering process dominates the opacity above 10 keV. These high energy photons are scattered back out of the slab and produce a 'hump' feature above 10 keV, which is called the reflection Compton hump. The Compton hump was observationally confirmed shortly after the discovery of the broad Fe Kα emission line when the spectral hardening is shown above 10 keV in the *Ginga* spectra of Sy1 AGN [e.g. 242, 204].

The ionisation of the disc is the main parameter in the model. In this work, the ionisation parameter is defined as $\xi = \frac{L}{nr^2}$, where L is the illuminating luminosity in the X-ray band

[7] The power-law model is defined as $F = NE^{-\Gamma}$, where F is in the flux unit (cts cm^{-2} s^{-1} keV^{-1}) and N is normalization.

[8], n is the number density and r is the distance between the illuminating source and the ionised region. The unit of the ionisation parameter is erg cm s^{-1} in this work. Here I discuss how the disc ionisation parameter changes the rest-frame disc reflection spectrum. First, the incoming photons heat up the slab and are absorbed or scattered to lower energies when going through the slab. The heating process of the slab drops at a certain optical depth where the cooling process due to recombination processes dominates. Second, a higher ionisation parameter ξ means higher illuminating flux L, assuming the same n and r. This temperature drop occurs at deeper depths when the illuminating flux/disc ionisation is higher.

Different disc ionisation causes a different temperature profile of the slab and thus affects the reflection spectrum. For example, 1) the temperature of the slab surface (Thomson depth $\tau_T < 10^{-2}$) is approximately 2×10^6 K for $\log(\xi) = 1$, assuming an illuminating power-law spectrum with $\Gamma = 2.0$ [83]. The temperature remains constant in the deeper regions of the slab until $\tau_T \approx 0.1$ and drops to 2×10^5 K. 2) At $\log(\xi) = 2$, a 10 times higher temperature is found in the surface of the slab. The temperature drops at a deeper optical depth ($\tau_T \approx 2$). In this higher-temperature more-ionised slab, excitations of more elements occur, such as Mg, Al, Si, S, Ar and Ca. Therefore there are more lines between 1–6 keV. The spectrum starts to show absorption features of highly ionised ions such as Fe XXVI and Fe XXV. See Fig. 1.7 for comparison of different reflection spectra. 3) At an even higher ionisation state (e.g. $\log(\xi) > 3$), the emission line is broader due to stronger velocity dispersion. The slab becomes so ionised that there are barely emission or absorption features. The continuum of the reflection spectrum is similar with the input continuum.

There are also other factors that affect the slab temperature profile and thus change the reflection spectra. For example, the transition of the temperature happens at deeper regions for softer input spectrum. More details can be found in García et al. [83].

Relativistic Disc Reflection Spectra

In this section, I briefly introduce the relativistic reflection spectrum by presenting the model package `relxill` [83]. The `relxill` model package includes both the calculation of relativistic effects of the disc [`relconv`, 50] and the rest-frame disc reflection model [`xillver`, 84].

Fig. 1.8 shows the relativistic disc reflection spectral models calculated by `relxilllp`, part of the `relxill` model package. These models assume a maximum BH spin, a disc inclination angle of 30°, and a simple point-like lamp-post corona 6 $r_{\rm g}$ above the disc. See

[8] The `reflionx` model calculates L between 1 eV–1 MeV [264] and the `xillver` model considers 100 eV–1 MeV [47].

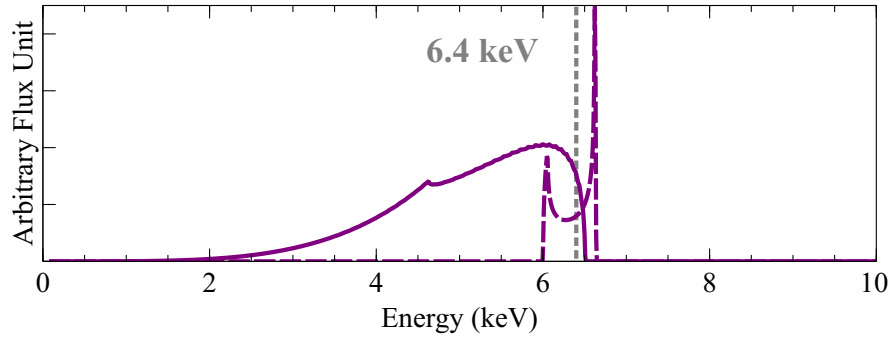

Fig. 1.6 Relativistic emission line models calculated by `relline`. The gray dotted line shows the rest frame energy of the Fe Kα emission line ($E_{\rm line} = 6.4$ keV). The dashed line shows the emission line from $R \approx 100 r_{\rm g}$ of a disc. The double-peak shape of the line profile is due to the Doppler Effects and the higher flux in the blue wing is due to the relativistic beaming. The solid line shows the emission line from $R \approx 2 - 10 r_{\rm g}$. The line profile is redshifted compared to the one from $R \approx 100 r_{\rm g}$ due to stronger gravitational redshift. A black hole spin of $a_* = 0.998$, a disc inclination angle of $i = 30°$, and a power-law disc emissvity profile of $q = 3$ are assumed.

Section 1.4.2 and 1.4.3 for more introduction about these parameters. As shown in the figure, the narrow emission lines in the rest-frame spectra in Fig. 1.7 are broadened and skewed. The prominent feature between 1–10 keV, where the effective area of most current soft X-ray CCDs peaks, is the broad Fe Kα emission line. The reflection Compton hump still remains above 10 keV after the relativistic blurring. See Fig. 1.5 for an example of the reflection spectrum in MCG -6−30−15. In addition to the broad Fe Kα emission line, the *NuSTAR* spectrum of MCG -6−30−15 shows a reflection Compton hump above 10 keV.

The models in the `relxill` package have two groups of parameters: one for the relativistic modelling and one for the rest-frame reflection spectral modelling. The parameters for the relativistic modelling are the disc emissivity profile, the BH spin a_*, the inner and outer disc radius $R_{\rm in,out}$, and the disc inclination angle i. Following is the introduction of these model parameters: 1) the emissivity profile of the disc can be set to be a phenomenological broken power law with three parameters (the inner emissivity index q_1, the outer emissivity index q_2, and the break radius $r_{\rm break}$). Alternatively, a simple point-like isotropic lamp-post corona can be used in the model `relxilllp`. The emissivity profile is then defined by only one parameter – the height of the corona above the disc h. A broken power-law emissivity profile is just an approximation of the emissivity profile in the lamp-post geometry. More details about the disc emissivity profile can be found in section 1.4.2. 2) The inner disc radius $r_{\rm in}$ is usually assumed to be at the ISCO. However this assumption is allowed to be relaxed in certain circumstances (e.g. the low flux hard state of BH XRBs). The red wing of the broad

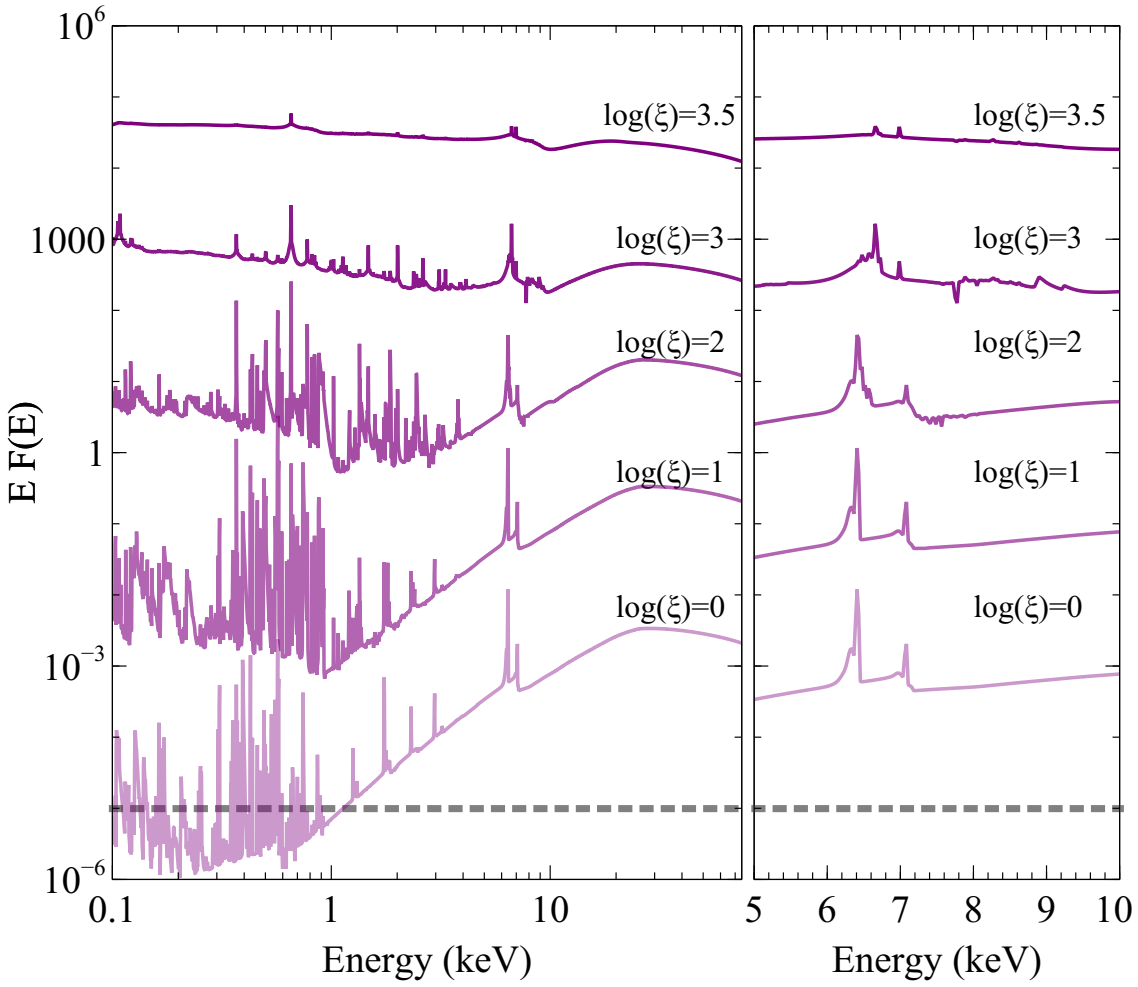

Fig. 1.7 Left: rest-frame disc reflection spectra for different ionisation parameters calculated by `xillver`. The input spectrum is a power-law model with $\Gamma = 2$ (dashed line). Right: a zoom-in figure of the spectra in the iron band.

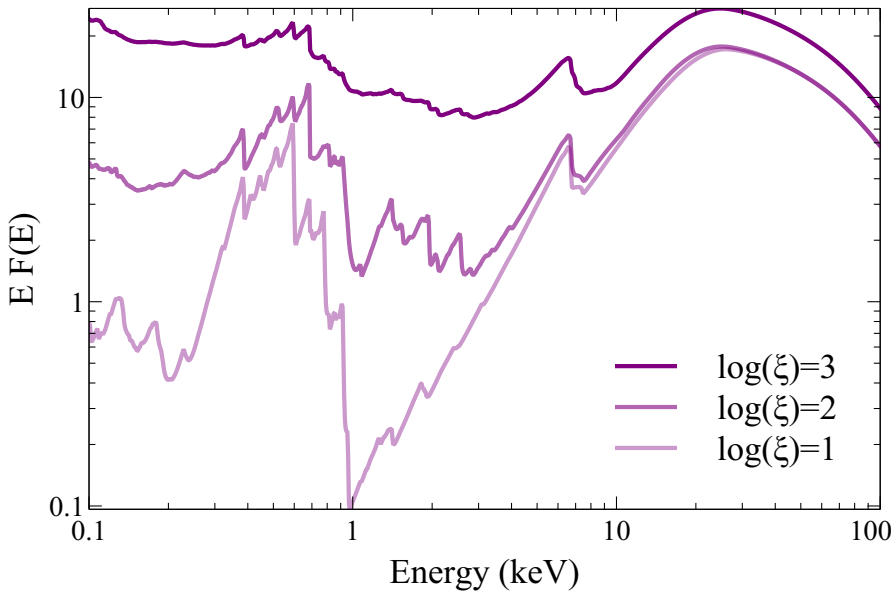

Fig. 1.8 Relativistic disc reflection spectral models calculated by `relxilllp` for different ionisation parameters, assuming a maximum BH spin of $a_* = 0.998$, a disc inclination angle of 30°, and a simple lamp-post corona $6r_{\rm g}$ above the disc.

Fe Kα emission line is sensitive to the inner radius of the disc or the BH spin parameter (see Section 1.4.3 for more details). All the parameters of length are reported in the unit of the gravitational radii ($r_{\rm g} = \frac{GM_{\rm BH}}{c^2}$). The outer radius is assumed to be at 400 r_g in this work as it is not sensitive to the spectral fitting.

The parameters for the rest-frame disc reflection model are the input illuminating spectrum, the disc ionisation ξ, and the disc iron abundance $Z_{\rm Fe}$. Following is the introduction of these model parameters: 1) the illuminating spectrum from the corona can be either a phenomenological simple power law (Γ) with a high energy cutoff ($E_{\rm cut}$) or a more physical model as in `relxillcp`, where the thermal Comptonisation model `nthcomp` [343] is considered. A power law with an exponential high energy cutoff is just an approximation of the Comptonisation model. See Section 1.3.2 for more introduction of the coronal emission. The `nthcomp` model has three main parameters: the photon index Γ, the disc seed photon temperature $kT_{\rm bb}$, and the coronal electron temperature $kT_{\rm e}$. In `nthcomp`, disc photons of $kT_{\rm bb}$ are up-scattered by hotter electrons in the coronal region. These coronal electrons are in a thermal distribution parameterised by the electron temperature $kT_{\rm e}$. The `relxillcp` model assumes a fixed disc photon temperature of $kT_{\rm bb} = 0.05$ keV. 2) More details of the disc ionisation parameter can be found in the previous session of Section 1.4.1. 3) The disc iron abundance parameter is reported in the unit of the solar abundance in the `relxill` model package. The solar abundances in `relxill` are from Grevesse and Sauval [96] and

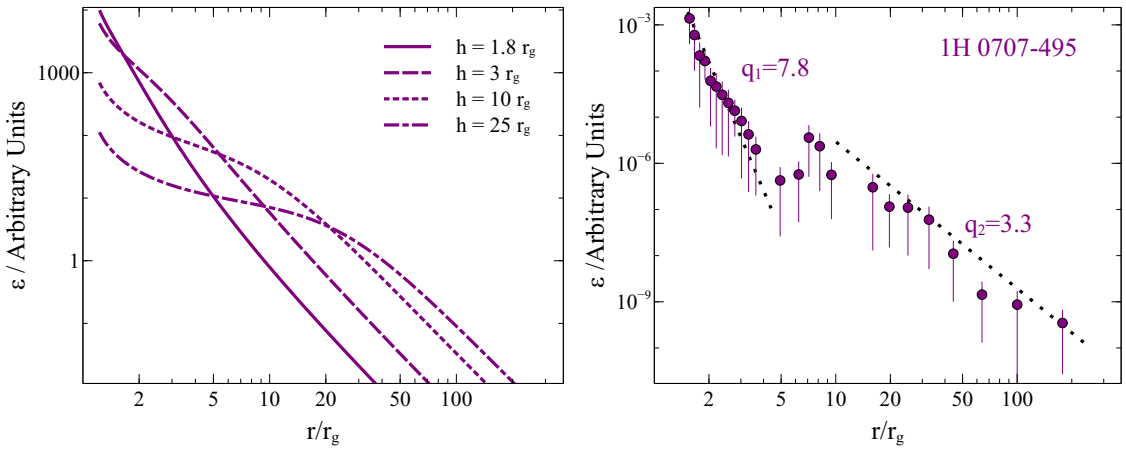

Fig. 1.9 Left: radial profiles of the irradiating flux from a lamp-post corona at different heights onto a thin disc calculated by Dauser et al. [49]. A BH spin of $a_* = 0.998$ and a power-law continuum with $\Gamma = 2$ are assumed. Right: the observed emissivity profile of the NLS1 1H 0707−495 obtained by Wilkins and Fabian [323] analysing its *XMM-Newton* observations. 1H 0707−495 has a BH spin of $a_* > 0.98$ [50].

the iron abundance is defined as 2.5×10^{-5} of the hydrogen abundance. Alternatively, the `reflionx` model is used to model the rest-frame reflection spectra in part of this work because `reflionx` allows a larger range of disc iron abundance or disc density parameters. The `reflionx` model uses the solar abundances in Morrison and McCammon [196]. See each chapter for more details.

1.4.2 Disc Reflection and the Corona

The Size of the Coronal Region

Fabian et al. [67] realized that the disc reflection process will naturally produce a reverberation (resonance/short-time variability) lag between the continuum emission from the coronal region and the reflection from the disc. The first X-ray reverberation lag was found in the narrow-line Seyfert 1 galaxy (NLS1) 1H 0707−495. A high frequency reverberation lag of ≈ 30s was found between the soft emission and the coronal emission in this source [9]. This lag is consistent with a compact coronal region within a few $r_{\rm g}$ [70]. Similar lags are also found for the broad Fe Kα emission lines [340] and the Compton hump [339]. These reverberation lags have been found in multiple sources, including Seyfert AGN [e.g. 51, 132] and BH XRBs in the hard state [138].

[9] The 0.3–1 keV soft emission lags behind the 1–4 keV emission.

In addition to the reverberation studies, we are able to estimate the size of the coronal region by modelling the disc reflection spectra. The left panel of Fig. 1.9 presents the irradiating flux from a simple point-like isotropic corona onto a thin disc calculated by Dauser et al. [46] based on their relativistic ray-tracing codes. The corona is located on the spin axis of the BH, probably the base of the jet [e.g. 143]. This scenario of the corona is called the lamp-post geometry. When the corona is only $1.8r_{\rm g}$ above the disc, the radial profile of the irradiating flux from the corona to the disc decreases steeply. By contrast, when the corona is more than $10r_{\rm g}$ above the disc, the irradiating flux decreases more slowly with r. When r approaches infinity, the flux is approximately $F \propto r^{-3}$, consistent with the emissivity in a flat spacetime [49]. The emissivity profile in the lamp-post scenario can be approximated by a broken power law with three parameters (the inner index q_1, the outer index q_2, and the break radius $r_{\rm break}$).

The right panel of Fig. 1.9 shows the observed emissivity profile of the NLS1 1H 0707−495 obtained by Wilkins and Fabian [323]. This observed emissivity profile is obtained by modelling the broad Fe Kα emission line in 1H 0707−495 with multiple disc line models `laor` [150]. Each emission line model accounts for emission from a certain region of the disc. The emissivity profile can be described by a broken power law with $q_1 = 7.8$ and $q_2 = 3.3$. The steepness of the emissivity profile is consistent with the result of ray-tracing for a compact coronal region within $5r_{\rm g}$ [70, 50].

The Electron Temperature of the Corona

Understanding the spectral shape of the coronal emission and its effects on the resulting disc reflection spectra is essential for understanding the physics of the corona.

The left panel of Fig. 1.10 presents the disc reflection models for different coronal electron temperature $kT_{\rm e}$ calculated by `relxillcp`. The `relxillcp` model assumes a corona consisting of hot electrons in a thermal distribution parameterised by $kT_{\rm e}$ [10]. The maximum value of $kT_{\rm e}$ in a thermal corona is limited by the run-away process of electron-positron pair production [287, 333].

However, there is increasing evidence for AGN with a much lower temperature corona than the expectation for a thermal corona [137, 298, 311, 292, 125]. One of the possible explanations is a mixed of thermal and non-thermal distributions of electrons in the coronal region [64]. Therefore AGN with low coronal temperatures are particularly interesting targets to study the corona. The right panel of Fig. 1.10 presents the *NuSTAR* spectra of the BH XRB MAXI J1535−571 and the Sy1 1H 0419−577. They share similarities in the X-ray

[10] The value of the high energy cutoff $E_{\rm cut}$ is approximately 2-3 times of $kT_{\rm e}$, depending on the optical depth of the corona.

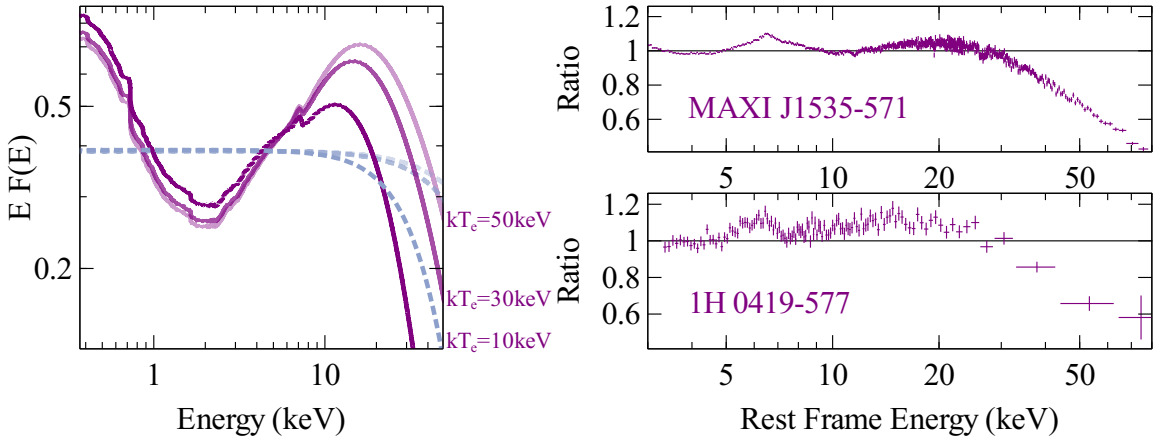

Fig. 1.10 Left: the relativistic disc reflection spectra (solid lines) for different coronal electron temperature $kT_{\rm e}$. The dashed lines show the corresponding illuminating spectra from the corona for different $kT_{\rm e}$. Right: the ratio plots of the *NuSTAR* combined FPM spectra of the BH XRB MAXI J1535−571 in the hard state and the Sy1 1H 0419−577 fit with Galactic absorbed power-law models. Despite very different BH mass, MAXI J1535−571 and 1H 0419−577 show similar broad Fe Kα emission line, reflection Compton hump and low high energy cut-off. See the text for more details.

spectra, such as a broad Fe Kα emission line. The coronal emission in these two sources shows a similar electron temperature despite their very different BH masses [e.g. $kT_{\rm e}$=10–30 keV, 329, 125]. At such low $kT_{\rm e}$, the hard band reflection spectrum is suppressed at higher energies, as shown in the left panel of Fig. 1.10. During the spectral analysis, there might be degeneracy between the Compton hump in a reflection-dominated spectrum and a 'true' low-temperature coronal continuum. Therefore, a careful broad band reflection spectral analysis is necessary for the measurements of the continuum emission. See Chapter 3 for an example of real data analysis concerning the measurement of the low coronal temperature in the Sy1 1H 0419−577.

1.4.3 Disc Reflection and the Spin of the Black Hole

One of the major purposes for developing the relativistic disc reflection spectroscopy is to measure the spins of BHs. A precise and accurate measurement of the BH spin is important in different aspects. For example, the spin of a SMBH may be able to drive jet that can extend to the galaxy scale [e.g. 23]. The distribution of the BH spins in AGN is also related with the growth of SMBHs [e.g. 310]: a high BH spin resulting from BH-disc accretion and a lower BH spin resulting from the mergers of smaller BHs or chaotic accretion. From the fundamental physics point of view, the method used to measure BH spins can be used to

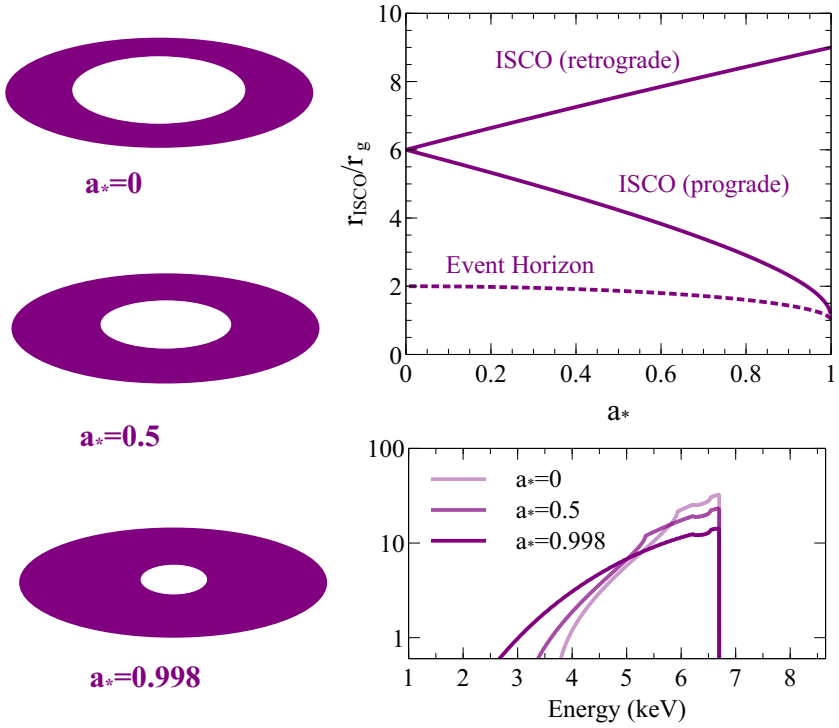

Fig. 1.11 Left: A schematic picture of discs with different BH spin parameters, assuming that the inner radius of the disc is at the ISCO. Right top: the solid line shows the relation between the radius of ISCO and BH spin a_* in Kerr spacetime. The dotted line shows the event horizon of a Kerr BH. Right bottom: relativistic iron emission line models for different a_*. The models are calculated using `relline_lp`, assuming a disc inclination angle of 30° and a coronal height of $5r_g$.

test Einstein's theory in the strong gravity region by looking for any statistical evidence for possible deviations from the Kerr metric [e.g. 127, 122]. However by studying the disc reflection spectra, current observations are so far still consistent with the Kerr description of both stellar-mass BHs and SMBHs [e.g. 329, 300].

Measure a_* with Reflection

The reflection method to measure the BH spin a_* is based on 1) the inner disc radius is at the ISCO; 2) the simple relation between $R_{\rm ISCO}$ and a_*. Fig. 1.11 presents how the inner disc radius changes with a_*. The ISCO for a Schwarzschild BH ($a_* = 0$) is at $6\,r_{\rm g}$. The radius of the ISCO decreases with increasing BH spin and approaches $1\,r_{\rm g}$ when the BH spin reaches the Kerr limit. The relativistic disc Fe Kα emission line changes with the inner radius correspondingly. The bottom right panel of Fig. 1.11 shows different line profiles for different a_* calculated by `relline_lp`, part of the `relxill` package. A disc inclination angle of 30° and a coronal height of $5r_{\rm g}$ are assumed. The relativistic line profile shows a stronger red wing at a higher BH spin due to a smaller inner disc radius, the emission line from which shows stronger gravitational redshift. See Brenneman [32], Miller et al. [189] and Reynolds [254] for reviews of the previous BH spin measurements using the reflection method. This reflection-based method is however not only to model the broad Fe Kα emission line but also the broad band spectra to constrain the continuum emission [e.g. see 256, 183, for technical details of the reflection method].

Compare with Other Methods

Another popular method to measure the spins of stellar-mass BHs in the X-ray band is the thermal continuum-fitting method [e.g. 252, 177]. The continuum-fitting method is based on the same assumptions as the reflection method (i.e. the inner radius of the disc is at the ISCO) and treats the disc thermal spectra as a relativistic-corrected disc blackbody. The flux of the disc blackbody is related to the inner radius of the disc. However, precise measurements for source distance, disc inclination angle and BH mass are required in order to obtain the dimensionless BH spin. This method is limited to BH XRBs in the soft state, where the X-ray spectra are dominated by the disc thermal component and the inner disc extends to the ISCO [282]. The spin measurements by the reflection method and the continuum-fitting method are consistent for most XRBs [283]. Rare sources show disagreement between two methods [e.g. $a_* = 0.3 \pm 0.1$ from reflection and $a_* = 0.8 \pm 0.1$ from continuum fitting for 4U1543−47, 189, 276].

Recently, the detection of the gravitational wave events from BH–BH mergers by aLIGO opened a new era for multi-messenger astronomy [157, 158]. The first BH–BH merger (GW150915) was detected on 15th September, 2015. Two orbiting BHs of $m_{\rm BH} = 30$ underwent their final merger one billion light years away from us. By modelling the gravitational wave signal, an effective spin of $\chi_{\rm eff} = -0.04^{+0.14}_{-0.16}$ is obtained for GW150915. The effective spin $\chi_{\rm eff}$ is defined as the mass-weighted average of the two BH spins projected onto the orbitting axis of the binary. Although $\chi_{\rm eff}$ is different from the dimensionless spin a_* measured using X-rays, the low absolute value of $\chi_{\rm eff}$ at least rules out two BHs that are rapidly spinning in the same direction.

Another method to estimate the disc inner radius is to measure the frequency of the high frequency quasi-periodic oscillations (HFQPOs) in the X-ray power density spectra [20, 197]. HFQPOs has been commonly reported in BH XRBs [e.g. 1] and occasionally in AGN [e.g. 6, 4]. Although the origin of the HFQPOs still remains unclear, we are still able to estimate the radius of the ISCO with given mass if HFQPOs are related to the inner accretion disc [145]. More recently, Pasham et al. [232] detected a QPO in the tidal disruption event ASASSN-14li where a star is disrupted by a BH of $m_{\rm BH} = 10^{5.8-7.1}$. They conclude that the BH spin is greater than $a_* = 0.7$ with given QPO frequency and BH mass.

1.4.4 Disc Reflection and the Density of the Disc

Previous reflection models assume a constant disk density of $\log(n_{\rm e}) = 15$ ($n_{\rm e}$ is reported in units of cm^{-3} hereafter), which is appropriate for the discs of very massive BHs ($m_{\rm BH} > 10^8$ and $\dot{M} \approx 0.2\dot{M}_{\rm Edd}$). However the disc density is expected to be higher than this value in less massive SMBHs ($m_{\rm BH} \approx 10^6$) and stellar-mass BHs, which was predicted by Shakura and Sunyaev [277]. Fig. 1.12 presents the temperature profiles of the slab and the disk reflection spectra for different disc densities. The temperature of the slab within $0.1\tau_{\rm T}$ increases by a factor of 10 when $\log(n_{\rm e})$ increases from 15 to 19. The temperature in the deeper region of the slab ($> 0.1\tau_{\rm T}$) increases by an even larger factor. The increase of temperature is because low energy photons in the disc are trapped by the free-free process and increase the temperature of the slab [265, 86]. Therefore, the reflected emission in the soft X-ray band turns into a quasi-blackbody spectrum. See the right panel of Fig. 1.12. Note that a change of the disc density and a change of the disc ionisation put different effects on the temperature profile of the slab: the increase of the disc ionisation parameter not only increases the average temperature of the slab but also pushes the temperature drop to occur in a deeper region of the slab (see section 1.4.1); the increase of the disc density however only increases the average temperature of the slab and the drop in the temperature profile occurs at a similar depth of the slab for different densities (see Fig. 1.12).

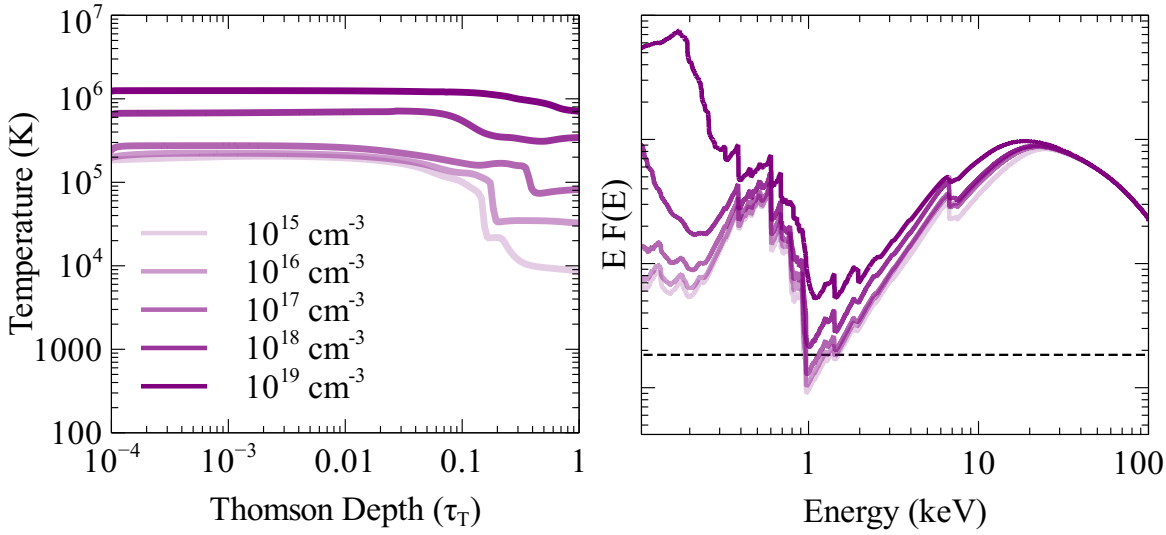

Fig. 1.12 Left: temperature profiles of the slab for different disc densities calculated by García et al. [86]. Right: relativistic disk reflection spectra calculated by `relxilld` for different densities corresponding to the left panel. A disc ionization of $\xi = 50$, an emissivity index of $q = 3$, a maximum BH spin, and a viewing angle of $i = 30°$ are assumed. A power-law illuminating spectrum with $\Gamma = 2$ is assumed (dashed line).

A common result obtained by reflection modelling of black hole X-ray spectra is high iron abundance compared to solar. For example, Chiang et al. [41] found a value of $Z_{\rm Fe} \approx 17 Z_\odot$ in the NLS1 IRAS 13224−3809. Similar results have been found in BH XRBs as well [e.g. GX 339−4, 230, 320]. Wang et al. [319] found that the metallicty of the outflows in different quasars can vary between 1.7–6.9 $Z_\odot$. Reynolds et al. [255] suggested that the radiation-pressure dominance of the inner disc may enhance the iron abundances. However radiative levitation effects make predictions for a change of the inner disc iron abundance, which is difficult to be observed in AGN due to their longer dynamical timescales. Instead, the high density disc reflection model might be a solution to these super-solar iron abundances. For example, Tomsick et al. [296] find the high density reflection model with a high disc density of $\log(n_{\rm e}) \approx 20$ is able to explain the intermediate state spectra of Cyg X-1 with solar iron abundance instead of $Z_{\rm Fe} = 4 - 6 Z_\odot$ when a density of $\log(n_{\rm e}) = 15$ is assumed [e.g. 227, 312].

Additionally, a high disc density model may be able to explain the excess emission commonly seen in the soft X-ray band of Seyfert AGN ('soft excess' emission hereafter). For example, a high density disc reflection model successfully explains the broad band spectrum of the NLS1 Mrk 1044, including the soft excess emission, the broad Fe Kα emission line, and the Compton hump in its *XMM-Newton* and *NuSTAR* spectra [164]. Recently, García et al. [87] suggest a high density disc reflection origin of the soft excess emission in the Sy1 galaxy

Mrk 509. It is also interesting to note that the best-fit flux and temperature of the blackbody component that accounts for the soft excess in IRAS 13224−3809 show a $F \propto T^4$ relation, indicating a constant area origin of the soft excess emission [41]. Higher densities may also potentially explain at least a fraction of the thermal component found in the hard state of the XRBs [e.g. $kT \approx 0.6 - 0.8$ keV in GX 339−4, 320]. The strongest supporting evidence for the reflection interpretation of the soft band emission is the increasing evidence for the reverberation lags in both AGN and XRBs in the hard state [e.g. 70, 340, 51, 132].

The ideal accretion systems to test for high density disks are the low-mass BHs (e.g. stellar-mass BHs and low-mass SMBHs). More details about my work of the high density disc reflection spectroscopy will be introduced throughout this thesis. For observations of BH XRBs, we apply an updated version of `reflionx` that allows a variable disc density parameter. The three-body (positive and negative ions) recombination is important for elements lighter than iron at high densities and has been included in `reflionx` code according to the recombination rate tables in Summers [286]. Three-body recombination of iron is neglected since it is only important at higher densities ($\log(n_{\rm e})$>22) [120]. So far, we have not detected any BH accretion discs that require a density higher than $\log(n_{\rm e})$=22.

1.4.5 Other Models

Other models have been suggested to explain X-ray spectra of AGN and XRBs. Here I briefly introduce some of them and explain some observational challenges for these models.

Some authors advocated a partial-covering absorption origin of the X-ray spectra of AGN [e.g. 303]. In this model, the broad emission line feature in the iron band is produced by the Fe K absorption edge from high density, low ionisation and partial-covering gas in the optical BLR. The soft excess is interpreted as part of the coronal continuum emission. This model is degenerate with reflection interpretations of X-ray spectra. However, the absorption model fails to explain some of other X-ray properties. For example, the variability of broad line feature on very short time scales has been found, which is however not expected by pure absorption in a large distance from the inner region [e.g. 340]. The absorption-based spectral model has been applied to XRBs as well [e.g. 193]. However, there is no counterpart of AGN BLRs in BH XRBs that have been observed to support the origin of these eclipsing absorbers. Some absorption features have been found in XRBs [e.g. 97] but they are from low density and high ionisation wind, which is opposite to the absorption model.

Another model for the soft excess commonly seen in Seyfert AGN is the Comptonisation process of the disc UV photons in a warm corona [e.g. 126, 54]. This Comptonisation process only accounts for the soft excess emission. An additional disc reflection component is still required to model the broad Fe K emission line in the iron band. In this model, the

warm corona is cooler and optically thicker compared to the hot corona introduced in Section 1.4.2, which is responsible for the power law-shaped X-ray continuum emission. For instance, the best-fit 'warm corona' for the Sy1 RX J0136.9−3510 has an electron temperature of $kT \approx 0.28$ keV and an optical depth of $\tau \approx 12$ [126]. However, detailed photoionisation calculations suggest that such an optically thick corona with a low temperature would produce strong absorption features instead of a smooth continuum as seen in the observed spectra [89].

Chapter 2

NuSTAR Observations of GX 339−4 in the Hard and Soft States

"Black holes do not suck!"
– Martin Gaskell

2.1 Introduction

The primary X-ray spectra from BHs can be described by a power-law continuum, which originates from a high temperature compact structure external to the black hole accretion disc. This high temperature compact structure is called the corona. The interaction between the primary power-law photons and the disc top layer can produce both emission, including fluorescence lines and recombination continuum, and absorption edges. These features are referred to as the disc reflection spectrum [e.g. 91, 84]. The disc reflection spectrum is highly affected by relativistic effects, such as Doppler effect and gravitational redshift, due to the strong gravitational field in the vicinity of black holes [e.g. 256]. For example, relativistic blurred Fe Kα emission line features have been detected in reflection spectra of both Active Galactic Nuclei [AGN, e.g. MCG-6−30−15, 291] and Galactic BH X-ray Binary sources [XRB, e.g. Cyg X-1, 17].

BH XRBs often show different flux states during an outburst. Its X-ray spectrum can change from a soft spectrum featured by a strong thermal component to a hard spectrum featured by a strong power-law component. The soft state, which is also characterised by no radio detection, is identified as the 'high' flux (HF) state and the hard state with associated radio detection, is identified as the 'low' flux (LF) state, due to the large flux variation during the transition. Measurements in the HF soft states of BH XRB offer good evidence that the accretion disc is extended to the innermost stable circular orbit [ISCO, e.g. LMC X-3, 282]. Most of the spin measurements of soft states are based on the assumption that the inner radius is located at ISCO [e.g. 93, 312]. In the LF hard state, the disc is predicted to be truncated at a large radius and replaced by an advective flow at small radii [59, 205]. Although there is evidence that the disc is truncated as measured by reflection spectroscopy at X-ray luminosities $L_{\rm X} \approx 0.1\% L_{\rm Edd}$ [297, 206], there is a substantial debate whether the disc is truncated in the intermediate flux hard state due to different spectral modelling or instrumental pile-up effects [see the discussion section in 320].

A common result obtained by reflection modelling of black hole X-ray spectra is high iron abundance compared to solar. For example, Walton et al. [312] found a value of $Z_{\rm Fe} \approx 4 Z_{\odot}$ in Cyg X-1 and Parker et al. [227] obtained $Z_{\rm Fe} \approx 4.7 Z_{\odot}$ in the same source. Similarly, an iron abundance of $Z_{\rm Fe} \approx 2-5 Z_{\odot}$ is required for another BH XRB V404 Cyg [313]. Such a high iron abundance has been commonly seen in AGNs as well [e.g. 41, 228]. A possible explanation for the high iron abundances is high density reflection. Most versions of available disc reflection models assume a constant electron density $n_{\rm e} = 10^{15} {\rm cm}^{-3}$ for the top layer of the BH accretion disc. At higher electron density, the free-free process becomes more important in trapping low energy photons, increasing the temperature of the top layer of the disc, and

thus turning the reflected emissions below 1 keV into a blackbody shaped spectrum [265, 86]. Such a model can potentially relieve the very high iron abundance required in previous reflection spectral modelling. For instance, Tomsick et al. [296] obtained an electron density of $n_{\rm e} \approx 3 \times 10^{20}{\rm cm}^{-3}$ by fitting the Cyg X-1 intermediate flux state spectra with the high electron density reflection model. Although the iron abundance was fixed at the solar value during the spectral fitting, the model successfully explains the spectra.

Higher densities may also potentially explain the weak thermal component found in the LF state of the XRBs [e.g. 249, 320] and at least some of the soft excess commonly seen in Seyfert galaxies [e.g. 70, 41, 124]. The inclusion of the high electron density effects significantly decreases the flux of the best-fit blackbody component in IRAS 13224−3809 required for the spectral fitting purpose [124]. It is also interesting to note that the best-fit flux and temperature of the blackbody component that accounts for the soft excess in IRAS 13224−3809 show a $F \propto T^4$ relation, indicating a constant area origin of the soft excess emission [41, 124].

GX 339−4 is a low mass X-ray binary (LMXB) and shows activity in a wide range of wavelengths from optical to X-ray. The mass of the central black hole still remains uncertain. For example, Heida et al. [110] obtained a black hole mass of $2 - 10 M_{\odot}$ by studying its near infrared spectrum and a mass of $> 5 M_{\odot}$ was obtained previously by Hynes et al. [116, 117], Muñoz-Darias et al. [198]. The distance has been estimated to be ≈ 7 kpc [334]. GX 339−4 has shown frequent outbursts and multiple X-ray observations have been taken during different spectral states of GX 339−4. In its hard state, its X-ray spectrum shows a broad iron emission line and a power-law continuum with a photon index varying between $\Gamma \approx 1.5 - 2.5$ across different flux levels [186–188]. Reis et al. [249] presented a systematic study of its high and low hard state *XMM-Newton* and *RXTE* spectra by taking the blackbody radiation from the disc as well as Comptonization effects into modelling, and obtained a black hole spin of $a_* = 0.94 \pm 0.02$. More recently, Parker et al. [230] obtained a disc iron abundance of $Z_{\rm Fe} \approx 6.6 Z_{\odot}$ for the HF soft state *NuSTAR* and *Swift* spectra of GX 339−4. In this study, the disc inner radius is assumed to be located at ISCO and a black hole spin of $a_* > 0.95$ is obtained by combining disc thermal spectral and reflection spectral modelling. Later, Wang-Ji et al. [320] found $Z_{\rm Fe} \approx 8 Z_{\odot}$ for the LF state of the same source observed by the same instruments. Similar conclusions were found by analysing its stacked *RXTE* spectra at the LF states [90] and *NuSTAR* spectra during the outburst of 2013 [74].

In this chapter, we present a high density reflection interpretation of both LF and HF state spectra of GX 339−4. The same *NuSTAR* and *Swift* spectra as in Parker et al. [230], Wang-Ji et al. [320] are considered. In Section 2.2, we introduce the data reduction process; in

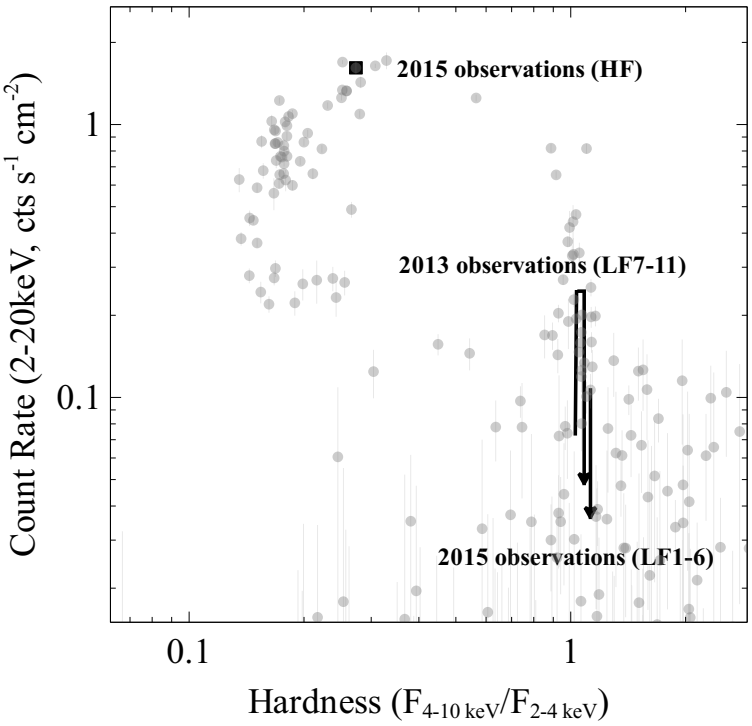

Fig. 2.1 Weekly *MAXI* hardness-intensity diagram for the 2009-2018 period of GX 339−4. The black square and the arrows correspond to the dates of the HF observations and the LF(1-11) observations analysed in this work. The arrows show the flux change during the *NuSTAR* monitoring of the outbursts. *NuSTAR* observations were taken during the rise and decay of the outburst in 2013, and only during the decay of the outburst in 2015.

Section 2.3, we introduce the details of high density reflection modelling of the LF and HF spectra of GX 339−4; in Section 2.4, we present and discuss the final spectral fitting results.

2.2 Observations and Data Reduction

The weekly *MAXI* hardness-intensity diagram (HID) for the 2009-2018 period of GX 339−4 [172] is shown in Fig. 2.1, showing a standard 'q-shaped' behaviour during the outbursts. GX 339−4 went through two outbursts each in 2013 and 2015. 11 *NuSTAR* observations in total, each with a corresponding *Swift* snapshot, were triggered during these two outbursts, shown by the arrow in Fig. 2.1. The *NuSTAR* LF observations in 2015 were taken only during the decay of the outburst. In this work, we consider all of the *NuSTAR* observations taken during these two outbursts. In March 2015, GX 339−4 was detected with strong thermal and power-law components by *Swift*, suggesting strong evidence of a HF state with a combination of disc thermal component and reflection component. One *NuSTAR* target of opportunity

Table 2.1 *NuSTAR* and *Swift* observations of GX 339−4 in 2013 and 2015. WT: window timing mode; PC: photon counting mode.

Obs	*NuSTAR* obsID	Date	exp.(ks)	*Swift* obsID	Date	exp.(ks)	Mode
HF	80001015003	2015-03-04	30.9	00081429002	2015-03-04	1.9	WT
LF1	80102011002	2015-08-28	21.6	00032898124	2015-08-29	1.7	WT
LF2	80102011004	2015-09-02	18.3	00032898126	2015-09-03	2.3	WT
LF3	80102011006	2015-09-07	19.8	00032898130	2015-09-07	2.8	WT
LF4	80102011008	2015-09-12	21.5	00081534001	2015-09-12	2.0	PC
LF5	80102011010	2015-09-17	38.5	00032898138	2015-09-17	2.3	WT
LF6	80102011012	2015-09-30	41.3	00081534005	2015-09-30	2.0	PC
LF7	80001013002	2013-08-11	42.3	00032490015	2013-08-12	1.1	WT
LF8	80001013004	2013-08-16	47.4	00080180001	2013-08-16	1.9	WT
LF9	80001013006	2013-08-24	43.4	00080180002	2013-08-24	1.6	WT
LF10	80001013008	2013-09-03	61.9	00032898013	2013-09-02	2.0	WT
LF11	80001013010	2013-10-16	98.2	00032988001	2013-10-17	9.6	WT

observation was triggered with a simultaneous *Swift* snapshot. See the black square in Fig. 2.1 for the flux and hardness state of the source during its HF observations. A full list of observations are shown in Table 2.1.

2.2.1 *NuSTAR* Data Reduction

The standard pipeline NUPIPELINE V0.4.6, part of HEASOFT V6.23 package, is used to reduce the *NuSTAR* data. The *NuSTAR* calibration version V20171002 is used. We extract source spectra from circular regions with radii of 100 arcsec, and the background spectra from nearby circular regions on the same chip. The task NUPRODUCTS is used for this purpose. The 3-78 keV band is considered for both FPMA and FPMB spectra. The spectra are grouped to have a minimum signal-to-noise (S/N) of 6 and to oversample by a factor of 3.

2.2.2 *Swift* Data Reduction

The *Swift* observations are processed using the standard pipeline XRTPIPELINE V0.13.3. The calibration file version used is V20171113. The LF observations taken in the WT mode are not affected by the pile-up effects. The source spectra are extracted from a circular region with a radius of 20 pixels [1] and the background spectrum spectra are extracted from an annular region with an inner radius of 90 pixels and an outer radius of 100 pixels. The LF observations taken in the PC mode are affected by the pile-up effects. By following Wang-Ji

[1] 1 pixel $\approx 2.36''$

et al. [320] where they estimated the PSF shape, a circular region with a radius of 5 pixels is excluded in the center of the source region. The 0.6–6 keV band of all the LF *Swift* XRT spectra are considered. The HF observation was taken in the WT mode and was affected by pile-up effects. By following Parker et al. [230], a circular radius of 10 pixels is excluded in the center of the source region. The 0.6–1 keV of the HF *Swift* XRT spectrum at a very high flux state is ignored due to known issues of the RMF redistribution issues in the WT mode[2]. The *Swift* XRT spectra are grouped to have a minimum S/N of 6 and to oversample by a factor of 3.

2.3 Spectral Analysis

XSPEC V12.10.0.C [9] is used for spectral analysis, and C-stat is considered in this work. The Galactic column density towards GX 339−4 remains uncertain. The value of combined $N_{\rm H_I}$ and $N_{\rm H_2}$ obtained by Willingale et al. [326] is 5.18×10^{21}cm^{-2}. However, Kalberla et al. [129] reported a column density of 3.74×10^{21}cm^{-2} in the Leiden/Argentine/Bonn survey. The Galactic column density values measured by different sets of broad band X-ray spectra are different too. For example, Wang-Ji et al. [320] obtained $\approx 4 \times 10^{21}$cm^{-2} while Parker et al. [230] obtained a higher value of $7.7 \pm 0.2 \times 10^{21}$cm^{-2}. We therefore fixed the Galactic column density at 3.74×10^{21}cm^{-2} in the beginning of our analysis and allow it to vary to obtain the best-fit value for each set of spectra. For local Galactic absorption, the `tbabs` model is used. The solar abundances of Wilms et al. [327] are used in `tbabs`. An additional constant model `constant` has been applied to vary normalizations between the simultaneous spectra obtained by different instruments to account for calibration uncertainties.

2.3.1 Low Flux State (LF) Spectral Modelling

We analyze all the LF *NuSTAR* observations publicly available prior to 2018 as discussed in Fürst et al. [74] and Wang-Ji et al. [320]. Fig. 2.2 shows the ratio plots of LF1-I1 spectra fitted with a Galactic absorbed power-law model obtained by fitting only the corresponding *NuSTAR* spectra. All the LF spectra show a broad emission line feature around 6.4 keV with a Compton hump above 20 keV. They provide a strong evidence of a relativistic disc reflection component. By following García et al. [90] and Wang-Ji et al. [320], we model the features with a combination of relativistic disc reflection and a distant reflector for the narrow emission line component. A more developed version of `relionx` [264] is used to

[2]See following website for more XRT WT mode calibration information. http://www.swift.ac.uk/analysis/xrt/digest_cal.php

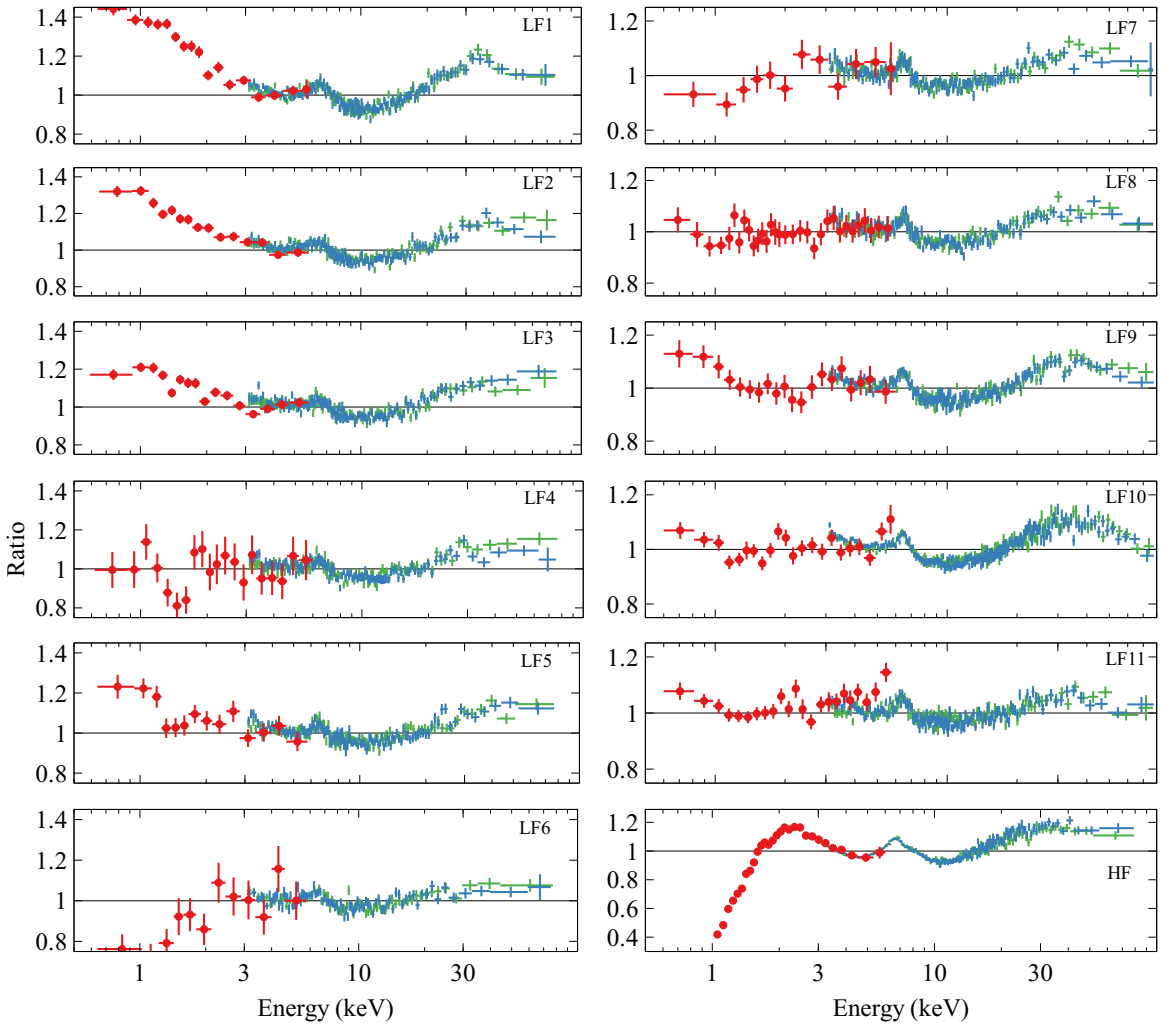

Fig. 2.2 First 11 panels: ratio plots of GX 339−4 FPM (blue crosses: FPMA; green crosses: FPMB) and XRT (red circles) spectra fitted with a Galactic absorbed power law for LF observations in 2015 (LF1-6) and 2013 (LF7-11). Last panel: ratio plot of HF spectra fitted with a Galactic absorbed power law plus a simple blackbody component for the very high flux soft state observation in 2015. All the spectra show a broad line emission feature around 6.4 keV and a strong Compton hump above 10 keV.

model the rest-frame disc reflection spectrum. The `reflionx` grid allows the following free parameters: disc iron abundance ($Z_{\rm Fe}$), disc ionization $\log(\xi)$, disc electron density $n_{\rm e}$, high energy cutoff ($E_{\rm cut}$), and photon index (Γ). All the other element abundances are fixed at the solar value [196]. The ionization parameter is defined as $\xi = 4\pi F/n$, where F is the total illuminating flux and n is the hydrogen number density. The photon index Γ and high energy cutoff $E_{\rm cut}$ are linked to the corresponding parameters of the coronal emission modelled by `cutoffpl` in XSPEC. A convolution model `relconv` [49] is applied to the rest frame ionized disc reflection model `reflionx` to apply relativistic effects. A simple power-law shaped emissivity profile is assumed ($\epsilon \propto r^{-q}$) and the emissivity index q is allowed to vary during the fit. Other free parameters are the disc viewing angle i and the disc inner radius $r_{\rm in}$/ISCO. The ionization of the distant reflector is fixed at the minimum value $\xi = 10$. The other parameters of the distant reflector are linked to the corresponding parameters in the disc reflection component. The BH spin parameter a_* is fixed at its maximum value 0.998 [141] to fully explore the $r_{\rm in}$ parameter. We use `cflux`, a simple convolution model in XSPEC, to calculate the 1–10 keV flux of each model component. For future reference and simplicity, we define an empirical reflection fraction as $f_{\rm refl} = F_{\rm ref}/F_{\rm pl}$ in the 1–10 keV band, where $F_{\rm ref}$ and $F_{\rm pl}$ are the flux of the disc reflection component and the coronal emission calculated by `cflux`. Note that this is not the same as the physically defined reflection fraction discussed by Dauser et al. [47]. The final model is `tbabs * ( cflux*(relconv*reflionx) + cflux*reflionx + cflux*cutoffpl)` in XSPEC format. This model can fit all LF spectra successfully with no obvious residuals. For example, it offers a good fit for the LF1 spectra with C-stat/ν = 1043.52/948. A ratio plot of LF1 spectra fitted with this model is shown in the top panel of Fig. 2.3. The best-fit values of some key parameters that affect the spectral modelling below 3 keV are following: $N_{\rm H} = 3.4^{+0.2}_{-0.1} \times 10^{21}$ cm^{-2}, $\log(\xi/{\rm erg\ cm\ s^{-1}}) = 3.18^{+0.07}_{-0.06}$, and $\log(n_{\rm e}/{\rm cm^{-3}}) = 20.6 \pm 0.3$. Our best-fit column density is consistent with the Galactic column density measured in Kalberla et al. [129].

We notice that previously the spectral modelling requires a low temperature multicolour disc thermal component `diskbb` ($kT = 0.46$ keV) when using the model with the disc electron density $n_{\rm e}$ fixed at $\log(n_{\rm e}/{\rm cm^{-3}}) = 15$ for LF1 observation [320]. However the normalization of this component is very low and weakly constrained. Similarly, a weak thermal component is also required in the analysis of its *XMM-Newton* hard state observations [249]. The difference in spectral modelling may result from the following two reasons: one is the high density reflection model, where a blackbody-shaped emission arises in the soft band when the disc electron density $n_{\rm e}$ becomes higher than 10^{15} cm^{-3}; the other is the uncertain neutral absorber column density, which was measured to be $N_{\rm H} = 4.12^{+0.08}_{-0.12} \times 10^{21}$ cm^{-2} in Wang-Ji et al. [320] and higher than our best-fit value for the LF1 spectra.

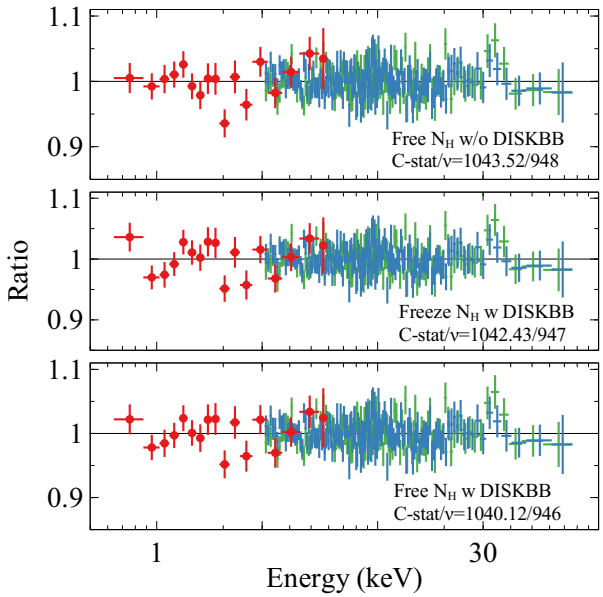

Fig. 2.3 Ratio plots for LF1 spectra against different continuum models. Red circles: XRT; blue crosses: FPMA; green crosses: FPMB. See text for more details.

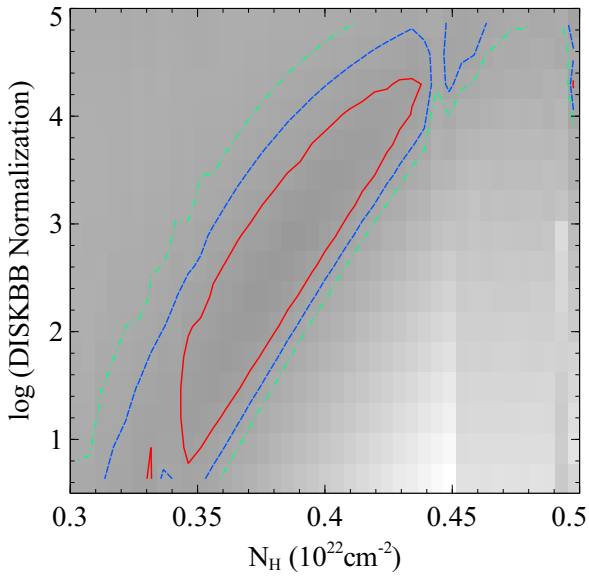

Fig. 2.4 A contour plot of C-stat distribution on the Galactic absorption column density $N_{\rm H}$ vs. `diskbb` model normalization parameter plane for LF1 spectra when fitted with `tbabs*(diskbb+cutoffpl+relconv*reflionx+reflionx)`. It shows a clear degeneracy between two parameters. The lines show the 1σ (red solid line), 2σ (blue dashed line), and 3σ contours (green dash-dot line). The grey scale shows the values of C-stat.

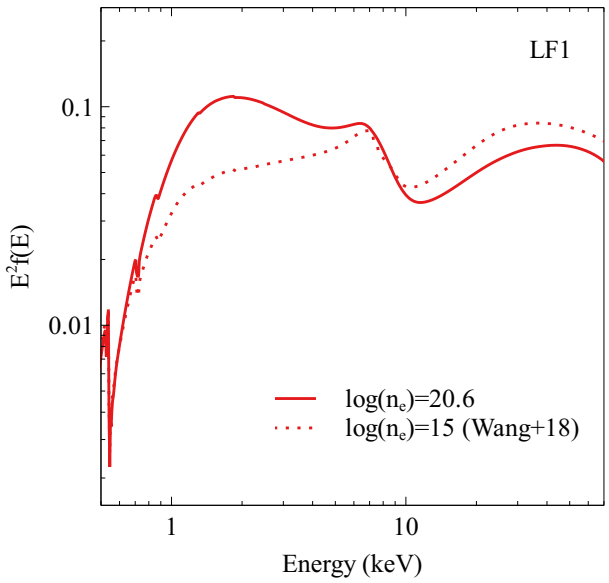

Fig. 2.5 The best-fit relativistic high density reflection unfolded model for LF1 spectra (solid line) and the best-fit relativistic reflection model obtained by Wang-Ji et al. [320] assuming $\log(n_{\rm e}) = 15$ (dotted line). The previous best-fit model has been renormalized only to show the difference of spectral shapes in the soft X-ray band. An additional `diskbb` component is required to fit the broad band spectra in Wang-Ji et al. [320].

In order to test for an additional `diskbb` component, we first fit the spectra with $N_{\rm H}$ fixed at the higher Galactic column density $N_{\rm H} = 5.18 \times 10^{21}$ cm^{-2} obtained by Willingale et al. [326] rather than the value from Kalberla et al. [129]. An additional `diskbb` component improves the fit by only ΔC-stat=1.1. See the middle panel of Fig. 2.3 for the corresponding ratio plot. Only an upper limit of the `diskbb` normalization is of $N_{\rm diskbb} < 1.5 \times 10^5$ found. Compared with the result in Wang-Ji et al. [320], a lower disc inner temperature of $kT = 0.24^{+0.08}_{-0.10}$ keV is required in this fit. Second, we fit LF1 spectra with the absorber column density as a free parameter (bottom panel of Fig 2.3). A contour plot of C-stat distribution on the $N_{\rm H}$ vs. $N_{\rm diskbb}$ parameter plane is calculated by STEPPAR function in XSPEC and shown in Fig. 2.4. It clearly shows a strong degeneracy between the absorber column density and the normalization of the `diskbb` component. The fit is only improved by ΔC-stat=3 with 2 more free parameters after including this `diskbb` component. See Fig. 2.3 for ratio plots against different continuum models. By varying the Galactic column density, it only slightly changes the fit of the *Swift* XRT spectrum. Therefore, we conclude that an additional `diskbb` component is not necessary for LF1 spectral modelling when the disc density parameter $n_{\rm e}$ is allowed to vary. In order to visualize the spectral difference with different $n_{\rm e}$, we show the best-fit reflection model component for LF1 in Fig. 2.5 in comparison with the best-fit

model for the same observation assuming $\log(n_{\rm e}) = 15\,{\rm cm}^{-3}$ in Wang-Ji et al. [320]. With a disc density as high as $\log(n_{\rm e}) = 20.6$, a quasi-blackbody emission arises in the soft band and accounts for the excess emission below 2 keV. Similar conclusions are found for the other sets of LF spectra. Future pile-up free high S/N observation below 2 keV, such as from *NICER*, may help constrain more detailed spectral shape of LF states of GX 339−4.

So far we have achieved the best-fit model for the LF spectra individually. We also undertake a multi-epoch spectral analysis with disc iron abundance $Z_{\rm Fe}$ and disc viewing angle i linked between LF1-11 spectra. All the other parameters are allowed to vary during the fit. A table of all the best-fit parameters are shown in Table. 2.2. The best-fit models and corresponding ratio plots are shown in Fig. 2.6. We allow the column density of the neutral absorber to vary in different epochs to investigate any variance. A slightly higher column density ($N_{\rm H} \approx 4.1 \times 10^{21}$ cm^{-2}) is required for LF6,7. The emissivity index of the relativistic reflection spectrum is weakly constrained in LF3-6 observations but largely consistent with the Newtonian value $q = 3$, except for the LF1 observation. We can also confirm that the disc is not truncated at a significantly large radius, such as $r = 100 r_g$ [238]. A slight iron over abundance compared to solar is required ($Z_{\rm Fe} = 1.5^{+0.12}_{-0.04}$) for the spectral fitting. The power-law continuum is softer in the first two observations taken at higher flux levels but remains constant at 90% confidence during the rest of the decay in 2015. The photon index in LF7-10 during the outburst in 2013 is constant at 90% confidence as well. The reflection fraction decreases with the decreasing total flux during the flux decay in 2015. This is likely caused by a receding inner disc radius at the very low flux states or a change of the coronal geometry (e.g. its height above the disc). Moreover, the multi-epoch spectral analysis of all LF observations shows tentative evidence for an anti-correlation between disc density and X-ray band flux. For example, the disc density increases from $\log(n_{\rm e}) = 20.60^{+0.23}_{-0.12}$ in the highest flux state (LF1) to $\log(n_{\rm e}) = 21.45^{+0.06}_{-0.13}$ in the lowest flux state (LF6). The flux level of the cold reflection component remains consistent, indicating that this emission arises from stable material at a large radius from the central black hole. We will discuss other fitting results, such as the electron density measurements, in Section 2.4.

2.3.2 High Flux State (HF) Spectral Modelling

The same *NuSTAR* and *Swift* observations of GX 339−4 in a HF state analysed in Parker et al. [230] are considered here. A ratio plot of the HF spectra fitted with a Galactic absorbed power-law model and a simple disc blackbody component `diskbb` is shown in the bottom panel of Fig. 2.2. The HF spectra show a broad emission line feature at the iron band and a Compton hump above 10 keV, indicating existence of a relativistic disc reflection component similar with all the LF spectra. A multicolour disc blackbody component `diskbb`

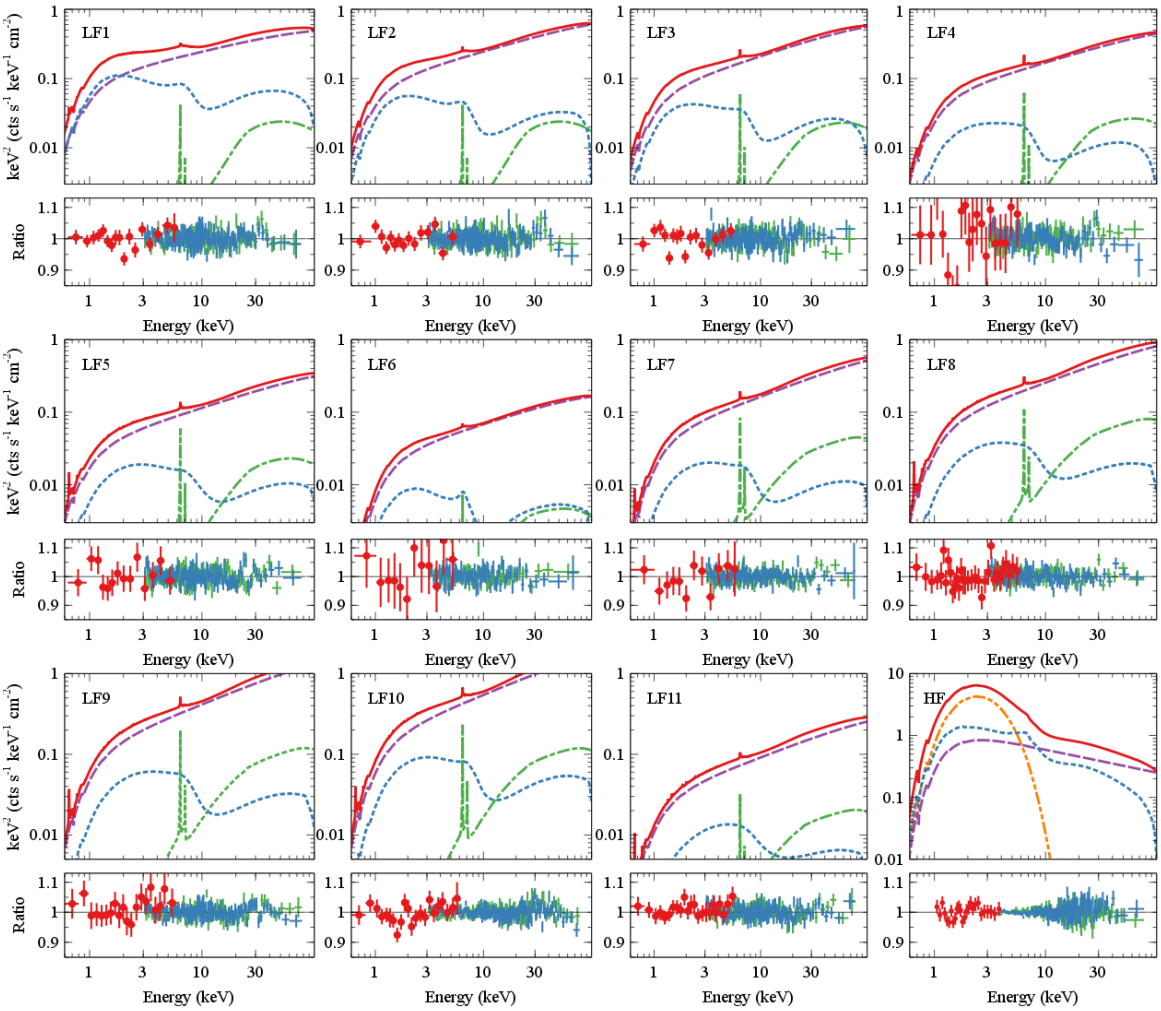

Fig. 2.6 Top: the first 11 panels show the best-fit models obtained by fitting LF1-11 spectra simultaneously. The last panel shows the best-fit model obtained by fitting only HF spectra. Red solid lines: total model; blue dotted lines: relativistic reflection model; purple dashed lines: coronal emission; green dash-dot lines: distant reflection component; orange dash-dot-dot lines: disc thermal spectrum (only needed in the HF spectral modelling). Bottom: ratio plots against the corresponding best-fit models shown in the upper panels. Red circles: XRT; blue crosses: FPMA; green crosses: FPMB.

Table 2.2 The best-fit parameters obtained by fitting 1) LF1-11 spectra simultaneously 2) only HF spectra. u: unconstrained; l: linked; f: fixed. $F_{\rm refl}$ is the flux of the relativistic disc reflection component measured between 1–10 keV; $F_{\rm pl}$ is the flux of the coronal emission measured at the same energy band; $F_{\rm dis}$ is for the distant cold reflector. The reflection fraction $f_{\rm refl}$ is defined as $F_{\rm refl}/F_{\rm pl}$ for simplicity. $L_{0.1-100{\rm keV}}$ is the 0.1–100 keV band Galactic-absorption corrected luminosity calculated using the best-fit model. A black hole mass $M_{\rm BH} = 10 M_\odot$ and a distance $d = 10$ kpc are assumed.

Parameter	Unit	LF1	LF2	LF3	LF4	LF5	LF6
$N_{\rm H}$	$10^{21}{\rm cm}^{-2}$	$3.22^{+0.14}_{-0.08}$	$3.20^{+0.10}_{-0.12}$	$3.1^{+0.3}_{-0.2}$	$3.4^{+0.5}_{-0.5}$	$3.2^{+0.2}_{-0.3}$	$4.1^{+0.8}_{-0.7}$
q	-	6^{+3}_{-2}	$2.5^{+3.6}_{-0.4}$	< 7	5(u)	6(u)	4(u)
$r_{\rm in}$	$r_{\rm ISCO}$	< 4.7	< 8	< 11	11^{+4}_{-7}	< 32	21^{+14}_{-12}
$\log(\xi)$	erg cm s^{-1}	$3.18^{+0.06}_{-0.39}$	$3.13^{+0.12}_{-0.08}$	$3.12^{+0.09}_{-0.17}$	$3.10^{+0.17}_{-0.04}$	$3.12^{+0.11}_{-0.08}$	$3.08^{+0.05}_{-0.02}$
$\log(n_{\rm e})$	cm^{-3}	$20.60^{+0.23}_{-0.12}$	$20.64^{+0.16}_{-0.13}$	$21.1^{+0.4}_{-0.2}$	$21.49^{+0.14}_{-0.13}$	$20.82^{+0.31}_{-0.15}$	$21.45^{+0.06}_{-0.13}$
a_*	-	0.998(f)	(l)	(l)	(l)	(l)	(l)
i	deg	34 ± 2	(l)	(l)	(l)	(l)	(l)
$Z_{\rm Fe}$	$Z_\odot$	$1.50^{+0.12}_{-0.04}$	(l)	(l)	(l)	(l)	(l)
$\log(F_{\rm refl})$	erg cm^{-2} s^{-1}	$-9.42^{+0.04}_{-0.09}$	$-9.72^{+0.07}_{-0.03}$	$-9.91^{+0.13}_{-0.05}$	$-10.13^{+0.11}_{-0.09}$	$-10.21^{+0.03}_{-0.06}$	$-10.53^{+0.10}_{-0.11}$
$E_{\rm cut}$	keV	350^{+92}_{-124}	> 287	> 255	> 290	> 350	> 420
Γ	-	$1.594^{+0.004}_{-0.010}$	$1.530^{+0.018}_{-0.045}$	$1.49^{+0.02}_{-0.05}$	$1.517^{+0.010}_{-0.030}$	$1.485^{+0.007}_{-0.029}$	$1.49^{+0.03}_{-0.02}$
$\log(F_{\rm pl})$	erg cm^{-2} s^{-1}	$-9.22^{+0.05}_{-0.03}$	-9.25 ± 0.03	$-9.32^{+0.02}_{-0.03}$	$-9.420^{+0.011}_{-0.028}$	$-9.601^{+0.009}_{-0.013}$	-9.82 ± 0.02
$f_{\rm refl}$	-	$0.631^{+0.010}_{-0.016}$	$0.3388^{+0.0041}_{-0.0010}$	$0.224^{+0.006}_{-0.002}$	$0.195^{+0.003}_{-0.002}$	$0.246^{+0.003}_{-0.002}$	$0.194^{+0.003}_{-0.002}$
$\log(F_{\rm dis})$	erg cm^{-2} s^{-1}	$-11.01^{+0.14}_{-0.20}$	$-11.58^{+0.16}_{-0.31}$	$-11.40^{+0.19}_{-0.33}$	$-11.4^{+0.2}_{-0.3}$	$-11.16^{+0.15}_{-0.20}$	< -11.69
C-stat/ν		11870.25/11305					
$L_{0.1-100{\rm keV}}/L_{\rm Edd}$	%	2.7	2.5	2.2	1.7	1.2	0.6

To be continued in Table 2.3.

Table 2.3 Continue after Table 2.2.

Parameter	Unit	LF7	LF8	LF9	LF10	LF11	HF
$N_{\rm H}$	$10^{21}\,{\rm cm}^{-2}$	$4.1^{+0.3}_{-0.2}$	$3.84^{+0.18}_{-0.16}$	$3.41^{+0.18}_{-0.17}$	$3.71^{+0.16}_{-0.23}$	$3.75^{+0.12}_{-0.14}$	6.2 ± 0.2
q	-	> 0.5	> 2	>3	>2.7	4(u)	$5.88^{+1.01}_{-0.77}$
$r_{\rm in}$	$r_{\rm ISCO}$	< 25	< 17	< 10	< 1.51	< 25	1(f)
$\log(\xi)$	erg cm s^{-1}	$3.29^{+0.04}_{-0.03}$	3.26 ± 0.03	$3.23^{+0.016}_{-0.020}$	$3.23^{+0.02}_{-0.05}$	$3.26^{+0.04}_{-0.03}$	$3.88^{+0.08}_{-0.12}$
$\log(n_{\rm e})$	cm^{-3}	21.0 ± 0.2	$21.25^{+0.23}_{-0.17}$	21.15 ± 0.15	$20.93^{+0.12}_{-0.08}$	$21.57^{+0.20}_{-0.17}$	$18.93^{+0.12}_{-0.16}$
a_*	-	(l)	(l)	(l)	(l)	(l)	> 0.93
i	deg	(l)	(l)	(l)	(l)	(l)	$35.9^{+1.6}_{-2.0}$
$Z_{\rm Fe}$	$Z_\odot$	(l)	(l)	(l)	(l)	(l)	$1.05^{+0.17}_{-0.15}$
$\log(F_{\rm refl})$	erg cm^{-2} s^{-1}	$-10.071^{+0.009}_{-0.010}$	-9.93 ± 0.04	$-9.71^{+0.03}_{-0.02}$	$-9.52^{+0.03}_{-0.04}$	$-10.41^{+0.02}_{-0.07}$	$-8.30^{+0.03}_{-0.02}$
$E_{\rm cut}$	keV	> 380	> 320	> 430	> 330	> 410	500(f)
Γ	-	$1.427^{+0.065}_{-0.016}$	$1.419^{+0.012}_{-0.010}$	$1.421^{+0.009}_{-0.015}$	1.42 ± 0.02	$1.478^{+0.011}_{-0.018}$	$2.357^{+0.019}_{-0.018}$
$\log(F_{\rm pl})$	erg cm^{-2} s^{-1}	$-9.467^{+0.007}_{-0.008}$	$-9.278^{+0.011}_{-0.013}$	$-9.068^{+0.010}_{-0.021}$	$-8.94^{+0.009}_{-0.008}$	$-9.701^{+0.015}_{-0.014}$	$-8.46^{+0.06}_{-0.05}$
kT	keV	-	-	-	-	-	$0.831^{+0.03}_{-0.05}$
$N_{\rm diskbb}$	-	-	-	-	-	-	1649^{+76}_{-49}
$f_{\rm refl}$	-	$0.249^{+0.005}_{-0.007}$	$0.22^{+0.02}_{-0.02}$	$0.228^{+0.017}_{-0.011}$	0.26 ± 0.02	$0.195^{+0.012}_{-0.030}$	$1.45^{+0.06}_{-0.03}$
$\log(F_{\rm dis})$	erg cm^{-2} s^{-1}	$-11.00^{+0.10}_{-0.12}$	$-10.73^{+0.02}_{-0.13}$	-10.62 ± 0.08	$-10.50^{+0.09}_{-0.08}$	$-1.06^{+0.08}_{-0.13}$	< -10.89
C-stat/ν							1048.68/971
$L_{0.1-100{\rm keV}}/L_{\rm Edd}$	%	1.2	2.0	3.1	4.0	0.7	26.7

is used to account for the strong disc thermal component. The full model is `tbabs * ( cflux*(relconv*reflionx) + cflux*reflionx + cflux*cutoffpl + diskbb)` in XSPEC format. This model provides a good fit with C-stat/ν=1048.68/971. The best-fit model is shown in the last panel of Fig. 2.6 and the best-fit parameters are shown in the last column of Table 2.2. A disc density of $\log(n_{\rm e}/{\rm cm}^{-3}) = 18.93^{+0.12}_{-0.16}$ is found in HF observations which is 100 times lower than the best-fit value in LF observations.

So far we have obtained a good fit for the HF spectrum of GX 339−4. A higher column density is required for the neutral absorber ($N_{\rm H} = 6.2 \pm 0.2 \times 10^{21}$ cm^{-2}) compared to the LF observations ($N_{\rm H} \approx 3.4 \times 10^{21}$ cm^{-2}). Parker et al. [230] obtained a higher column density of $N_{\rm H} = 7.2 \pm 0.2 \times 10^{21}$ cm^{-2} for the same observation assuming $n_{\rm e} = 10^{15}$cm^{-3} for the disc. Both our result and Parker et al. [230] are higher than the Galactic absorption column density estimated at other wavelengths [e.g. 129], indicating a possible extra variable neutral absorber along the line of sight. Only an upper limit of the flux of the distant cold reflector is achieved ($\log(F_{\rm dis}) < -10.89$). The 1–10 keV band flux values of the disc reflection component and the coronal emission increase by a factor of 13 and 6 respectively compared to LF1. The best-fit broad band model shows the highest reflection fraction among all the observations considered in this work, indicating a geometry change of the disc corona system such as a small inner disc radius. A solar iron abundance ($1.05^{+0.17}_{-0.15}$) is required for the HF spectra, which is lower than the value obtained by Parker et al. [230], where a disc density of $n_{\rm e} = 10^{15}$cm^{-3} is assumed.

2.4 Results and Discussion

We have obtained a good fit for the LF and the HF spectra of GX 339−4. The LF spectral modelling requires a high disc density of $\log(n_{\rm e}) \approx 21$ with no additional low temperature thermal component. The HF spectral modelling requires a 100 times lower density ($\log(n_{\rm e}) = 18.93^{+0.12}_{-0.16}$) compared to LF observations. In this section, we discuss the spectral fitting results by comparing with previous data analysis and accretion disc theories.

2.4.1 Comparison with Previous Results

First, the most significant difference from previous results is the close-to-solar disc iron abundance. Previously, Parker et al. [230] and Wang-Ji et al. [320] obtained a disc iron abundance of $Z_{\rm Fe} = 6.6^{+0.5}_{-0.6} Z_{\odot}$ and $Z_{\rm Fe} \approx 8 Z_{\odot}$ respectively by analysing the same spectra considered in this work. A similar result was achieved by Fürst et al. [74]. A high iron abundance of $Z_{\rm Fe} = 5 \pm 1 Z_{\odot}$ was also found by analysing stacked *RXTE* spectra [90]. All of

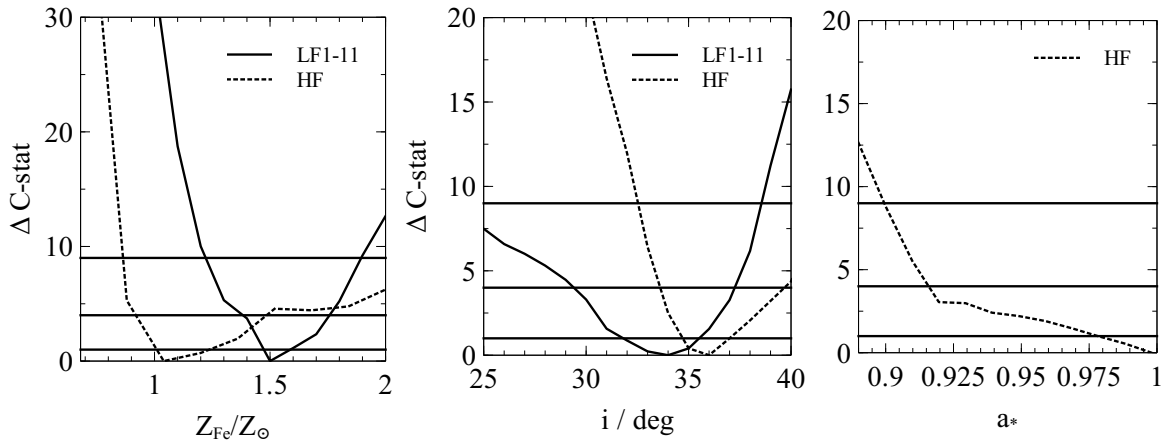

Fig. 2.7 C-stat contour plots for the disc iron abundance and the relativistic reflection parameters obtained by fitting LF 1-11 spectra simultaneously (solid lines) and only the HF spectra (dashed line). The solid lines show the 1σ, 2σ, and 3σ ranges.

their work was based on the assumption for a fixed disc density $n_{\rm e} = 10^{15}$ cm^{-3}. By allowing the disc density $n_{\rm e}$ to vary as a free parameter during spectral fitting, we obtained a close-to-solar disc iron abundance ($Z_{\rm Fe} = 1.50^{+0.12}_{-0.04} Z_\odot$ for LF observations and $Z_{\rm Fe} = 1.05^{+0.17}_{-0.15} Z_\odot$ for HF observations). The best-fit disc iron abundance for the LF spectra is slightly higher than the value for the HF spectra at 90% confidence. However they are consistent within a 2σ confidence range. See the left panel of Fig. 2.7 for the constraints on the disc iron abundance parameter. A similar conclusion was achieved by analysing the intermediate flux state spectra of Cyg X-1 [296] with a variable density reflection model. However an iron abundance fixed at the solar value was assumed in their modelling.

Second, the best-fit disc viewing angle measured for GX 339−4 is different in different works. The middle panel of Fig. 2.7 shows the constraint of the inclination given by multi-epoch LF spectral analysis and HF spectral analysis. The two measurements are consistent at the 90% confidence level ($i = 34 \pm 2$ deg for the LF observations and $i = 35.9^{+1.6}_{-2.0}$ deg for the HF observations). Although our best-fit value is lower compared with the measurement in Wang-Ji et al. [320] ($i = 40^\circ$) and higher than the measurement in Parker et al. [230] ($i = 30^\circ$), all the previous reflection based measurements are consistent with our results at 2σ level. Similarly Tomsick et al. [296] measured a different viewing angle for Cyg X-1 compared with previous works. It indicates that a slightly different viewing angle measurement might be common when allowing the disc density $n_{\rm e}$ to vary as a free parameter during the spectral fitting.

Third, a high black hole spin ($a_* > 0.93$) is given by the disc reflection modelling in the HF spectral analysis. Due to the lack of a precise measurement of the source distance and

the central black hole mass, we can only give a rough estimation of the inner radius through the normalization of the `diskbb` component in the HF observations. The normalization parameter is defined as $N_{\rm diskbb} = (r_{\rm in}/D_{\rm 10kpc})^2 \cos i$, where the $D_{\rm 10kpc}$ is the source distance in units of 10 kpc and i is the disc viewing angle. The best-fit value is $N_{\rm diskbb} = 1649^{+76}_{-49}$, corresponding to an inner radius of $r_{\rm in} \approx 45\,{\rm km} \approx 3r_g$ assuming $M_{\rm BH} = 10M_\odot$ and $D = 10\,{\rm kpc}$. We also fitted the thermal component with `kerrbb` model [155] as in Parker et al. [230]. `kerrbb` is a multi-colour blackbody model for a thin disc around a Kerr black hole, which includes the relativistic effects of spinning black hole. The BH spin and the disc viewing angle are linked to the corresponding parameters in `relconv`. However we found the source distance and the central black hole mass parameters in `kerrbb` are not constrained during the spectral fitting. `kerrbb` model gives a slightly worse fit with ΔC-stat≈ 7 and 2 more free parameters compared to the `diskbb` model. Since the black hole mass and distance measurement is beyond our purpose, we decide to fit the thermal spectrum in the HF observation with `diskbb` for simplicity. See Parker et al. [230] for more discussion concerning the black hole mass and the source distance measurements obtained by fitting with `kerrbb`. In conclusion, the high spin result in this work is obtained by modelling the relativistic disc reflection component in the HF state of GX 339−4 and is consistent with previous reflection-based spectral analysis [e.g. 238, 90, 230, 320]. Kolehmainen and Done [146] found an upper limit of $a_* < 0.9$ by analysing *RXTE* spectra. However they assumed the disc viewing angle is the same as the binary orbital inclination, which is not necessarily the case [e.g. 295, 312].

Fourth, there is a debate whether the disc is truncated at a significant radius in the brighter phases of the hard state. Compared with the results obtained by modelling the same spectra with $n_{\rm e} = 10^{15}{\rm cm}^{-3}$ and an additional `diskbb` component [320], we find larger upper limits of the inner radius in the LF2-5 observations. For example, an upper limit of $r_{\rm in} < 8R_{\rm ISCO}$ is obtained for the LF2 observation, larger than $r_{\rm in} = 1.8^{+3.0}_{-0.6}R_{\rm ISCO}$ found by Wang-Ji et al. [320]. Such a difference could be due to different modelling of the disc reflection component. The constraints on the inner radius $r_{\rm in}$ are shown in the right panel of Fig. 2.8. Nevertheless, we confirm that the inner radius is not as large as $r_{\rm in} \approx 100r_g$ as proposed by previous results [e.g. 238].

2.4.2 High Density Disc Reflection

The LF and HF *NuSTAR* and *Swift* spectra of GX 339−4 can be successfully explained by high density disc reflection model with a close-to-solar iron abundance for the disc. In the low flux hard states, no additional low-temperature `diskbb` component is required in our modelling. Instead, a quasi-blackbody emission in the soft band of the disc reflection

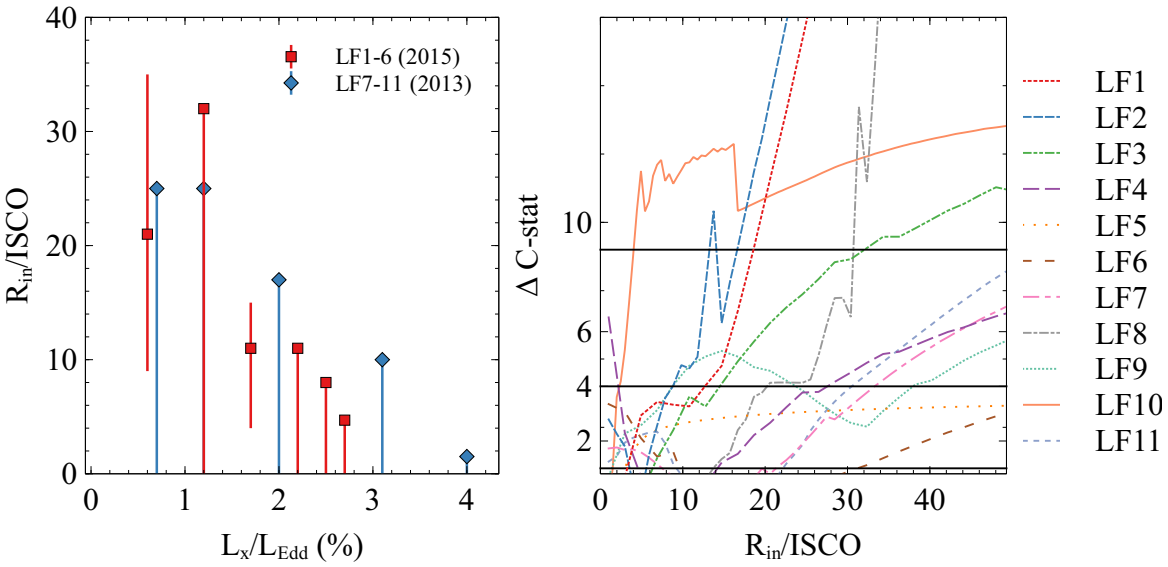

Fig. 2.8 Left: the best-fit inner radius of the disc vs. the X-ray luminosities for LF observations. Red points represent LF1-6 observations and blue points represent LF7-11 observations. The X-ray luminosity $L_{\rm X}$ is the 0.1–100 keV band Galactic-absorption corrected luminosity calculated using the best-fit model. A black hole mass $M_{\rm BH} = 10 M_{\odot}$ and a distance d=10 kpc are assumed. The error bars show the 90% confidence ranges of the measurements. See Table 2.2 for values. Right: the constraints on the inner disc radius for each LF spectra shown in different colours. The solid lines show the 1σ, 2σ, and 3σ ranges.

model fits the excess below 2 keV. At higher disc density, the free-free process becomes more important in constraining low energy photons, increasing the disc surface temperature, and thus turning the reflected emission in the soft band into a quasi-blackbody spectrum. See Fig. 2.5 for a comparison between the best-fit high density reflection model for LF1 observation and a constant disc density model ($n_{\rm e} = 10^{15}$ cm^{-3}).

In LF states of GX 339−4, a disc density of $n_{\rm e} \approx 10^{21}$ cm^{-3} is required for the spectral fitting. Our multi-epoch spectral analysis shows tentative evidence that the disc density increases from $\log(n_{\rm e}) = 20.60^{+0.23}_{-0.12}$ in the highest flux state (LF1) to $\log(n_{\rm e}) = 21.45^{+0.06}_{-0.13}$ in the lowest flux state (LF6) during the decay of the outburst in 2015, except for LF5 observation. See Table 2.2 for $n_{\rm e}$ measurements. A similar pattern can be found in LF7-10 observations. In the HF state of GX 339−4, we measure a disc density of $n_{\rm e} \approx 10^{19}$ cm^{-3} by fitting the broad band spectra with a combination of high density disc model and a multi-colour disc blackbody model. The disc density in the HF state is 100 times lower than that in LF states. The 0.1–100 keV band luminosity of GX 339−4 in HF state ($L_{\rm X} \approx 0.28 L_{\rm Edd}$) is 10 times the same band luminosity in LF states ($L_{\rm X} = 0.01 - 0.04 L_{\rm Edd}$). While the accretion rate is rather small, the anti-correlation between the disc density and the X-ray luminosity $\log(n_{\rm e1}/n_{\rm e2}) \propto -2\log(L_{\rm X1}/L_{\rm X2})$ is found to agree with the expected behaviour of a standard radiation-pressure dominated disc [e.g. 277, 288]. See Section 2.4.3 for more detailed comparison between the measurements of the disc density and the predictions of the standard disc model.

2.4.3 Accretion Rate and Disc Density

Svensson and Zdziarski [288] (hereafter SZ94) reconsidered the standard accretion disc model [277, hereafter SS73] by adding one more parameter to the disc energy balance condition - a fraction of the power associated with the angular momentum transport is released from the disc to the corona, denoted as f. Only $1 - f$ of the released accretion power is dissipated in the colder disc itself.

By following SZ94, we can obtain a relation between $n_{\rm e}$ and f for a radiation-pressure dominated disc:

$$n_{\rm e} = \frac{1}{\sigma_{\rm T} R_{\rm S}} \frac{256\sqrt{2}}{27} \alpha^{-1} R^{3/2} \dot{m}^{-2} [1 - (R_{\rm in}/R)^{1/2}]^{-2} [\xi'(1-f)]^{-3}, \tag{2.1}$$

where $\sigma_{\rm T} = 6.64 \times 10^{-25}$cm^2 is the Thomson cross section; R_S is the Schwarzschild radius; R is in the units of $R_{\rm S}$; $\dot{m}$ is defined as $\dot{m} = \dot{M}c^2/L_{\rm Edd} = L_{\rm Bol}/\epsilon L_{\rm Edd}$; $L_{\rm Edd} = 4\pi G M m_{\rm p} c/\sigma_{\rm T} = 2\pi(m_{\rm p}/m_{\rm e})(m_{\rm e}c^3/\sigma_{\rm T}) R_{\rm S}$ is the Eddington luminosity; ξ' is the conversion factor in the radiative diffusion equation and chosen to be 1, 2 or 2/3 by different authors

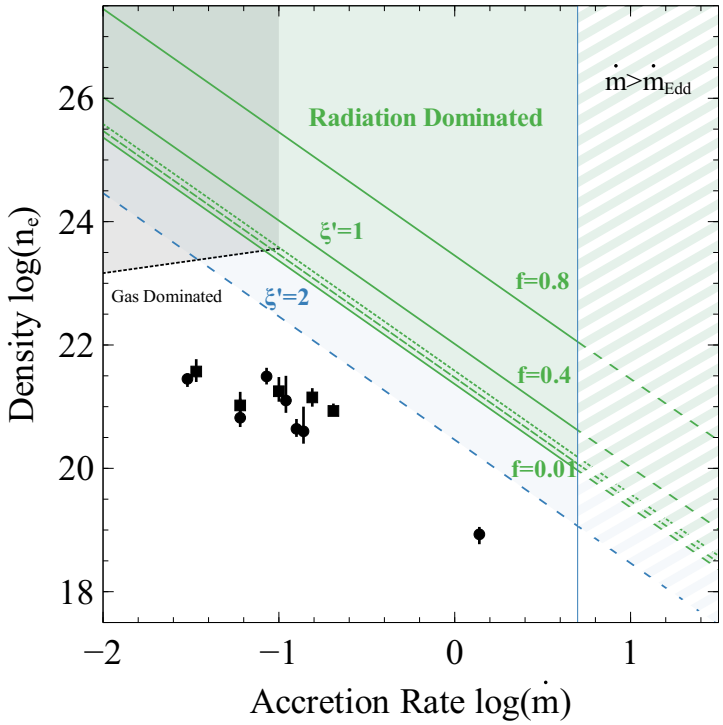

Fig. 2.9 Disc density $\log(n_{\rm e})$ vs. accretion rate $\log(\dot{m})$ based on the radiation-pressure dominated (green) and gas-pressure dominated (black) disc solutions in SZ94, assuming $M_{\rm BH} = 10 M_{\odot}$ and $\alpha = 0.1$. The solid green lines show the solutions with different coronal power fraction f at $R = 2R_{\rm S}$. The dashed and dotted green lines show the radiation pressure-dominated solution with $f = 0.01$ at $R = 6, 8R_{\rm S}$ respectively. The black circular points show the surface disc density and the mass accretion rate measurements of GX 339−4 in LF and HF states in 2015 and the black squares show the measurements for observations in 2013. The mass accretion rate is estimated using $\dot{m} = L_{\rm Bol}/\epsilon L_{\rm Edd} \approx L_{0.1-100{\rm keV}}/\epsilon L_{\rm Edd}$ in this work. A Novikov-Thorne accretion efficiency $\epsilon = 0.2$ [214, 2] and an inner disc radius of $R_{\rm in} = 1R_{\rm S}$ is assumed for a spinning black hole with $a_* = 0.95$. The black vertical line shows the Eddington accretion limit $\dot{m}_{\rm Edd} = 1/\epsilon \approx 5$. $\xi' = 1$ is assumed during the calculation as in SZ94. The blue solid line is shown for the radiation-pressure dominated disc solution with $R = 2R_{\rm S}$ and $f = 0.01$, assuming $\xi' = 2$.

(SZ94); α is the viscosity parameter and $\alpha = 0.1$ is assumed. For a radiation-pressure dominated disc, the disc density $n_{\rm e}$ decreases with increasing accretion rate $\dot{m}$. In Fig. 2.9, we plot the radiation-pressure dominated disc solutions for $\xi' = 1$ [3] in green lines and a solution for $\xi' = 2$ in blue.

When $\dot{m} < 0.1$ and f approaches unity, the radiation-pressure dominated radius disappears and gas pressure starts dominates the disc. The relation between $n_{\rm e}$ and f for a gas-pressure dominated disc is

$$n_{\rm e} = \frac{1}{\sigma_{\rm T} R_{\rm S}} K \alpha^{-7/10} R^{-33/20} \dot{m}^{2/5} [1 - (R_{\rm in}/R)^{1/2}]^{2/5} [\xi'(1-f)]^{-3/10}, \tag{2.2}$$

where $K = 2^{-7/2} (\frac{512\sqrt{2}\pi^3}{405})^{3/10} (\alpha_{\rm f} \frac{m_{\rm p}}{m_{\rm e}})^{9/10} (\frac{R_{\rm S}}{r_{\rm e}})^{3/10}$. $\alpha_{\rm f}$ is the fine-structure constant; $m_{\rm p}$ is the proton mass; $m_{\rm e}$ is the electron mass; $r_{\rm e}$ is the classical electron radius. An example of a gas-pressure dominated disc solution for $R = 2R_{\rm S}$ and $f = 0.01$ is shown by the black line in Fig. 2.9 for comparison. For a gas-pressure dominated disc, the disc density increases with increasing accretion rate.

The best-fit disc density and accretion rate values obtained by fitting GX 339−4 LF1-11 and HF spectra with high density reflection model are shown by black points in Fig. 2.9. The accretion rate is calculated using $\dot{m} = L_{\rm Bol}/\epsilon L_{\rm Edd} \approx L_{0.1-100{\rm keV}}/\epsilon L_{\rm Edd}$, where ϵ is the accretion efficiency and $L_{0.1-100{\rm keV}}$ is the 0.1–100keV band absorption corrected luminosity calculated using the best-fit model. According to Novikov and Thorne [214] and Agol and Krolik [2], an accretion efficiency of $\epsilon = 20\%$ is assumed for a spinning black hole with $a_* = 0.95$ measured in Section 2.3.2. A black hole mass of $10 M_\odot$ and a source distance of 10 kpc are assumed.

The 0.1–100 keV band luminosity in the HF state of GX 339−4 is approximately 10 times the same band luminosity in the LF states. The disc density in the HF state is 2 orders of magnitude lower than the density in the LF1-6 states. The anti-correlation between its density and accretion rate is expected according to the radiation-pressure dominated disc solution in SZ94 ($\log(n_{\rm e}) \propto -2\log(\dot{m})$, as in Eq. 2.1). However the disc density measurements for GX 339−4 are lower than the predicted values for corresponding accretion rates. See Fig. 2.9 for comparison between measurements and theoretical predictions in SZ94. Following are possible explanations for the mismatch: 1. the disc density shown in Eq. 2.1 is assumed to be constant throughout the vertical profile of the disc (SS73). The $n_{\rm e}$ parameter we measure using reflection spectroscopy is however the surface disc density within a small optical depth [265]. 2. the accretion rate might be underestimated by assuming $L_{\rm Bol} \approx L_{0.1-100{\rm keV}}$, although we do not expect other bands of GX 339−4 to make a large

[3] The prime symbol is to distinguish from the disc ionisation parameter ξ.

contribution to its bolometric luminosity; 3. there is a large uncertainty on the black hole mass, the disc accretion efficiency, and the source distance measurements for GX 339−4. For example, the most recent near-infrared study shows that the central black hole mass in GX 339−4 could be within $2 - 10 M_{\odot}$ [110]. Nevertheless, the use of the high density reflection model enables us to estimate the density of the disc surface in different flux states of an XRB and an anti-correlation between $n_{\rm e}$ and $L_{\rm X}$ has been found in GX 339−4.

2.4.4 Future Work

In our work, we conclude that the high density reflection model can explain both the LF and HF spectra of GX 339−4 with a close to solar iron abundance. No additional blackbody component is statically required during the spectral fitting of the LF states. On one hand, the strong degeneracy between the `diskbb` component and the absorber column density is due to the low S/N of the *Swift* XRT observations. More pile-up free soft band spectra are required to obtain a more detailed spectral shape at the extremely LF state of GX 339−4, such as from *NICER*. On the other hand, more detailed spectral modelling is required. For example, a more physics model, such as Comptonization model, is required for the coronal emission modelling in the broad band spectral analysis. The disc thermal photons from the disc to the reflection layer need to be taken into account in future reflection modelling, especially in the XRB soft states where a strong thermal spectrum is shown.

Chapter 3

NuSTAR Observations of GRS 1716−249 in the Hard and Intermediate States

"Rule 1 for building X-ray observatories: no moving parts!"
– George Fraser

3.1 Introduction

XRBs are accretion-powered binary systems that are luminous in X-rays, and typically made up of a compact object accreting from a 'normal' stellar companion. Many BH XRBs show transient events that are characterised by outbursts in the X-ray band. Some outbursts last for only few weeks [e.g. MAXI J1659−152, 199] while some last for years before they return to the quiescent state [e.g. Swift J1753.5−0127, 281]. Two different spectral states are commonly seen during the outbursts of BH XRBs: 1) the hard state where the spectrum is dominated by a power-law shaped continuum; 2) the soft state where the spectrum is dominated by a disc blackbody emission. In the hard state, the spectra often show broad Fe K emission line and a strong Compton hump above 10 keV in addition to the power-law emission that is associated with the corona [e.g. 144]. These features are very similar with the ones found in Seyfert galaxies despite different BH mass scales [e.g. 316] and are referred to as the disc reflection component. In some cases, BH XRBs show an intermediate state between the soft and hard states, where a hard power-law continuum and a disc thermal emission component co-exist in the same spectrum [e.g. 283, 296].

GRS 1716−249 is a low mass XRB first discovered in 1993 [13, 107]. It reached a peak flux of 1.4 Crab in the 20–100 keV band within five days. By studying the Na D absorption lines, della Valle et al. [52] obtained an upper limit of $d \approx 2.8$ kpc for the distance of GRS 1716−249. In our work, we adopt $d = 2.4$ kpc, the same value applied for luminosity calculations in della Valle et al. [52]. Masetti et al. [170] obtained a lower limit for the mass of the central BH ($M_{\rm BH}/M_{\odot} = m_{\rm BH} > 4.9$). GRS 1716−249 was then detected in another outburst in 1995 with a simultaneous radio flare [113].

GRS 1716−249 was found in an outburst 21 years later by *MAXI* on 18th December, 2016 [171, 212]. By analysing the spectra from the *Swift* monitoring programme of this outburst, Bassi et al. [19] found that the source approached the soft state three times but never reached the canonical soft state. Simultaneous radio observations also show GRS 1716−249 is located on the radio-quiet branch of the X-ray–radio luminosity parameter plane [19].

In this chapter, we conduct detailed spectral analysis of the seven *NuSTAR* [108] observations of GRS 1716−249 triggered during the outburst in 2016. Simultaneous *Swift* snapshot observations in the soft X-ray band are considered as well if available. The first three *NuSTAR* observations did not have simultaneous *Swift* observations because of the sun violation for *Swift*. In Section 3.2, we introduce the data reduction processes; in Section 3.3, we present the broad band spectral modelling by using high density disc reflection model, study the spectral variability, and conduct multi-epoch spectral analysis to obtain the disc viewing angle and the disc iron abundance; in Section 3.4, we discuss our spectral analysis results.

3.2 Data Reduction

3.2.1 *NuSTAR* Data Reduction

We use the standard pipeline NUPIPELINE v0.4.6 in HEASOFT V6.25 to reduce the *NuSTAR* data. The calibration file version is v20171002. In addition to the science mode (mode 1) data, we also extracted the products from the spacecraft science (mode 6) event files by following Walton et al. [312]. The mode 6 events are considered because the star tracker was blinded by the sun during the early observations of GRS 1716−249 and was unable to provide an aspect solution. Therefore the source coordinate in the sky was calculated using the spacecraft bus attitude solution for mode 6 observations. The accuracy of the source coordinates is $\approx 2'$ by using the spacecraft bus and $\approx 8''$ using the star tracker [108]. The inclusion of the spacecraft science data maximizes the usable exposure of our observations. See Table 3.1 for the exposure time in two different modes. The mode 1 source spectra are extracted from a circular region with radii of 120 arcsec, and the background spectra are extracted to be circular regions near the source region on the same chip. The mode 6 source spectra are extracted from a circular region with radii of 110–140 arcsec. We generate spectra using the NUPRODUCTS command. The FPMA and FPMB spectra are grouped to a minimum signal-to-noise (S/N) of 6 and to oversample the energy resolution by a factor of 3. The *NuSTAR* data are modelled over the full 3–78 keV band in this work.

3.2.2 *Swift* Data Reduction

We use the standard pipeline XRTPIPELINE v0.4.6 to reduce the *Swift* XRT data [36]. The calibration file version is v20171113. The source spectra are extracted from an annulus region to avoid pile-up effects. The inner radius of the annulus is 5 arcsec and the outer radius of the annulus is 40 arcsec. The XRT spectra are grouped to a minimum S/N of 6 and to oversample the energy resolution by a factor of 3. The *Swift* data are modelled over the 1–8 keV band in this work. We ignore the spectra below 1 keV due to the known calibration issue of the window timing mode.

3.3 Data Analysis

In this section, we first present an overview of the spectral transition through the outburst of GRS 1716−249 in 2016-2017. Second, we conduct detailed broad band spectral modelling using a high density disc reflection model. In the end, we discuss the changes of the disc-

Table 3.1 A list of observations considered in this work.

Obs No.	*NuSTAR* ObsID	Date	Mode 1 Exp. (ks)	Mode 6 Exp. (ks)	*Swift* ObsID	XRT Exp. (ks)
1	80201034002	2016-12-26	-	23	-	-
2	80201034004	2016-12-31	0.4	18	-	-
3	80201034006	2017-01-05	6	47	-	-
4	80201034007	2017-01-28	7	6	0034924001	1.0
5	90202055002	2017-04-07	18	1.8	0034924029	1.7
6	90202055004	2017-04-10	16	1.8	0034924031	1.9
7	90301007002	2017-07-28	89	10	0088233001	3.7

coronal geometry and the disc properties during the outburst by conducting a multi-epoch spectral analysis.

3.3.1 Spectral State Transition

The *MAXI* lightcurves of GRS 1716−249 in different energy bands are shown in Fig. 3.1. The outburst of this source lasted for 8 months until it returned to the quiescent state. The X-ray flux rose for the first 2 months of the outburst before starting a slow decay. The bottom panel of Fig. 3.1 shows the hardness ratio between the 4–10 keV and 2–4 keV bands. The hardness ratio curve from *MAXI* indicates that the source spent majority of the outburst in the hard state before approaching the soft state near the end of the outburst, although the total X-ray flux remained decaying across this period. GRS 1716−249 returned to the hard state before fading back to quiescence, indicating an outburst with failed transition to the soft state. We refer interested readers to Bassi et al. [19] for a complete hardness-intensity diagram (HID) of this outburst obtained by *Swift*, which monitored GRS 1716−249 throughout this outburst.

The black arrows in Fig. 3.1 mark the dates when the *NuSTAR* observations were taken during the outburst. The spectra of all the *NuSTAR* and *Swift* observations unfolded through a constant model are shown in Fig. 3.2. The left panel of Fig. 3.2 shows the spectra of the first four observations during the rising phase of the outburst. These four observations show very similar spectral shape but different flux levels. The right panel shows the spectra extracted from the rest of the observations. Obs 5 and 6, which were taken 2 months after the 4th observation, show a softer broad band spectral shape but a similar X-ray flux level compared with the observations in the rising phase of the outburst. Such a change in the spectral shape matches the indication from the *MAXI* lightcurves in Fig. 3.1. Obs 7 was taken 7 months after the beginning of the outburst. The spectra of obs 7 are shown in the right

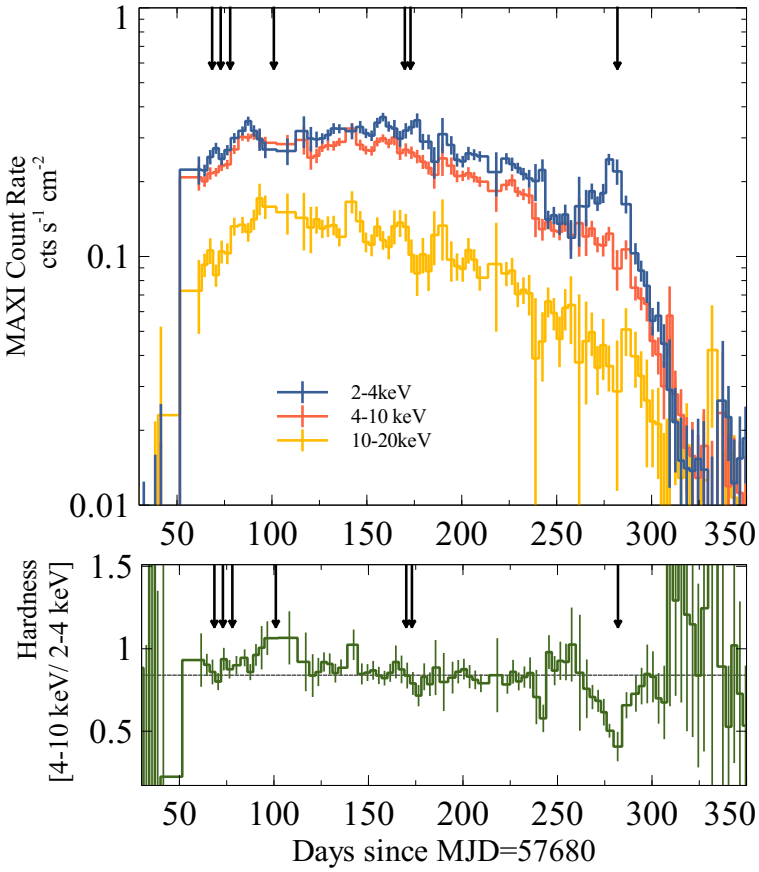

Fig. 3.1 Top: *MAXI* light curves of GRS 1716−249 in 3-day bin during the outburst in 2016–2017 (blue: 2–4 keV; red: 4–10 keV; yellow: 10–20 keV). The black arrows mark the dates when the *NuSTAR* observations were taken. Bottom: the hardness ratio curve obtained by *MAXI*. The hardness ratio is calculated by the flux ratio between the 4–10 keV and 2–4 keV bands.

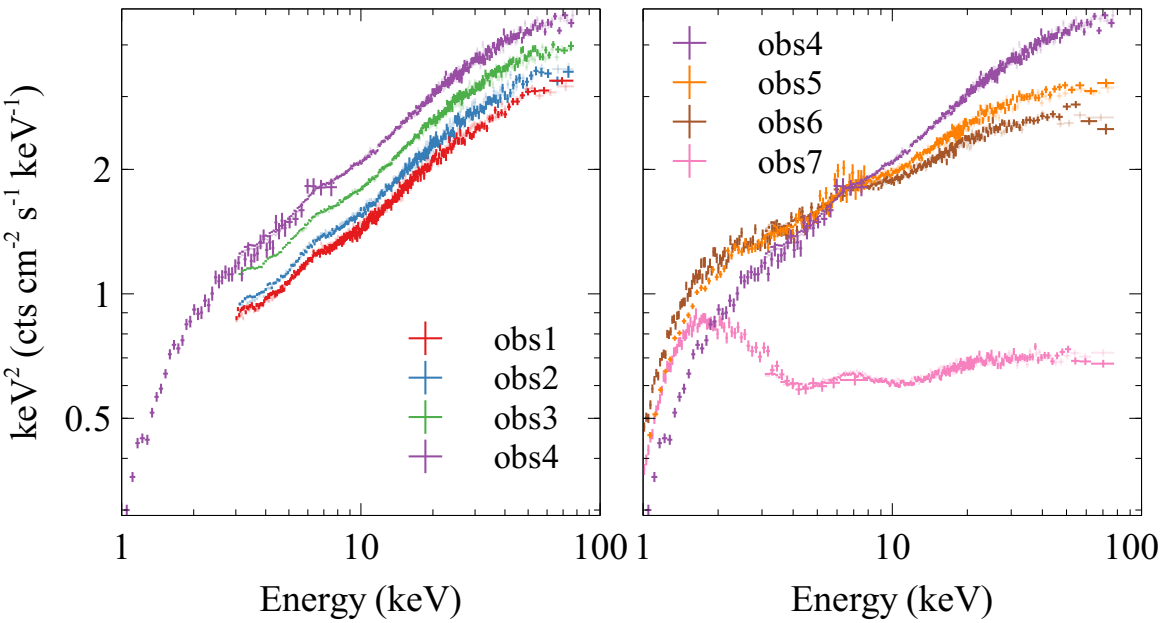

Fig. 3.2 The *NuSTAR* FPMA, FPMB (fainter colours) and *Swift* spectra of obs 1-4 (left) and obs 4-7 (right) unfolded through a constant model. The spectra of obs 1-4 show a similar spectral shape but different flux levels. The *Swift* XRT spectra have been shifted to match the *NuSTAR* spectra in the overlapping energy band (3–8 keV). The `constant` model is used to account for the cross-calibration factor during our detailed spectral modelling.

panel of Fig. 3.2 for comparison with previous observations. The last observation shows the lowest total X-ray flux level but a very strong blackbody-shaped soft emission below 3 keV.

3.3.2 Spectral Modelling

We use XSPEC V12.10.1b [9] for spectral analysis and C-stat is used in this work. The upper limit of the Galactic column density in the line of sight towards GRS 1716−249 is 3.97×10^{21} cm^{-2} [326]. We fix the column density of the Galactic absorption at this value when fitting the spectra with absorbed power-law models. Then we model with the column density as a free parameter for the final results.

We first fit the spectra with absorbed power-law models. Data/model ratio plots for these models are shown for each epoch in Fig. 3.3. All the spectra show a broad emission line feature in the iron band and a Compton hump above 10 keV. In addition to these relativstic reflection features, the soft energy band of obs 7 is dominated by a strong excess emission. Based on the evidence for broad Fe K emission line and the strong Compton hump in the spectra, we model the broad band spectra with a combination of a coronal emission component and a relativistic disc reflection component. The former component is modelled using the simple power-law model `cutoffpl` with a high energy exponential cut-off. The latter component is calculated using `relconvlp * reflionx`. A more developed version of `reflionx` [264, 265] is used to model the disc reflection model in the rest frame with following parameters: disc iron abundance ($Z_{\rm Fe}$), disc ionization ($\log(\xi)$), disc density ($n_{\rm e}$), high energy cut-off ($E_{\rm cut}$), and photon index (Γ). The solar abundance in `reflionx` is calculated by Morrison and McCammon [196]. The ionisation parameter is defined as $\xi = 4\pi F/n$ in the unit of erg cm s^{-1}, where n is the hydrogen number density and F is the illuminating flux. The high energy cut-off parameter and the photon index in the reflection model are linked to the corresponding parameters of `cutoffpl` in XSPEC. A convolution model `relconvlp` [49] is used to apply relativistic effects to the rest-frame reflection model. The `relconvlp` model calculates the emissivity profile according to a simple lamp-post model parameterised by the height of the corona above the disc. Other free parameters in this model are the disc inner radius $r_{\rm in}/r_{\rm ISCO}$ and the disc inclination angle i. The spin parameter is fixed at the maximum value 0.998 to fully study the inner disc radius parameter. The outer radius of the disc is assumed to be at 400 $r_{\rm g}$ as the fits are insensitive to this parameter. The convolution model `cflux` is used to calculate the flux of each model component between 1–78 keV band. We define the reflection fraction as $f_{\rm refl} = F_{\rm refl}/F_{\rm pl}$, where $F_{\rm refl}$ and $F_{\rm pl}$ are the best-fit flux values given by `cflux`. A `constant` model is used to account for the cross-calibration uncertainity between different instruments. The total model is `constant *`

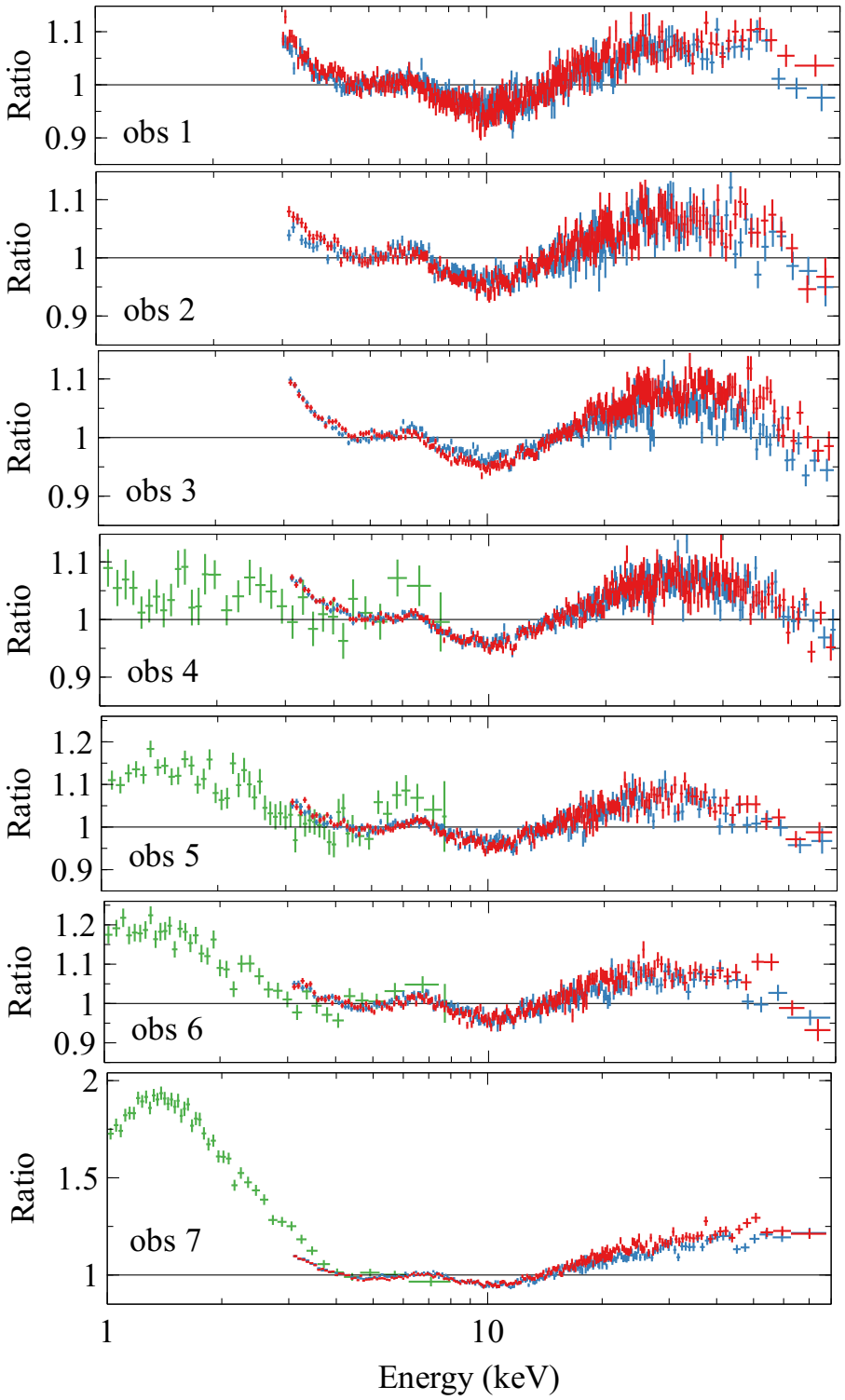

Fig. 3.3 The ratio plots of *NuSTAR* FPMA (red), FPMB (blue) and *Swift* XRT (green) spectra against the best-fit power-law model in the 3–80 keV band. All the spectra show a broad emission line at 6.4 keV and a strong Compton hump above 10 keV.

`tbabs * (cflux * ( relconv * reflionx ) + cflux * cutoffpl )` (`MODEL1`) in the XSPEC format.

The combination of relativistic disc reflection and power law-shaped coronal emission models offers a very good fit to the spectra of first 6 observations with C-stat/$\nu \approx 1.0$, where ν is the number of degrees of freedom. For example, we obtain a good fit with no evidence for structured residuals and C-stat/$\nu = 2665.32/2613$ by modelling the spectra of obs1 with `MODEL1`. In order to test for any narrow emission line in the iron band, we also tried adding one Gaussian line model `gauss` with the line energy fixed at 6.4 keV. This additional line model only improves the fit by ΔC-stat=2 with 2 more free parameters (normalization and line width) for obs1. Only an upper limit of the equivalent width of the line model is obtained (EW<3 eV). A similar conclusion is found when analysing the spectra of obs 2–6. Therefore we conclude that there is no evidence for a distant reflector in our observations.

As shown in Fig. 3.2 and Fig. 3.3, the low energy spectrum of obs 7 shows clear evidence for an additional blackbody-shaped component. By modelling the *Swift* and *NuSTAR* spectra simultaneously with `MODEL1`, we fail to obtain a good fit for obs 7. The high density disc reflection model is unable to model the strong 'soft excess' emission with C-stat/ν=5250.68/1512. By adding an additional `diskbb` component, we improve the fit by ΔC-stat=3486 with 2 more parameters. The full model is `constant * tbabs * (cflux * ( relconv * reflionx ) + cflux * cutoffpl + diskbb)` (`MODEL2`) in the XSPEC format. The requirement for an additional disc-blackbody component agrees with previous analysis [e.g. 8, 19], marking a transition to an intermediate state where both the disc thermal emission and the coronal emission contribute significantly to the total observed X-ray flux. Similarly, a combination of high density disc reflection and disc thermal emission has been also found in the intermediate state of Cyg X-1 [296].

In order to test whether the spectra of the hard state spectra (obs 1-6) require an additional `diskbb` component, we re-analysed the spectra with `MODEL2`. There is a degeneracy between the `diskbb` component and the high disc density parameter in obs 1-3 due to the lack of simultaneous soft X-ray observations. However in obs 4-6, an additional `diskbb` component only improves the fit by ΔC-stat$= 4 - 7$ with two more free parameters. We conclude that an additional `diskbb` component is statistically not required for the spectral fitting for the hard state observations. A similar conclusion has been found in the previous analysis of the hard state observations of GX 339-4 with a variable disc density parameter (see Chapter 2).

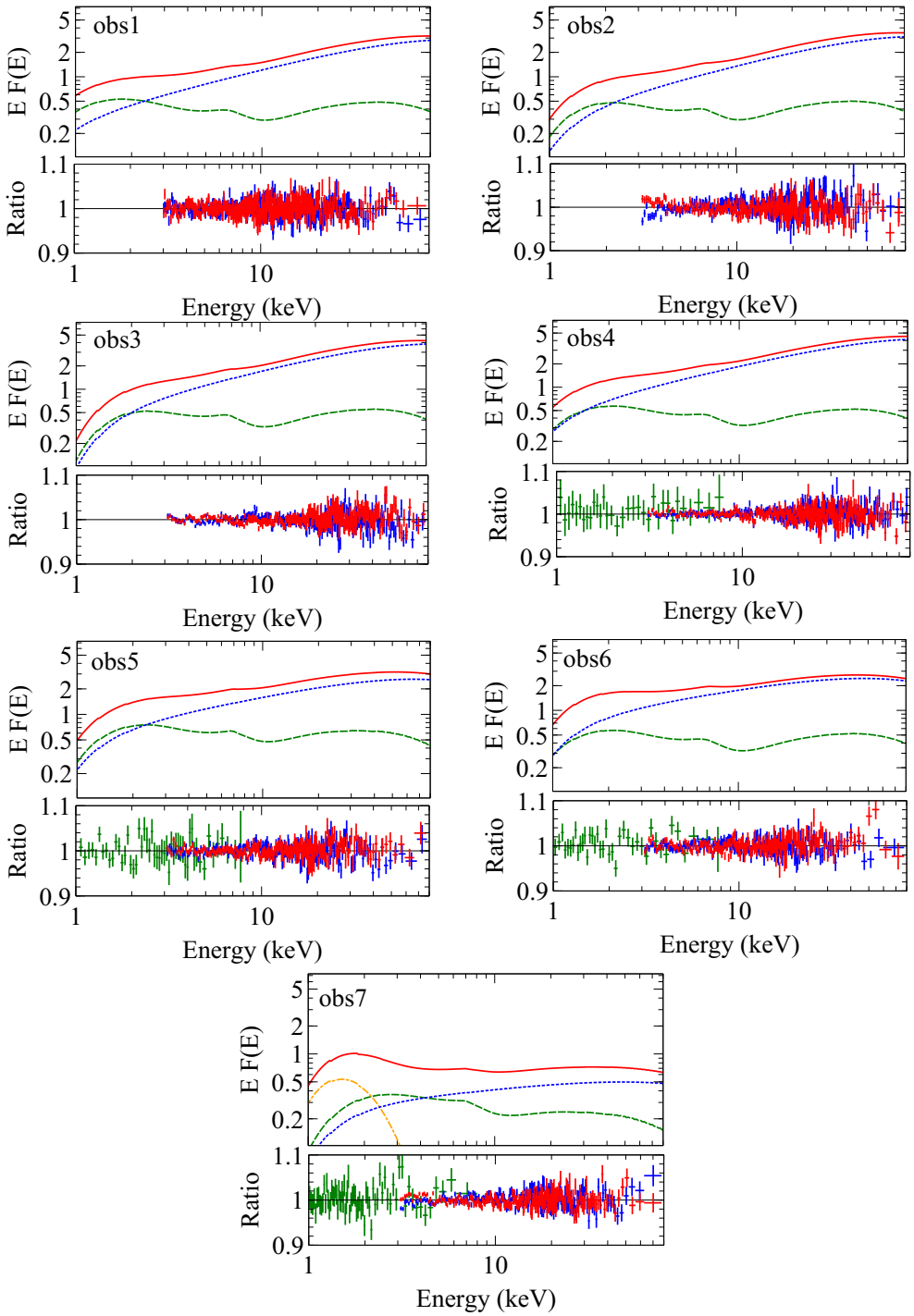

Fig. 3.4 Top panels: the best-fit spectral models (red: total model; blue: coronal emission; green: relativistic reflection; yellow: disc blackbody component). The y-unit is $\mathrm{keV}^2(\mathrm{cts\,cm^{-2}\,s^{-1}\,keV^{-1}})$. Bottom panels: corresponding ratio plots (red: FPMA; blue: FPMB; green: XRT).

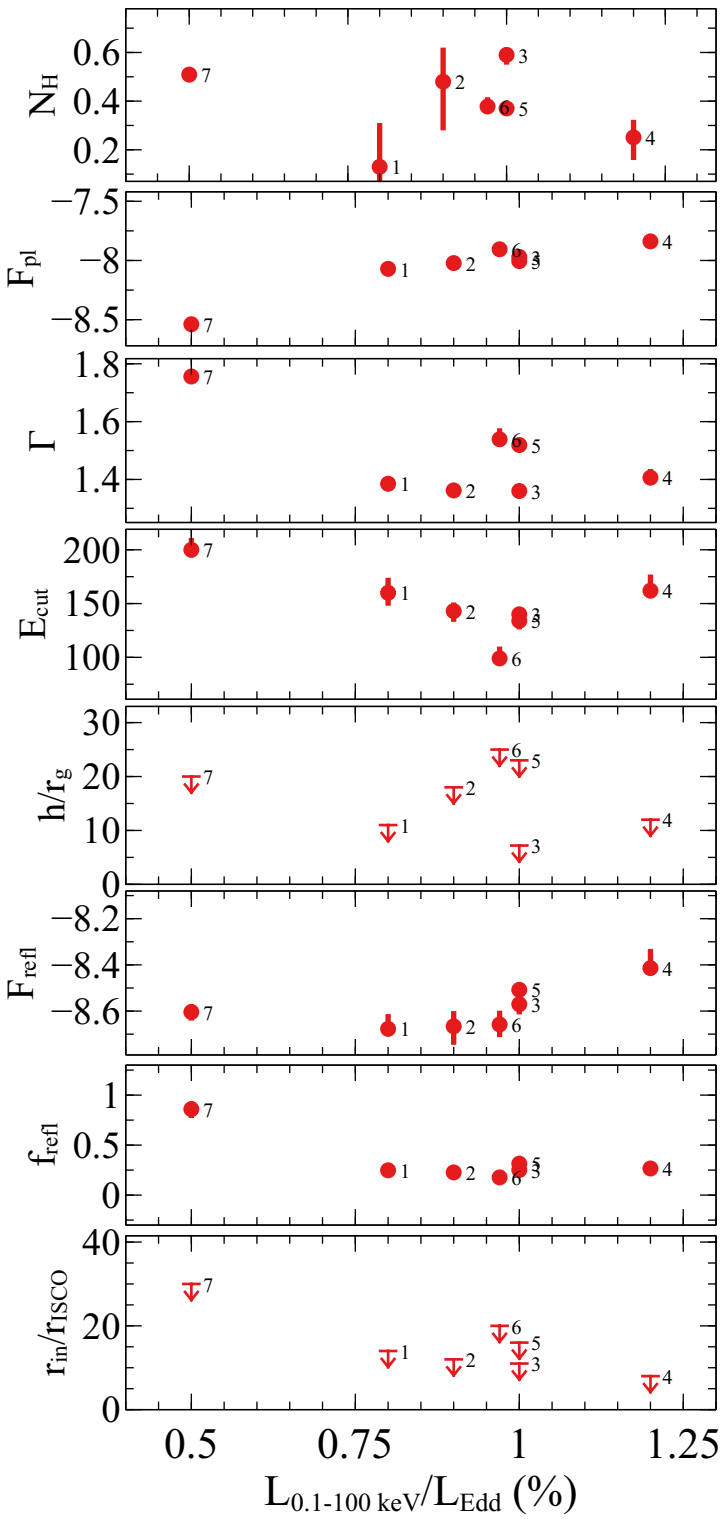

Fig. 3.5 Best-fit parameters at different luminosities in the unit of the Eddington luminosity for a 10$M_\odot$ BH. The best-fit parameter values are in the same unit as the ones in Table 3.2

3.3.3 Multi-epoch Spectral Analysis

In the previous section, we successfully model the spectra of obs1–6 with `MODEL1` and obs7 with `MODEL2` individually. The best-fit disc inclination angles i for all the epochs are consistent with $i \approx 30^{\circ}$ and the disc iron abundances $Z_{\rm Fe}$ are consistent with the solar iron abundance. Therefore, we conduct a multi-epoch spectral analysis by linking the disc iron abundance and the disc inclination angle parameters. `MODEL1` is used for obs 1-6 and `MODEL2` is used for obs 7. The best-fit model for each observation is shown in Fig. 3.4 and the best-fit parameters are shown in Table 3.2. We obtain a very good fit with C-stat/$\nu = 10299.69/9299$. A small disc viewing angle of $i = 31^{+3}_{-2}{}^{\circ}$ and a near-solar iron abundance ($Z_{\rm Fe} = 1.1 \pm 0.5 Z_{\odot}$) are found. All the observations require a disc density significantly higher than $n_{\rm e} = 10^{15}$ cm^{-3}, which was assumed in most of previous reflection-based analysis for other XRB. More discussions about the disc density can be found in Section 3.4. We also notice that the FPMA and FPMB data of obs 2 and 7 show difference of 6% in the spectra below 4 keV. Similar disagreement between FPMA and FPMB spectra has also been found in other *NuSTAR* observations [e.g. 163] due to possible calibration uncertainty.

Fig. 3.5 presents the changes of the best-fit parameters with the Eddington ratio. $L_{0.1-100{\rm keV}}$ is the 0.1–100 keV band absorption corrected luminosity calculated using the best-fit model. Only a lower limit of $m_{\rm BH}$ is obtained [e.g. $m_{\rm BH}$>4.9, 170]. A black hole mass of $10 M_{\odot}$ is assumed for the calculation of the Eddington luminosity for simplicity. The relative luminosity change between epochs does not change even if this mass assumption is incorrect. Because the same mass value is used for the calculation of the Eddington luminosity for all the epochs.

The first panel of Fig. 3.5 shows the best-fit column density of the X-ray absorption. The upper limit of the Galactic column density along the line of sight is estimated being 3.97×10^{21} cm^{-2} [326]. Most of the best-fit values obtained in this work are consistent with this value. The column densities obtained for obs 3 and 7 are significantly higher than 4×10^{21} cm^{-2}, indicating a possible line-of-sight variable neutral absorption. More work concerning possible degeneracy between the column density and other parameters in this analysis needs to be done [e.g. 123].

The next four panels of Fig. 3.5 present the evolution of the coronal properties through the outburst. The absolute flux of the coronal emission ($F_{\rm pl}$) increases with the total X-ray flux. The photon index of the coronal emission remains consistent with $\Gamma = 1.4$ in obs 1-4, although $F_{\rm pl}$ increases by a factor of 2. As shown in Fig 3.2, the coronal emission becomes softer in obs 5 and 6 with $\Gamma = 1.5$. The spectra show the softest continuum in obs 7 when the source is in an intermediate state. The high energy cut-off parameter ($E_{\rm cut}$) shows an anti-correlation with the Eddington ratio, except for obs 4 when the source is in the highest

flux state. Obs 6, where a softer continuum is found compared to obs 1-4, has the lowest $E_{\rm cut}$, corresponding to a cooler corona. By contrast, obs 7, where the source is in the lowest flux state, has the highest $E_{\rm cut}$, corresponding to a hotter corona. This suggests the temperature of the corona may respond to the accretion rate of the disc. At a higher luminosity/accretion rate, more disc photons are up-scattered in the coronal region, which increases the radiative cooling and lowers the coronal temperature. The fifth panel shows the height of the corona h for each epoch. Only upper limits of h are found. No obvious coorelation between h and the X-ray luminosity is found. Future observations with a higher spectral resolution in the iron band may be able to better constrain the geometry of the corona in BH transients by measuring the emissivity profile of the broad Fe K emission line in more details.

The variability of the disc reflection component is shown in the last three panels of Fig. 3.5. The absolute flux of the disc reflection component remains consistent when $L_{0.1-100\rm keV}/L_{\rm Edd} < 1\%$ and increases when $L_{0.1-100\rm keV}/L_{\rm Edd} > 1\%$. Due to the decrease in the absolute flux of the coronal emission, obs 7 shows the highest reflection fraction in all the epochs, indicating a more compact coronal region during obs 7. Note that the definition of $f_{\rm refl}$ in this work is different from the reflection fraction defined in Dauser et al. [47], where the value is calculated according to specific coronal geometry. Only upper limits of the inner radius have been obtained in all the observations. However, a larger upper limit is found at low luminosities, indicating that disc truncation is possible (e.g. $r_{\rm in} \approx 20 r_{\rm g}$) at $L_{0.1-100\rm keV}/L_{\rm Edd} = 0.5\%$.

3.4 Discussion

We have undertaken an analysis of the broadband (1–78 keV) X-ray spectra of the BH XRB GRS 1716−249 taken by NuSTAR and Swift during its recent 'failed' outburst. Following our recent work on GX 339−4 [123], we focus on modeling the data with reflection models that allow the density of the disc to be fit as a free parameter (see also Tomsick et al. [296]).

We first summarize the spectral fitting results: the first four observations were taken at the rising phase of the outburst. The spectra show a consistent spectral shape but an increasing X-ray luminosity (from 0.8% to 1.2% of $L_{\rm Edd}$). The inner radius of the disc is found to be $< 8 r_{\rm ISCO}$ in obs 4 when the source reaches the highest X-ray luminosity, indicating a disc extending to ISCO or a slightly truncated disc. The spectra of obs 5 and 6 become softer than obs 1-4 although the source remains at a similar X-ray luminosity as the previous analysis. During this transition, obs 6 shows the lowest high energy cut-off in the coronal emission, indicating a cool coronal temperature (e.g. T=30–50 keV[1]). At the same time, the density in the surface of the disc increases by a factor of 5 compared to the density in obs

[1]The value of $E_{\rm cut}$ is approximately 2–3 times of $kT_{\rm e}$, depending on the optical depth of the corona.

Table 3.2 The best-fit parameters obtained in the multi-epoch spectral analysis. More details can be found in Section 3.3.3. The flux values of the reflection component ($F_{\rm refl}$) and the coronal emission ($F_{\rm pl}$) are calculated between 1–78 keV in the unit of erg cm^{-2} s^{-1}.

Parameter	Unit	Obs1	Obs2	Obs3	Obs4	Obs5	Obs6	Obs7
$N_{\rm H}$	10^{21} cm^{-3}	$1.3^{+1.8}_{-0.8}$	$4.8^{+1.4}_{-2.0}$	$5.9^{+0.3}_{-0.4}$	$2.5^{+0.7}_{-0.9}$	3.7 ± 0.3	$3.8^{+0.4}_{-0.3}$	5.0 ± 0.2
kT	keV	-	-	-	-	-	-	$0.401^{+0.003}_{-0.002}$
norm	-	-	-	-	-	-	-	6220^{+520}_{-320}
h	$r_{\rm g}$	< 11	< 18	< 7	< 12	< 23	< 25	< 20
$R_{\rm in}$	$r_{\rm g}$	< 14	< 12	< 11	< 8	< 16	< 20	< 30
i	degrees	31^{+3}_{-2}	-	-	-	-	-	-
$\log(\xi)$	-	$3.50^{+0.04}_{-0.03}$	$3.50^{+0.02}_{-0.15}$	$3.53^{+0.07}_{-0.05}$	$3.49^{+0.03}_{-0.04}$	$3.45^{+0.05}_{-0.08}$	$3.13^{+0.09}_{-0.10}$	3.72 ± 0.02
$Z_{\rm Fe}$	$Z_{\odot}$	1.1 ± 0.5	-	-	-	-	-	-
$n_{\rm e}$	10^{19}cm^{-3}	6 ± 3	$7.1^{+2.4}_{-1.1}$	6^{+3}_{-4}	6^{+3}_{-2}	17^{+13}_{-7}	40^{+20}_{-23}	15^{+10}_{-5}
$\log(F_{\rm refl})$	erg cm^{-2} s^{-1}	$-8.68^{+0.06}_{-0.02}$	$-8.67^{+0.07}_{-0.08}$	$-8.57^{+0.03}_{-0.04}$	$-8.41^{+0.08}_{-0.03}$	$-8.51^{+0.03}_{-0.05}$	$-8.66^{+0.06}_{-0.05}$	$-8.60^{+0.03}_{-0.04}$
Γ	-	$1.385^{+0.017}_{-0.014}$	$1.362^{+0.009}_{-0.016}$	$1.360^{+0.011}_{-0.014}$	$1.41^{+0.03}_{-0.02}$	$1.519^{+0.009}_{-0.010}$	$1.54^{+0.04}_{-0.03}$	$1.756^{+0.018}_{-0.015}$
$E_{\rm cut}$	keV	160^{+14}_{-12}	143^{+8}_{-10}	140^{+5}_{-6}	162^{+15}_{-7}	134^{+9}_{-8}	99^{+11}_{-5}	200^{+11}_{-7}
$\log(F_{\rm pl})$	erg cm^{-2} s^{-1}	$-8.071^{+0.009}_{-0.013}$	$-8.022^{+0.014}_{-0.016}$	$-7.97^{+0.011}_{-0.009}$	$-7.839^{+0.005}_{-0.002}$	-8.005 ± 0.013	$-7.906^{+0.008}_{-0.009}$	$-8.538^{+0.018}_{-0.029}$

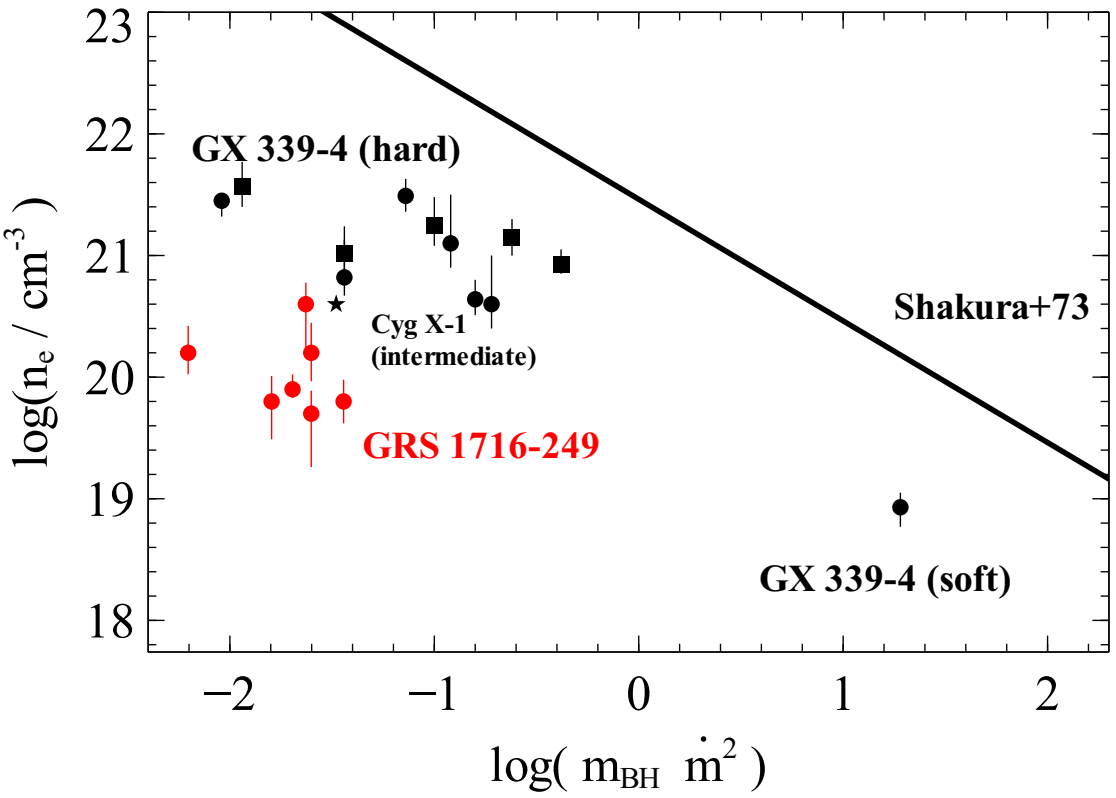

Fig. 3.6 Disc density vs. BH mass and mass accretion rate $m_{\rm BH}\dot{m}^2$. Black circles: GX 339-4 hard and soft state observations in 2015 [123]; black squares: GX 339-4 hard state observations in 2013 [123]; black star: Cyg X-1 in the intermediate state [296]; red diamonds: GRS 1716−249 hard and intermediate state observations in 2016. A black hole mass of $10M_{\odot}$ and an accretion efficiency of 20% are assumed during the calculation of the mass accretion rates for GRS 1716−249. The solid line is the solution for a radiation pressure-dominated disc at $r = 2R_S$ calculated by Shakura and Sunyaev [277], assuming $r_{\rm in} = 1R_S$ and $\xi' = 2$. More details can be found in Jiang et al. [123].

1-4. The last observation, obs 7, was taken 7 months after the beginning of the outburst. The spectra of obs 7 show a combination of a disc thermal emission ($kT = 0.4$keV), a softer coronal emission ($\Gamma = 1.76$), and a strong disc reflection component, indicating the source is in a very low flux intermediate state. GRS 1716−249 shows the lowest X-ray luminosity in obs 7 compared to obs 1-6, but has a similar absolute flux from the disc reflection component to these higher flux observations, indicating a possible change in the geometry of the corona. However only upper limits of the coronal height are obtained.

Second, we discuss the disc density measurements during the outburst of GRS 1716−249. The disc densities measured in this work are shown by the red diamonds in Fig. 3.6. Black circles represent the observations of GX 339−4 in 2015 and black squares represent the observations of the same source in 2012 obtained in Chapter 2. The black star shows the disc density of Cyg X-1 in the intermediate state [296]. The mass accretion rate $\dot{m}$ is estimated using $\dot{m} = L_{\rm Bol}/\epsilon L_{\rm Edd} \approx L_{0.1-100{\rm keV}}/\epsilon L_{\rm Edd}$, where ϵ is the accretion efficiency. A black hole mass of $10M_{\odot}$ and an accretion efficiency of $\epsilon = 20\%$ are assumed. Assuming the distance measurements of GX 339-4 and GRS 1716−249 are accurate and the BH mass used for calculation is correct, the hard states of two sources show similar X-ray luminosity. However the disc density in GRS 1716−249 is 10 times lower than the density in GX 339-4. The difference of the disc density could be due to different BH mass, accretion efficiency, and intrinsic bolometric luminosity. The intermediate state of GRS 1716−249 shows a similar disc density as the intermediate state of Cyg X-1 but a much lower luminosity in the X-ray band. Nevertheless, we conclude that the disc density required for the broad band spectral analysis of GRS 1716−249 is significantly larger than $n_{\rm e} = 10^{15}$ cm^{-3}, which was assumed in previous reflection-based spectral modelling.

The solid line in Fig. 3.6 shows the disc density at $r = 2R_{\rm S}$ of a radiation pressure-dominated disc varying with the parameter $m_{\rm BH}\dot{m}^2$. $r_{\rm in} = 1R_{\rm S}$ is assumed for the disc inner radius and $\xi' = 2$ is assumed for the conversion factor in the radiative diffusion equation. We refer interested readers to Svensson and Zdziarski [288] for more details and Chapter 2 for the complete equations. In this thin disc model, the density of the disc has an anti-correlation with the BH mass accretion rate ($\log(n_{\rm e}) \propto -2\log(\dot{m})$). However, a significantly lower disc density has been found in various BH transients compared to the thin disc model. The reasons of the offset might be 1) the uncertainties of the BH mass and distance measurements. This may also be able to explain a lower disc density in GRS 1716−249 than in GX 339-4 due to the underestimation of $m_{\rm BH}\dot{m}^2$. 2) The vertical structure of the disc is still uncertain. The disc density in the standard disc density model is assumed to be uniform across the height of a thin disc [277, 288]. Future detailed MHD

simulations for stellar-mass BH accretion disc at $L_{0.1-100\mathrm{keV}}/L_{\mathrm{Edd}} < 1\%$ may be able to solve this problem.

Chapter 4

The 1.5 Ms *XMM-Newton* Observing Campaign on IRAS 13224−3809

"We are on one side of the looking glass."
– Commander Michael Burnham, 'Star Trek: Discovery'

4.1 Introduction

The primary X-ray emission from black holes can be described by a power-law continuum with a high energy cutoff, often explained by inverse Comptonization of the thermal disk photons in a coronal region [e.g. 105]. The corona is known to be compact, though its exact nature still remains unknown. Advanced imaging and timing analyses show the X-ray emitting regions are highly compact and only a few gravitational radii from the black hole [250]. For example, the discovery of a soft X-ray reverberation lag of 30 s in 1H0707-495, a narrow line Seyfert 1 galaxy (NLS1), has indicated the X-ray emitting region is very compact [70], which will be discussed more later. Moreover, in the microlensed galaxy the microlensing duration in the X-ray band is much shorter than the UV/optical band, which indicates a much smaller X-ray emitting region than the optical emitting region [e.g. 195, 39]. Some progress on modeling the disk emissivity profile with different compact corona geometries has also been made [e.g. 323, 324], and is consistent with a compact coronal region, close to the event horizon. The compact corona also agrees with the predictions of the Comptonization model with magnetic reconnection [e.g. 180], where the corona is described as a region of smooth magnetic field with increasing strengths towards small radii. A coronal geometry in which the continuum originates from a small region on the spin axis at height h above the central black hole can describe X-ray data from many luminous accreting black holes well [e.g. MCG-6-30-15, 68, 190, 308]. Such a geometry is usually called the lamp-post geometry.

The reprocessing of the coronal radiation by the colder material in the disk produces a hump above 20 keV and a series of atomic lines, most notably the strong Fe Kα emission line at 6.4 keV. These features are referred to as the disk reflection component. The interaction between the primary power-law photons and the disk material can produce both emission, including fluorescence lines and recombination continuum, and absorption edges [91, 84]. X-ray reflection off the inner part of the accretion disk is highly affected by strong gravitational effects including gravitational redshift and Doppler effects [e.g. 256], which can offer information on the geometry of the corona and the spin of the central black hole. Relativistic broad Fe line features have been detected in the reflection spectra of many AGN sources, such as MCG-6-30-15 [e.g. 291, 328, 68, 165]. Recent work on AGN X-ray variability has shown time lags where the soft excess and Fe Kα line lag behind the power law continuum [e.g. 70, 341, 342, 340, 132].

IRAS 13224−3809 [$z = 0.066$, 3] is classified as a NLS1 hosting a supermassive black hole [$M_{\rm BH} = 10^6 - 10^7\ M_\odot$, 338]. It has been studied in multiple bands previously. It was identified by Boller et al. [25] as a radio quiet source, with 1.4 GHz flux of 5.4 mJy and no

clear jet emission yet observed [71]. UV continuum variability of 24 per cent in three years has been observed [260]. Leighly [152] found asymmetric high ionisation emission lines in the HST UV spectrum, indicating evidence of an outflow. Ly_α line variability has been detected with variation in the line profile and flux level [169]. Though there is no significant rapid optical variability detected [331], it exhibits extreme and rapid variability in the X-ray band on very short time scales of hundreds of seconds [25, 77, 62]

IRAS 13224−3809 was observed by the *XMM-Newton* satellite [121] in 2002 and 2011, showing a steep spectrum [e.g. $\Gamma = 2.5-2.7$, 27, 62] with an obvious soft excess below 1.5 keV and a sharp spectral drop around 8 keV [27, 239, 62, 41]. The spectrum shows very strong Fe K and Fe L emission lines [239, 62] which are explained as the indication of reflection off the inner accretion disk around a rapidly rotating black hole [e.g. $a_* = 0.988 \pm 0.001$, 65, 62]. By analyzing the disk emissivity profile in the 500 ks long *XMM-Newton* observation in 2011, Fabian et al. [62] found that the corona is located within a few gravitational radii. Chiang et al. [41] fitted the soft excess in the EPIC spectra successfully with the combination of the reflection model `reflionx` [263] and a black body. The RGS spectra do not exhibit any evidence for absorption features produced by a warm absorber [236] or partial covering clouds [41], and there is no evidence for absorption in the UV spectra [153].

A soft (0.3–1 keV) lag behind the 1–4 keV band was found in IRAS 13224−3809 by Ponti et al. [239], similar to the lag detected in 1H0707−495 [70, 341], though the significance of the lags is limited due to the short duration of the *XMM-Newton* observation in 2002. A more detailed timing study of the longer observation in 2011 found a strong Fe K feature in the lag-energy spectrum and suggested that the frequency and the amplitude of the lag varies in high flux intervals and quiescent periods [133]. These changes in the lag properties with flux are thought to be due to a more compact disk/corona system. Chainakun et al. [38] simulated the time-averaged model and lag-energy model in the lamp-post scenario and the model also supports a reflection origin for the soft excess of IRAS 13224−3809 and an X-ray source very close to the central black hole ($h \approx 2\,\mathrm{R_g}$).

IRAS 13224−3809 was recently observed with a *XMM-Newton* quasi-simultaneous 1.5 Ms and *NuSTAR* [108] observing campaign in 2016 (P.I. A. C. Fabian). In Parker et al. [229], we reported the discovery of a series of strongly blueshifted ($v = 0.236 \pm 0.006\,\mathrm{c}$) absorption lines from O, Ne, and Fe in the *XMM-Newton* EPIC-pn and RGS spectra, indicating the presence of an ultra-fast outflow (UFO). These features in IRAS 13224−3809 were found to be strongly dependent on the source flux, varying on timescales as short as a few kiloseconds. Similar outflows have been detected in many sources by studying the blue-shifted Fe K-shell absorption lines in the 7–10 keV energy band [e.g. 294], but none has ever been seen to vary as rapidly, or to have strong correlation with flux [225, 236]. The flux dependence

can be explained as the increased source flux ionising the outflowing gas, saturating the absorption lines. Alternatively, the absorption features could be produced in a layer on top of the accretion disk, where these relativistic velocities occur naturally. In this case, the change in strength of the absorption is due to the change in reflection fraction with flux, as only the reflected emission is absorbed [78]. This model has been successfully applied to PG 1211+143 [79]. Following on from the detection of the UFO, in Parker et al. [225] we showed that the Fe XXV/XXVI absorption features are strongly present in simple variability spectra, along with the Mg XII, Si XIV, S XVI, Ar XVIII and Ca XX Ly α lines. Again, all of these features are strongly flux dependent and extremely rapidly variable.

IRAS 13224−3809 is well known as a twin to another bright, rapidly variable NLS1: 1H 0707-495, which also shows very strong Fe L and Fe K emission in the *XMM-Newton* spectrum [70]. A reverberation lag of 30 s from the bright Fe L emission line was found by Fabian et al. [70], Zoghbi et al. [341]. Kara et al. [134] found a low-frequency hard lag corresponding to the disk fluctuation propagation, and a high-frequency soft lag corresponding to the time delay between the coronal emission and the disk reflection in a 1.3 Ms observing campaign. In addition, Dauser et al. [50] first found a highly ionised outflowing wind with velocity changing from 0.11 c to 0.18 c by studying the 500 ks long *XMM-Newton* and 120 ks *Chandra* quasi-simultaneous observations. Boller et al. [26] found a sharp spectral drop around 7 keV in the *XMM-Newton* spectra, suggesting a neutral Fe K edge. Hagino et al. [106] interpreted the absorption feature above 7 keV with a disk wind model. More data analysis on the ionised outflow in this source will be published in near future.

In this work, we analyze the 1.5 Ms *XMM-Newton* observing campaign of IRAS 13224−3809 using broad band spectroscopy. We focus on the spectral characteristics of the AGN, and compare our results with previous studies. In Section 4.2, we briefly describe the data reduction and briefly introduce the X-ray variability shown in the light curve; in Section 4.3, we focus on the stacked spectral analysis; in Section 4.4, we study the spectral differences between different flux levels; in Section 4.5, we divide the whole exposure into 12 slices and study the spectral variability.

4.2 Data Reduction and Light Curves

Our data analysis is conducted using all the data from the 2016 *XMM-Newton* observing campaign. A list of the observations used in this chapter for spectral analysis, with a total exposure of ≈ 1.5 Ms, is given in Table 4.1. A list of quasi-simultaneous *NuSTAR* observations used in this work is shown in Table 4.2.

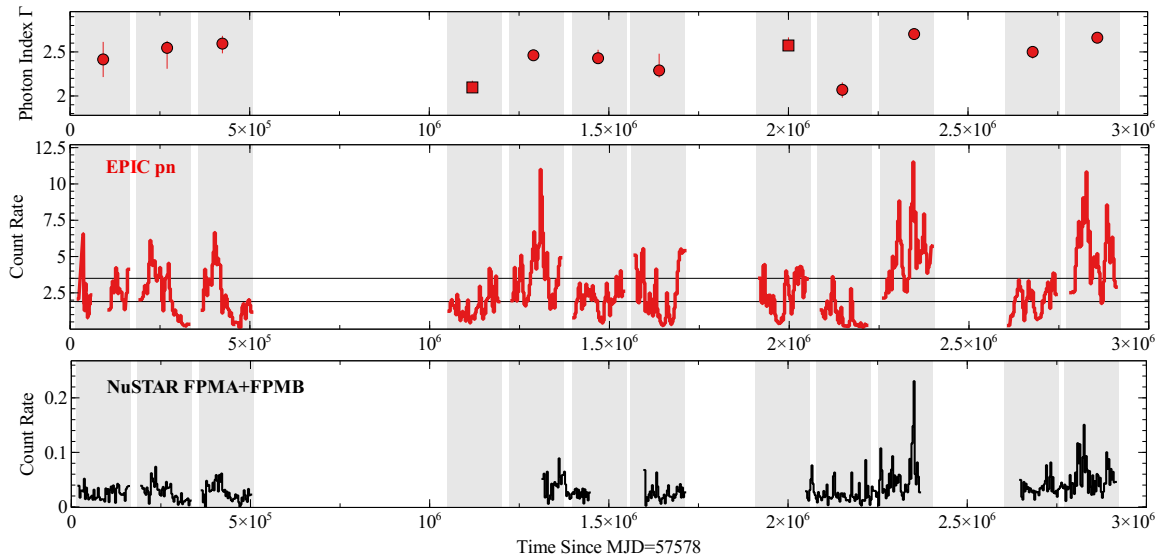

Fig. 4.1 Top: the best-fit photon index of the power-law continuum Γ vs. time. (See Section 4.5 for more details). The circles are the best-fit values obtained by analyzing the *NuSTAR* FPM and *XMM-Newton* EPIC spectra simultaneously while the squares are the ones obtained by analyzing only the *XMM-Newton* EPIC spectra. Middle: the 0.3–10 keV EPIC pn light curve with 3 ks bins. The observing campaign is divided into 12 observation intervals, each of around 120 ks. The time coverage is shown in the grey shaded region. A time-resolved spectral analysis on each observation is introduced in Section 4.5. The light curve is also divided into three flux intervals, each with a similar number of counts, by horizontal solid lines. A flux-resolved spectral analysis of the three flux states is introduced in Section 4.4. Three peaks (12 cts s^{-1}) are detected during the whole observation. Bottom: the 3.0–78.0 keV *NuSTAR* FPMA+FPMB 3 ks light curve. The time axis has been coordinated with the *XMM-Newton* EPIC pn light curve. The *NuSTAR* observing campaign is separated into seven intervals. The 4th, 6th and 7th *NuSTAR* observations are divided into 2 time slices to conduct simultaneous time-resolved spectral analysis with the *XMM-Newton* data in Section 4.5.

4.2.1 *XMM-Newton* Data Reduction

We reduce the *XMM-Newton* data using V15.0.0 of the *XMM-Newton* Science Analysis System (SAS) software package and calibration files (ccf) v.20160201. First, the clean calibrated event lists are created by running EMPROC (for EPIC-MOS data) and EPPROC (for EPIC-pn data). Good time intervals are selected by removing intervals dominated by flaring particle background, defined as intervals where the single event (PATTERN=0) count rate in the >10 keV band is larger than 0.35 counts s^{-1} for EPIC-MOS data and that in the 10–12 keV band larger than 0.4 counts s^{-1} for EPIC-pn data. By running the EVSELECT task, we select single and double events for EPIC-MOS (PATTERN<=12) and EPIC-pn (PATTERN<=4, FLAG==0) source event lists from a circular source region with radius of 35 arcsec. An annulus shaped source region with an inner radius of 5 arcsec is chosen to reduce pile-up if necessary for the observations with a very high count rate (see the last column of Table 4.1). The inner radius is chosen by running `epatplot`, with which the observed/model singles and doubles pattern fractions ratios are consistent with 1 within statistical errors. The EPIC-MOS cameras were being operated in the Small Window (SW) mode while the EPIC-pn camera was being operated in the Large Window (LW) mode. Background regions are chosen as circular regions with radii of 40 arcsec, close to the source region in the same unit on the camera. The background count rate remains ≈ 0.1 cts s^{-1}. Then we create redistribution matrix files and auxiliary response files by running RMFGEN and ARFGEN tasks separately. We consider the EPIC spectra between 0.3–10 keV, unless otherwise specified. ADDSPEC is used to make a stacked spectrum for each camera, along with corresponding background spectra and response matrix files. The averaged EPIC-pn background count rate is 0.05205 ± 0.00001 cts s^{-1} and the averaged EPIC-pn source count rate is 1.649 ± 0.001 cts s^{-1}.

4.2.2 *NuSTAR* Data Reduction

IRAS 13224−3809 was observed by the *NuSTAR* satellite seven times, listed in Table 4.2. The first observation interval (ObsIDs 60202001002, 60202001004 and 60202001006) was performed continuously followed by the second (ObsIDs 60202001008 and 602002001010) and the third intervals (ObsIDs 60202001012 and 60202001014), each slightly separated in order to better overlap with the *XMM-Newton* observations. We reduce the *NuSTAR* data using the standard pipeline NUPIPELINE V0.4.5, part of HEASOFT V6.19 package, and instrumental responses from *NuSTAR* caldb V20161021. Source spectra are selected from circular regions with radii of 35 arcsec, and the background is obtained from nearby circular regions with radii of 120 arcsec. Spectra are extracted from the cleaned event files using

NUPRODUCTS for both FPMA and FPMB. The observed flux in the 3–30 keV band is also added in Table 4.2.

4.2.3 Light Curves and Time Variability

The 0.3–10 keV EPIC pn light curve of 2016 observation is shown in the middle panel of Fig. 4.1. The data are grouped into bins with interval widths of 3 ks. Extreme flux peaks (12 ct s^{-1}) happened three times during the 1.5 Ms observing campaign with the count rate 100 times the lowest level (0.13 ct s^{-1}). The 0.3–10 keV band light curve shows rapid variability with a time scale of kiloseconds. The first flux peak happened in the gap between two *NuSTAR* observations, but the *NuSTAR* FPMs capture the second and the third flux peak in the *XMM-Newton* observation. This new observing campaign captures stronger flux peaks, compared with the light curves of the *XMM-Newton* observations in 2011 [e.g. 8 ct s^{-1} in 41].

Fig. 4.2 shows the unfolded spectra of all the *XMM-Newton* and *NuSTAR* observations against a constant model. The 1–4 keV band shows 10 times flux difference between the highest (obs 0780561601) and the lowest flux state (obs 0792180301) while the iron band (4–7 keV) and the hard band (>10keV) shows approximately 3 times flux difference and smaller variability than the 1–4 keV band. The averaged spectrum shows a strong soft component below 1 keV and a very broad strong Fe Kα emission line at the 4–7 keV band. The spectrum becomes softer and shows a weaker Fe Kα emission at higher flux states.

In order to group the spectra and reconstruct the response matrix in a more optimal way, we use the method in Kaastra and Bleeker [128] by taking both every bin's averaged energy and photon counts into account[1]. The unfolded spectra against a constant model of all the observations show shown in Fig. 4.2. The flux at the iron band and the <1 keV band is less variable than that in the 1-4 keV band (approximately 10 times difference).

For the spectral analysis, we use the XSPEC(12.9.1k) software package [9] to fit all the spectra discussed, and C-statistics [37] is considered in this work, as required by the spectral binning method. The χ^2 test is not used due to possible biased estimation of errors [128]. The Galactic column density towards IRAS 13224−3809 is fixed at the nominal value 5.3×10^{20} cm^{-2} from Kalberla et al. [130] if not specified. The column density calculated by the method in Willingale et al. [326] is 6.78×10^{20} cm^{-2} after accounting for the effect of molecular hydrogen. In the end of our stacked spectral analysis in Section 4.3.3, we will measure the Galactic column density with our X-ray spectra and fix it at our best-fit value in the following analysis. The photoionisation cross section is from Balucinska-Church and McCammon [15] and He cross section is from Yan et al. [330]. The solar abundances of

[1]The python code is written by Carlo Ferrigino. https://cms.unige.ch/isdc/ferrigno/developed-code/

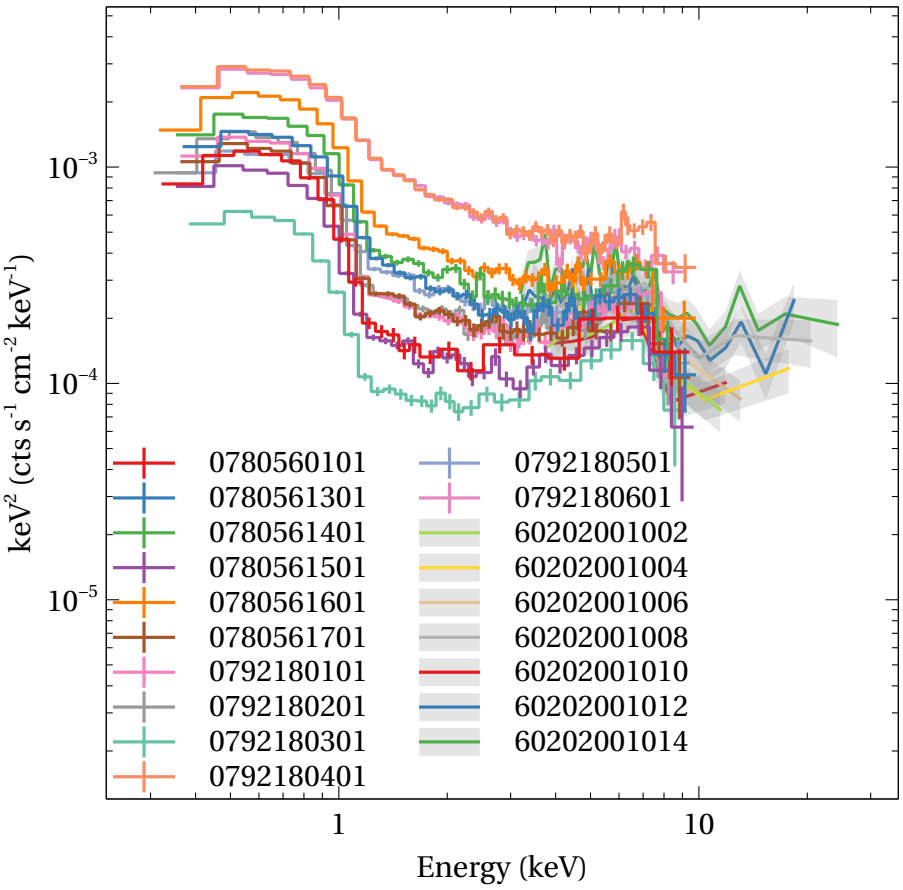

Fig. 4.2 The unfolded spectra against a constant model of all the *XMM-Newton* (lines with errorbars) and *NuSTAR* (shaded lines) observations. The spectra have been grouped for clarity.

Wilms et al. [327] were used. The fit parameters are reported in the observed frame. The quoted errors of best fit parameter values are at the 90% confidence level. The best-fit model parameters are all reported in the observer's frame unless explained explicitly. We assume the cosmological parameters $H_0 = 73\,\mathrm{km\,s^{-1}\,Mpc^{-1}}$, $\Omega_{\mathrm{matter}} = 0.27$, and $\Omega_{\mathrm{vacuum}} = 0.73$. An isotropic model of emission is adopted when calculating the source luminosity. For local galactic absorption, the `tbnew` model [327] is used. An additional constant model `constant` has been applied to vary normalizations between different instruments to account for calibration uncertainties.

Hereafter, black points with error bars are for FPMA; red points are for FPMB; green points are for MOS1; blue points are for MOS2; dark red points are for pn in figures unless explained specifically.

4.3 Time-Averaged Spectral Analysis

In this section, we focus on studying the ionised reflection from the accretion disk around the central BH and identifying UFO absorption lines by analyzing the time-averaged spectra. We first fit *XMM-Newton* and *NuSTAR* data independently and then a quasi-simultaneous spectral analysis is conducted on both sets of data. The best fit model will be used as a template for further spectral analysis in Section 4.4 and Section 4.5.

4.3.1 Continuum Fit

NuSTAR FPM Data

We first fit the stacked FPMA and FPMB spectra with an absorbed power law. The ratio plot in the top panel of Fig. 4.3 shows a broad Fe line feature present around 6.4 keV and a Compton hump above 10 keV. To fit the reflection feature, an extended version of `reflionx` [263] with wider iron abundance range (up to 30 times solar abundance) is used. The Fe Kα line in `reflionx` is treated as the recombination lines of Fe XXV and Fe XXVI combined with the fluorescence lines of Fe VI-XVI. `relconv` is convolved with the local reflection model for relativistic effects [49]. After adding the relativistic reflection model `relconv*reflionx`, it reduces the statistics to $C - stat/\nu = 114.50/102$[2](see the bottom panel of Fig. 4.3). The best-fit model parameters are listed in Table 4.3. The fit requires a central black hole with spin $a_* > 0.94$ viewed from an inclination angle of $i = 54$ deg. The fit puts a weak constraint on the iron abundance ($Z_{\mathrm{Fe}} < 18$). In order to test a possible low energy cutoff in the broad band spectrum, the high energy cutoff parameter is allowed to vary and we

[2] ν is the number of degrees of freedom.

Table 4.1 *XMM-Newton* Observation Log. The duration is the length of scheduled observation. The 'annulus' column indicates where an annulus-shaped source region with an inner radius of 5 arcsec is used to extract spectra during the data reduction to reduce the pile-up effects. The usable percentage of each EPIC-pn exposure after correcting for flaring particle background is shown after the corresponding net exposure length. The observed flux is calculated by the best-fit model for EPIC pn spectra in the 0.3-10 keV band in the unit 10^{-12} ergs cm^{-2} s^{-1}.

Revolution	Obs.ID	Start Date	EPIC pn Net Exposure (ks) & Usage Percentage	Observed Flux (10^{-12} ergs cm^{-2} s^{-1})	Annulus
3037	0780560101	2016-07-08, 19:33:33	18 (95%), 36 (92%)	3.68 ± 0.01	MOS & pn
3038	0780561301	2016-07-10, 19:25:31	122 (94%)	3.77 ± 0.01	MOS & pn
3039	0780561401	2016-07-12, 19:34:13	78 (94%), 36 (95%)	3.27 ± 0.01	-
3043	0780561501	2016-07-20, 19:01:53	120 (98%)	2.57 ± 0.01	-
3044	0780561601	2016-07-22, 18:36:58	118 (98%)	5.66 ± 0.01	MOS & pn
3045	0780561701	2016-07-24, 18:28:28	117 (97%)	3.15 ± 0.01	MOS
3046	0792180101	2016-07-26, 18:18:44	123 (98%)	3.36 ± 0.01	MOS & pn
3048	0792180201	2016-07-30, 18:02:21	120 (98%)	3.52 ± 0.01	MOS & pn
3049	0792180301	2016-08-01, 17:54:51	108 (99%)	1.53 ± 0.01	-
3050	0792180401	2016-08-03, 17:47:25	108 (94%)	8.05 ± 0.01	MOS & pn
3052	0792180501	2016-08-07, 17:40:58	112 (97%)	3.21 ± 0.01	MOS
3053	0792180601	2016-08-09, 18:29:52	116 (97%)	7.84 ± 0.01	MOS & pn

Table 4.2 *NuSTAR* Observation Log. Similar with Table 4.1. The observed flux is the total flux of the best-fit model for FPMA and FPMB spectra in the 3-30 keV band in the unit of 10^{-13} ergs cm^{-2} s^{-1}.

Obs.ID	Start Date	Duration (ks)	Observed Flux (10^{-13} ergs cm^{-2} s^{-1})
60202001002	2016-07-08, 19:36:08	67.6	5.2 ± 0.1
60202001004	2016-07-10, 20:01:08	67.4	6.0 ± 0.3
60202001006	2016-07-12, 18:36:08	67.5	6.2 ± 0.3
60202001008	2016-07-23, 19:01:08	70.2	8.2 ± 0.4
60202001010	2016-07-27, 02:16:08	62.6	5.0 ± 0.3
60202001012	2016-08-01, 07:46:08	171.7	7.8 ± 0.2
60202001014	2016-08-08, 05:46:08	136.9	9.8 ± 0.3

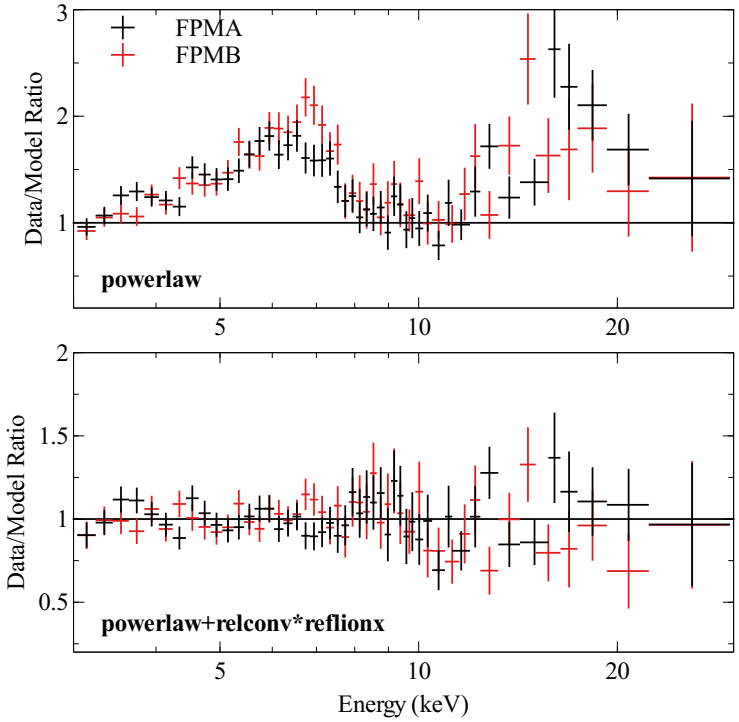

Fig. 4.3 Top: the data/model ratio plot of two *NuSTAR* FPM spectra fitted with a simple Galactic absorbed power-law model. The ratio plot shows clear signatures of a disk reflection component, including a broad iron emission line and a reflection hump above 10 keV. Bottom: the ratio plot of only the FPM spectra fit with an absorbed power law plus a single relativistic disk reflection model. The total model reads `constant*tbnew*(powerlaw+relconv*reflionx)`. More details can be found in the first column of Table 4.3.

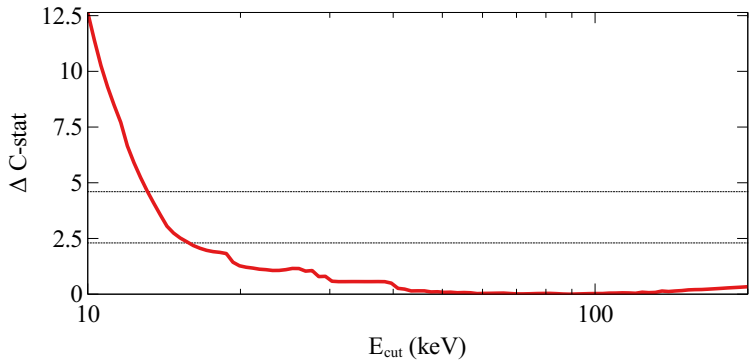

Fig. 4.4 Δ*C-stat* vs. power-law cutoff. The red solid line is obtained by fitting the 3-30 keV band of two *NuSTAR* FPM spectra. The two horizontal solid lines are 1 σ and 2 σ measurement lines.

obtained $E_{\rm cut} > 15$ keV (2σ) by fitting the 3-30 keV band FPM spectra (refer to Fig. 4.4). Only the lower limit of the cutoff can be obtained. The curvature of the high energy emission can be well described with the Compton hump, part of the reflection model, with the high energy cutoff fixed at the maximum value in the following analysis. In Section 4.3.2, we will conduct a simultaneous 0.3–30.0 keV broad band analysis on both EPIC and FPM spectra.

XMM-Newton EPIC Data

We first fit the 1–4 keV energy band of the EPIC spectrum with a simple absorbed power law ($\Gamma = 2.8$). The ratio plot is extended to the whole band and the power law is renormalized for only illustration purpose. Fig. 4.5 shows the EPIC pn data/model ratio plot, indicating a strong soft excess below 1.5 keV. Two strong broad emission lines are shown in the Fe K and L bands, associated with the disk reflection and consistent with Ponti et al. [239], Fabian et al. [62] and Chiang et al. [41].

To fit the soft excess, we separately try a phenomenological single temperature blackbody model `bbody` and a cutoff power-law model `cutoffpl`. The normalization of the `bbody` model is defined as L_{39}/D^2, where L_{39} is the source luminosity in 10^{39} erg s^{-1} and D_{10} is the distance in 10 kpc. In the end of this Section 4.3.4, we will discuss another possible interpretation of the soft excess by a new high density disk reflection model. A distant reflection model fails to fit the broad Fe K emission line feature at the iron band (see the 1st panel of Fig. 4.6). So we initially use the simple and fast relativistic convolution model `kdblur2`, a convolution model adapted from `laor` [150], which has a broken power law emissivity profile. For further analysis, we switch to the more sophisticated relativistic kernel model `relconv` [49].

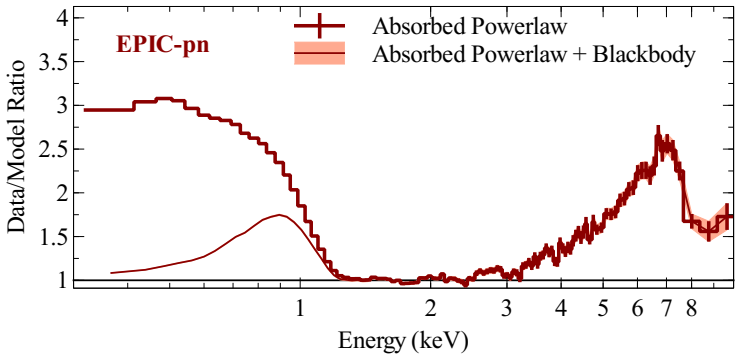

Fig. 4.5 The data/model ratio plot for a fit of *XMM-Newton* EPIC-pn spectrum with a power-law model ($\Gamma = 2.8$), two simple relativistic lines and blackbody ($kT = 89$ eV). Shaded region: the two relativistic line models are removed to show the line shapes in the Fe K and L bands; points with error bars: two relativistic line models and `bbody` are all removed to show the soft excess below 1 keV. This ratio plot shows a strong soft excess, a strong disk relativistic Fe K and L emission line.

We first fit the soft excess with a soft cutoff power-law model (see the 2nd panel of Fig. 4.6) and a combination of a soft cutoff power law and an additional relativistic reflection model (see the 3rd panel of Fig. 4.6). In the latter case, the photon index parameters in two `reflionx` models are tied to that of the `powerlaw` model. The iron abundance parameter is tied between two `reflionx` models. The additional reflection model decreases the residuals of the Fe L emission line but the cutoff model fails to fit the spectral shape below 0.7 keV. We fit the soft excess with a blackbody model `bbody` instead of a soft cutoff power law, which decreases the statistics by more than 1000 (see the 4th panel of Fig. 4.6). In order to fit the residuals at <0.8 keV, we add another reflection model to fit the soft excess. It can reduce the residuals from 10σ to 4σ at energies below 0.6 keV and *C-stat* by 1000 (see the 5th panel of Fig. 4.6). Finally, we replace `kdblur2` with `relconv` for more accurate relativistic effects on the broad line features. A broken power-law emissivity profile is assumed. While the outer emissivity index is first fixed at 3 to meet the emissivity in flat spacetime, the inner emissivity index is left free to vary (see the second columns of Table 4.3). The inner edge of the accretion disk is assumed to be at the innermost stable circular orbit (ISCO) and the outer edge of the disk is fixed at 400 $R_{\rm g}$ for simplicity. Limb-darkening effects are included in the model. The total continuum model combination now reads `constant*tbnew*(relconv*(reflionx1+reflionx2)+powerlaw +bbody)`. This model combination provides the best fit with *C-stat*/ν=1237.73/454. The 6th panels of Fig. 4.6 and lower panel of Fig. 4.8 show the residual and data/model ratio plots respectively.

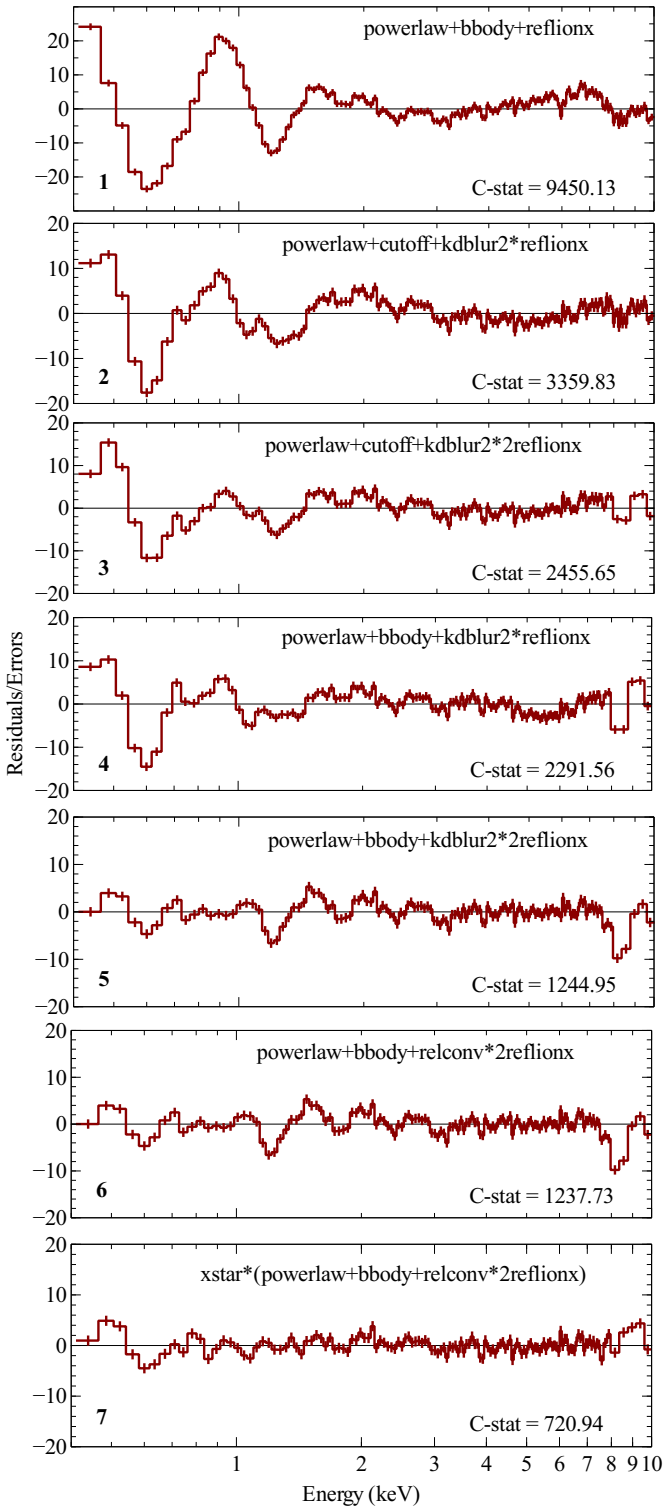

Fig. 4.6 The residual/error plots for the different model combinations fit to the time-averaged *XMM-Newton* EPIC spectra (only the pn spectrum is shown here for clarity). All models are fit from 0.3–10.0 keV. The corresponding model and the statistics are marked in each panel. See the text for more details.

So far we have obtained the best-fit continuum model but there are still some narrow atomic features visible. For example, the absorption features in 1–2 keV, 2–4 keV, >8 keV band will be further discussed in Section 4.3.2 and be fitted with a photoionised absorber model `xstar`.

4.3.2 Detailed Spectral Analysis

In this section, in addition to the Fe absorption feature discussed in Parker et al. [229], we conduct a more detailed spectral analysis on *XMM-Newton* EPIC spectra first by identifying more UFO blueshifted absorption lines in the broad band fitting and then fitting these lines with the more physical ionised absorption model `xstar`.

Blueshifted Absorption Features

As discussed in the introduction section, a UFO from the disk of this source has been identified in this source [229, 225]. Here we present a detailed analysis and physical modeling of blueshifted Si XIV, S XVI, Ne X, Mg XII absorption features in the EPIC spectra (see the 6th panel of Fig. 4.6 for the residual plot, and Fig. 4.8 and Fig. 4.7 for the ratio plots).

We first fit the absorption feature at around 1.2 keV in the observed frame with a Gaussian line model `gauss` and obtain a better fit with *C-stat* reduced by 280.79 for three additional degrees of freedom (line energy, FWHM and normalization). The best fit line energy of Ne X absorption line is $1.258^{+0.011}_{-0.009}$ keV in the source rest frame (1.181 ± 0.010 keV in the observer frame) and consistent with the measurement in the RGS data (10.0 ± 0.5Å, [229]) within the measurement error. Leighly et al. [154] also found similar absorption features at 1–1.3 keV band in the ASCA data. Similarly to the Ne X line, we applied three more Gaussian line models for the rest of the absorption features. Parameters are given in Table 4.4. The blueshifted Ne X and S XVI are stronger and broader than the other two lines. In order to put limits on the strength of the Ar XVIII and Ca XX lines found in the PCA analysis in Parker et al. [225], we fit the Gaussian line models to EPIC spectra with the line energy parameter fixed as 4.0 keV and 4.9 keV. The inclusion of the two lines does not offer significant improvement to the fit and the equivalent width is negligible (see the last two rows of Table 4.4).

xstar Modelling

For further study, we model the absorption features in the 1–5 keV band (in Fig. 4.7) and Fe absorption feature above 8 keV (in Fig. 4.5) with the physical model `xstar` and try to measure the overall ionisation level and the averaged line-of-sight velocity of the disk outflow.

Table 4.3 Best-fit model parameters for *NuSTAR* FPM (3.0–30.0 keV) and *XMM-Newton* EPIC (0.3–10.0keV) spectra. The flux is calculated by `cflux` in 0.3–10 keV band and in log base 10. The normalization of `bbody` model is defined as L_{39}/D^2, where L_{39} is the source luminosity in 10^{39} erg s^{-1} and D_{10} is the distance in 10 kpc.

Model	Parameter	Unit	Value			
			Only FPM `relconv & reflionx`	Only EPIC `relconv & reflionx`	FPM & EPIC `relconv & reflionx`	FPM & EPIC `relxilld`
`tbnew`	$N_{\rm H}$	10^{20}cm^{-2}	5.3	5.3	$6.39^{+0.22}_{-0.14}$	6.4 ± 0.2
`xstar1`	$N_{\rm H1}$	10^{22}cm^{-2}	-	14^{+34}_{-7}	$3.2^{+3.7}_{-0.3}$	$7.2^{+0.3}_{-2.1}$
	$\log \xi_{1,\rm outflow}$	erg cm s^{-1}	-	$3.64^{+0.22}_{-0.16}$	$3.72^{+0.05}_{-0.12}$	3.62 ± 0.03
	$Z_{\rm Feoutflow}$	solar abundance	-	$3.1^{+0.5}_{-0.9}$	3.4 ± 0.2	$2.0^{+1.3}_{-0.5}$
	redshift z_1		-	$-0.187^{+0.004}_{-0.002}$	-0.189 ± 0.003	-0.188 ± 0.002
`xstar2`	$N_{\rm H2}$	10^{22}cm^{-2}	-	$0.75^{+0.14}_{-0.17}$	$0.78^{+0.14}_{-0.15}$	$0.82^{+0.12}_{-0.21}$
	$\log \xi_{2,\rm outflow}$	erg cm s^{-1}	-	$3.070^{+0.011}_{-0.035}$	3.05 ± 0.02	$3.11^{+0.19}_{-0.12}$
	redshift z_2		-	-0.154 ± 0.004	-0.152 ± 0.002	-0.157 ± 0.002
`bbody`	T	eV	-	$94.7^{+0.7}_{-0.7}$	$91.7^{+0.5}_{-0.4}$	$98.5^{+1.1}_{-1.6}$
	Normalization	10^{-5}	-	$7.56^{+0.08}_{-0.10}$	$6.04^{+0.12}_{-0.80}$	5.7 ± 0.3
`relconv`	Incl	degree	54^{+3}_{-4}	$63.35^{+0.18}_{-0.26}$	$67.0^{+2.3}_{-1.2}$	77^{+3}_{-7}
	a_*	J/M^2	>0.94	$0.9960^{+0.0013}_{-0.0028}$	$0.989^{+0.002}_{-0.003}$	> 0.975
	Inner Emissivity Index		$5.0^{+1.2}_{-0.7}$	$6.57^{+0.16}_{-0.14}$	$6.04^{+0.12}_{-0.20}$	$7.6^{+0.5}_{-1.5}$
	Outer Emissivity Index		3 (fixed)	3 (fixed)	$2.85^{+0.71}_{-0.10}$	$3.5^{+0.2}_{-2.1}$
	$R_{\rm break}$	R_g	$3.2^{+1.4}_{-0.5}$	$4.4^{+3.4}_{-1.2}$	< 5.8	<5.4
reflection 1	$\log \xi_1$	erg cm s^{-1}	2.4 ± 0.3	3.22 ± 0.07	$3.13^{+0.07}_{-0.04}$	2.50 ± 0.07
	$Z_{\rm Fe}$	solar abundance	< 18	$24.14^{+2.1}_{-1.4}$	24^{+3}_{-4}	$6.6^{+0.8}_{-2.1}$
	Electron Density log(n_e)	cm^{-3}	15	15	15	>18.7
	log(Flux)	erg cm^{-2} s^{-1}	$-12.4^{+0.3}_{-0.2}$	$-11.78^{+0.07}_{-0.10}$	-11.70 ± 0.03	$-11.86^{+0.02}_{-0.03}$
reflection 2	$\log \xi_2$	erg cm s^{-1}	-	$1.68^{+0.02}_{-0.13}$	$1.48^{+0.14}_{-0.10}$	0 (fixed)
	log(Flux)	erg cm^{-2} s^{-1}	-	$-12.60^{+0.04}_{-0.06}$	$-12.55^{+0.04}_{-0.07}$	-12.14 ± 0.02
`powerlaw`	$\Gamma_{\rm FPMA}$		$2.44^{+0.51}_{-0.12}$	-	$2.37^{+0.05}_{-0.02}$	2.78 ± 0.12
	$\Gamma_{\rm FPMB}$		$2.5^{+0.6}_{-0.2}$	-	2.41 ± 0.06	$2.82^{+0.04}_{-0.12}$
	$\Gamma_{\rm MOS1}$		-	$2.45^{+0.53}_{-0.10}$	$2.495^{+0.02}_{-0.02}$	2.69 ± 0.04
	$\Gamma_{\rm MOS2}$		-	$2.46^{+0.18}_{-0.04}$	2.51 ± 0.03	$2.71^{+0.05}_{-0.03}$
	$\Gamma_{\rm pn}$		-	$2.45^{+0.20}_{-0.02}$	2.49 ± 0.03	2.69 ± 0.03
	log(Flux)	erg cm^{-2} s^{-1}	$-12.37^{+0.14}_{-0.37}$	$-11.78^{+0.03}_{-0.04}$	-11.74 ± 0.02	-11.67 ± 0.02
C-stat/ν			114.50/102	720.94/448	*797.73/567*	*822.32/566*

Table 4.4 The best-fit absorption line parameters, including line energy in observer frame, FWHM, equivalent width and the ΔC-*stat* value. *C-stat*/ν obtained by the continuum model in section 4.3.1 is 1237.73/455.

Line	E (keV)	FWHM (keV)	EW (eV)	ΔC-*stat*
Ne X	1.181 ± 0.010	$0.24^{+0.07}_{-0.05}$	$37.5^{+0.2}_{-0.3}$	280.79
S XVI	3.16 ± 0.03	$0.42^{+0.07}_{-0.05}$	$50.90^{+11.0}_{-1.5}$	81.75
Mg XII	$1.769^{+0.02}_{-0.03}$	$0.12^{+0.07}_{-0.05}$	$10.0^{+0.2}_{-0.4}$	54.6
Si XIV	2.42 ± 0.03	0.09 ± 0.07	$10.1^{+4.0}_{-1.2}$	28.69
Ar XVIII	4.0 (fixed)	0.001 fixed	<2.7	-
Ca XX	4.9 (fixed)	0.001 fixed	<6.9	-

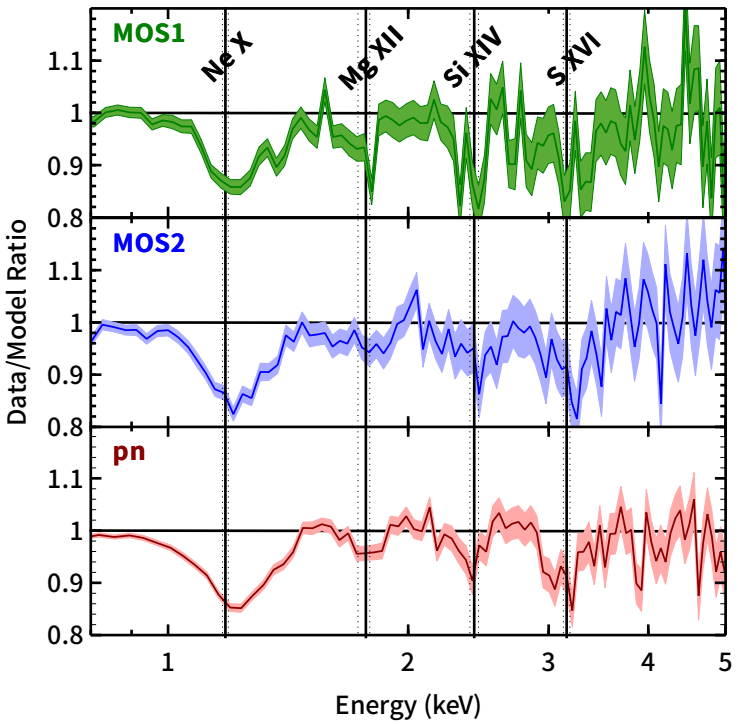

Fig. 4.7 The data/model ratio plots for a time-averaged *XMM-Newton* EPIC spectral fit with the continuum model plus four additional Gaussian absorption lines. The Gaussian absorption line models in this plot are removed to show the line profiles. Blueshifted Ne X, Mg XII, Si XIV and S XVI absorption features are visible and labelled in 1–4 keV band. The best fit line parameter values can be found in Table 4.4. The vertical solid lines are the best-fit line energy and the dotted vertical lines are the measurement errors of the corresponding line energy values.

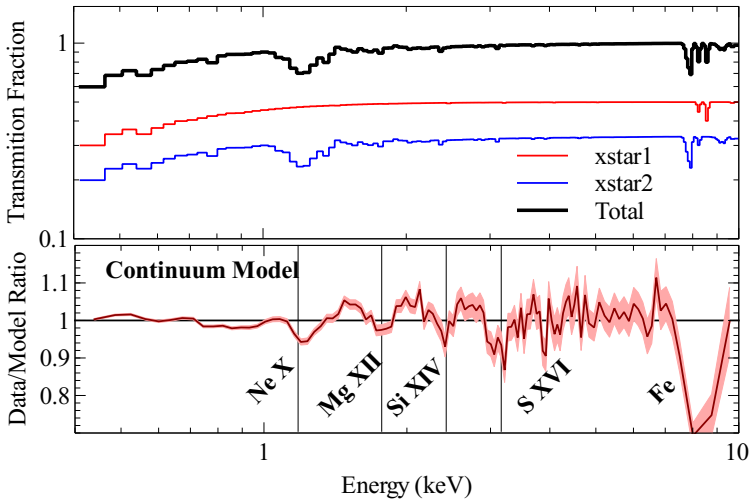

Fig. 4.8 Top panel: Best-fit `xstar` transmission model convolved with the instrumental spectral resolution after being grouped (in black) and two different ionised components (the more ionised absorber `xstar1` in red and the less ionised absorber `xstar2` in blue). Bottom panels: The ratio plots for time-averaged *XMM-Newton* EPIC pn spectra fit without `xstar` (only pn is shown here for clarity). All the relevant absorption lines are labeled with dashed lines.

We construct custom photoionised plasma absorption models with `xstar` [131]. The grids are calculated assuming solar abundances except for that of iron, a fixed turbulent velocity of 2000 km s^{-1} [229] and an ionising luminosity of 10^{43} erg s^{-1}. Free parameters are the ionisation of the plasma ($\log \xi_{\rm outflow}$), the column density ($N_{\rm H}$), the iron abundance ($Z_{\rm Fe}$) and the redshift (z).

We first fit the EPIC spectra with only one `xstar` model and it reduces the *C-stat* by 99.23. See the blue line in the top panel of Fig. 4.8 for the model shape. This model perfectly fits the absorption features below 5 keV, including the blueshifted Ne X, S XVI, Mg XII and Si XIV absorption lines identified in Section 4.3.2. However, a single `xstar` model is not broad enough to fit the Fe absorption feature above 8 keV. A second `xstar` model is required to fit the blue wing of the Fe absorption line (see the red line in the top panel of Fig. 4.8 for the model shape). These two additional `xstar` models provide a significant improvement of fit by reducing the *C-stat*/ν of the EPIC spectra fit by 516.79 to $720.94/448$. The iron abundances of the two `xstar` models are tied together. Parameters are given in Table 4.3. According to the best fit model in the top panel of Fig. 4.8, the more ionised absorber ($\log(\xi_{1,\rm outflow}/{\rm erg\ cm\ s^{-1}})$ = 3.6) is also more blueshifted than the less ionised absorber ($\log(\xi_{2,\rm outflow}/{\rm erg\ cm\ s^{-1}})$ = 3.1). The residual plot for the fit is shown in the bottom panel of Fig. 4.6. Two absorbers require column density $N_{\rm H1} = 14^{+34}_{-7} \times 10^{22}$ cm^{-2}, $N_{\rm H2} = 0.75^{+0.14}_{-0.17} \times 10^{22}$ cm^{-2} and redshift $z_1 = -0.187^{+0.004}_{-0.002}$, $z_2 = -0.154 \pm 0.004$ respectively corresponding to line-of-sight

outflowing velocity of v=0.26, 0.23c. In the following section, we will conduct simultaneous spectral analysis on both *NuSTAR* and *XMM-Newton* data using the same model combination.

4.3.3 Simultaneous Spectral Fitting

Finally, we present the simultaneous fit of *NuSTAR* FPM and *XMM-Newton* EPIC spectra based on the best-fit continuum model in Section 4.3.1 and the outflow model in Section 4.3.2. The total model is `constant*tbnew*xstar*powerlaw+bbody+relconv*(2reflionx)`. The photon index parameters of different instruments are left to vary independently because this source is extremely variable and *NuSTAR* and *XMM-Newton* observations are not strictly simultaneous (compare two light curves in Fig. 4.1). We assume a broken power-law emissivity for the disk reflection component and allow both emissivity indices to vary.

The best-fit parameter values are listed in the third column of Table 4.3. The best-fit model is shown in Fig. 4.9. The two `xstar` models have blueshift up to $z_1 = 0.189 \pm 0.003$ and $z_2 = 0.152 \pm 0.002$, corresponding to velocity of $v_1 = 0.267^{+0.004}_{-0.003}$ c and $v_2 = 0.225 \pm 0.002$ c respectively for bulk motion in the radial direction. The best-fit column density of the outflow is $3.2^{+0.7}_{-0.2} \times 10^{22}$ cm^{-2} and $0.78^{+0.14}_{-0.15} \times 10^{22}$ cm^{-2}, which is slightly lower than the value obtained by analyzing the RGS spectra [$9.5 \pm 0.5 \times 10^{22}$ cm^{-2} 229].

The averaged spectrum in this analysis is harder than the previous fit with the same model combination in [41] ($\Gamma = 2.71 \pm 0.02$), which could be due to the change of the averaged temperature or optical depth of the corona through the whole observation. The best-fit relativistic parameters indicate a fast rotating black hole ($0.989^{+0.002}_{-0.003}$) viewed from an inclination of $67.0^{+2.5}_{-1.2}$ deg. The different emissivity index from the result in [41] may be due to a change of the geometry of the primary source [325]. For example, the larger inner emissivity index means that the primary power law photons are more concentrated on the inner disk due to the light bending effects. A very steep emissivity profile indicates a very compact primary X-ray source.

The absorber has $Z_{\rm Fe} = 3.4 \pm 0.2$ solar iron abundance while the two disk reflection components require $Z_{\rm Fe} > 20$. This is not expected as the outflowing wind from the disk should share the element abundances of the disk. However, in Section 4.3.4 we find a good fit with a high density disk reflection model which only requires the disk iron abundance $Z_{\rm Fe} = 6.6^{+0.8}_{-2.1}$ so can potentially solve this problem.

The best-fit Galactic column density obtained by analyzing our X-ray spectra is $6.39^{+0.22}_{-0.14} \times 10^{20}$ cm^{-2}, which is slightly higher than 5.3×10^{20} cm^{-2} predicted by Kalberla et al. [130] but consistent with the value obtained in Willingale et al. [326] ($N_{\rm H} = 6.78 \times 10^{20}$ cm^{-2}). We will use our best-fit Galactic column density value in the following analysis.

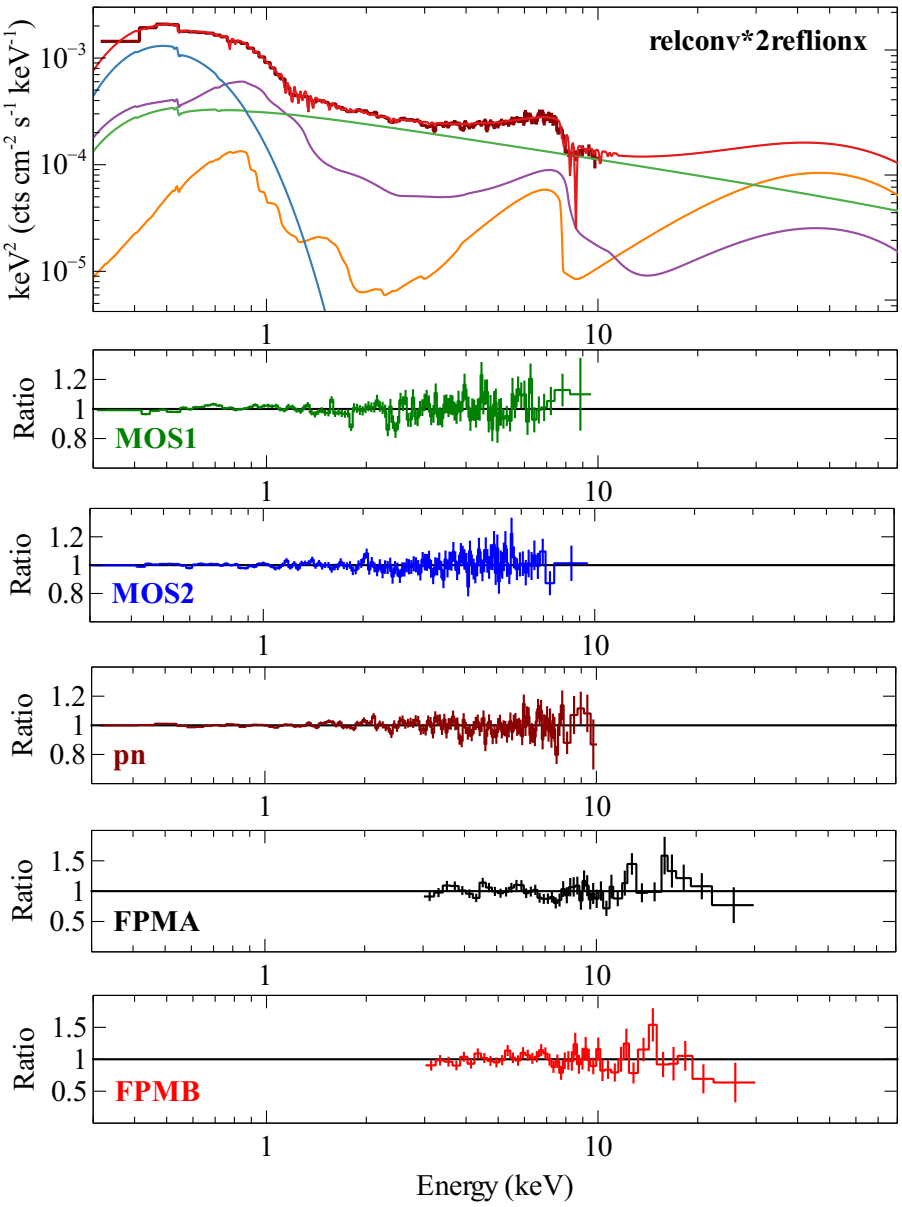

Fig. 4.9 The best-fit EPIC pn model for the simultaneous fit of the quasi-simultaneous *XMM-Newton* and *NuSTAR* data. The rest-frame disk reflection model used here is `reflionx`. Green: power-law continuum; blue: blackbody model; purple: the disk reflection component with higher ionisation; yellow: the disk reflection component with lower ionisation; red: the total model. The dark red with errorbars are the unfolded spectra of EPIC pn. The bottom 5 panels show the ratio/model plots of *XMM-Newton* EPIC spectra and *NuSTAR* FPM fitted with the best-fit model.

4.3.4 High Electron Density Reflection Model

A very high iron abundance ($Z_{\rm Fe} = 24$) is required by fitting the soft excess with relativistic reflection model combination `relconv*reflionx` which assumes a constant electron density $n_e = 10^{15}$cm^{-3}. In order to obtain a more reliable measurement on the disk iron abundance, we also try to fit the *XMM-Newton* and *NuSTAR* spectra with the recently developed model `relxillD` [86] which allows the electron density parameter to vary between $n_e = 10^{15}$ and 10^{19}cm^{-3} while `reflionx` assumes $n_e = 10^{15}$cm^{-3}. At higher n_e, the spectrum shows a higher temperature `bbody` shaped soft excess due to the increased influence of the free-free process on the spectrum at higher densities. Free-free absorption increasingly traps low energy photons, increasing the temperature of the top layer of the disk and turning the reflected emissions at energies below 1 keV into a quasi-blackbody spectrum. García et al. [86] show that a high electron density disk in 1H 0707−495 with $n_{\rm e} \approx 10^{19}$ cm^{-3} reduces the amplitude of the soft excess by 30%. Tomsick et al. [296] obtain a better fit of the intermediate state spectra of Cyg X-1 with the electron density as a free parameter ($n_e = (3.98^{+0.12}_{-0.25} \times 10^{20}$ cm^{-3}) and only solar iron abundances.

Here we fit the *XMM-Newton* EPIC and *NuSTAR* spectra in the 0.3–30 keV energy band with a `powerlaw`, a `bbody` and two relativistic reflection models `relxillD`. The reflection fraction parameters of the two `relxillD` are fixed as -1 to return only the reflection components. The cutoff energy parameter $E_{\rm cut}$ is fixed as 300 keV. The best fit model is shown in the top panel of Fig. 4.10 and it can offer a good fit with *C-stat*/ν=822.32/566. One low-ionisation ($\log(\xi_1$/erg cm s^{-1})=0) and one ionised ($\log(\xi_2$/erg cm s^{-1})=2.50$\pm$0.07) reflection component are required. The best fit iron abundance $Z_{\rm Fe} = 6.6^{+0.8}_{-2.1}$, which is much lower than the iron abundance obtained in Section 4.3. The two `rexillD` models require disk density $n_{\rm e} > 10^{18.7}$cm^{-3} (see Fig.4.11 for reference). The fit almost reaches the upper limit of the n_e parameter in the current model. The best-fit high density disk reflection model is shown in Fig. 4.10. With such a high density, the soft band of the two reflection models has more emission than the best-fit `reflionx` models shown in Fig.4.9. This is still work in progress and further fits will be presented in a future paper (Jiang et al. in prep).

4.4 Flux-Resolved Spectral Analysis

Parker et al. [229] found that the Fe, O and Ne absorption features are strongly flux dependent, suggesting that the UFO responds to the AGN continuum. In order to confirm whether the other absorption lines identified in Section 4.3.2 follow the same rule and probe

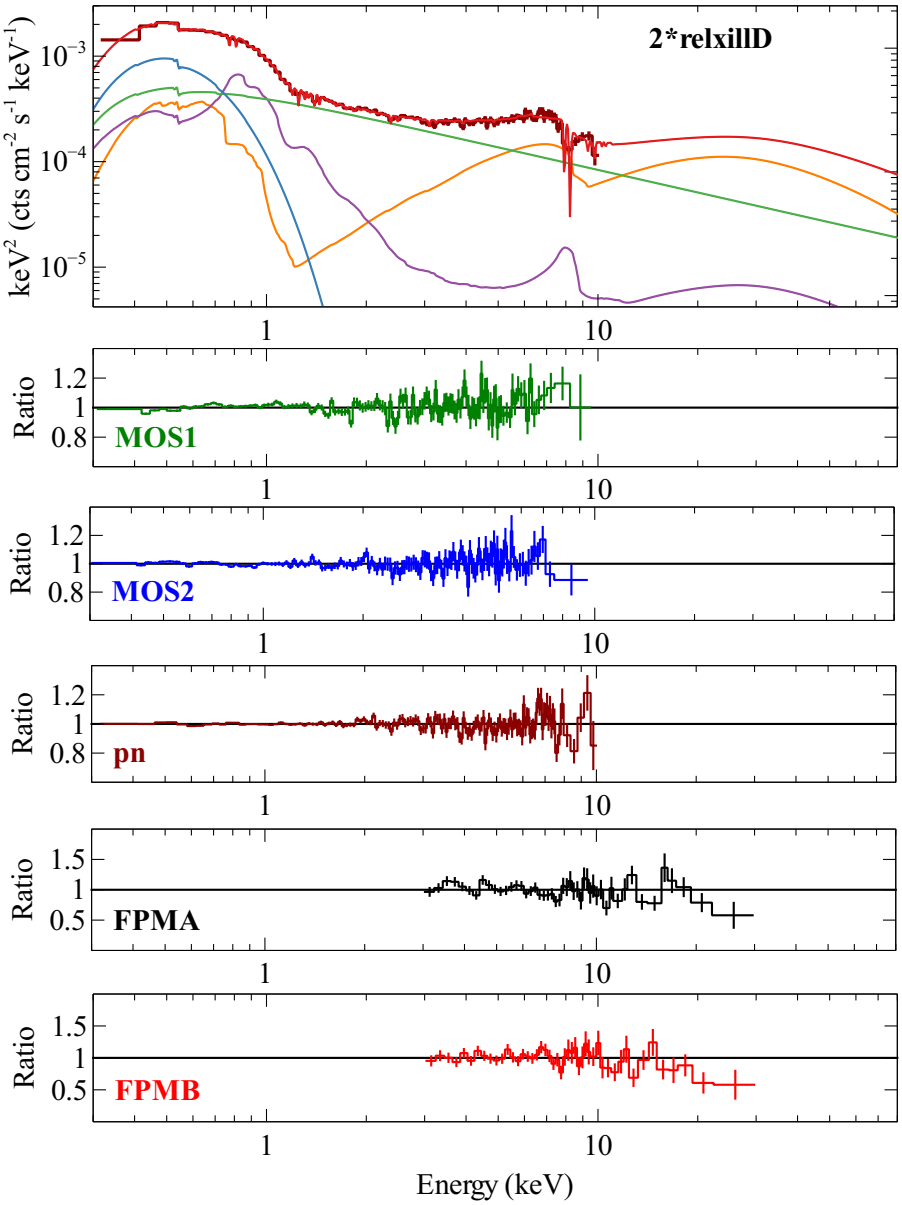

Fig. 4.10 Same as Fig. 4.9. The relativistic disk reflection model used here is `relxillD`.

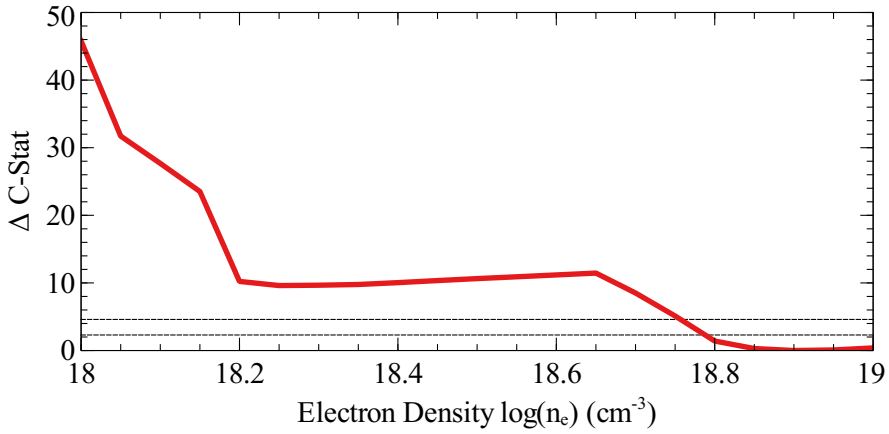

Fig. 4.11 ΔC-*stat* vs. electron density value in logarithmic units. The two horizontal solid lines are 1 σ and 2 σ measurement lines.

more information on the overall spectral characteristics at different flux levels we conduct a broad band spectral analysis on three flux resolved spectra.

We divide the EPIC pn dataset into three flux levels, HF (high flux), MF (middle flux) and LF (low flux). The flux levels are chosen to have a similar number of total counts, as in Parker et al. [229].

We first fit all three flux-resolved spectra with the same model template discussed above, `tbnew*xstar*(powerlaw+relconv*2reflionx+bbody)`. As the spin measured in the time-averaged analysis approaches to the spin limit in General Relativity, and is consistent with previous results [239, 62, 41, 229], we fix it at the best-fit value obtained in the time-averaged analysis. The data/model ratio plots after removing the `xstar` absorption components to display the line profiles are shown in Fig. 4.12.

The power-law continuum and the corresponding disk reflection components show large different among three flux states. The `bbody` shows the lowest flux in the LF state, indicating a weakest soft excess. The 0.3-10 keV band flux values of all the components increase with increasing flux levels. The coronal emission shows a softer continuum (Γ=2.66 for HF state) compared with two lower flux states (e.g. $\Gamma = 2.03$ for LF state). The reflection components and the primary power-law continuum show higher flux at higher flux state. The primary power-law emission shows more than 10 times flux difference between the LF and HF states while the flux of the reflection components only show 4 times difference. This can be explained by the light-bending model: the reflection component is less affected by the light bending effects as more lights are focused onto the inner area of the disk, resulting in increasing reflection fraction.

Table 4.5 Best-fit parameter values for three flux-resolved spectra. The units of the parameters are defined the same as in Table 4.3.

Model	Parameter	High Flux (HF)	Middle Flux (MF)	Low Flux (LF)
`xstar1`	$N_{\rm H1}$ (10^{22}cm^{-2})	-	< 1.0	$4.2^{+1.3}_{-2.1}$
	$\log \xi_{1,\rm outflow}$ (log(erg cm s^{-1}))	-	$4.3^{+0.8}_{-0.7}$	$3.7^{+0.2}_{-0.5}$
	redshift z$_1$	-	$-0.170^{+0.002}_{-0.005}$	-0.175 ± 0.006
`xstar2`	$N_{\rm H2}$ (10^{22}cm^{-2})	-	0.6 ± 0.4	13.7 ± 1.4
	$\log \xi_{2,\rm outflow}$ (log(erg cm s^{-1}))	-	3.07 ± 0.07	$3.0^{+0.4}_{-0.3}$
	redshift z$_2$	-	$-0.143^{+0.05}_{-0.02}$	-0.132 ± 0.007
`bbody`	kT (eV)	$93.7^{+0.2}_{-1.2}$	$91.3^{+0.2}_{-1.1}$	$92.3^{+0.3}_{-0.5}$
	norm (10^{-5})	9.7 ± 0.3	$8.15^{+0.12}_{-0.20}$	$3.63^{+0.07}_{-0.11}$
`relconv`	Inner Emissivity Index	$5.2^{+0.4}_{-0.3}$	$6.3^{+1.2}_{-2.0}$	$6.0^{+1.0}_{-3.5}$
	R (R_g)	< 9	< 8	69^{+11}_{-56}
`reflionx1`	$\log \xi_1$ (erg cm s^{-1})	$3.36^{+0.02}_{-0.04}$	$3.24^{+0.19}_{-0.06}$	$2.70^{+0.17}_{-0.12}$
	log(Flux) (erg cm^{-2} s^{-1})	-11.41 ± 0.03	$-11.84^{+0.06}_{-0.09}$	$-12.58^{+0.08}_{-0.04}$
`reflionx2`	$\log \xi_2$ (erg cm s^{-1})	$1.53^{+0.13}_{-17}$	$2.12^{+0.04}_{-0.08}$	$1.80^{+0.14}_{-0.21}$
	log(Flux) (erg cm^{-2} s^{-1})	$-12.35^{+0.12}_{-0.15}$	$-12.45^{+0.20}_{-0.12}$	-12.77 ± 0.08
`powerlaw`	$\Gamma_{\rm pn}$	2.66 ± 0.04	$2.31^{+0.04}_{-0.02}$	2.03 ± 0.04
	log(Flux) (erg cm^{-2} s^{-1})	$-11.33^{+0.03}_{-0.04}$	$-11.90^{+0.07}_{-0.04}$	$-12.28^{+0.04}_{-0.03}$
	C-stat/ν	166.79/135	157.46/120	141.58/119

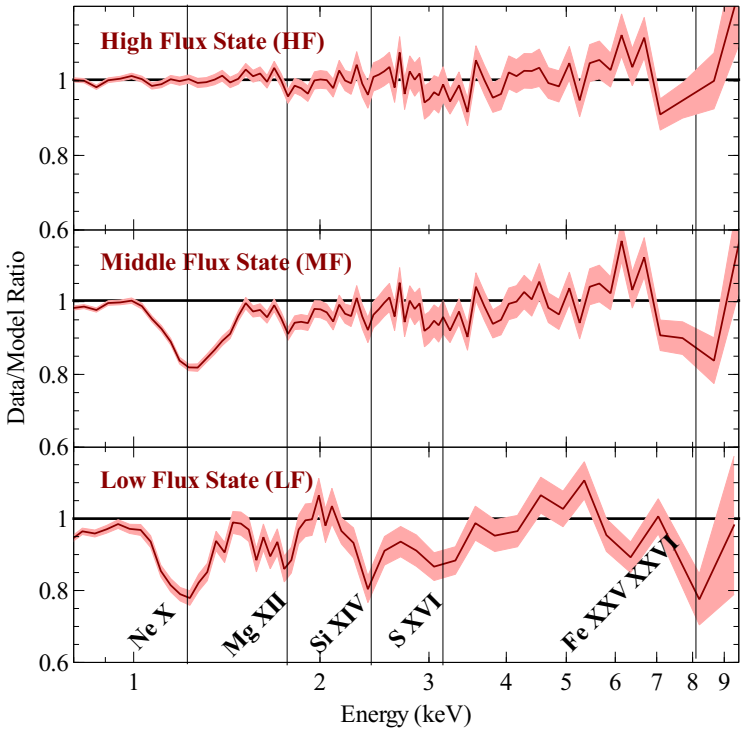

Fig. 4.12 The ratio plot of the fits for three flux-resolved spectra, high flux (HF) state, middle flux (MF) state and low flux (LF) state to the best-fit UFO absorbed continuum model. The `xstar` models are removed in this plot to show the line shapes more clearly. All the relevant blueshifted absorption features are marked with solid black lines.

The best fit parameter values obtained by including the xstar models can be found in Table 4.5. Moreover, the blueshifted Mg XII, Si XIV and S XVI absorption signatures are only visible in the lower flux states, MF and LF. To fit these absorption features, the same xstar model generated in Section 4.3 is applied to LF and MF spectra. xstar models significantly reduce the residuals from the continuum fit. In order to obtain the upper limit of the absorption features in HF state, we fit the HF spectrum with one xstar model ($\log(\xi_{\rm outflow}$/erg cm s $^{-1}$) $\equiv 3.0$ and $z \equiv$-0.13). The column density we obtain is $N_{\rm H}$<2×10^{20} cm^{-2}. The best-fit outflow column density for the LF state is higher than the best-fit value for the MF state, showing a flux-dependent outflow.

4.5 Time-Resolved Spectral Analysis

Fig. 4.1 shows the extreme variability of IRAS 13224-3809 in the EPIC 0.3–10 keV band on timescales of ks or less. In order to further study the spectral variability with respect to time and the averaged flux, we conduct spectral analysis on each of the twelve observations. A simultaneous 0.3–30 keV broad band spectral analysis is conducted if simultaneous *NuSTAR* data are available during that *XMM-Newton* observation. The simultaneous *NuSTAR* spectra are extracted according to the time coverage of the *XMM-Newton* observations (compare the grey shaded region and *NuSTAR* combined FPM light curve Fig. 4.1).

All the time-resolved spectra are fitted with the same model combination as the one obtained above, with relativistic parameters and the column density fixed at the best-fit value obtained in the time-averaged analysis. RDC and PLC are, respectively, the reflection and power-law continuum flux between 0.3–10 keV in log scale in the unit of erg cm^{-2} s^{-1} calculated by cflux model in XSPEC. The reflection fraction is simply defined as the ratio of the reflection flux over the power-law continuum flux. The bbody normalization is defined as L_{39}/D_{10}^2, where L_{39} is the source luminosity in units of 10^{39}erg s^{-1} and D_{10} is in unit of 10 kpc. All the best-fit parameters are plotted in Fig. 4.13.

The following conclusions can be drawn from Fig. 4.13:

1. When the blackbody flux is higher, the temperature of the blackbody tends to be higher, indicating a steeper soft excess. The temperature and luminosity of the bbody component follows the Stefan-Boltzmann $F \propto T^4$ relation, as found in the previous study of [41], indicating a constant emission area of the soft excess. The flux of the blackbody follows the same trend as that of the power-law component (see the first panel of Fig. 4.13).

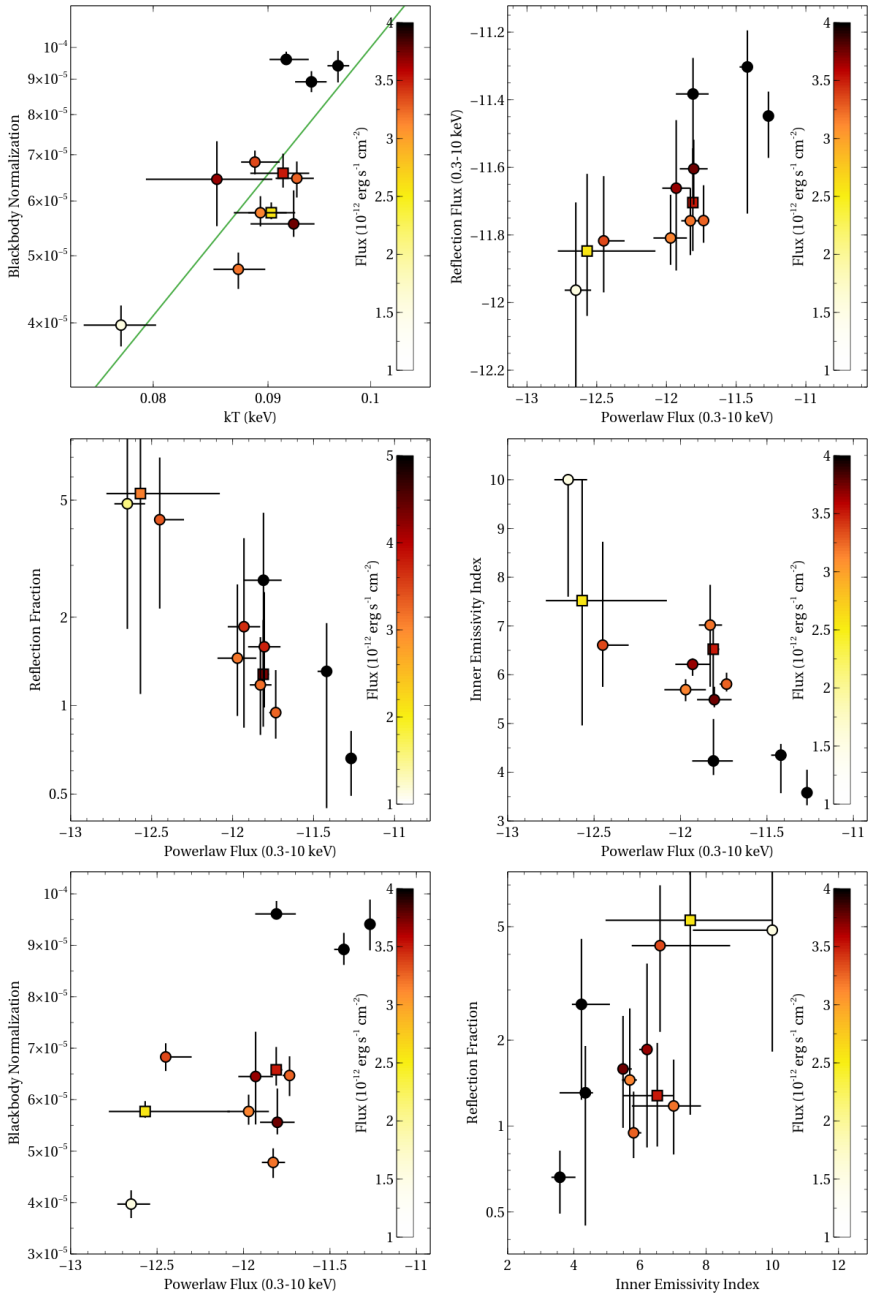

Fig. 4.13 Time-resolved spectral analysis results. PLC and RDC are, respectively, the power-law continuum and the reflection flux in log scale calculated by `cflux` between 0.3–10 keV. The reflection fraction is defined as the ratio of the reflection flux to the power law continuum flux in that band. The Stefan-Boltzmann relation $F \propto T^4$ is plotted with a green line in the first panel for reference. The emissivity index here is the inner emissivity index while the outer emissivity index is fixed at 3. The color bar of the plot symbol indicates the average flux in the corresponding time slice. The best-fit values obtained by analyzing two *XMM-Newton* observations without simultaneous *NuSTAR* data are marked in squares.

2. The reflection component is highly positively correlated with the power-law continuum. However, as the reflection component is less variable than the power-law component, the reflection fraction is negatively correlated with the power-law flux (refer to the second and the third panel of Fig. 4.13). They show that the flux of the reflection components in the 0.3–10.0 keV change by a factor of 3-4 and the flux of the power-law component changes by a factor of 30. This can potentially be explained by the light-bending model: when the corona is closer to the black hole, the power-law flux decreases drastically due to more photons lost to the event horizon. The reflection component is less affected by the light bending affects as more light is focused onto the inner disk, resulting in an increasing reflection fraction.

3. From the Spearman's Rank Correlation ($\mathrm{SRCC} = -0.634$, $\mathrm{P-value} = 0.27$ using t-distribution), we find that the inner emissivity index and the power-law flux have a weak negative correlation. This can also be explained by a change of primary source height in the lamp-post geometry as in the point above. The inner emissivity tends to be higher when the source is close to the black hole and the primary photons are more concentrated to the inner area of the disk due to the light-bending effects. The primary power-law component is weaker, caused by the loss of the primary photons to the central black hole (refer to the forth panel of Fig. 4.13).

4. In Fig. 4.1 we show the best-fit power-law photon index to compare with the light curve. There is a positive correlation between the source brightness in 0.3-10.0 keV band and the power-law photon index. The brighter the source is, the softer the power law is.

4.6 Discussion

4.6.1 Overall Bolometric Luminosity Estimation

In this section, we calculate the bolometric luminosity in three ways. We first apply a simple bolometric correction to the observed flux in the 2–10 keV band. Second, we apply the linear relation between the spectral index and the Eddington ratio found in Brightman et al. [34]. Thirdly, a continuum fitting method is applied to the UV/optical-X-ray band first with a phenomenological model (`bbody+powerlaw`). As the mass is uncertain, we leave a factor of $10^7\ M_\odot/M$ in our estimates of Eddington fraction.

First, the best fit model for time-averaged spectra in Table 4.3 shows the source has flux of 6.87×10^{-13} in the 2–10 keV band. Given the measurement that the luminosity distance

of IRAS 13224−3809 is 288Mpc, $L_{2-10\mathrm{keV}} = 6.82 \times 10^{42}$ erg s^{-1}. L_{Edd} for central object with mass $10^7 \mathrm{M}_\odot$ is 12.6×10^{44} erg s^{-1}. According to the estimation of the bolometric correction given for the 2–10 keV flux for NLS1 [see the top panel of Fig. 12 in 306], the overall bolometric luminosity $L_{\mathrm{bol}}^{\mathrm{ave}} = \kappa_{2-10\mathrm{keV}} \times L_{2-10\mathrm{keV}} \approx 50 \times 6.82 \times 10^{42}$ erg s^{-1}=3.4×10^{44} erg s^{-1}. The best fit model flux for the flux peak spectrum is around 9.28×10^{-13} between 2–10 keV, corresponding to bolometric luminosity $L_{\mathrm{bol}}^{\mathrm{peak}} = 4.65 \times 10^{44}$ erg s^{-1}. This means that the source remains sub-Eddington both on average ($0.27 \frac{10^7\ M_\odot}{M} L_{\mathrm{Edd}}$) and at peaks ($0.37 \frac{10^7\ M_\odot}{M} L_{\mathrm{Edd}}$) according to the calculation of only the X-ray band. This result is roughly consistent with Sani et al. [269].

Second, according to the estimation of the bolometric ratio given by the power-law photon index, $\lambda_{\mathrm{Edd}} = 69.78$ for the peak spectra ($\Gamma = 2.86$) and $\lambda_{\mathrm{Edd}} = 4.22$ on average ($\Gamma = 2.47$) by using the correlation $\Gamma = (0.32 \pm 0.05) \log \lambda_{\mathrm{Edd}} + (2.27 \pm 0.06)$ [34]. The extremely high Eddington ratio obtained for the flux peak however is very uncertain, because the samples in Brightman et al. [34] do not have sources with the primary continuum softer than $\Gamma = 2.2$.

Third, we try to estimate the accretion rate by fitting the SED with phenomenological model. The Optical Monitor (OM) on *XMM-Newton* was operated with only one filter during the observing campaign. So we extract the photometry data from simultaneous *Swift* (uvot) observations [35]. We used a circular source region of 5 arcsec radius and circular background region of 15 arcsec radius from a nearby source free area. UV fluxes have been corrected for Galactic reddening $E(B-V) = 0.06$. We first try to fit with the phenomenological continuum model `bbody+powerlaw`. The `bbody` model is for the disk thermal component and the `powerlaw` is for the primary continuum in the harder band. We fix the photon index of the `powerlaw` as 2.5, the same as we obtained in the time-averaged spectral analysis. The temperature of the thermal component is fixed at 1 eV and 10 eV to obtain upper limit and lower limits on the broad band luminosity. The fit with kT=1 eV gives a total model luminosity between 1-10^4 eV around 4×10^{-11} , corresponding to $0.3 \frac{10^7\ M_\odot}{\mathrm{M}} L_{\mathrm{Edd}}$, and the fit with kT=10 eV gives 4×10^{-10} , corresponding to $3.0 \frac{10^7\ M_\odot}{\mathrm{M}} L_{\mathrm{Edd}}$. Therefore, the estimation of the bolometric luminosity by the continuum fitting with a phenomenological continuum model is $0.3 - 3 \frac{10^7\ M_\odot}{\mathrm{M}} L_{\mathrm{Edd}}$. This measurement is consistent with the results obtained by Ponti et al. [239], where they fit the UV and 2–10 keV *XMM-Newton* data with `diskpn` and estimated $\lambda_{\mathrm{Edd}} \approx 1$ for a 10^7 M$_\odot$.

The estimation of the bolometric luminosity suggests that the source is close to the Eddington limit and may suffer accretion instability causing extreme X-ray variability. This may also be relevant to the launching of the UFO and the rapid X-ray variability [e.g. 55]. It is generally thought that the most powerful outflows are launched near to the Eddington limit,

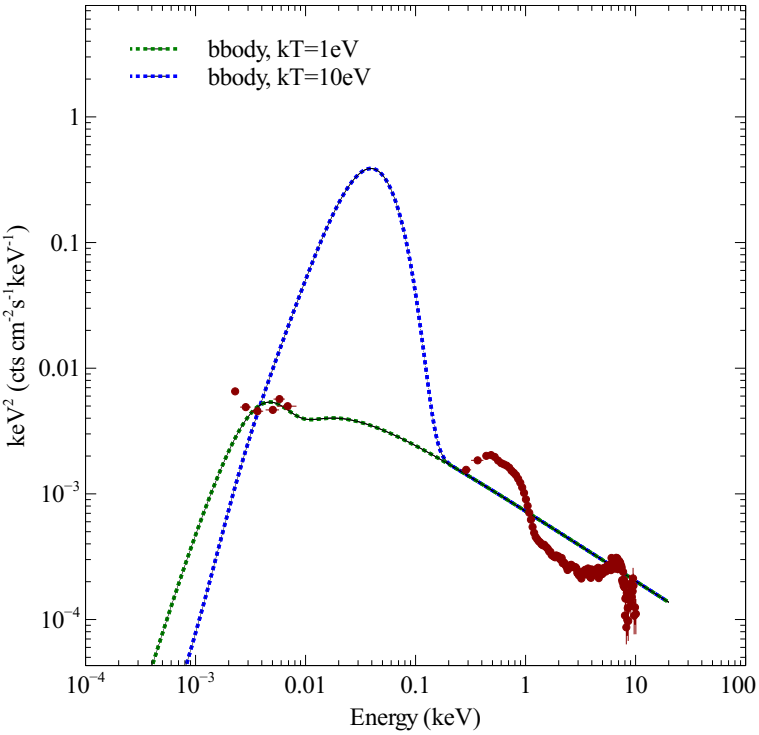

Fig. 4.14 Continuum fitting with `bbody+powerlaw` to IRAS 13224−3809 *XMM-Newton* and *Swift* (uvot) data. The blue and green dotted lines are the best-fit phenomenological continuum models with kT=1, 10 eV. See the text for more details.

and powerful outflows are observed in the ultra-luminous X-ray sources [237, 312, 236, 147] , at least some of which are super-Eddington neutron stars [10, 75, 118, 119]. Similarly, Leighly [152] also found there are more high ionisation emission lines observed in the UV band that are dominated by wind emission in the objects close the Eddington limit.

4.6.2 Soft Excess

In our analysis, the soft excess can be fit very well with a simple `bbody` component and an additional relativistic reflection component. The `bbody` temperature and flux follow $F \propto T^4$ relation, which indicate a constant emission area for the soft excess. Chiang et al. [41] discussed possible explanations of the soft excess as reprocessing of both the coronal emission and the reflection. Strong gravitational effects can cause the thermal and reflected disk photons to return to the disk surface [45]. The innermost area of the disk is thus heated sufficiently to emit blackbody radiation in the soft band.

In Section 4.3.4, we explore the possibility of the soft excess as part of the disk reflection. `relxillD` is an extended version of `relxill` and models a relativistic reflection spectrum from an accretion disk with the electron density on the surface of the disk allowed to vary freely (`reflionx` assumes $n_{\rm e} \equiv 10^{15}$ cm^{-3}). We successfully fit the EPIC spectra in the 0.3–10 keV energy band by replacing `reflionx` with `relxillD` models. The fit favours `reflionx` over `relxillD` with smaller value of *C-stat*. But the best fit iron abundance $Z_{\rm Fe} = 6$, which is much lower than the iron abundance obtained in Section 4.3. We have obtained a strong constrain on the lower limit of the electron density $n_{\rm e} > 10^{18.7}$cm^{-3} of the top layer of the disk by fitting the soft excess with a combination of high density reflection models and a phenomenological blackbody-shaped model. The two `xstar` models are consistent with the ones obtained in Section 4.3.2.

The high density disk reflection model proposed in García et al. [86] is based on an extended model of the standard accretion disk. The electron density at high accretion rates is $n_e \dot{m}^2 \propto (1-f)^{-3}$, where f is the fraction of power released by the disk onto the corona and $\dot{m}$ is the accretion rate in Eddington unit [288]. If 90 per cent of the disk power is taken by the corona (f=0.9), $n_e \dot{m}^2 \approx 10^{19} - 10^{18}$cm^{-3} for black hole masses of 10^6-10^7 M$_\odot$ (see Fig 1. of García et al. [86]). At the electron density n_e as high as $10^{18.7}$cm^{-3}, the reflection spectrum shows a higher temperature `bbody` shaped soft excess. This is due to the increased influence of the free-free process on the spectrum at higher densities. Free-free absorption increasingly traps low energy photons, forcing the surface temperature of the reflecting material to rise and turning the reflected emissions at energies below 1 keV into a quasi-blackbody spectrum. The continuum shape can also depend on the density of the disk. The power-law continuum is usually interpreted as the thermal Comptonization of the seed

photons from the disk. The spectral index of this continuum has a positive correlation with the corona temperature and the optical depth τ [335]. In our time-resolved spectral analysis result, the power law continuum is softer when the `bbody` temperature is higher. The change of power-law hardness is caused by either by a change of the temperature of the primary source or a change of geometry. Since the former factor increases when n_e increases, τ, the geometry dependent parameter, must change and the optical depth must be lower when the source is softer and brighter.

The current version of `relxillD` still requires improvement. For instance, more element abundances are expected to be higher than the solar level as well as iron. This is still work in progress and further fits will be presented in a future paper (Jiang et al. in prep).

4.6.3 Disk Reflection

To better model a turbulent accretion disk, two reflection components with different ionisations are used, one with a moderate ionisation of $\log(\xi_1/\mathrm{erg\ cm\ s^{-1}})$=3.13 and one with a low ionisation $\log(\xi_2/\mathrm{erg\ cm\ s^{-1}})$=1.48. The current model requires overabundant iron while the other elements are assumed to be solar due to the limitations of the `reflionx` model we use for analysis. However, as discussed above the need for a very high iron abundance and additional `bbody` can be potentially reduced by replacing the `reflionx` model with extended version of `relxillD` with higher disk density (discussed in Section 4.6.2). The disk iron abundance is $Z_{\mathrm{Fe}} = 6.6^{+0.8}_{-2.1}$ with `relxillD` and more consistent with the iron abundance of the UFO we obtain by fitting the absorption lines with `xstar`. The high iron abundance, even when fitted with high density disk reflection model, indicates that the other elements might be more abundant than solar. Wang et al. [319] presented a strong correlation between the outflow strength in quasars, measured by the blueshift and asymmetry index (BAI), and the metallicity, measured by Si IV O IV/ C IV, based on the quasar samples built in the Sloan Digital Sky Survey. For example, a significantly higher metallicity ($Z > 5$) is indicated for quasars with BAI>0.7. The metallicity may play an important role and be connected with the quasar outflow.

Various authors [167, 166, 324, 49] have shown that for simple coronal geometries the radial emissivity index decreases very sharply with source height in the most inner area of the disk (as low as $q = 1$ when the source height is up to 100 R_g). It tends to approximate as $q = 3$ in the outer area of the disk where the spacetime can be approximated to be flat. This effect reduces sharply with the source height. When the source height is 3 R_g, the emissivity profile is well approximated by a broken power law (outer emissivity index $q = 3$) with a very low break radius. A high inner emissivity index and a low break radius as in IRAS 13224−3809 indicates a very small source height (<2 R_g for instance).

IRAS 13224−3809 was observed by *XMM-Newton* for 500ks in 2011. Chiang et al. [41] estimated the spectral variability during the observation and obtained a steeper emissivity profile for the time-averaged spectra (inner emissivity index $q_1 > 9$, outer emissivity index $q_2 = 3.4^{+0.3}_{-0.2}$ and $R_{\rm break} = 2.1 \pm 0.1$ R$_g$) than we find. This could be caused by differences in the averaged source height in two observations. Moreover, the new campaign captures stronger flux peaks (12 cts/s) than Chiang et al. [41] (8 cts/s), which is consistent with a higher source and therefore less extreme emissivity profile.

The second and the third panels of Fig. 4.13 show that the power-law continuum is more variable than the reflection component. The reflection fraction has an inverse relation with the power-law flux though the reflection component flux follows the same trend with the power-law flux. The light-bending solution [190] is potentially a good explanation for this: when the corona is closer to the central black hole the trajectories of more photons will be bent towards the black hole and more primary continuum photons will be lost. The reflection component is however less affected by the light bending effects, as more light is focused onto the inner disk, resulting in an increasing reflection fraction. Similar results have been found in other sources, such as MCG−6−30−15[190, 308], NGC 3783 [248], and XRB XTE J1650−500 [267, 251], where the variability is dominated by the power-law continuum. An extreme case is the *NuSTAR* observation on Mrk 335 in 2013. Parker et al. [231] found the reflection fraction decreases sharply with the increasing flux. The low-flux spectra of Mrk 335 are well described by only disk reflection model and indicates extreme light bending effects happening within 2R$_g$. The anti-correlation between the inner emissivity index and the flux of the power law continuum (the fourth panel of Fig. 4.13) in IRAS 13224−3809 also supports this interpretation. When the source is closer to the central black hole, the flux of the primary continuum decreases due to stronger light bending and the emissivity index is higher due to photons being focused onto the inner disk.

4.6.4 Ultra Fast Outflow

The combined spectral analysis of the stacked *NuSTAR* and *XMM-Newton* spectra shows two relativistic outflowing absorbers in the source. The more ionised absorber ($\log(\xi_{1,\rm outflow}$)=$3.72^{+0.05}_{-0.12}$) has a higher blueshift ($z_1 = 0.18 \pm 0.003$, corresponding to line of sight velocity $v_1 = 0.267^{+0.04}_{-0.03}$ c) while the less ionised absorber ($\log(\xi_{2,\rm outflow}$)=3.05 ± 0.02) has a lower blueshift ($z_2 = 0.152 \pm 0.002$, corresponding to line of sight velocity $v_2 = 0.225 \pm 0.002$ c). We note that a similar UFO is found in 1H0707−495: Dauser et al. [50] identified blueshifted narrow features at 2–5 keV band from H-like ions (Si, S, Ca) in 1H0707−495 *XMM-Newton* spectra as ultra-fast wind absorption features. The ionisation of the disk wind in 1H0707-495 has small fluctuations ($\log(\xi)$≈3.5) but the velocity has a difference of 0.07 c between different

observations. Hagino et al (2016) also found evidence for an Fe absorption feature at 7.1–7.5 keV, with a velocity of 0.18c, also consistent with the velocity found by Dauser et al. [50] (v=0.11–0.18 c).

As found in Parker et al. [229], the inclusion of the UFO absorption lines does not have any significant impact on the measured reflection parameters. Similarly, in 1H0707−495, Dauser et al. [50] find no large difference on the relativistic parameters, such as the corona height in the lamp-post scenario, the black hole spin and the viewing angle, after including the wind component. This is contrary to the results of Hagino et al. [106], who found that the relativistic blurring parameters for 1H 0707-495 were less extreme when UFO absorption was taken into account. This difference is likely due to the much higher data quality and broader energy band used here, where we consider stacked spectra with very high signal-to-noise, whereas Hagino et al. [106] examine individual observations and largely limit their analysis to the 2–10 keV band.

The lower ionisation absorber is mainly used to fit the low energy absorption lines below 5 keV such as Ne X line and the red wing of the Fe absorption line, while the more ionised absorber is to fit the blue wing of the iron absorption above 8 keV. Parker et al. [229], Pinto et al. [235] fit the UFO absorption in the RGS and high-energy EPIC-pn spectra with a single absorber, with a velocity intermediate between the two we find here. The significant improvement that we find for fitting with two zones instead of one is likely an indication that there is structure or stratification of the UFO material, which we discuss below. The increasing level of ionisation increases the rest-frame energy of the atomic feature lines and removes some of them as well (compare the red and blue lines in Fig. 4.8 for reference). Thanks to the high signal/noise of the *XMM-Newton* EPIC cameras in the soft band, in addition to the iron absorption feature at 8.1 keV found in the EPIC-pn spectrum [229] we have identified Ne X (equivalent width 37.5 eV), S XVI (equivalent width 50.90 eV), Mg XII (equivalent width 10.0 eV) and Si XIV (equivalent width 10.1 eV) absorption lines (see Fig. 4.7 for reference). When the source is at high fluxes, the absorption features are weaker, consistent with the wind being more photoionised due to more photons emitted from the continuum source to the outflowing wind (see Fig. 4.12).

There are several different scenarios that could explain the observed outflow properties. An accelerating wind model was proposed in Murray et al. [200] where the outflowing velocity increases along the outflow stream line. However, our data show that the faster absorber has higher photon ionisation, which is contrary to the expectation in this model. Another possible interpretation is that the highly ionised layer lies inside a low ionised layer of the wind, and is more exposed to the continuum photons. This model was also used to explain the properties of the UV data of NGC 5548 in [58]. Alternatively, Gallo and Fabian [78]

proposed that the absorption features result from ionised materials corotating with the disk in a surface layer. A different line of sight through this layer, caused by changes in coronal geometry, can result in a different observed optical depth and therefore different absorption feature. Such a model has been successfully applied to PG 1211+143 [79]. According to this model, the coexistence of a more ionised faster absorber and a less ionised slower absorber in our analysis can be interpreted as a layer in the inner disk which is more photoionised and faster than the layer further out.

These two absorbers do not show significant changes with time during the observation. It indicates a relatively constant outflow from the disk in the timescale of kiloseconds, confirming the result of Parker et al. [229], Pinto et al. [235], where we show that the Fe XXV/XXVI absorption feature has been approximately constant since 2011. This is interesting, as the UFO in PDS 456 , which has a much larger $M_{\rm BH} \approx 10^9$ $\rm M_\odot$, shows significant changes in velocity during observations [e.g. 176, 175]. Why this would not be seen in the far more rapidly variable AGN IRAS 13224−3809 is not obvious. It is possible that there are velocity changes on timescales that we cannot resolve, so we see averaged (and therefore broadened) absorption lines, or it could instead be that there is an intrinsic difference between these outflows.

4.7 Conclusions

We fit the spectra from the 1.5 Ms *XMM-Newton* and 500 ks *NuSTAR* observing campaign on the extreme NLS1 IRAS 13224−3809 with physical broad-band models. We analyze stacked spectra, as well as flux-resolved and time-resolved spectra. Our main results are as follows:

1. IRAS 13224−3809 is the most extremely variable AGN. The 0.3–10.0 keV band light curve shows rapid variability on timescle down to kiloseconds, and we find a peak flux 100 times the lowest level.

2. Two reflection components with different ionisation ($\log(\xi_{1,2}$/erg cm $\rm s^{-1}$)=3.13, 1.48) are required to fit the stacked spectra, as found by previous authors.

3. The emissivity profile of the reflected emission steepens as the power-law flux drops. This can be explained by a variable primary source height in the lamp post scenario.

4. The variable blackbody component, used to fit some of the soft excess, follows the $F \propto T^4$ relation, indicating a constant emission area in the soft band.

5. Four blueshifted absorption lines (Ne X, S XVI, Mg XII and Si XIV) are detected in the stacked EPIC spectra. They can be fitted by two `xstar` absorbers, with ionisation

$\log(\xi_{1,2\mathrm{outflow}}/\mathrm{erg\ cm\ s^{-1}})$=3.72,3.05 and velocity $v_{1,2} = 0.267, 0.225$ c, confirming the presence of the UFO found by Parker et al. [229]. The inclusion of these absorption features does not have any significant impact on the relativistic blurring parameters, indicating that the measurements made using relativistic reflection are robust.

6. The UFO absorption lines are prominent at low flux levels (MF and LF), which may result from the increasing ionisation of the gas by the increasing X-ray flux.

7. A high density disk model with number density $n_\mathrm{e} > 10^{18.7}\ \mathrm{cm}^{-3}$ can potentially fit the soft excess and lessen the super-solar iron abundance requirement for the reflection components.

Chapter 5

Multi-Epoch Observations of 1H 0419−577

"Black hole sun, won't you come?
And wash away the rain?"
– Chris Cornell

5.1 Introduction

In General Relativity, the spacetime geometry around a black hole (BH) is described by the Kerr solution [142] assuming charge neutrality, where the black hole is characterized by its mass $M_{\rm BH}$ and its dimensionless spin parameter $a_* = a/M_{\rm BH} = Jc/GM_{\rm BH}^2$ (where J is the angular momentum). The dimensionless spin parameter affects the spacetime around BHs in either X-ray Binaries ($M_{\rm BH} \approx 5 - 20 M_\odot$), or in Active Galactic Nuclei (AGN) ($M_{\rm BH} \approx 10^{6-10} M_\odot$), in a similar behavior once the distance, timescale and luminosity scaled up by the corresponding BH mass [178, 317].

One method of measuring black hole spins is using relativistic reflection spectroscopy. This approach has been applied to both the stellar-mass BHs in X-ray binaries and the SMBHs in AGN. The central assumption of this method is that the inner edge of the accretion disc around the central BH is located at the inner-most stable circular orbit (ISCO). The measurement of the spin is based on the simple positive correlation between the spin and ISCO: $R_{\rm ISCO} = 6R_g$ for Schwarzschild black hole ($a_* = 0$) and decreases to $R_{\rm ISCO} = 1R_g$ for a maximumly spinning Kerr black hole [$a_* \approx 1$; 16]. The accretion disc is irradiated by a high temperature compact structure external to the disc, producing a reflected component called the disc reflection spectrum. This high temperature structure is called the corona. The disc reflection spectrum consists of broad emission lines and a Compton back-scattered continuum. The emission line features are broadened by strong Doppler effects and gravitational redshifts in the vicinity of BHs. The most prominent broad emission line feature is the broad iron Kα emission line, which has now been seen in various AGN, such as MCG-6-30-15 [e.g. 291, 328, 68, 165].

1H0419−577 [z=0.104, 293] is identified as a Seyfert 1 galaxy [101]. The centre of 1H0419−577 hosts a SMBH with $M_{\rm BH} = 1.3 \times 10^8 M_\odot$ by measuring its Hβ line width [$FWHM = 2580 \pm 200$ km s^{-1}, 100]. A highly variable soft band (<2 keV) has been found in 1H0419−577 with *ROSAT* [e.g. 101]. Also a variable power-law continuum emission in the high energy band was noticed in later *XMM-Newton* observations [243, 244, 241]. A long *XMM-Newton* observation in 2010 shows a thin, lowly ionised warm absorber in its high resolution grating spectrum [53]. By fitting the *XMM-Newton* spectrum at an extreme low flux state with the relativistic reflection model, Fabian et al. [66] obtained a disc inner radius of $r_{\rm in} < 2r_{\rm g}$, indicating a black hole spin of $a_* > 0.95$. Similarly, Walton et al. [314] obtained a black hole spin measurement of $a_* > 0.88$ by analysing its *Suzaku* observation which also shows a broad iron Kα emission line at a high X-ray flux state. No significant evidence of a fast outflow has been found in 1H0419−577 [294]. A possible low coronal temperature has been reported by fitting the hard X-ray *NuSTAR* spectra with an absorption model [304]. However

Table 5.1 The list of the observations analysed in this work. The exposure time for the *XMM-Newton* observations is clean of the time intervals of high flaring particle background. LW: large window mode; SW: small window mode; PC: photon counting mode.

Satellite	Obs ID	Start Date	Exp(ks)	Mode
XMM (pn)	0148000201	2002-09-25	11.5	LW
	0148000301	2002-12-27	0.3	LW
	0148000401	2003-03-30	11.0	LW
	0148000501	2003-06-25	5.8	LW
	0148000601	2003-09-16	11.3	LW
	0604720301	2010-05-30	71.0	SW
	0604720401	2010-05-28	42.3	SW
NuSTAR	60101039002	2015-06-03	170	-
Swift (XRT)	00081695001	2015-06-03	2.2	PC

Parker et al. [227] studied the principal components in the X-ray variability of 1H0419−577, finding that the suppression of the primary component at the iron band and low energies cannot be explained by variable absorption models.

In this work, we study the inner BH accretion disc in 1H0419−577 by analysing its different X-ray flux states captured by all the archival *XMM-Newton* and *NuSTAR* observations and try to explain the spectral variability with light-bending effects. A robust measurement of the relativistic parameters, including the black hole spin a_* and the disc viewing angle i, is obtained by conducting a multi-epoch spectral analysis and running Markov chain Monte Carlo (MCMC) chains.

5.2 Data Reduction

1H0419−577 was observed by a series of 12-18 ks *XMM-Newton* short looks in 2002 and 2003. Two longer *XMM-Newton* observations were obtained in 2010 with a total exposure of ≈ 160 ks. Note that during one of the *XMM-Newton* observations (Obs ID 0148000701), the EPIC-pn exposure is dominated by a high flaring particle background, and thus ignored for this work. The hard X-ray satellite *NuSTAR* observed 1H0419−577 for a net exposure of 170 ks in 2015 with a simultaneous 2 ks *Swift* short look. A list of all the observations considered in this work is shown in Table 5.1. In this section, we introduce our data reduction process for all these observations.

5.2.1 *XMM-Newton* Data Reduction

The *XMM-Newton* data are reduced using the *XMM-Newton* Science Analysis System (SAS) V15.0.0 and calibration files (ccf) v.20160201. We only consider EPIC-pn data in this work. The tool EPPROC is used to create clean calibrated event lists. We filter the data for flaring particle background and the background-dominated intervals are defined as the intervals where the single event count rate in the 10–12 keV band larger than 0.4 counts s^{-1}. The spectra are extracted using the tool EVSELECT, selecting both the single and double events in a circular region with a radius of 35 arcsec. Background regions are chosen on the same chip in the region to avoid any issues due to background Cu K emission lines from the electronic circuits on the back side of the detector[1]. A circular background region with a radius of 50 arcsec in a source-free region near the source is used for observations in the small window (SW) mode (obsID 0604720301-0604720401). None of *XMM-Newton* observations suffer from obvious pile-up effects. The ARFGEN and RMFGEN tasks are used to generate redistribution matrix files and auxiliary response files. We concentrate on the EPIC-pn spectra in the energy range of 0.5–10 keV for multi-epoch spectral analysis, due to its high effective photon collecting area. The *XMM-Newton* spectra are grouped to have a minimum number of 50 counts per bin.

5.2.2 *NuSTAR* Data Reduction

1H0419−577 was observed by the *NuSTAR* satellite in 2015 for ≈ 170 ks. The *NuSTAR* data are reduced using the standard pipeline NUPIPELINE V0.4.6 and instrumental responses from *NuSTAR* caldb V20171002. We extract the source spectra from circular regions with radii of 100 arcsec, and the background spectra from nearby circular regions on the same chip. The tool NUPRODUCTS is used for this purpose. The 3-78 keV band is considered for both FPMA and FPMB spectra. The FPM spectra are grouped to have a minimum number of 50 counts per bin.

5.2.3 *Swift* Data Reduction

One short *Swift* observation was taken during the *NuSTAR* observation in 2015. The XRT was operated in the photon counting (PC) mode for ≈ 2 ks. The calibration file version used is 20160609. The source spectrum is extracted from a circular region with a radius of 50 arcsec and the background spectrum is extracted from a circular region with a radius of

[1] See following link for more details. https://xmm-tools.cosmos.esa.int/external/xmm_user_support/documentation/uhb/epicintbkgd.html

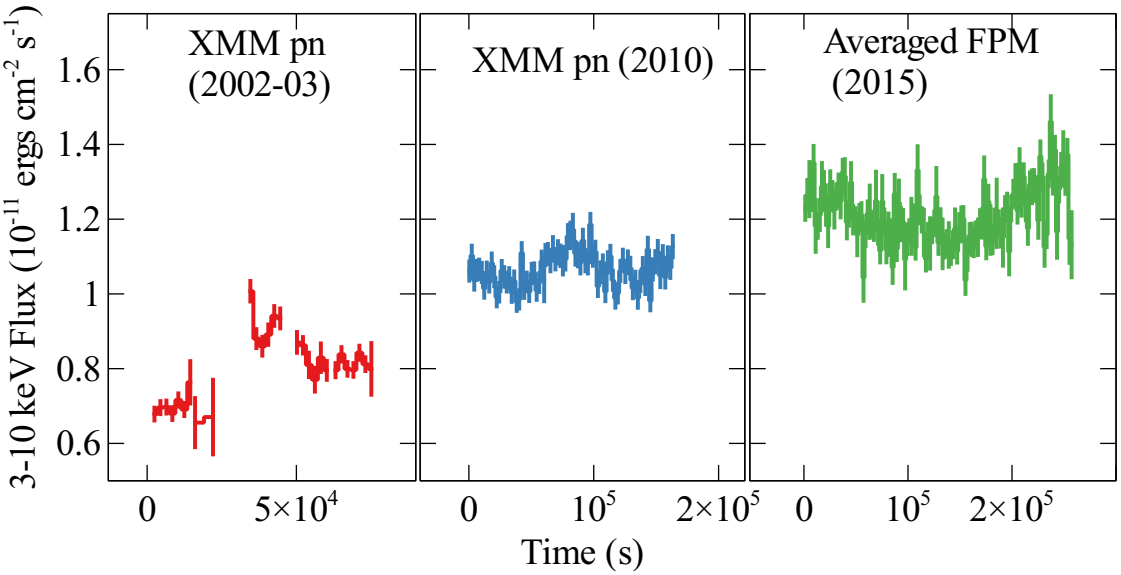

Fig. 5.1 The 3-10 keV light curves of the archival *XMM-Newton* (red and blue) and *NuSTAR* (green) 1H0419−577 observations in 2 ks bin. The first series of *XMM-Newton* observations in 2002-2003 (red) show that the source is at the lowest flux state. The second 160 ks *XMM-Newton* observation in 2010 (blue) shows an intermediate flux state. The *NuSTAR* (green) observations show a higher flux state.

200 arcsec nearby. The spectrum is binned to have a minimum count of 50 per bin. The averaged count rate is only 0.36 counts s^{-1} in the 0.5–6 keV band, which is lower than the pile-up threshold.

5.3 Broad Band Spectral Analysis

The 3–10 keV band lightcurves of all the observations in 2 ks bin are shown in Fig. 5.1. The first series of *XMM-Newton* observations in 2002 and 2003 was taken when the source is at the lowest flux (LF, red in figures) level among the observations analysed in this work; a longer *XMM-Newton* look of the source in 2010 show a middle flux (MF, blue in figures) state; the *NuSTAR* observation shows a high flux (HF, green in figures) state. The HEASARC tool ADDSPEC is used to make a stacked spectrum for each of the three flux levels, along with corresponding background spectra and response matrix files. All the spectra are grouped to have a minimum count of 50 per bin.

The spectra of all the observations considered in this work unfolded through a constant model are shown in Fig. 5.2. The soft band (e.g. 0.5–2 keV) shows a larger flux variability (2 times) than the iron band (1.4 times). The simultaneous HF *Swift* spectrum is shown in grey points in figures hereafter. The MF EPIC-pn spectrum and the HF FPM spectra show

a similar continuum at the iron band with a small difference on the flux level. However the spectral shape below 2 keV is very different in MF and HF spectra. The HF *Swift* XRT spectrum shows a dip feature at 0.6–0.8 keV compared to the MF EPIC-pn spectrum. In this section, we initially focus on the spectral fitting of the broad band LF and HF state spectra - which represent the extremes of the observed spectral variability - to provide a model template for the subsequent multi-epoch spectral analysis.

XSPEC V12.10.0.C [9] is used for spectral analysis, and χ^2 is considered in this work. The Galactic column density towards 1H0419−577 is fixed at $N_{\rm H} = 1.34 \times 10^{20}$ cm^{-2} [326]. The photoionisation cross sections of all elements are from Balucinska-Church and McCammon [15] except that a new He cross section from Yan et al. [330] is used. The solar abundances of Wilms et al. [327] were used. For local Galactic absorption, the `tbnew` model [327] is used. An additional constant model `constant` has been applied to vary normalizations between the simultaneous spectra obtained by different instruments to account for calibration uncertainties. The following cosmology constants are considered: $H_o = 73$ km s^{-1} Mpc^{-1}, $\Omega_{\rm matter} = 0.27$, and $\Omega_{\rm vacuum} = 0.73$. Errors are calculated by estimating the 90% confidence range of parameters using the ERROR command in XSPEC.

5.3.1 *XMM-Newton* Low Flux State Spectral Analysis

Firstly, we fit the 2–10 keV band with a Galactic absorbed `powerlaw` model and extend the ratio plot to 0.5 keV without changing the fit. The ratio plot is shown in the top left panel of Fig. 5.3. It shows a very strong soft excess below 2 keV. The right panel shows the zoom-in of the iron band. A broad emission line is visible between 4 and 10 keV. By fitting the emission feature with a simple gaussian line model `zgauss` with the rest frame energy of the Fe Kα emission line ($E_{\rm line} = 6.4$ keV) and the redshift fixed at the source redshift, we obtained a best-fit line model with a line width of $\sigma = 0.39^{+0.20}_{-0.12}$ keV and an equivalent width of 130 ± 10 eV. No additional narrow line component is required.

Secondly, we fit the LF spectrum with the relativistic reflection model `relxillcp` (V1.0.4) [82], following the indications in Fabian et al. [66] and Walton et al. [314]. The relativistic reflection model `relxillcp` calculates the relativistic disc reflection spectrum given a thermally compotonized continuum, `nthcomp` [343]. A temperature (low energy rollover) of $kT_0 = 0.05$ keV and a disc blackbody distribution is assumed for the seed photons. The relativistic effects, including both the Gravitational Redshift and the relativistic Doppler Effects, are all included in the `relxillcp` model [48]. We assume a simple broken power-law shaped emissivity profile for simplicity. The reflection fraction parameter is defined as the ratio of intrinsic intensity emitted from the corona towards the disc compared to the observer [47]. The coronal electron temperature kT is fixed at a high value (100 keV)

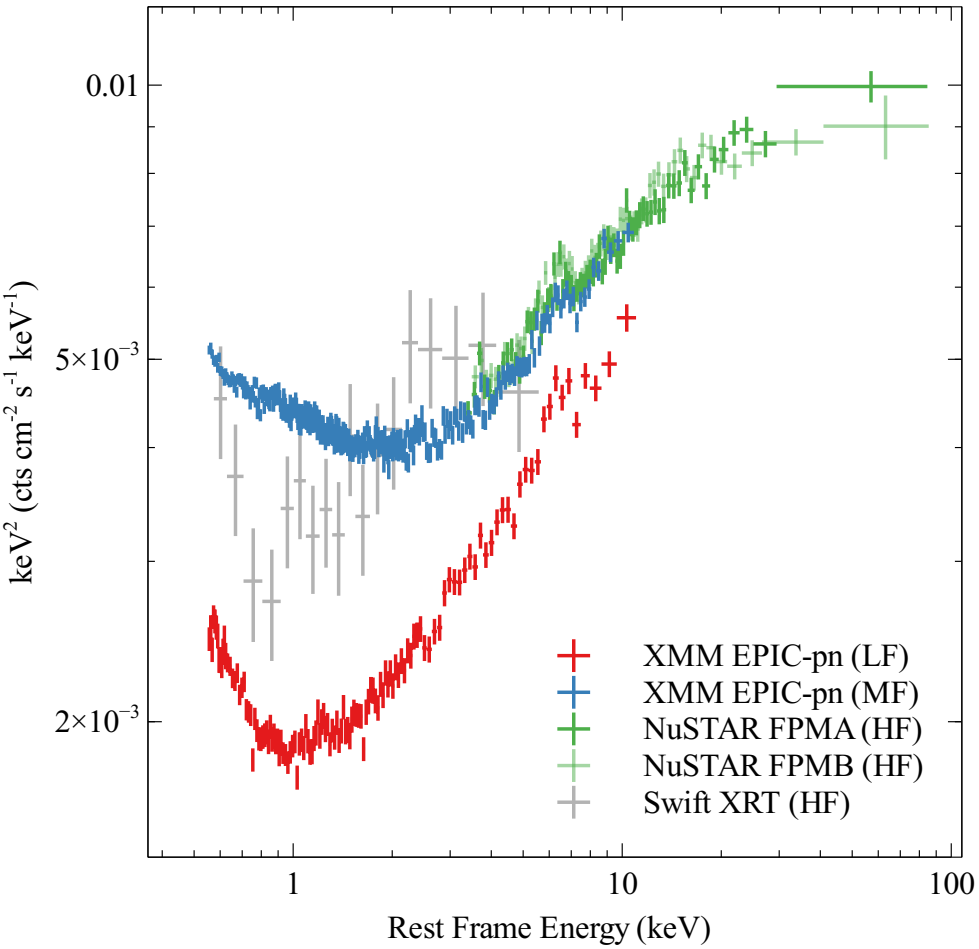

Fig. 5.2 The unfolded spectra of all the observations considered in this work against a constant model . Red: LF *XMM-Newton* EPIC-pn spectrum; blue: MF *XMM-Newton* EPIC-pn spectrum; green and light green: HF *NuSTAR* FPMA and FPMB spectra; grey: HF *Swift* XRT spectrum.

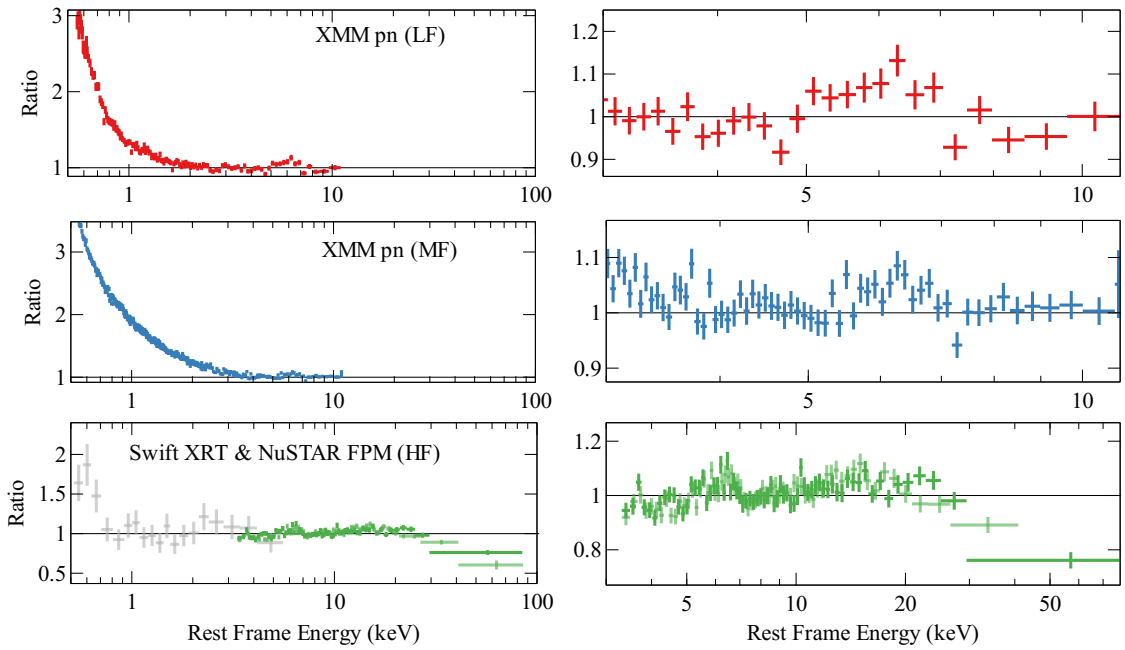

Fig. 5.3 The ratio plots of three flux state spectra against Galactic absorbed power-law models. All three sets of spectra show an iron emission line profile at the iron band and strong soft excess at the low energy band. The HF state spectra show a low high-energy turnover.

because of the lack of high-energy coverage during this epoch. The `relxillcp` model gives a good fit with χ^2/ν=887.90/819. The ratio plot against the best-fit relativistic reflection model shows a weak absorption feature between 0.6–0.9 keV. See the top panel of Fig. 5.4.

Finally, by following the discovery of a weak and cool warm absorber by Di Gesu et al. [53], we also fit the absorption feature in the soft band with a warm absorber model. We constructed custom ionised absorption grids with `xstar` [131]. The grids are calculated assuming solar abundances, a fixed turbulent velocity of 200 km $^{-1}$, and an ionzing luminosity of 10^{43} erg s^{-1}. A power-law input spectrum with a photon index of $\Gamma = 2$ is used. Free parameters are the column density $N_{\rm H}$ and $\log \xi_{\rm warm}$. The ionisation $\xi_{\rm warm}$ is in unit of erg cm s^{-1}. This warm absorber improves the fit by $\Delta\chi^2 = 23$ with 2 more free parameters. See Fig. 5.4. An ionisation state of $\log \xi_{\rm warm} = 1.40^{+0.04}_{-0.13}$ is required for the warm absorber. The additional warm absorber fits the absorption feature with a series of low ionised absorption lines, such as OIV-VI lines and does not significantly change the key parameters of the continuum model. The best-fit parameters can be found in Table 5.2 and the ratio plot can be found in the bottom panel of Fig. 5.4.

An additional distant reflector `xillver` [83] was added for further test. All the parameters of the distant reflection component are linked to the corresponding parameters in the relativistic disc reflection component, except the normalization and the ionisation

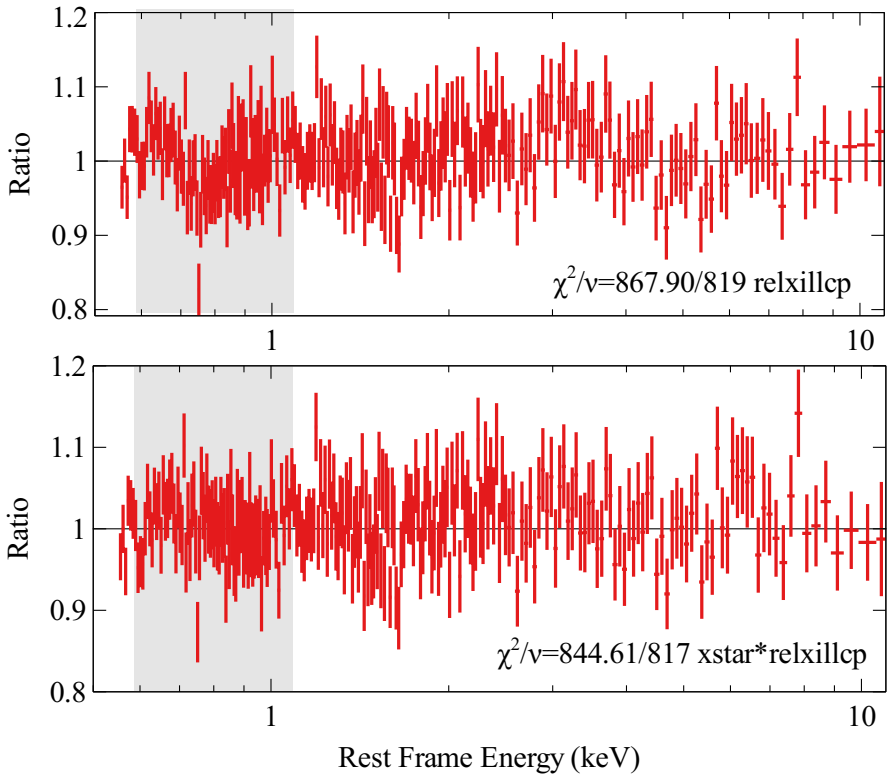

Fig. 5.4 The ratio plot of the LF spectrum against the best-fit `relxillcp` (top) and `xstar*relxillcp` (bottom) model. An additional warm absorber can improve the fit at the <1 keV band (grey shaded region).

Table 5.2 The best-fit `xstar*relxillcp` parameters for the LF and HF spectra respectively. q1 and q2 are the inner and outer emissivity index respectively.

Model	Parameter	LF	HF
`xstar`	$N_{\rm H}$ (10^{21} cm^{-2})	1.5 ± 0.3	< 7.0
	$\log(\xi_{\rm warm}/{\rm erg\ cm\ s^{-1}})$	$1.40^{+0.04}_{-0.13}$	< 1.8
`relxillcp`	q1	> 6	> 7.1
	q2	$3.9^{+0.6}_{-0.7}$	3.3 ± 0.4
	$R_{\rm break}$ (r_g)	$2.1^{+1.0}_{-0.3}$	3.1 ± 0.8
	a_*	> 0.98	> 0.96
	i (deg)	22^{+7}_{-4}	28^{+6}_{-9}
	Γ	$2.06^{+0.02}_{-0.04}$	1.76 ± 0.09
	$\log(\xi/{\rm erg\ cm\ s^{-1}})$	0.9 ± 0.5	$3.0^{+0.2}_{-0.3}$
	$Z_{\rm Fe}$ ($Z_\odot$)	$0.8^{+0.7}_{-0.4}$	$0.7^{+0.8}_{-0.2}$
	kT (keV)	100 (fixed)	27^{+43}_{-3}
	$f_{\rm refl}$	10^{+3}_{-2}	$3.2^{+0.3}_{-1.2}$
	χ^2/ν	844.61/817	964.44/954

parameter. An additional distant reflection component only improves the fit by $\Delta\chi^2 = 4$ with 2 more free parameters. The normalization of the `xillver` is $< 1.0 \times 10^{-5}$ with 90% confidence level. We conclude that no additional narrow reflection components are required in our analysis.

The current version of `relxillcp` assumes a constant electron density $n_{\rm e} = 10^{15}$ cm^{-3} for the top layer of the BH accretion disc. However, recent spectral analysis of both Seyfert 1 AGN with strong soft excess [e.g. IRAS 13224−3809, 124] and XRBs [CygX-1 in the intermediate state, 296] show that the electron density assumed in the reflection model can have an important effect on some of the results obtained from spectral fitting. A more developed version `relxillD` [86] which allows the density to vary to between $n_{\rm e} = 10^{15}$ and 10^{19} cm^{-3} is used to test any possible high electron density in 1H0419−577. A simple power-law shaped continuum is assumed for the coronal emission in `relxillD`. The same parameters are allowed to vary during the fit and we obtained $n_{\rm e} < 10^{15.3}$ cm^{-3} at a 90% confidence level. The high density reflection model only improves the fit by $\Delta\chi^2 = 4$ with one more free parameter compared to `relxillcp`. We conclude that no higher electron density than $n_{\rm e} = 10^{15}$ cm^{-3} is required for the spectral fitting. This result is appropriate for a disc around a BH of mass $> 10^8 {\rm M}_\odot$, as in the case for 1H0419−577 – a disc electron density of $n_{\rm e} < 10^{16}$ cm^{-3} is expected at $r = 20 r_g$ away from a BH with $M_{\rm BH} > 10^8 {\rm M}_\odot$ according to the solution by Svensson and Zdziarski [288]. See Fig. 1 in García et al. [86] for instance.

We checked the constraints of all the parameters obtained in the LF spectral analysis by using the MCMC algorithm. The XSPEC/EMCEE code by Jeremy Sanders based on the python implementation [72] of the Goodman-Weare affine invariant MCMC ensemble sampler [92] was used for this purpose [2]. We use 100 walkers with a length of 25000, burning the first 1000. A convergence test has been conducted and the Gelman-Rubin scale-reduction factor $R < 1.3$ for every parameter. No obvious degeneracy was found. The contour plots of the two relativistic parameters a_*, i and the disc iron abundance $Z_{\rm Fe}$ are shown in the top left panel of Fig. 5.5. By fitting only the EPIC-pn low flux state spectrum with `relxillcp`, we obtained $a_* > 0.98$ and $i = 22^{+7}_{-4}$ by running the ERROR command in XSPEC, which are consistent with our MCMC analysis.

5.3.2 *NuSTAR* and *Swift* High Flux State Spectral Analysis

The *NuSTAR* and simultaneous *Swift* observations are taken when the source is in a high flux state (see Fig. 5.2 for the unfolded spectra). We first fitted the *NuSTAR* FPM and *Swift*

[2] The code can be found on following page. https://github.com/jeremysanders/xspec_emcee

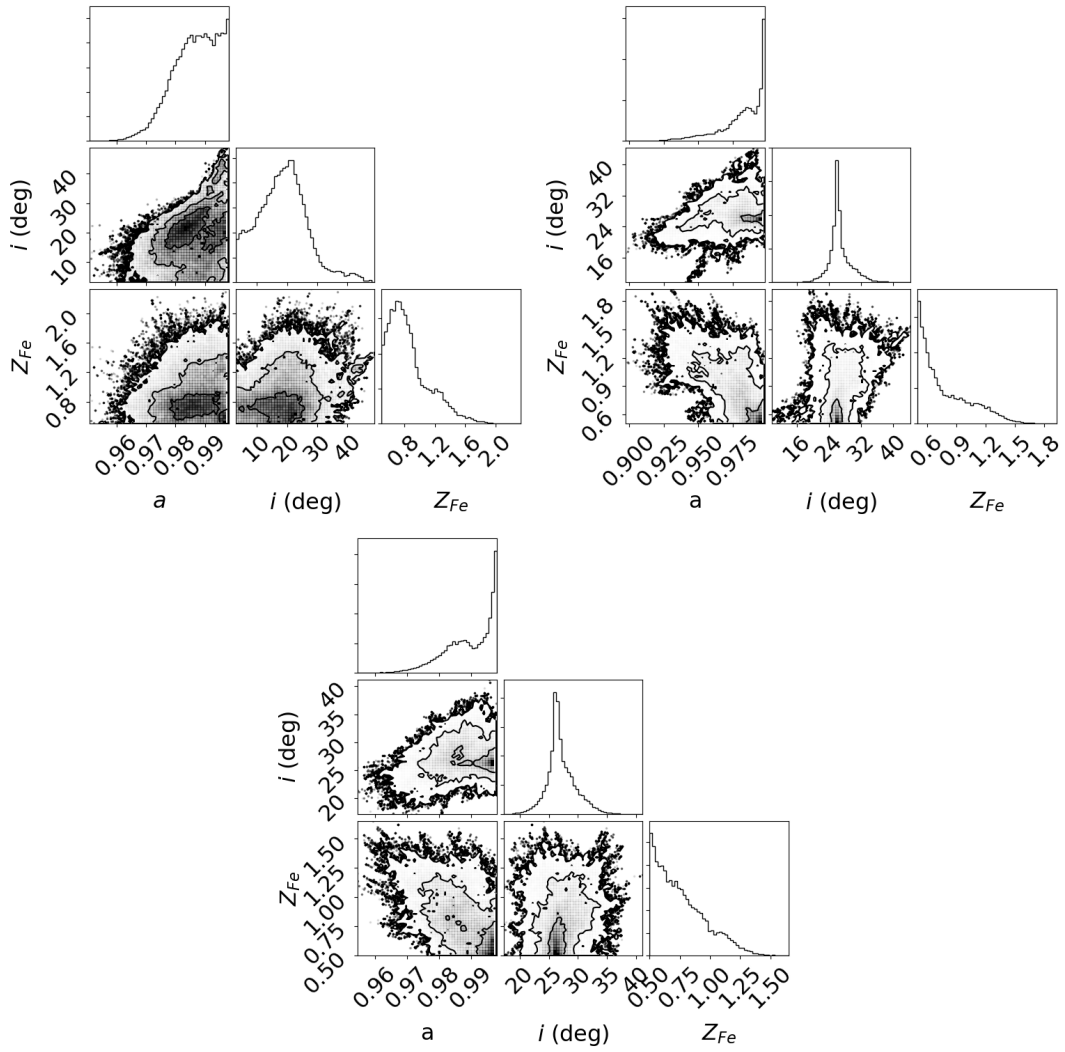

Fig. 5.5 Output distributions for the MCMC analysis of the best-fit models of the broad band spectra of 1H0419−577. Contours correspond to 1, 2 and 3σ. Only the spin a_*, the disc viewing angle i, and the disc iron abundance $Z_{\rm Fe}$ are shown here. Left: only the LF *XMM-Newton* EPIC-pn spectrum; middle: only the HF *NuSTAR* and *Swift* spectra; right: multi-epoch spectral analysis of three flux state spectra.

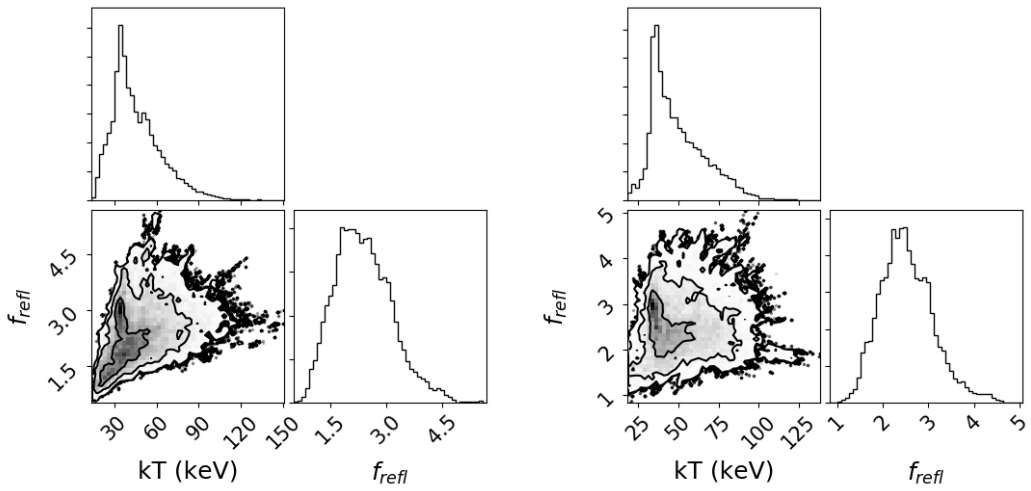

Fig. 5.6 Same as Fig. 5.5 but for the disc reflection fraction and energy cutoff parameters. Left: only the *NuSTAR* and *Swift* (HF) spectra; right: multi-epoch spectral analysis of all three flux state spectra.

XRT spectra simultaneously with a Galactic absorbed power-law model. The ratio plot is shown in the bottom panel of the Fig. 5.3. A broad emission line feature is shown at the iron band with the low energy tail extending to 5 keV. By fitting the broad emission line feature with a simple `gauss` model, the fit is improved by $\Delta\chi^2 = 68$ with 3 more free parameters. The ratio plot against a power-law model also shows a Compton hump above 10 keV and a very low energy turn-over above 30 keV (see the bottom right panel for the zoom-in of the FPM spectra).

Following the analysis of the LF state spectrum in Section 5.3.1, we fitted the HF spectra with the same model as in Section 5.3.1. An additional `constant` model is added in XSPEC to account for cross-calibration uncertainty. `xstar*rexillcp` offers a good fit with $\chi^2/\nu = 964.44/954$. The warm absorber fits the absorption feature at 0.6–0.8 keV, similar to the warm absorber in the LF state spectrum. However, due to a low signal-to-noise of the XRT spectrum, we only obtained an upper limit on the column density and the ionisation of the warm absorber.

We conducted a similar MCMC analysis for this fit as in Section 5.3.1. The constraints of the spin, the disc viewing angle, and the disc iron abundance are shown in the top right panel of Fig. 5.5. The constraints on the three parameters are weaker compared to the fit of the LF spectrum but consistent within 1σ uncertainty range. These quantities are not expected to vary on observable timescales, and so this gives us added confidence in our results. The low energy turn-over shown in the bottom panel of Fig. 5.3 could be due to either a low energy cutoff in the coronal emission or the Compton hump in a reflection dominated

Table 5.3 The same as Table 5.2 but for the multi-epoch joint spectral fitting. The flux of the best-fit model is calculated by using `cflux` model in XSPEC at 1–10 keV band in erg cm^{-2} s^{-1}.

Parameter	LF	MF	HF
$N_{\rm H}$ (10^{21} cm^{-2})	1.1 ± 0.2	< 0.15	< 1.3
$\log(\xi_{\rm warm}$/erg cm s$^{-1})$	$1.40^{+0.04}_{-0.13}$	< 1.8	< 1.8
q1	$5.7^{+2.3}_{-0.5}$	5 ± 2	$7.8^{+1.2}_{-0.3}$
q2	$2.7^{+0.2}_{-0.3}$	$4.6^{+0.5}_{-0.2}$	$3.1^{+0.2}_{-0.4}$
$R_{\rm break}$ ($r_{\rm g}$)	$5.5^{+0.2}_{-1.2}$	<12	$4.2^{+0.2}_{-1.8}$
a_*		>0.987	
i (deg)		26^{+8}_{-4}	
Γ	$2.07^{+0.02}_{-0.05}$	$2.308^{+0.008}_{-0.011}$	$1.887^{+0.063}_{-0.007}$
$\log(\xi$/erg cm s$^{-1})$	$1.04^{+0.07}_{-0.11}$	< 0.03	$2.85^{+0.03}_{-0.15}$
$Z_{\rm Fe}$ ($Z_\odot$)		$0.7^{+0.5}_{-0.3}$	
kT (keV)		30^{+22}_{-7}	
$f_{\rm refl}$	10^{+4}_{-2}	$5.3^{+1.2}_{-0.2}$	$2.8^{+1.0}_{-1.3}$
$\log(F_{1-10\ \rm keV})$	$-10.914^{+0.003}_{-0.002}$	$-10.740^{+0.001}_{-0.002}$	-10.70 ± 0.01
χ^2/ν		$3337.79/3272$	

spectrum. A contour plot on the coronal electron temperature kT and the disc reflection fraction $f_{\rm refl}$ parameter plane is shown in the left panel of Fig. 5.6. Note that there is a weak degeneracy at 3σ confidence level. However, the reflection fraction is constrained at a low value $f_{\rm refl} < 3$ within 1σ uncertainty range, precluding a reflection-dominated scenario.

5.3.3 Multi-Epoch Spectral Analysis

In previous sections, we have obtained a good fit for 1H0419−577 LF and HF state spectra by using the combination of a warm absorber and a relativistic disc reflection model `xstar*relxillcp`. The analysis has found consistent results of the key reflection parameters (spin, disc viewing angle, iron abundance). In this section we therefore undertake the multi-epoch spectral analysis of all three flux state spectra to more robustly probe the spectral variability shown by this source.

The same disc reflection model `relxillcp` was used. The BH spin parameter, the disc viewing angle, and the disc iron abundance are not expected to vary in the time scale of our observations and they are linked during the joint spectral analysis. The LF and MF state *XMM-Newton* observations were taken with lack of simultaneous high energy observations above 10 keV. We therefore also linked the coronal electron temperature parameter kT for all three flux state spectra. The best-fit continuum model parameters for the lower flux

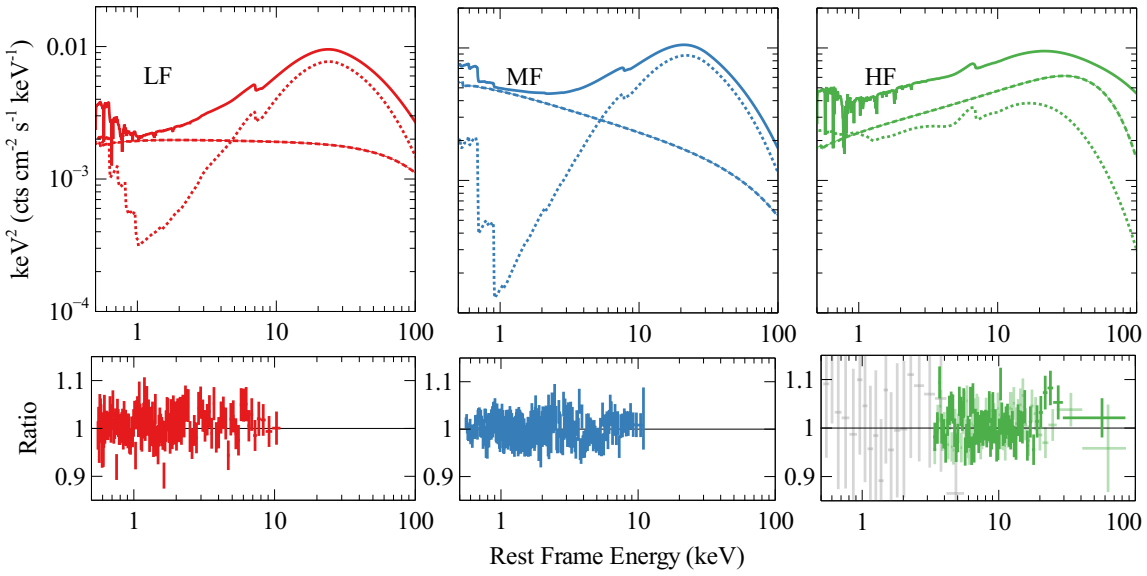

Fig. 5.7 Top: the best-fit `xstar*relxillcp` model for three sets of spectra (red: LF; blue: MF; green: HF) obtained in the multi-epoch spectral analysis. The dashed lines show the best-fit unabsorbed coronal emission model `nthcomp` modelled in `relxillcp`; the dotted lines show the best-fit unabsorbed disc reflection component. Bottom: three ratio plots of three flux state spectra against the best-fit `xstar*relxillcp` models correspondingly.

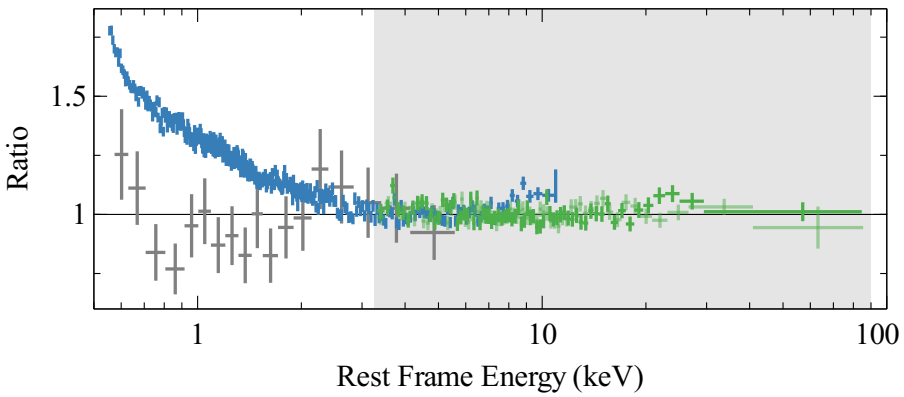

Fig. 5.8 The ratio plot of MF and HF spectra against the best-fit `relxillcp` model obtained by fitting the MF EPIC-pn (blue) and HF FPM spectra (green) simultaneously at the 3–78 keV band (grey shaded region). The plot is extended to 0.5 keV without changing the model. See text for more details.

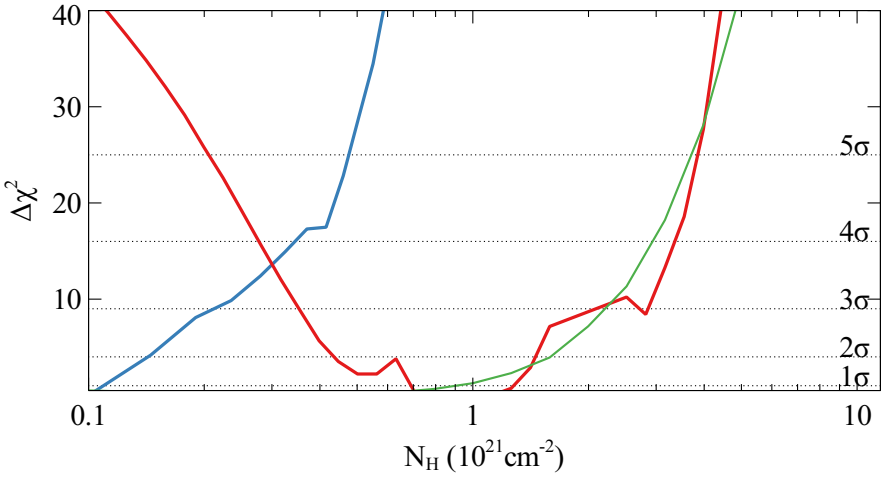

Fig. 5.9 The χ^2 contour plot for the column density of the warm absorber in the multi-epoch joint spectral analysis (red: LF; blue: MF; green: HF). The 1–5σ measurement rage is marked in dotted lines.

state spectra obtained after linking the coronal temperature parameters are consistent with the values obtained by fitting them alone within their 90% confidence errors. The other parameters are all allowed to vary during the fit. The best-fit model parameter values are shown in Table 5.3. The best-fit `xstar*relxillcp` models and the ratio plot against the best-fit models are shown in Fig. 5.7. A similar MCMC analysis has been conducted for the multi-epoch spectral analysis as in previous sections. 200 walkers are used for a larger number of degrees of freedom to keep the Gelman-Rubin scale-reduction factor $R < 1.3$ in the convergence test. The constraints on the relativistic parameters and $Z_{\rm Fe}$, and a kT and $f_{\rm refl}$ are shown in the right panels of Fig. 5.5 and Fig. 5.6 respectively. The parameter measurements given by running ERROR command in 90% confidence level are all consistent with MCMC analysis results.

By combining all three flux state spectra, we obtained a close-to-maximum black hole spin of $a_* > 0.987$ and a disc viewing angle of $i = 26^{+8}_{-4}{}^\circ$. By fitting the *Suzaku* observation with a similar model, Walton et al. [314] obtained a viewing angle of $\approx 45^\circ$ and a weaker spin constraint $a_* > 0.89$. The difference between the two inclination angles could be due to the model development or instrumental systematic uncertainty (see discussion in Brenneman 32) or stacking two different observations at different flux and ionisation states.

A very high reflection fraction $f_{\rm refl} \approx 10$ is obtained for the LF state while a lower reflection fraction $f_{\rm refl} \approx 3-6$ is measured for the HF and MF state. The light-bending model can potentially explain the higher reflection fraction found in the LF state of 1H0419−577. In the light-bending model, more primary continuum photons will be lost to the BH and

the trajectories of photons will be bent towards the central object when the corona is closer to the BH [e.g. the LF state in 1H0419−577 corresponds to the reflection-dominated regime I or I/II in 191]. In order to rule out the possibility that the $f_{\rm refl}$ obtained above is only due to the variable soft excess, we fitted all three spectra at the 3–10 keV band with a simple `tbabs*(powerlaw+zgauss)` model, where `zgauss` accounts for the broad Fe Kα emission line at the iron band. The redshift z of the `zgauss` model is fixed at the source redshift and the rest-frame energy is fixed at 6.4 keV. The equivalent widths of the best-fit `zgauss` against the simple Galactic power-law continuum are 130 ± 10 eV for the LF state, 62^{+23}_{-41} eV for the MF state, and 78^{+23}_{-21} eV for the HF state. A higher equivalent width of the Fe Kα emission line at the LF state matches the result obtained by fitting the broad band spectra.

A thin and low ionisation warm absorber with a column density of $N_{\rm H} \approx 10^{21}$ cm^{-2} and an ionisation state of $\log(\xi) \approx 1.5$ is required to fit the dip features in the LF state spectra. A χ^2 contour plot for the warm absorber column density is shown in Fig. 5.9. We can conclude that no warm absorber or at least an even smaller column ($N_{\rm H} \approx 10^{20}$ cm^{-2}) is required for the MF state. The result matches the RGS spectral analysis of the MF observations ($N_{\rm H} \approx 10^{19.9}$ cm^{-2}) in Di Gesu et al. [53]. The warm absorber in the HF state can account for the spectral difference between the MF and HF spectra at the 0.6–0.8 keV band, in addition to the continuum variability.

5.3.4 Further Comparison Between the MF and HF Spectra

The HF FPM and MF EPIC-pn spectra show a similar spectral shape with only 15% different flux level in the 3–10 keV band, although two observations were taken 5 years apart. However in the soft band (<2keV), the HF XRT and the MF EPIC-pn observations show a very different spectral shape. See Fig. 5.2 for the unfolded spectra. By modelling the spectra with `warmabs*relxillcp`, we found that both the disc reflection component and the warm absorber need to be variable to account for the large spectral variability below 2 keV despite a similar spectral shape at the iron band. For example, different photon index Γ, different column of the warm absorber $N_{\rm H}$, and different disc ionisation state ξ. are all required in the multi-epoch spectral fitting.

However there might be other solutions to the soft band spectral variability. For instance, only a different warm absorber can account for the soft band spectral variability with a similar disc reflection and coronal emission for both two flux states. In order to test this scenario, we first ignored the HF XRT spectrum, and fitted the MF EPIC-pn spectrum (3–10 keV) and the HF FPM spectrum (3–78 keV) simultaneously with the same `relxillcp` model. An additional `constant` model in XSPEC is used to account for the flux difference between two epochs. We obtained a good fit with $\chi^2_{\rm red} = 1.10$. The best-fit `relxillcp`

requires a photon index of $\Gamma \approx 1.87$, an ionisation of $\log(\xi) \approx 2.7$, a reflection fraction of $f_{\rm refl} \approx 3.3$, a black hole spin of $a_* > 0.96$, and a disc viewing angle of $i \approx 28^\circ$. The best-fit model is similar with the best-fit continuum model obtained by using `warmabs*relxillcp` in Section 5.3.2. The ratio plot extended to 0.5 keV without changing the fit is shown in Fig. 5.8. The HF XRT spectrum is added for reference in the figure. First, we notice that the best-fit `relxillcp` fails to fit the hard band of the MF EPIC-pn spectrum with 20% residuals above 7 keV. It indicates a different emissivity profile is required for the relativistic disc line modelling. Second, by extending the ratio plot to 0.5 keV without changing the fit, the best-fit `relxillcp` model obtained by fitting the hard band fails to fit the soft excess of the MF EPIC-pn spectrum but more agrees with the HF XRT spectrum. The fit of the HF XRT spectrum can be improved by fitting the remaining residuals shown in Fig. 5.8 with an additional thin warm absorber (see Section 5.3.2). We therefore conclude that both a variable continuum model `relxillcp` and and a variable thin warm absorber `warmabs` are required to account for the spectral variability below 2 keV.

5.4 Discussion and Conclusions

We fitted all three flux state spectra of the Seyfert 1 1H0419−577 successfully with a combination of a thin warm absorber and a variable relativistic disc reflection model. In this section, we discuss the accretion rate of the disc, the black hole spin obtained by fitting the multi-epoch broad band spectra with relativistic disc reflection model, the broad band spectral variability, and the properties of the cool corona region.

5.4.1 Eddington Ratio Estimation

We calculated the Eddington ratio $\lambda_{\rm Edd}$ by applying an averaged bolometric luminosity correction factor $\kappa = 20$ [306] to the 2–10 keV band absorption corrected luminosity $2.45 \sim 3.84 \times 10^{44}\,{\rm erg\,s^{-1}}$. A black hole mass of $M_{\rm BH} = 1.3 \times 10^8 M_\odot$ [100] is considered. We obtained $\lambda_{\rm Edd} = \kappa L_{\rm x}/L_{\rm Edd} \approx 20 \times 0.015 \sim 0.024 = 0.30 \sim 0.48$. Note that the bolometric luminosity correction factor κ can be even higher than 20 when the $\lambda_{\rm Edd}$ is at a high value. We therefore conclude that the disc around the SMBH in 1H0419−577 is accreting at an accretion rate approaching the Eddington limit.

5.4.2 Black Hole Spin Measurement

Previously, Walton et al. [314] obtained a BH spin of $a > 0.88$ by fitting the *Suzaku* observation of 1H0419−577 at high flux state with relativistic disc reflection model `reflionx` and

Fabian et al. [66] obtained an inner accretion disc radius of $R_{\rm in} < 2R_{\rm g}$ by fitting the low flux state spectra captured by *XMM-Newton* with an ionised reflection model convolved with `kdblur` and concluded a spin of $a > 0.95$. In this work, we have conducted a robust measurement of the central BH spin by conducting careful MCMC analysis and obtained a black hole spin of $a_* > 0.987$ (see the right panel of Fig. 5.5 for MCMC analysis). By excluding the spectra below 3 keV where the strong soft excess is, we still obtained a high black hole spin of $a_* > 0.96$ (see Section 5.3.4).

1H0419−577 is a Seyfert 1 galaxy hosting a SMBH with $M_{\rm BH} > 10^8 M_\odot$ [100]. A significant fraction of the SMBH spin measured by using relativistic reflection spectroscopy are very close to the maximum [e.g. see the sample list in 32, 314]. By compiling the AGN spin measurements obtained through reflection spectroscopy in the literature, Reynolds [253] pointed out that there is tentative evidence that the most massive black holes ($M_{\rm BH} > 10^8 M_\odot$) and the least massive black holes ($M_{\rm BH} < 10^6 M_\odot$) may have more modest spins. One of the possible explanations is the effect of host galaxy properties on the evolution of the black hole spin [274]. However, 1H0419−577 shows both a high black hole spin and a large black hole mass ($\approx 10^8 M_\odot$).

5.4.3 The Spectral Variability

In previous section, we introduce the spectral analysis of 3 different flux states captured by *XMM-Newton*, *Swift* and *NuSTAR* observations. The soft band (0.5–2 keV) of 1H0419−577 shows a larger flux variability (2 times) than the iron band (1.4 times). See Fig. 5.2 for unfolded spectra after correcting for the effective area of the detectors. The MF state and HF state shows a similar spectral slope at 1–10 keV band but a very different soft band. By fitting the broad Kα emission line and the soft excess simultaneously with only one `relxillcp` model, we obtained a higher reflection fraction for the LF state compared to the higher flux states. The best-fit reflection fraction for the MF state spectrum is slightly higher than HF state. The equivalent width of the Fe Kα also shows a similar correlation with the source flux level. Such an anti-correlation between the X-ray band flux and the disc reflection fraction can be explained by the light-bending effect in the vicinity of the black hole. The light-bending model has been discussed in previous literatures. For example, the LF state of 1H0419−577 corresponds to the regime I and I/II discussed in [191], where the spectrum is dominated by the disc reflection component. When the coronal region is closer to the central black hole, more continuum photons from the coronal region are lost to the event horizon. Both the direct emission from the coronal component and the reflection component decrease with decreasing flux while the reflection fraction increases.

The light-bending effects have successfully explained the X-ray spectral variability in others sources as well, such as Mrk335 [227] and IRAS13224−3809 [41, 124].

The coronal emission shows an interesting variability versus flux in different epochs compared with other typical Seyfert 1 sources: the spectrum is hardest at the HF flux state ($\Gamma \approx 1.8$) compared to the lower flux states ($\Gamma \approx 2.0 - 2.3$), although the MF state spectrum has a slightly softer continnum than the LF state spectrum. It agrees with previous analysis of the same source: Walton et al. [314] stacked the two archival *Suzaku* observations, one of which was taken at a 16% higher flux state than the *NuSTAR* observation in this work and the other was at a 7% lower flux state, and obtained a hard continuum too ($\Gamma = 1.98$). Fabian et al. [66] analysed the first orbits of the *XMM-Newton* observations, which were taken at this source's lowest flux state, and obtained a very soft continuum ($\Gamma \approx 2.2$). The continuum emissions are commonly found to be softer at higher luminosities [e.g. 278]. For example, the narrow-line Seyfert 1 IRAS 13224−3809 accretes at an accretion rate around the Eddington limit and shows a softer continuum at higher X-ray luminosities (see Chapter 4). One explanation for an exception, as in 1H0419−577, is a possible advective flow in the innermost region [59, 205]. The Compton parameter in such a flow increases as the accretion rate increases and thus produces a harder continuum. This scenario applies to either XRBs in the intermediate hard state or AGN with a low accretion rate. Indeed the harder-when-brighter continuum is commonly seen in low-luminosity AGN [e.g. $L_{\rm x}/L_{\rm Edd} < 10^{-2}$, 42]. However 1H0419−577 has a very high accretion rate. The detection of a broad iron Kα emission line, a strong soft excess and high UV flux in its broad band SED [304] indicate the existence of an inner disc. A second explanation is potential jet contribution to the X-ray spectrum [e.g. 148, 337]. However 1H0419−577 is a radio-quiet source with no significant detection of a radio jet. Additional observations covering more flux states of this source will be required to confirm and study the origin of the harder-when-brighter continuum.

5.4.4 Low High-Energy Cutoff

In this work, we fitted the broad band spectra carefully with the relativistic reflection model `relxillcp` and tested any possible degeneracy between the energy cutoff and the disc reflection fraction by conducting an MCMC analysis. A low energy spectral turn-over could be due to either a cool coronal temperature or a reflection dominated spectrum. We conclude that the HF *NuSTAR* observation shows a cool corona with a temperature of $kT = 30^{+22}_{-7}$ keV and a disc reflection fraction of $f_{\rm refl} = 2.8^{+1.0}_{-1.3}$, precluding the very high reflection scenario.

In order to seek for any possible variability of the energy cutoff $E_{\rm cut}$ in a long timescale, we fitted the *Swift* 105-month BAT spectrum [216] together with the *NuSTAR* spectrum. The ratio plot is shown in Fig. 5.10. The *Swift* BAT spectrum shows a very steep soft spectral

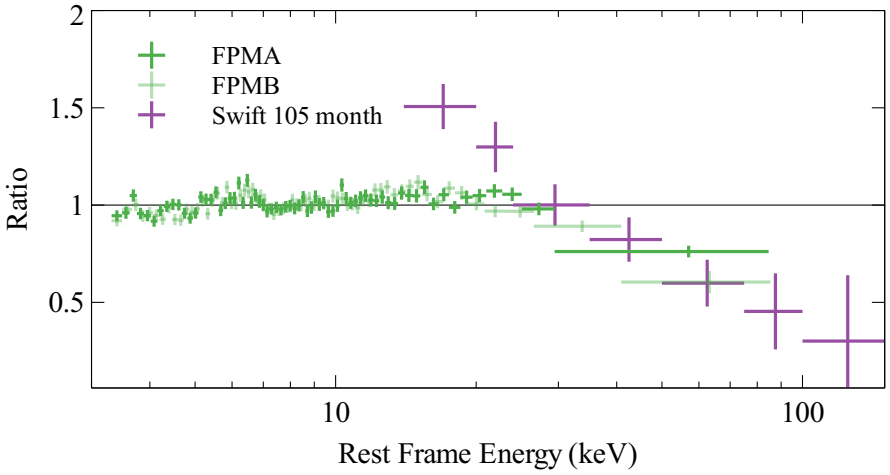

Fig. 5.10 The ratio plots of *NuSTAR* FPM spectra and *Swift* BAT 105-month survey spectrum (15–150 keV) against the best-fit galactic absorbed power-law model. The cross-calibration constant for BAT is 0.75.

shape and agrees with the *NuSTAR* FPM spectra above 30 keV. More *NuSTAR* observations are required to confirm any variability of $E_{\rm cut}$ in a wider flux range [e.g. 63].

Such a low energy cutoff is also seen in other sources, such as Ark564 [$kT = 15 \pm 2$ keV, 137], GRS 1734−292 [$kT = 11.9^{+1.2}_{-0.9}$ keV, 298], IRAS 13197−1627 [$kT < 42$ keV, 311], and 4C 50.55 [$kT \approx 30$ keV, 292]. Except the Seyfert 1 galaxy GRS 1734−292 ($\lambda_{\rm Edd} \approx 0.03$) and the Seyfert 1.8 Galaxy IRAS 13197−1627 ($\lambda_{\rm Edd} \approx 0.05 - 0.1$), all the other sources mentioned above are accreting at a very high accretion rate. A very extreme example is the narrow line Seyfert 1 galaxy Ark564 which accretes at the Eddington limit and shows the coolest coronal temperature so far. One possibility is that a high accretion rate disc is cooling down the coronal region more than a low accretion rate disc by providing more seed photons.

5.4.5 Future Observations

In this work, we successfully explained the spectral variability, especially the soft band, with the combination of a variable disc reflection model and a thin warm absorber. The strong soft excess and soft band variability make this source a promising candidate with detections of disc reverberation lags, as seen in other sources, such as 1H0707−495 [e.g. 62, 135] and Ark564 [e.g. 137]. However a large black hole mass $> 10^8 M_\odot$ means a much longer observation is needed to detect any reverberation lag compared with the narrow-line Seyfert 1 galaxies mentioned above. Moreover, the hard band *NuSTAR* spectrum of 1H0419−577 reveals a cool coronal region. More *NuSTAR* observations at different flux states are required to monitor possible variation on the coronal temperature.

Chapter 6

An *XMM-Newton* View of High Density Disc Reflection in Seyfert Galaxies

"If you feel you are in a black hole, don't give up –
there's a way out."
– Stephen Hawking

6.1 Introduction

High density disc reflection spectroscopy allows the density in the top layer of the inner disc to be a free parameter during the analysis of the disc reflection spectra in both X-ray binaries (XRBs) and active galactic nuclei (AGN). Previously, a fixed disc density of $\log(n_{\rm e}/{\rm cm}^{-3}) = 15$ was commonly assumed. However, there has been increasing evidence for a disc density higher than $\log(n_{\rm e}) = 15$ in both XRBs and AGN[1]. For instance, we find that a high disc density of $\log(n_{\rm e}) > 18.5$ can significantly decrease the inferred iron abundance by modelling the *XMM-Newton* and *NuSTAR* spectra of the narrow-line Seyfert 1 galaxy (NLS1) IRAS 13224−3809 in Chapter 4. In Section 1.4.4, we demonstrate how the number density of electrons affects the temperature profile of an ionised slab and thus changes the reflected emission in the soft X-ray band. At high disc densities, the reflected emission in the soft X-ray band turns into a blackbody-shaped spectrum due to strong free-free absorption [265, 86]. This blackbody-shaped feature may be able to explain excess emission that is commonly seen in the soft X-ray band (<3 keV) of Seyfert galaxies. For example, a high disc density reflection model successfully explains the spectrum of the NLS1 galaxy Mrk 1044, including the soft excess emission, the broad Fe K emission, and the Compton hump in the *XMM-Newton* and *NuSTAR* spectra [164]. Recently, Garcia et al. [88] suggest a high density disc reflection origin of the soft excess emission in the Seyfert 1 galaxy Mrk 509.

I study the disc densities of individual BH XRBs in different accretion states in Chapter 2–3 and test for high density discs in AGN in Chapter 4–5. In this chapter, I measure the inner disc densities of AGN at different BH mass scales by modelling *XMM-Newton* EPIC-pn spectra with a variable density disc reflection model. By conducting photometry with *XMM-Newton* OM observations, we are able to estimate the mass accretion rate for each BH, and thus compare disc density with BH mass and accretion rate. In Section 6.2, we introduce our source sample and data reduction; in Section 6.3, we introduce the analysis method for EPIC-pn and OM observations; in Section 6.4, we present a short introduction and details of the EPIC-pn spectral analysis for each individual AGN; in Section 6.5 and 6.6, we briefly summarize and discuss our results.

6.2 Sample Selection and Data Reduction

We select 17 Seyfert 1 galaxies for our work. These Seyfert 1 galaxies include all 13 Seyfert 1 galaxies in the AGN Black Hole Hβ Reverberation Mapping Mass Database [21] that have

[1]The value of $n_{\rm e}$ is reported in the unit of cm^{-3} hereafter.

Table 6.1 The sample of Seyfert 1 galaxies considered in this work. The Galactic column density and extinction values are calculated by Willingale et al. [326]. The source distances are from NED. The sixth column shows the total EPIC-pn exposure after filtering flaring particle background. $L_{\rm X}$ is the averaged Galactic absorption-corrected luminosity in the 0.5–10 keV band. The upper table shows all the optical reverberation mapped Seyfert 1 galaxies in the AGN Black Hole Mass Database [21]. The lower table shows a sample of Seyfert 1 galaxies with BH mass measurements obtained by measuring Hβ line width [22]. [1]UGC 6728 only has MOS observations as its pn observation is dominated by flaring background.

Name	$\log(M_{\rm BH}/M_{\odot})$	$N_{\rm H}$ (10^{20} cm^{-2})	$E(B-V)$	D (Mpc)	Expo (ks)	$\log(L_{\rm X})$
Ark 120	$8.07^{+0.05}_{-0.06}$	14.5	0.126	148	504	44.338 ± 0.002
Mrk 110	7.29 ± 0.10	1.39	0.014	151	33	$44.161^{+0.009}_{-0.006}$
Mrk 1310	$6.21^{+0.07}_{-0.09}$	2.66	0.029	86.7	35	$41.67^{+0.05}_{-0.03}$
Mrk 279	$7.44^{+0.10}_{-0.13}$	1.72	0.018	129	113	$43.960^{+0.008}_{-0.124}$
Mrk 335	7.23 ± 0.04	4.11	0.044	111	298	$43.51^{+0.03}_{-0.02}$
Mrk 590	$7.57^{+0.06}_{-0.07}$	2.93	0.031	107	36	43.143 ± 0.012
Mrk 79	$7.61^{+0.11}_{-0.14}$	6.73	0.071	94.3	100	$43.384^{+0.012}_{-0.013}$
NGC 4748	$6.41^{+0.11}_{-0.18}$	4.07	0.052	65.5	26	43.033 ± 0.011
PG 0804+761	8.74 ± 0.05	3.51	0.032	475	32	44.728 ± 0.009
PG 0844+349	$7.86^{+0.15}_{-0.23}$	3.13	0.032	279	18	$43.663^{+0.008}_{-0.007}$
PG 1229+204	$7.76^{+0.18}_{-0.22}$	2.92	0.030	276	17	$43.80^{+0.03}_{-0.04}$
PG 1426+015	$9.01^{+0.11}_{-0.16}$	2.88	0.033	383	0.6	$44.49^{+0.03}_{-0.04}$
UGC 6728	$5.85^{+0.19}_{-0.36}$	6.74	0.068	29.3	8.4, 8.8[1]	$42.053^{+0.015}_{-0.019}$
1H1934−063	6.5 ± 0.5	19.5	0.278	42.5	105	43.037 ± 0.006
Ark 564	6.2 ± 0.5	6.74	0.068	106	402	43.972 ± 0.006
Swift J2127.4+5654	7.2 ± 0.5	91.4	1.532	61.1	326	$43.380^{+0.005}_{-0.009}$
Ton S180	6.9 ± 0.5	1.54	0.016	263	148	$44.01^{+0.07}_{-0.09}$

been observed by *XMM-Newton* and 4 Seyfert 1 galaxies where broad Fe Kα emission line was found and supersolar iron abundance was required in previous spectral analyses. The Seyfert 1 galaxies in our sample show no complex warm absorption, ultra-fast outflow absorption, or heavy obscuration along the line of sight. Therefore, we are able to have a clear view of the soft X-ray emission from the innermost regions of these AGN. For the similar reason, we ignore Seyfert 2 galaxies as they are mostly obscured in the X-ray band [259]. Table 6.1 presents the basic information for each source.

For BHs without a reverberation-mapping mass, we quote the mass measurement from Hβ line width [22]. Due to the unknown geometry of the broad line region (BLR), the relation between Hβ line width and BLR velocity distribution has a large uncertainty. For example, Kaspi et al. [139] assume a spherical BLR with an isotropic velocity distribution and predict $v_{\rm BLR} = \frac{\sqrt{3}}{2} FWHM({\rm H}\beta)$. But McLure and Dunlop [179] assume a disc-shaped BLR which predicts a velocity $\sqrt{3}$ times larger and a black hole mass 3 times larger than in Kaspi et al. [139]. For this reason, we consider a conservative uncertainty $\log(\Delta M_{\pm}/M_{\rm BH}) = \pm\log(3) \approx \pm 0.5$. Figure 6.1 shows the BH mass distribution in our sample. 75% of sources in the sample have a BH mass between $\log(M_{\rm BH}/M_{\odot}) = \log(m_{\rm BH}) = 6-8$.

We consider all the available archival *XMM-Newton* observations for each AGN. A complete list of the *XMM-Newton* observations considered in this work is in Table 6.2. We extract EPIC-pn products using SAS 16.1.0, after filtering intervals dominated by flaring particle background. The task EPATPLOT is used to test for any pile-up effects. An annulus-shaped source region is used to extract source products if there is evidence for pile-up. The inner radius of the annulus is chosen to keep distribution patterns consistent with the model curves given by EPATPLOT. Background products are extracted from a nearby region on the same chip, avoiding the areas dominated by background Cu K emission lines from the underlying electronic circuits. We concentrate on the EPIC-pn spectra between 0.5–10 keV due to its higher effective area compared to two EPIC-MOS instruments. For UGC 6728, we extract EPIC-MOS spectra as its pn observation is dominated by flaring background. All the spectra are grouped to have a minimum signal-to-noise of 6 and oversample by a factor of 3. Net pn exposures and averaged X-ray luminosities after correcting for Galactic absorption are shown in the last column of Table 6.1. In Fig 6.2, we present the distribution of the averaged X-ray luminosities in the full pn band and source redshifts of our sample.

*XMM-Newton*Optical Monitor (OM) data are extracted using the task OMICHAIN, and the count rates are converted to Galactic extinction-corrected flux for each filter. The flux conversion factors are provided by SAS Watchout Website[2]. The Galactic extinction curve calculated by Pei [233] is used to convert $E(B-V)$ to extinction at another wavelength.

[2]https://www.cosmos.esa.int/web/xmm-newton/sas-watchout-uvflux

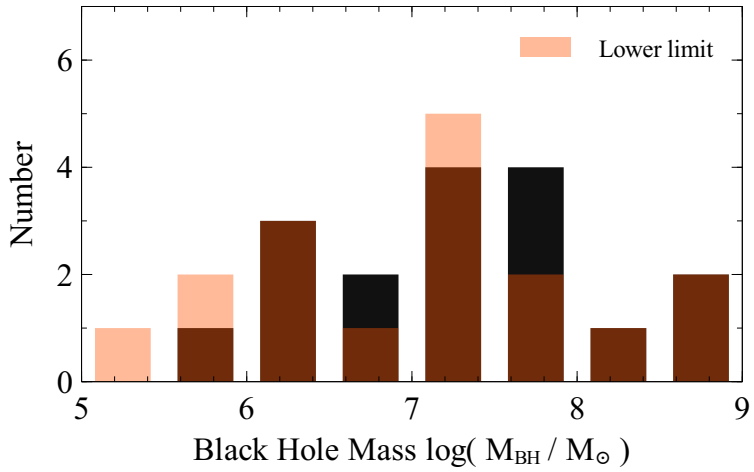

Fig. 6.1 Black hole mass distribution in our sample shown in black. Orange bars show the distribution of the lower limits of mass measurements. The brown bars show the overlaps of the orange and black bars.

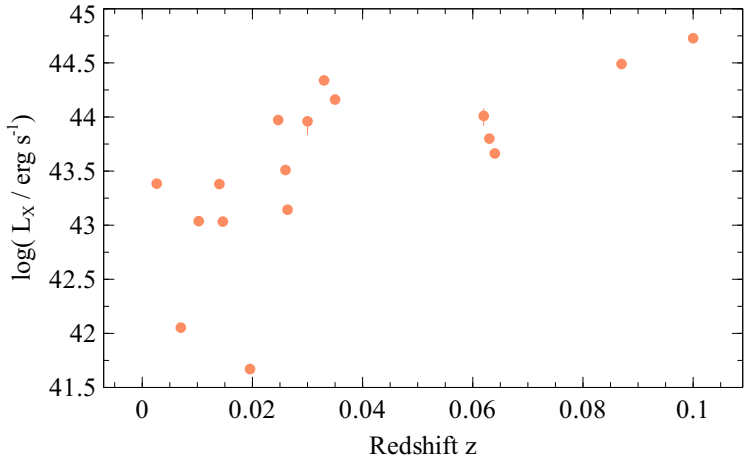

Fig. 6.2 Source redshift and X-ray luminosity distribution. The luminosities are calculated in the full *XMM-Newton* band (0.5–10 keV).

Table 6.2 A list of all the *XMM-Newton* observations considered in this work. SW: small window mode; FF: full frame mode; LW: large window mode. Expo: net pn exposure after correcting flaring particle background

Name	obs ID	Expo (ks)	Date	pn mode	Name	obs ID	Expo (ks)	Date	pn mode
1H1934	0550451701	12	2009-04-28	SW	Mrk 335	0101040101	28	2000-12-25	FF
	0761870201	93	2015-10-03	SW		0306870101	90	2006-01-03	SW
Ark 120	0147190101	76	2003-08-24	SW		0510010701	16	2007-07-10	LW
	0693781501	85	2013-02-18	SW		0600540501	53	2009-06-13	FF
	0721600201	86	2014-03-18	SW		0600540601	76	2009-06-11	FF
	0721600301	85	2014-03-20	SW		0741280201	36	2015-12-30	FF
	0721600401	85	2014-03-22	SW	Mrk 590	0109130301	7	2002-01-01	SW
	0721600501	87	2014-03-24	SW		0201020201	29	2004-07-04	SW
Ark 564	0006810101	7.4	2000-06-17	SW	Mrk 79	0103862101	5.3	2000-10-09	SW
	0006810301	7.0	2001-06-19	SW		0400070201	14	2006-09-30	SW
	0206400101	69	2005-01-05	SW		0400070301	14	2006-09-30	SW
	0670130201	41	2011-05-24	SW		0400070401	14	2007-03-19	SW
	0670130301	39	2011-05-31	SW		0502091001	53	2008-04-26	SW
	0670130401	38	2011-06-06	SW	NGC 4748	0723100401	26	2014-01-14	LW
	0670130501	47	2011-06-12	SW	PG 0804	0605110101	16	2010-03-10	SW
	0670130601	42	2011-06-17	SW		0605110201	16	2010-03-12	SW
	0670130701	32	2011-06-26	SW	PG 0844	0103660201	6	2000-11-04	FF
	0670130801	29	2011-06-29	SW		0554710101	12	2009-05-03	LW
	0670130901	39	2011-07-01	SW	PG 1229	0301450201	17	2005-07-09	SW
Mrk 110	0201130501	33	2004-11-15	SW	PG 1426	0102040501	0.6	2000-07-28	FF
Mrk 1310	0723100301	35	2013-12-09	SW	UGC 6728	0312191601	8.4, 8.8	2006-02-23	FF
Mrk 279	0083960101	13	2002-05-07	FF	Ton S180	0110890401	21	2000-12-14	SW
	0302480401	40	2005-11-15	SW		0110890701	13	2002-06-30	SW
	0302480501	38	2005-11-17	SW		0764170101	93	2015-07-03	SW
	0302480604	22	2005-11-19	SW		0790990101	21	2016-06-13	SW
Swift J2127	0601741901	5	2009-11-11	FF					
	0655450101	84	2010-11-29	SW					
	0693781701	94	2012-11-04	SW					
	0693781801	93	2012-11-06	SW					
	0693781901	50	2012-11-08	SW					

6.3 *XMM-Newton* Data Analysis

In this section, we first introduce the broad band EPIC-pn spectral analysis using a variable density disc reflection model. Second, we estimate the BH mass accretion rates by measuring the source flux at an optical band with OM.

6.3.1 EPIC-pn Spectral Analysis and Disc Density Measurement

The X-ray data analysis software XSPEC [9] is used for broad band spectral analysis of EPIC-pn data. C-stat [37] is used. The model `tbabs` in XSPEC is used to account for the Galactic absorption. Galactic column densities $N_{\rm H_{1,2}}$ calculated by Willingale et al. [326] are used and fixed during the spectral fitting. The values of Galactic column density can be found in Table 6.1.

First, we fit EPIC-pn spectra with an absorbed power-law model in the 2–3 keV and 8–10 keV band, ignoring the iron band and the soft excess. We extend the ratio plots to the full energy band and renormalize the power-law models without changing the photon index for illustration purpose (see Figure 6.3). All the AGN in our sample show very strong soft excess below 2 or 3 keV. Most AGN show evidence for emission features in the iron band. Some sources show a combination of broad and narrow emission lines.

Second, we model the soft excess and the broad emission line in the iron band using the relativistic reflection model `relxilld` [v1.2.0, 86]. `relxilld` combines the convolution model `relconv` [49] and the illuminated ionised disc reflection model `xillverd` [86]. The `relconv` model calculates the relativistic effects and corresponding emissivity profiles for emission lines in the reflection spectrum. A broken power-law emissivity profile (inner index q_1, outer index q_2, threshold radius $R_{\rm r}$) is assumed. In cases where q_2 and $R_{\rm r}$ are not constrained, we assume a simple power-law emissivity profile. The disc reflection model `xillverd` allows the disc density parameter to vary between $\log(n_{\rm e})$ =15–19. The solar abundance in `xillverd` is provided by Grevesse et al. [95]. The ionisation parameter ξ is defined as $\xi = 4\pi F/n$ in unit of erg cm s^{-1}. The reflection model `xillver` in the same model package is used to account for the narrow emission line feature if shown in the iron band. A simple power-law model is used to model the coronal emission. The convolution model `cflux` is used to calculate the flux of each component in the 0.5–10 keV band. An empirical reflection fraction ($F_{\rm refl}/F_{\rm pl}$) is used for simplicity and future comparison with other reflection models [e.g. `reflionx`, 265]. In summary, the following models are used in XSPEC:

- `tbabs * ( cflux * relxilld + cflux * powerlaw + cflux * xillver)` (`MODEL1`) for sources that show a narrow emission feature in the iron band.

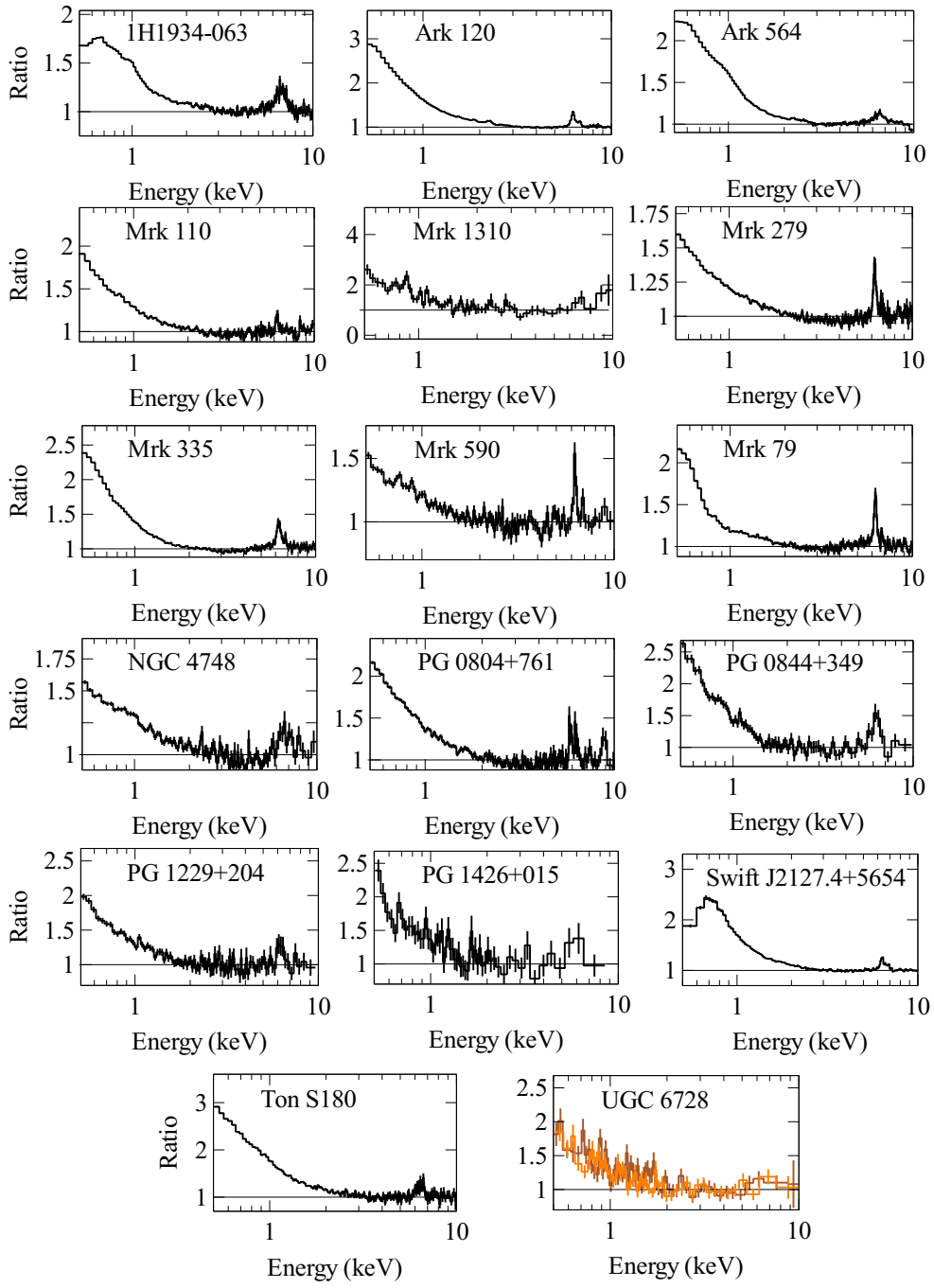

Fig. 6.3 Ratio plots for pn spectra fitted with Galactic-absorbed power-law models. MOS1 (orange) and MOS2 (brown) spectra are shown for UGC 6728 as its pn observation is dominated by flaring particle background.

- `tbabs * ( cflux * relxilld + cflux * powerlaw )` (MODEL2) for sources that show evidence for strong soft excess emission or/and a broad emission line feature in the iron band.
- `tbabs * ( cflux * relxilld + cflux * powerlaw + zgauss + zgauss)` (MODEL3) for sources that show complex ionised narrow emission lines in the iron band [e.g. Ark 120, 173, 210].
- `tbabs * ABSORBER * ( cflux * relxilld + cflux * powerlaw + cflux * xillver)` (MODEL4) for sources that show a thin warm absorber [e.g. Mrk 335, 160, 231] or little obscuration [e.g. Swift J2127.4+5654, 192]. ABSORBER stands for the model that accounts for absorptions. For example, `warmabs` is used to model warm absorber and `ztbabs` is used to model neutral obscuration.

6.3.2 OM Photometry and Mass Accretion Rate

The same method as in Raimundo et al. [245] is used to determine the BH mass accretion rate with *XMM-Newton* OM observations, assuming a simple disc model with a steady accretion rate $\dot{M}$ and isotropic emission. The mass accretion rate is given by the following equation:

$$\dot{M} = 1.53 \frac{\nu L_\nu}{10^{45}\cos(i)}^{3/2} \frac{10^8}{m_{\rm BH}} (M_\odot/{\rm yr}) \tag{6.1}$$

where L_ν is the luminosity in an optical band ν; i is the viewing angle, which is obtained in the disc reflection analysis in Section 6.3.1. As explained in Raimundo et al. [245], the lower energy band is less affected by the changes in BH spin. For this reason, we choose B band (4500Å) as the priority wavelength for the calculation, as in Raimundo et al. [245]. If a source has no observation in B band in the *XMM-Newton* archive, we choose the lowest energy band for calculation. Notice that L_ν used to calculate accretion rates has been corrected for Galactic extinction using the Galactic extinction curve calculated by Pei [233]. Table 6.3 presents the observed flux F_ν in the optical band named in the second column and corresponding mass accretion rate $\dot{m} = \dot{M}/\dot{M}_{\rm Edd}$, where $\dot{M}_{\rm Edd}$ is the Eddington accretion rate.

Note that we did not calculate the accretion rate by calculating the bolometric luminosity due to the large uncertainty of the bolometric conversion factor for the X-ray band flux [306] and the accretion efficiency in AGN [245].

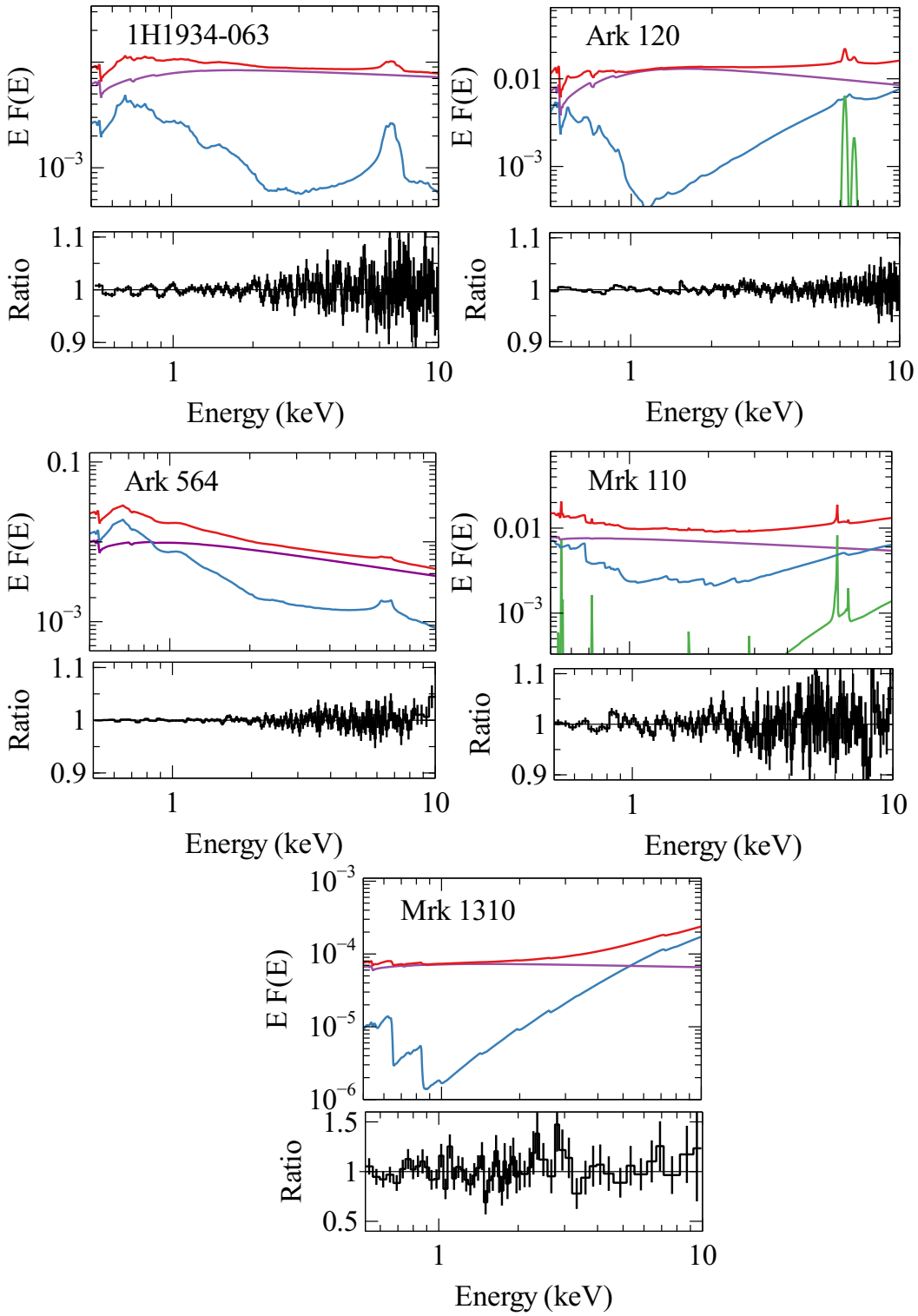

Fig. 6.4 The best-fit model and corresponding ratio plot for each source . Red: total model; blue: relativistic reflection model; green: distant reflector; purple: power-law shaped coronal emission.

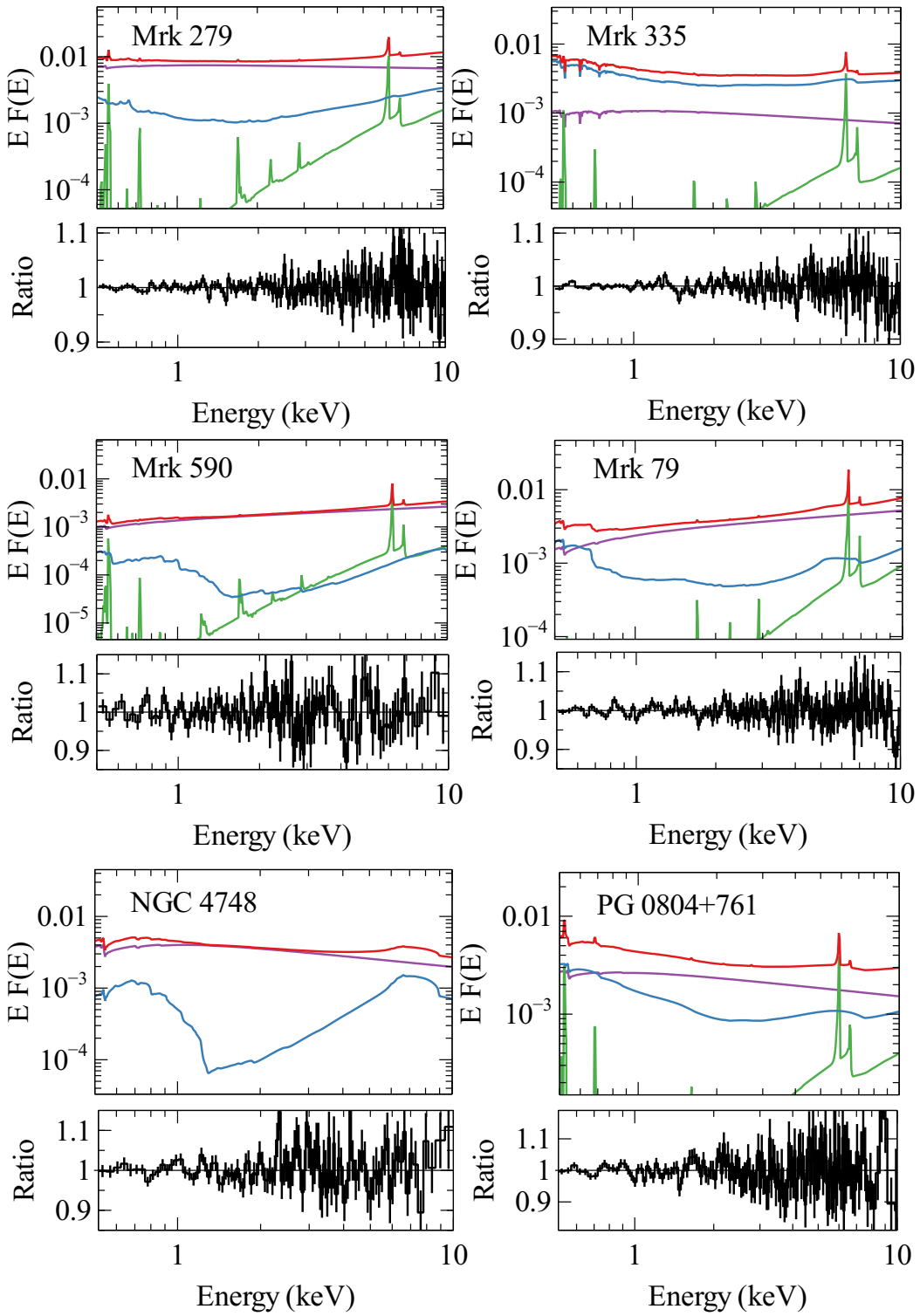

Fig. 6.5 Continued.

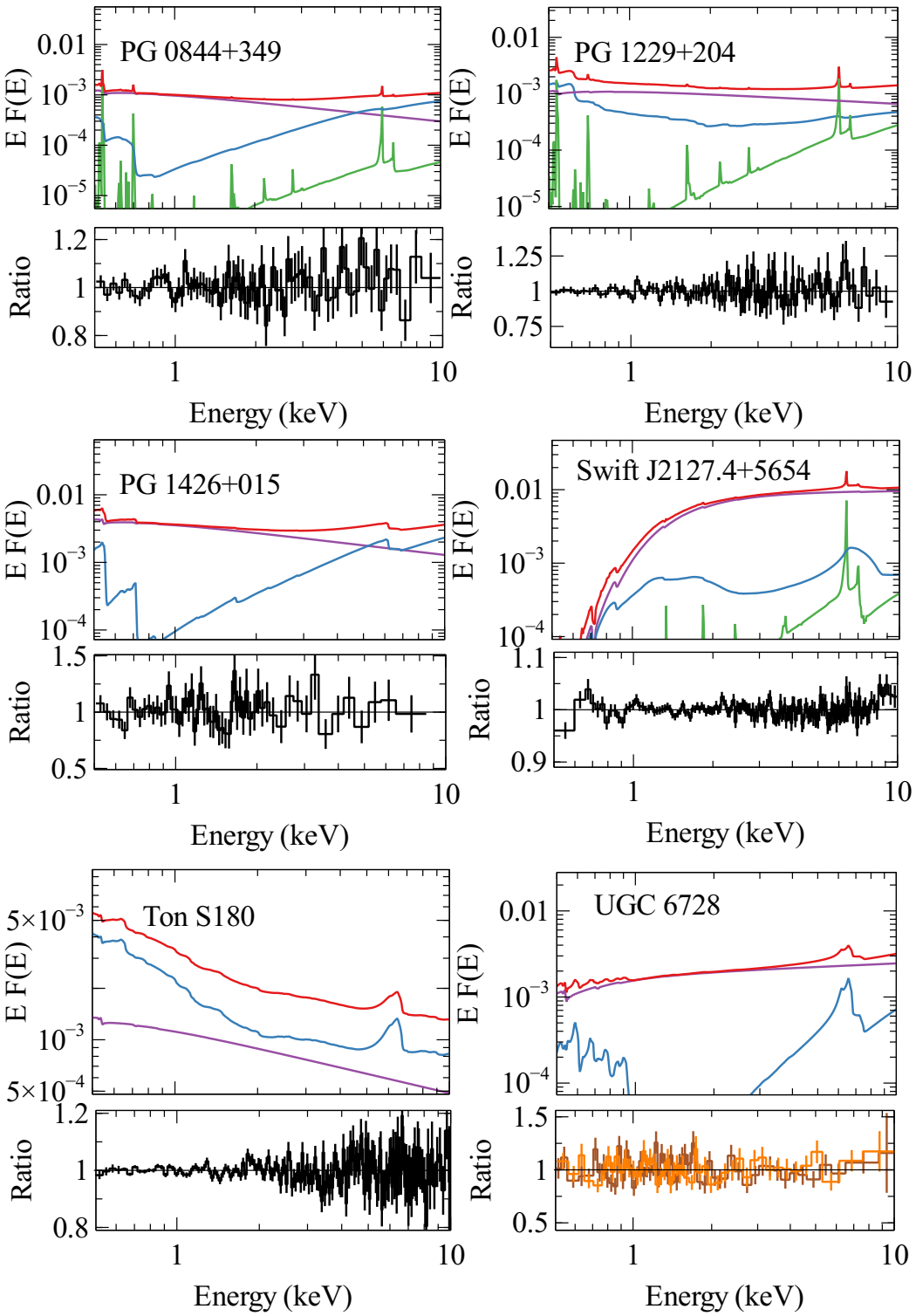

Fig. 6.6 Continued.

Table 6.3 The flux of each source in an optical band measured by performing photometry with *XMM-Newton* OM observations. F_ν is the observed flux in the unit of 10^{-16} erg s^{-1} cm^{-2} Å^{-1} in the band shown in the second column. The mass accretion rate $\dot{m}$ is in the unit of the Eddington accretion rate.

Name	Band	F_ν	$\dot{m}$
1H1934	U	59.8 ± 0.3	$1.1^{+2.3}_{-0.6}$
Ark 120	V	110.9 ± 0.7	$0.76^{+0.12}_{-0.08}$
Ark 564	UVW1	71.7 ± 0.6	$1.7^{+1.7}_{-1.1}$
Mrk 110	B	72.8 ± 0.4	$0.90^{+0.23}_{-0.19}$
Mrk 1310	U	14.88 ± 0.13	$0.6^{+0.14}_{-0.10}$
Mrk 279	U	144.6 ± 0.7	$0.75^{+0.27}_{-0.16}$
Mrk 335	B	88.3 ± 0.5	$0.74^{+0.08}_{-0.07}$
Mrk 590	B	50.7 ± 0.4	$0.31^{+0.06}_{-0.05}$
Mrk 79	B	52.0 ± 0.3	$0.13^{+0.05}_{-0.07}$
NGC 4748	U	81.5 ± 0.3	$2.2^{+1.2}_{-0.5}$
PG 0804	V	105.3 ± 0.3	$1.13^{+0.15}_{-0.12}$
PG 0844	B	65.7 ± 0.4	$1.20^{+1.0}_{-0.4}$
PG 1229	UVM2	69.9 ± 0.8	$0.5^{+0.4}_{-0.2}$
PG 1426	UVM2	302.9 ± 1.7	$0.28^{+0.13}_{-0.06}$
Swift J2127	B	2.43 ± 0.06	$1.0^{+0.5}_{-0.2}$
Ton S180	U	49.3 ± 0.5	6^{+12}_{-5}
UGC 6728	U	53.7 ± 0.4	$0.58^{+0.76}_{-0.21}$

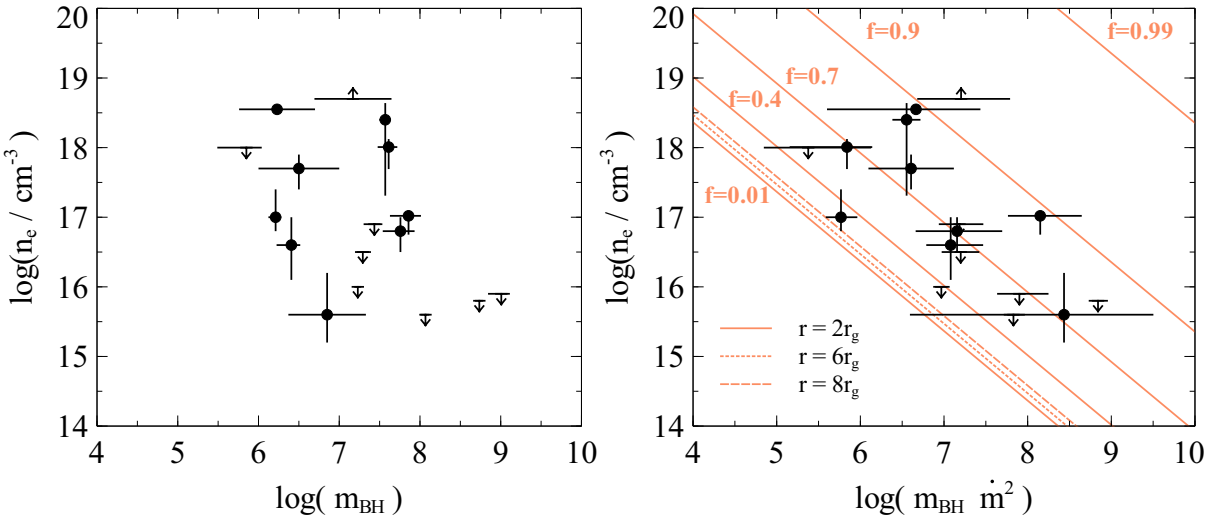

Fig. 6.7 Left: disc density $\log(n_{\rm e})$ versus BH mass $\log(m_{\rm BH})$. Only upper limits of disc density are obtained for black holes with $\log(m_{\rm BH}) > 8$, indicating a lower disc density in high-$m_{\rm BH}$ AGN. Right: disc density $\log(n_{\rm e})$ versus $\log(m_{\rm BH}\dot{m}^2)$. The solid orange lines are the solutions for disc density at $r = 2\,r_{\rm g}$ for different fraction (f) of disc energy that is transferred to the coronal region [288]. The inner radius is assumed to be at $R_{\rm ISCO}$ of a maximally spinning BH ($R_{\rm in} = 1r_{\rm g}$). The dotted and dashed straight lines are for r =6, 8 $r_{\rm g}$.

6.4 Individual Spectral Analysis Details

6.4.1 1H 1934−603

1H 1934−603 is a narrow-line Seyfert 1 galaxy [NLS1, 202] that shows fast variability in the X-ray band. Previously by analysing the archival *XMM-Newton* and *NuSTAR* observations of 1H 1934−603, Frederick et al. [73] discovered that the disc reflection component lags behind the coronal power-law continuum by ≈ 20 s. By conducting a novel spectral analysis using a fixed disc density reflection model, a super solar iron abundance ($Z_{\rm Fe} > 9Z_{\odot}$) is required for the reflection spectral modelling [73].

A ratio plot for an averaged EPIC-pn spectrum of 1H 1934−603 against an absorbed power-law model is shown in Figure 6.3. A broad emission line feature is visible in the iron band. By fitting the emission line with a simple Gaussian line model zgauss, we obtain a best-fit rest-frame line energy at $E_{\rm line} = 6.65 \pm 0.05$ keV with $\sigma = 0.49^{+0.08}_{-0.07}$ keV. The equivalent width (EW) of the emission line is 264^{+8}_{-7} eV. Small residuals are visible at 5 keV when the line feature is modelled by a simple Gaussian line model, requiring a more physical modelling for the broad emission line (e.g. relativistic disc line). No obvious narrow line component has been found.

Table 6.4 Best-fit parameters for each source.

Name	q_1	q_2	$R_{\rm r}$	a_*	i (deg)	$\log(\xi)$	$Z_{\rm Fe}$	$\log(n_{\rm e})$	Γ
1H1934	$1.9^{+1.2}_{-0.3}$	-	-	> 0.45	44^{+4}_{-3}	2.79 ± 0.02	$5.9^{+0.6}_{-1.4}$	$17.7^{+0.2}_{-0.3}$	2.106 ± 0.005
Ark 120	> 8	$1.7^{+2.1}_{-0.2}$	< 4	> 0.85	67^{+4}_{-5}	$0.33^{+0.05}_{-0.04}$	$0.7^{+1.0}_{-0.2}$	< 15.6	$2.284^{+0.010}_{-0.006}$
Ark 564	$5.62^{+0.8}_{-0.7}$	$0.8^{+0.4}_{-0.3}$	14^{+7}_{-5}	> 0.9	57^{+4}_{-3}	2.723 ± 0.003	$3.4^{+0.2}_{-0.4}$	18.55 ± 0.07	$2.496^{+0.003}_{-0.002}$
Mrk 110	8 ± 2	3 ± 2	$4.3^{+1.2}_{-0.2}$	$0.994^{+0.002}_{-0.008}$	35^{+3}_{-4}	$2.08^{+0.07}_{-0.31}$	$0.7^{+0.5}_{-0.2}$	< 16.5	$2.15^{+0.04}_{-0.02}$
Mrk 1310	3 (f)	-	-	0.998 (f)	36^{+12}_{-8}	< 0.35	< 2.7	$17.0^{+0.4}_{-0.2}$	$2.08^{+0.12}_{-0.10}$
Mrk 279	> 8.5	$4^{+0.5}_{-1.2}$	$3.1^{+1.2}_{-0.2}$	> 0.95	37^{+8}_{-17}	$2.29^{+0.19}_{-0.41}$	0.9 ± 0.2	< 16.9	$2.064^{+0.038}_{-0.017}$
Mrk 335	$8.0^{+1.8}_{-0.4}$	$3.5^{+0.2}_{-0.4}$	$2.80^{+0.20}_{-0.12}$	> 0.988	33^{+4}_{-5}	$3.00^{+0.02}_{-0.04}$	$2.3^{+0.4}_{-0.6}$	< 16.0	2.225 ± 0.002
Mrk 590	6^{+3}_{-4}	2 ± 2	4^{+7}_{-2}	> 0.1	79^{+7}_{-4}	$1.4^{+0.5}_{-0.3}$	$1.7^{+1.5}_{-1.2}$	$18.4^{+0.2}_{-1.1}$	$1.74^{+0.08}_{-0.07}$
Mrk 79	$7.8^{+2.1}_{-2.3}$	$3.0^{+0.6}_{-0.4}$	9^{+12}_{-6}	> 0.5	21 ± 6	$2.5^{+0.3}_{-0.2}$	1.6 ± 0.5	$18.01^{+0.12}_{-0.32}$	$1.712^{+0.014}_{-0.012}$
NGC 4748	> 5	2 ± 2	< 4.2	> 0.8	62^{+2}_{-6}	$1.0^{+0.2}_{-0.3}$	$3.9^{+2.4}_{-0.3}$	$16.6^{+0.4}_{-0.5}$	$2.38^{+0.02}_{-0.03}$
PG 0804	$8.2^{+1.0}_{-2.3}$	3 ± 2	< 4.2	> 0.94	65^{+14}_{-9}	$2.98^{+0.04}_{-0.19}$	$0.91^{+0.68}_{-0.09}$	< 15.8	2.26 ± 0.03
PG 0844	3^{+3}_{-2}	2 ± 2	< 60	> 0.95	32^{+12}_{-15}	< 0.06	$1.4^{+0.6}_{-0.2}$	$17.02^{+0.06}_{-0.27}$	$2.54^{+0.03}_{-0.05}$
PG 1229	> 6	$4^{+1.5}_{-2.0}$	5^{+2}_{-3}	$0.93^{+0.06}_{-0.02}$	22^{+18}_{-10}	$2.3^{+0.7}_{-0.9}$	< 1.5	$16.8^{+0.2}_{-0.3}$	$2.24^{+0.13}_{-0.08}$
PG 1426	3 (f)	-	-	0.998 (f)	30 (f)	$3.0^{+0.4}_{-0.5}$	$1.3^{+1.2}_{-0.3}$	< 15.9	$2.03^{+0.11}_{-0.14}$
Swift J2127	> 6	$2.2^{+0.4}_{-1.2}$	3^{+2}_{-1}	$0.72^{+0.14}_{-0.20}$	67^{+3}_{-2}	2.32 ± 0.02	$2.0^{+1.2}_{-1.3}$	> 18.7	1.953 ± 0.008
Ton S180	> 8	$2.5^{+0.6}_{-0.4}$	$3.5^{+0.8}_{-0.6}$	> 0.98	36^{+4}_{-6}	$3.32^{+0.10}_{-0.12}$	3 ± 2	$15.6^{+0.3}_{-0.2}$	$2.377^{+0.015}_{-0.020}$
UGC 6728	$2.4^{+3.0}_{-0.2}$	-	-	0.998 (f)	17^{+20}_{-8}	$2.7^{+0.2}_{-0.3}$	$2.5^{+1.2}_{-0.8}$	< 18	$1.86^{+0.08}_{-0.04}$

Table 6.5 Continue after Table 6.4. The flux of each model component is calculated between 0.5–10 keV by using the convolution model `cflux` in XSPEC in the unit of erg cm^{-2} s^{-1}. The reflection fraction is defined as $F_{\rm refl}/F_{\rm pl}$ for simplicity.

Name	$\log(F_{\rm refl})$	$\log(F_{\rm pl})$	$\log(F_{\rm dis})$	$f_{\rm refl}$	C-stat/ν
1H1934	-11.02 ± 0.03	-10.387 ± 0.004	-	$0.232^{+0.017}_{-0.016}$	242.35/180
Ark 120	$-10.745^{+0.007}_{-0.008}$	$-10.1853^{+0.0019}_{-0.0007}$	-	0.276 ± 0.005	288.61/168
Ark 564	$-10.548^{+0.013}_{-0.008}$	$-10.383^{+0.005}_{-0.009}$	-	$0.68^{+0.03}_{-0.02}$	191.32/180
Mrk 110	-10.74 ± 0.02	$-10.480^{+0.004}_{-0.003}$	$-11.75^{+0.08}_{-0.12}$	0.55 ± 0.03	205.35/161
Mrk 1310	$-12.75^{+0.11}_{-0.10}$	-12.46 ± 0.03	-	$0.51^{+0.17}_{-0.11}$	109.90/94
Mrk 279	$-11.10^{+0.02}_{-0.03}$	$-10.450^{+0.008}_{-0.017}$	$-11.64^{+0.06}_{-0.07}$	$0.225^{+0.013}_{-0.017}$	155.59/177
Mrk 335	-10.78 ± 0.02	$-11.30^{+0.10}_{-0.08}$	$-12.40^{+0.03}_{-0.02}$	$3.3^{+0.4}_{-0.6}$	251.39/169
Mrk 590	$-12.11^{+0.10}_{-0.12}$	$-11.050^{+0.005}_{-0.010}$	-12.31 ± 0.10	0.08 ± 0.02	187.41/174
Mrk 79	-11.32 ± 0.03	-11.93 ± 0.07	-10.775 ± 0.012	0.28 ± 0.02	225.60/177
NGC 4748	-11.48 ± 0.02	$-10.750^{+0.012}_{-0.013}$	-	$0.186^{+0.011}_{-0.010}$	152.66/144
PG 0804	-11.06 ± 0.02	$-11.0042^{+0.0012}_{-0.0008}$	$-12.07^{+0.10}_{-0.11}$	0.88 ± 0.04	226.26/173
PG 0844	$-11.95^{+0.03}_{-0.02}$	$-11.432^{+0.004}_{-0.006}$	$-12.96^{+0.15}_{-0.12}$	$0.306^{+0.023}_{-0.014}$	163.0/129
PG 1229	$-11.71^{+0.08}_{-0.12}$	$-11.34^{+0.03}_{-0.02}$	$-12.4^{+0.2}_{-0.3}$	0.43 ± 0.10	111.08/128
PG 1426	$-11.39^{+0.10}_{-0.17}$	$-10.87^{+0.03}_{-0.02}$	-	$0.30^{+0.09}_{-0.10}$	53.43/52
Swift J2127	$-11.03^{+0.02}_{-0.05}$	$-10.365^{+0.003}_{-0.004}$	$-11.94^{+0.07}_{-0.18}$	$0.217^{+0.013}_{-0.022}$	246.21/182
Ton S180	$-11.09^{+0.08}_{-0.10}$	$-11.36^{+0.14}_{-0.20}$	-	1.9 ± 0.7	301.71/179
UGC 6728	$-11.87^{+0.08}_{-0.14}$	$-11.013^{+0.012}_{-0.013}$	-	$0.14^{+0.03}_{-0.04}$	254.61/209

Based on the spectral analysis in the iron band, we then model the broad band spectrum with MODEL2. MODEL2 can provide a very good fit with C-Stat/ν=242.35/180. The best-fit model and corresponding ratio plot are shown in Figure 6.4. No structural residuals are found in the ratio plot. A disc density of $\log(n_{\rm e}) = 17.7^{+0.2}_{-0.3}$ is required with a disc iron abundance of $Z_{\rm Fe}/Z_{\odot} = 5.9^{+0.6}_{-1.4}$. The iron abundance obtained with the disc density as a free parameter is much lower than the value obtained in previous analysis [73]. We obtain a lower limit of the BH spin $a_* > 0.4$, which is higher than the previous analysis [$a_* < 0.1$, 73]. Note that the previous analysis in Frederick et al. [73] models the soft excess emission with an additional blackbody model and assumes a fixed disc density at $\log(n_{\rm e}) = 15$. In this work, we model both the soft excess emission and the broad iron emission line with only one disc reflection model by allowing the disc density to be a free parameter.

6.4.2 Ark 120

Ark 120 is a nearby Seyert 1 galaxy [e.g. 220] that is well-studied in the X-ray band. This source shows little or no evidence for X-ray absorption [e.g. 246]. Previous spectral analysis of Ark 120 shows evidence for three line components in the iron band [210]. Two of the three line components are narrow emission lines, corresponding to a neutral Fe Kα emission line and an ionized Fe Kα emission line. The third line component is broader with FWHM$\approx$ $5000\,{\rm km\,s^{-1}}$.

A ratio plot for an averaged EPIC-pn spectrum of Ark 120 against an absorbed power-law model is shown in Figure 6.3. A combination of narrow emission lines and a broad emission line is shown in the iron band. The line shapes are similar to these found in Nardini et al. [210]. By fitting the line features with three Gaussian line model zgauss, we obtain two of the three line components are at $6.43^{+0.05}_{-0.02}$ keV (EW=38^{+42}_{-12} eV) and $7.03^{+0.03}_{-0.02}$ keV (EW=27^{+20}_{-12} eV). The best-fit line widths for these two line components are < 0.01 keV and $0.06^{+0.04}_{-0.05}$ keV correspondingly. The 6.43 keV emission line can be interpreted as the neutral Fe Kα emission line and the other line can be interpreted as the hydrogenic iron. The third line component is located at $6.49^{+0.05}_{-0.02}$ keV (EW=100^{+14}_{-13}). The width of the line is $0.30^{+0.06}_{-0.05}$ keV, indicating a broad emission line from the inner disc region.

Based on the existence of both a neutral and ionized narrow iron emission lines, we model the broad band spectrum with MODEL3. MODEL3 can provide a good fit with C-stat/ν=288.61/168. The best-fit model and corresponding ratio plot are shown in Figure 6.4. Only an upper limit of the disc density is found $\log(n_{\rm e}) < 15.6$. A solar iron abundance is required for the spectral modelling. A fixed spin $a_* = 0$ and a fixed viewing angle $i = 30^{\circ}$ are assumed in Nardini et al. [210]. In contrast, we obtain a high black hole spin $a_* > 0.85$ and a high viewing angle $i = 67^{+4}_{-5}{}^{\circ}$, which are consistent with previous reflection-based

analysis of *Suzaku* observations of the same source [e.g. $a_* \approx 0.81$, $i \approx 54°$, 314] and other spin measurement methods [e.g. 240].

6.4.3 Ark 564

Ark 564 is a very variable NLS1 in the X-ray band. Detailed studies of its X-ray reverberation lags with *XMM-Newton* observations have been done in previous analyses [e.g. 135]. A high iron abundance ($Z_{\rm Fe}/Z_{\odot} \approx 3$) was obtained by analysing the simultaneous *Suzaku* and *NuSTAR* spectra above 1 keV [137].

We present a broad band spectral analysis of the averaged EPIC-pn spectrum of Ark 564 with a total net pn exposure of 402 ks. A ratio plot against an absorbed power-law model is shown in Figure 6.3. A very strong emission line feature is shown in the iron band and a very strong soft excess is shown below 3 keV. Fitting the emission line in the iron band with `zgauss` offers a good fit with some remaining residuals at 5.5 keV, requiring more physical modelling (e.g. relativistic disc reflection model). The central energy of the line is at $E_{\rm line} = 6.59^{+0.06}_{-0.07}$ keV in the source frame with a line width of $\sigma = 0.44^{+0.09}_{-0.08}$ keV. The equivalent width of the best-fit line model is 120^{+12}_{-8} eV. No obvious narrow emission line feature at 6.4 keV is found in the iron band.

We fit the full band spectrum with `MODEL2` due to the lack of evidence for narrow emission lines in the iron band. `MODEL2` offers a very good fit for the averaged EPIC-pn spectrum of Ark 564 with C-stat/ν=191.32/180. The best-fit model and corresponding ratio plot are shown in Figure 6.4. A close-to-solar iron abundance is obtained and a very high disc density of $\log(n_{\rm e}) = 18.55 \pm 0.07$ is required for the spectral fitting. No additional component is required to model the soft excess. A high BH spin of $a_* > 0.9$ is found, similar to the previous analysis by analysing *Suzaku* observations of the same source [$a_* \approx 0.96$, 314]. The BH spin parameter was however not constrained in Kara et al. [137]. An inclination angle of $i = 57^{+4\circ}_{-3}$ is obtained, which is consistent with the results in Walton et al. [314] and Kara et al. [137].

6.4.4 Mrk 110

Mrk 110 is a NLS1 [309] and has been observed by *XMM-Newton* once for a net pn exposure of 33 ks. Boller et al. [24] shows a complete analysis of the RGS and EPIC spectra. Only a narrow Fe K emission line was found previously.

By fitting the EPIC-pn spectrum of the only *XMM-Newton* observation of Mrk 110, we confirm that only a narrow emission line is shown in the iron band. A ratio plot of the EPIC-pn spectrum fitted with an absorbed power-law model is shown in Fig. 6.3. By using

a simple Gaussian line model zgauss, we obtain the best-fit line width of $\sigma < 0.127$ keV and the best-fit line energy of $E_{\rm line} = 6.44 \pm 0.04$ keV for this narrow emission line. The equivalent width of the line component is 51^{+13}_{-22} eV. The narrow emission line is at 6.44 keV and can be interpreted as the neutral Fe Kα emission line.

Based on the narrow neutral Fe Kα emission line in the iron band, we model the broad band spectrum with MODEL1. MODEL1 offers a very good fit with C-stat/ν=205.35/161. The best-fit model and corresponding ratio plot are shown in Fig. 6.4. The relativistic disc reflection model accounts for mainly the soft excess below 2 keV. The lack of the broad Fe Kα emission line in the iron band might be due to the extremely blurred reflection component, as seen in our modelling. Only an upper limit of the disc density ($\log(n_{\rm e}) < 16.5$) is found.

6.4.5 Mrk 1310

Mrk 1310 is a Seyfert 1 galaxy [309] and has only one *XMM-Newton* observation with a net pn exposure of 35 ks. The iron band does not show strong evidence for emission features. A power-law model can offer a very good fit for the spectra between 3–10 keV with C-stat/ν=52.02/46. By adding an additional line model zgauss with the line energy fixed at 6.4 keV, the fit can be improved by ΔC-stat=4 with 2 more free parameters. The equivalent width of the line component is < 20 eV. In the soft band, Mrk 1310 however shows a strong soft excess, as in other AGN in our sample.

We model the broad band spectrum of Mrk 1310 with MODEL2. MODEL2 offers a very good fit with C-stat/$\nu = 109.90/94$. The best-fit model and corresponding ratio plot are shown in Figure 6.4. The high density disc reflection component accounts for the soft excess emission. However, due to the lack of a broad Fe Kα emission line, we are unable to constrain the disc emissivity profile and the spin of the BH. We assume the emissivity index in a flat spacetime ($q_1 = q_2 = 3$) and a maximum spin parameter. The best-fit parameters are shown in Table 6.4. By modelling the soft excess emission with high density disc reflection model, a high disc density of $\log(n_{\rm e}) = 17^{+0.4}_{-0.2}$ is required.

6.4.6 Mrk 279

Previous analysis of the long *XMM-Newton* observations of the Seyfert 1 galaxy Mrk 279 [309] in 2005 by Costantini et al. [44] shows very complex emission features in the iron band, indicating both a broad Fe Kα emission line from the disc and a narrow Fe XXVI line potentially from the outer layer of the torus.

A ratio plot of the stacked pn spectrum of Mrk 279 fitted with an absorbed power law is shown in Fig. 6.3. The iron band of the spectrum shows two narrow emission features and

a broad line component. By modelling the line features with multiple zgauss models, we obtained a very good fit in the 3–10 keV band. Three zgauss models are required: a broad line at $6.6^{+0.5}_{-0.3}$ keV (EW=50^{+22}_{-13} eV, $\sigma = 0.38^{+0.12}_{-0.08}$eV); a narrow line at $6.41^{+0.02}_{-0.04}$ keV (EW=85^{+14}_{-12} eV, $\sigma < 0.02$eV); a second narrow line at $6.98^{+0.06}_{-0.12}$ keV (EW=<22 eV, $\sigma < 0.02$eV). The second narrow line at 6.98 keV is consistent with previous analysis by Costantini et al. [44]. However, the line feature is too weak to be constrained with an unconstrained equivalent width and a small statistical improvement when the line model is added to the fit (ΔC-stat=3 with three more parameters).

Based on the indication of the iron band, we model the broad band spectrum of Mrk 279 with MODEL1. MODEL1 offers a very good fit with C-stat/$\nu = 155.59/177$. The best-fit model is shown in Fig. 6.5. The relativistic disc reflection model accounts for both the soft excess and the broad Fe Kα emission line in Mrk 279 A high BH spin of $a_* > 0.95$ is required for the spectral modelling and only an upper limit of the disc density $\log(n_{\rm e}) < 16.9$ is achieved. We obtain a disc viewing angle of $i = 37^{+8}_{-17}{}^{\circ}$, which is consistent with previous analysis [$i < 30^{\circ}$, 44].

6.4.7 Mrk 335

Mrk 335 is a NLS1 [309] that has been well studied in the X-ray band. This source experienced several extremely low flux states in history [e.g. 98, 231]. Grupe et al. [99] found that the complex spectral variability can be explained by a variable disc reflection component. Parker et al. [231] and Gallo et al. [81] explain the low flux state spectrum of Mrk 335 with a reflection-dominated emission from the inner disc region. The spectral variability is due to strong light-bending effects in the vicinity of the central BH. The strongest supporting evidence for the reflection interpretation of the spectrum of Mrk 335 is the discovery of the reverberation lag between the reflected disc photons and the coronal continuum photons [135].

We first fit the stacked spectrum of Mrk 335 with an absorbed power-law model and the ratio plot is shown in Fig. 6.3. The ratio plot shows a strong broad Fe Kα emission line feature and a strong soft excess below 2 keV. The result is similar to Parker et al. [231]. By following the indication in Parker et al. [231], we model the broad band spectrum with MODEL4. MODEL4 offers a very good fit with C-stat/$\nu = 251.39/169$. The best-fit model and corresponding ratio plot are shown in Figure 6.5. One thin warm absorber modelled by warmabs with $N_{\rm H} = 2.45^{+0.39}_{-0.17} \times 10^{20}$ cm^{-2} and $\log(\xi) = 1.38 \pm 0.02$ is found. We obtain a very high reflection fraction $f_{\rm refl} = 3.3^{+0.4}_{-0.6}$, indicating a reflection-dominated scenario, similar with previous analysis [e.g. 231]. By fitting the broad Fe Kα emission line and the soft excess with the same reflection model, we obtain a very steep disc emissivity profile (see Table 6.4 for best-fit parameters). The large inner emissivity index q_1 and the low broken

radius $R_{\rm r}$ indicate a very compact coronal region [e.g. <3$r_{\rm g}$, 231]. Only an upper limit of the disc density $\log(n_{\rm e}) < 16.0$ is achieved. We find a very BH spin of $a_* > 0.988$ and a small inclination angle of $i = 33^{+4}_{-5}$, which are consistent with previous analysis of *NuSTAR* observations of the same source[e.g. $a_* \approx 0.99$, $i \approx 25°$, 231]. Our best-fit inclination angle is however lower than the value measured using *Suzaku* observations [e.g. $i \approx 50 - 58°$, 314, 81].

6.4.8 Mrk 590

Mrk 590 is a Seyfert 1 galaxy [309]. Previous analysis of the quasi-simultaneous *XMM-Newton* and *Chandra* observations in 2004 shows evidence for a strong soft excess and narrow Fe Kα, Fe XXV and Fe XXVI emissions [159].

We first fit the 3–10 keV band spectrum with an absorbed power-law model and the ratio plot is shown in Fig.6.3. By fitting the narrow lines features with simple zgauss models, Two narrow line models are required, one line at 6.407 ± 0.02 keV (EW=135^{+12}_{-23} eV, $\sigma < 0.06$ keV) and the other line at $7.04^{+0.06}_{-0.10}$ keV (EW=46^{+23}_{-35}, $\sigma < 0.12$ keV). The former line can be interpreted as Fe Kα emission line and the latter can be interpreted as Fe XXVI line. We do not find strong evidence for a narrow Fe XXV emission line as in Longinotti et al. [159] or a broad emission feature.

Based on the analysis of the iron band, we model the broad band spectrum of Mrk 590 with MODEL1. MODEL1 can provide a very good fit with C-stat/ν=187.41/174. The best-fit model and corresponding ratio plot are shown in Figure 6.5. The disc reflection component with a very high disc density of $\log(n_{\rm e}) = 18.4^{+0.2}_{-1.1}$ accounts for the soft excess, as shown in Fig. 6.5. We obtain a lower limit of the BH spin of $a_* > 0.1$ and a high inclination angle of $i = 79^{+7}_{-4}°$.

6.4.9 Mrk 79

Mrk 79 is a Seyfert 1 galaxy [309] that shows very large X-ray flux variability by a factor of 10 in multi-epoch observations [80]. The spectrum of Mrk 79 shows a variable soft excess and strong narrow emission line features in the iron band.

We stack all the EPIC-pn spectra in the archive and find two narrow emission lines in the iron band. The first line is at 6.27 ± 0.02 keV (EW=173^{+32}_{-14} eV, $\sigma = 0.086^{+0.019}_{-0.020}$ keV) and the second line is at 6.83 ± 0.05 keV (EW=30^{+22}_{-13} eV, $\sigma < 0.08$ keV), corresponding to Fe Kα and Fe Kβ line.

Based on the analysis of the iron band, we model the broad band spectrum of Mrk 79 with MODEL1. MODEL1 offers a very good fit with C-stat/ν=225.60/177. The best-fit model is shown in Fig. 6.5. Mrk 79 has the hardest continuum emission in our sample with $\Gamma = 1.712^{+0.014}_{-0.012}$.

According to our calculation of the mass accretion rate using B band flux, Mrk 79 indeed has the lowest accretion rate in our sample ($\dot{m} = 0.13^{+0.05}_{-0.07}$). A high disc density of $\log(n_{\rm e}) = 18.01^{+0.12}_{-0.32}$ is required by our spectral modelling. We obtain a BH spin of $a_* > 0.5$ and an inclination angle of $i = 21 \pm 6°$, which is consistent with previous analyses [$a_* \approx 0.7$, $i \approx 21°$, 78].

6.4.10 NGC 4748

NGC 4748 is a NLS1 [309] that is not well studied in the X-ray band. Only one *XMM-Newton* observation with a net pn exposure of 26 ks is available in the archive.

The spectrum of NGC 4748 in the iron band shows a broad emission feature. See Fig. 6.3 for a ratio plot of the spectrum of NGC 4748 fitted by an absorbed power-law model. By fitting the line model with one zgauss model, the line width of the emission line is $\sigma = 0.7^{+0.6}_{-0.3}$ keV and the line is at $6.7^{+0.3}_{-0.2}$ keV. The equivalent width of the line is 373^{+42}_{-17} eV. This strong, broad 6.7 keV emission line can be interpreted as the relativistic disc Fe K emission line. A simple zgauss modelling of the line feature leaves some residuals between 7–8 keV. No significant evidence for a narrow core is found.

Based on the evidence for a broad iron emission line feature and a soft excess, we model the broad band spectrum with MODEL2. MODEL2 offers a very good fit with C-stat/ν=152.66/144. Fig. 6.5 shows the best-fit model and the corresponding ratio plot. One relativistic reflection model is able to model both the soft excess mission and the broad iron line feature. An intermediate disc density is required $\log(n_{\rm e}) = 16.6^{+0.4}_{-0.5}$. A high BH spin of $a_* > 0.8$ is preferred by our model.

6.4.11 PG 0804+761

PG 0804+761 is a Seyfert 1 galaxy [309] and has three *XMM-Newton* observations in the archive. The first observation in 2000 (obsID 0102040401) was entirely dominated by flaring particle background. The other two observations were taken in 2010 and have a total net pn exposure of 32 ks. By fitting the stacked pn spectrum of PG 0804+761 with an absorbed power-law model, two strong emission lines are shown in the iron band. A strong soft excess is found below 2 keV. See Fig. 6.3 for the ratio plot. We first model the line features with simple zgauss models. The line width of both emission line is $\sigma < 0.08$ keV, indicating two narrow lines from distant reflector. The first line is at 6.44 ± 0.04 keV (EW=99^{+35}_{-17} eV) and the second line is at $6.88^{+0.06}_{-0.07}$ keV (EW=91^{+13}_{-24} eV). These two lines can be interpreted as Fe Kα and Fe XXVI lines. The spectrum shows no evidence for a broad line component.

Based on the evidence for only narrow Fe K emission lines, we model the broad band spectrum with MODEL1. MODEL1 can offer a very good fit with C-stat/ν=226.26/173. The relativistic disc reflection model accounts for the soft excess. See Fig. 6.5 for the best-fit model and corresponding ratio plot. Only an upper limit of the disc density $\log(n_{\rm e}) < 15.8$ is found.

6.4.12 PG 0844+349

PG 0844+349 is a Seyfert 1 galaxy [309] that has shown a large flux variability of a factor of 10 in history. Gallo et al. [80] analysed the *XMM-Newton* observation taken during the X-ray weak state of PG 0844+349 and found the spectrum is dominated by the disc reflection component, indicating strong light-bending effects.

We first fit the spectrum with an absorbed power-law model and the ratio plot is shown in Fig. 6.3. By fitting the emission features with two simple zgauss models, we obtain a broad line component at 6.6 ± 0.2 keV (EW=349^{+32}_{-24} eV, $\sigma = 0.31^{+0.26}_{-0.13}$ keV) and a narrow core at 6.4 keV (EW<42 eV, $\sigma < 0.05$ keV). Both two line components are consistent with the results in Gallo et al. [80]. However only an upper limit of the equivalent width of the second line is obtained due to a short net exposure of only 18 ks.

Based on the analysis in the iron band, we model the broad band spectrum with MODEL1. MODEL1 can offer a very good fit with C-stat/ν=163.0/129. Fig. 6.6 presents the best-fit MODEL1 for PG 0844+349. A disc reflection component with a high disc density parameter of $\log(n_{\rm e}) = 17.2^{+0.06}_{-0.27}$ can account for both the broad iron line and the soft excess emission. We obtain a high BH spin of $a_* > 0.95$ and an inclination angle of $i = 32^{+12\circ}_{-15}$. The inclination angle is consistent with the measurement in Gallo et al. [80, $i \approx 34^\circ$].

6.4.13 PG 1229+204

PG 1229+204 is a Seyfert 1 galaxy [309] and has only one *XMM-Newton* observation with a net pn exposure of only 17 ks. Fig. 6.3 shows a ratio plot of the EPIC-pn spectrum of PG 1229+204 against an absorbed power-law model. The spectrum shows a strong soft excess below 2 keV and an emission feature in the iron band. By fitting the emission line with one zgauss model, we find that the line central energy is $6.59^{+0.15}_{-0.14}$ keV and the line width is $\sigma = 0.23^{+0.22}_{-0.11}$ keV. The line feature is very strong with an equivalent width of EW=209^{+23}_{-14} eV. The short exposure of this observation does not allow us to distinguish a mildly broad emission feature or a combination of several emission lines (e.g. Fe Kα, Fe Kβ).

Because of the uncertainty of the nature of the emission feature in the iron band, we first fit the broad band spectrum with MODEL2 to check if the relativistic disc reflection model

is able to model both the soft excess emission and the emission feature in the iron band. MODEL2 can offer a good fit with C-stat/ν=122.23/129. However there are still residuals in the iron band indicating that the emission feature can not be modelled with a relativistic disc reflection model. Second, we fit the spectrum with MODEL1, including a distant neutral reflector. MODEL1 is able to improve the fit by ΔC-stat=11 with one more parameter with no structural residuals in the iron band. The best-fit model and the corresponding ratio plot are shown in Fig. 6.6. The relativistic disc reflection component with a modest disc density of $\log(n_{\rm e}) = 16.8^{+0.2}_{-0.3}$ accounts for the soft excess emission. We obtain a high BH spin of $a_* = 0.93^{+0.06}_{-0.02}$ and an inclination angle of $i = 22^{+18\circ}_{-10}$.

6.4.14 PG 1426+015

PG 1426+015 is a Seyfert 1 galaxy [309] and shows a blackbody-like soft excess emission [e.g. kT≈ 0.1 keV, 222]. Fig. 6.3 presents a ratio plot of PG 1426+015 EPIC-pn spectrum fitted with an absorbed power-law model. The spectrum shows evidence for weak emission feature in the iron band and a strong soft excess emission. By fitting the emission feature of a zgauss model with a fixed line energy at 6.4 keV, we obtain an upper limit of the line width $\sigma < 0.40$ keV. Although the spectrum shows tentative evidence for a broad emission feature, the short exposure of the observation does not allow us to better constrain the line shape.

We model the broad band spectrum of PG 1426+015 with MODEL2. MODEL2 offers a very good fit with C-stat/ν=53.43/52. The best-fit model and corresponding ratio plot are shown in Figure 6.6. The emissivity profile, the BH spin and the viewing angle are not constrained during our fit due to the short exposure. Therefore we fix the emissivity index at $q_1 = q_2 = 3$, a maximum BH spin, and a viewing angle of $i = 30^\circ$. We only obtain an upper limit of the disc density $\log(n_{\rm e}) < 15.9$.

6.4.15 Swift J2127.4+5654

Swift J2127.4+5654 is a Seyfert 1 galaxy [309] that has been well studied in the X-ray band. Miniutti et al. [192] analysed the *Suzaku* observations of this source and obtained a BH spin of $a_* = 0.6 \pm 0.2$. This result has been confirmed by Marinucci et al. [165] as well where *XMM-Newton* observations are considered. A combination of broad Fe Kα emission line and a narrow core is found in the iron band. The *Suzaku* spectrum of Swift J2127.4+5654 shows a blackbody-shaped soft excess Miniutti et al. [192]. Kara et al. [136] analysed the *NuSTAR* and found a reverberation lag of both the iron line and the Compton hump, supporting the disc reflection interpretation of the broad band spectrum of this source.

By following the indication of Marinucci et al. [165], we model the broad band spectrum with MODEL4. An additional neutral absorber is required and the model ztbabs is used for this purpose. The redshift parameter of ztbabs is fixed at the value of the source. The best-fit column density of this neutral absorber is $N_{\rm H} = (8.03 \pm 0.10) \times 10^{21} {\rm cm}^{-2}$. The best-fit model is shown in Fig. 6.6. MODEL4 offers a good fit with C-stat/ν=246.21/182. An intermediate spin of $a_* = 0.72^{+0.14}_{-0.20}$ is found and is consistent with previous spin measurements [e.g. 192, 165]. A higher inclination angle ($i = 67^{+3}_{-2}{}^\circ$) is found by fitting with a high density disc reflection model compared with previous analysis [e.g. 40°, 192]. A lower limit of the disc density ($\log(n_{\rm e}) > 18.7$) is obtained, indicating a potential high disc density.

6.4.16 Ton S180

Ton S180 is a NLS1 galaxy [309] that shows both a broad Fe K emission line and a strong soft excess [e.g. 307, 289, 209, 228]. Takahashi et al. [289] demonstrate that the soft excess emission shown in the *Suzaku* spectrum of Ton S180 can be described as a disc blackbody-shaped model with a temperature of kT=0.075 keV. Nardini et al. [209] found that the broad band *XMM-Newton* and *Suzaku* spectra of Ton S180 can be modelled by a combination of two reflection components, one from the inner disc and one from a distant reflector. A more recent study by Parker et al. [228] succssfully model the broad band *XMM-Newton* spectrum of Ton S180 with a combination of a soft Comptonisation component, a hard Comptonisation component from the corona, and a relativistic disc reflection component. The soft Compotonisation component accounts for the soft excess. However the relativistic reflection component requires a very high iron abundance $Z_{\rm Fe} > 9 Z_\odot$.

We first fit the stacked EPIC-pn spectrum of Ton S180 with an absorbed power-law model. The corresponding ratio plot is shown in Fig. 6.3. Similar to previous analysis, a broad emission line in the iron band and a strong soft excess below 3 keV are found in the spectrum. Second, we model the broad band spectrum with MODEL2. MODEL2 offers a very good fit of both the broad emission line feature and the soft excess emission with C-stat/ν=301.71/179. The best-fit model is shown in Fig. 6.6 and the best-fit parameters can be found in Table 6.4. By modelling the broad line and the soft excess with the same model, we obtain a high BH spin of $a_* > 0.98$. A very steep emissivity profile is found, indicating a very compact coronal region. A disc viewing angle of $36^{+4}_{-6}{}^\circ$ is found, which is consistent with the previous measurement [e.g. $\approx 39^\circ$, 228]. As shown from the plot of the best-fit model, the spectrum is dominated by the disc reflection component with a reflection fraction $f_{\rm refl} = 1.9 \pm 0.7$, making it the second highest reflection fraction in our sample. A modest high disc density of $\log(n_{\rm e}) = 15.6^{+0.3}_{-0.2}$ is required by spectral fitting.

6.4.17 UGC 6728

UGC 6728 is a Seyfert 1 galaxy [309] that has one of the known lowest black hole masses [$7.1 \times 10^5 M_\odot$, 21]. Only one *XMM-Newton* observation is available in the archive. The EPIC-pn observation of UGC 6728 is dominated by flaring particle background. Therefore, we use EPIC-MOS observations instead. The MOS spectra of UGC 6728 show tentative evidence for emission features in the iron band, similar with PG 1426+015, and a strong soft excess below 2 keV.

We model the broad band spectrum with `MODEL2`. The relativistic reflection model accounts mainly for the soft excess. The BH spin parameter is not constrained so we assume a maximum BH spin during the fit. `MODEL2` offers a good fit with C-stat/ν=254.61/209. The best-fit model and corresponding ratio plot are shown in Figure 6.6. Only an upper limit of the disc density $\log(n_{\rm e}) < 18$ is found. The best-fit model predicts a very strong broad Fe K emission line, which cannot be resolved by current data quality. More future observations with longer exposures will enable us to study the iron band of UGC 6728 in more details.

6.5 Results

Section 6.4 presents the details of EPIC-pn spectral analysis for individual sources in our sample and compares our measurements of BH spins and inclination angles with previous analysis. The best-fit parameters are reported in Table 6.4 and the best-fit models with corresponding best-fit ratio plots are shown in Fig. 6.4, 6.5, and 6.6. In this section, we summarise the results of the disc density measurements, and the impact of a high density disc model on the inferred iron abundances.

6.5.1 Disc Densities in Seyfert 1 Galaxies

We present the best-fit disc density values versus BH mass in the left panel of Figure 6.7. No obvious correlation between disc densities and BH masses is found. However, only upper limits of disc density are achieved for sources with $\log(m_{\rm BH}) > 8$. It matches the previous analysis of another Seyfert 1 galaxy 1H 0419−577 where the mass of the central BH is estimated to be $\log(m_{\rm BH}) \approx 8$ and a disc density of $\log(n_{\rm e}) < 15.2$ with 90% confidence (see Chapter 5). Disc densities significantly higher than $\log(n_{\rm e}) = 15$ are found in AGN with $\log(m_{\rm BH}) < 7$. By comparing the best-fit disc densities with BH masses, we find that the assumption for a fixed disc density of $\log(n_{\rm e}) = 15$ is mostly appropriate for SMBH with $\log(m_{\rm BH}) > 8$ while a larger disc density is required for SMBH with $\log(m_{\rm BH}) < 7$.

A second factor that changes the disc density is the BH mass accretion rate. Shakura and Sunyaev [277] predicts that the disc density of a radiation pressure-dominated disc and the mass accretion rate has the following relation $\log(n_{\rm e}) \propto -2\log(\dot{m})$. The right panel of Fig. 6.7 presents the disc density solution in Svensson and Zdziarski [288], where f is the fraction of power released from the disc to the corona. When $f = 0$, the solutions reproduce the results in Shakura and Sunyaev [277]. The solid lines show the disc densities at $R = 2R_{\rm g}$ for different f, assuming: 1) a maximum BH spin; 2) the inner radius of the disc is $R_{\rm ISCO}$; 3) the conversion factor in the radiative diffusion equation $\xi' = 1$ [3]. The dotted and dashed lines show the disc densities at $R = 6, 8R_{\rm g}$ for $f = 0.01$. We find that the radius R has less impact on the disc density than other factors, such as f. Detailed calculation can be found in Section 2.4 or Svensson and Zdziarski [288].

We present our results in the $\log(n_{\rm e})$ vs. $\log(m_{\rm BH}\dot{m}^2)$ diagram in the right panel of Fig. 6.7. We use a Monte-Carlo approach to estimate the significance of the correlation between two parameters by using the same method as in Parker et al. [226]. We assume $\log(n_{\rm e})$ and $\log(m_{\rm BH}\dot{m}^2)$ follow normal distributions. 100,000 sets of points are drawn from distributions with the same mean (mean $\log(m_{\rm BH}\dot{m}^2) = 7.1, \log(n_{\rm e}) = 16.89$) and deviation ($\sigma_{\log(m_{\rm BH}\dot{m}^2)} = 0.92, \sigma_{\log(n_{\rm e})} = 1.17$) of the sample. We find 11304 sets of points that exceed the Spearman correlation coefficient of our result (-0.67). This gives 11% probability of the observed correlation from randomly distributed points. The correlation between these two parameters is weak in our sample due to the following reasons: 1) the uncertainties of the BH mass measurements; 2) other physics, such as the vertical structure of the disc density and the fraction of power that is released from the disc to the coronal region (f). We will discuss the effect of f on the disc density in Section 6.6.

In summary, we find a trend that high disc density is commonly seen in AGN that show low $m_{\rm BH}\dot{m}^2$ values. It is important to note that the Galactic BH GX 339-4 shows a similar pattern. The disc density is higher in the low-flux hard state, where $\dot{m}$ is low, than that in the high-flux soft state, where $\dot{m}$ is high. See Chapter 2 for more details.

6.5.2 Disc Iron Abundance

A super solar iron abundance was commonly seen in previous reflection-based spectral analysis where a fixed disc density ($n_{\rm e} = 10^{15}$ cm^{-3}) was assumed. A significant decrease of iron abundance is found in our new disc reflection modelling. Fig. 6.8 presents the disc iron abundance in this work in black and the best-fit iron abundance in previous work in

[3] The prime symbol is to distinguish the conversion factor from the disc ionisation parameter ξ.

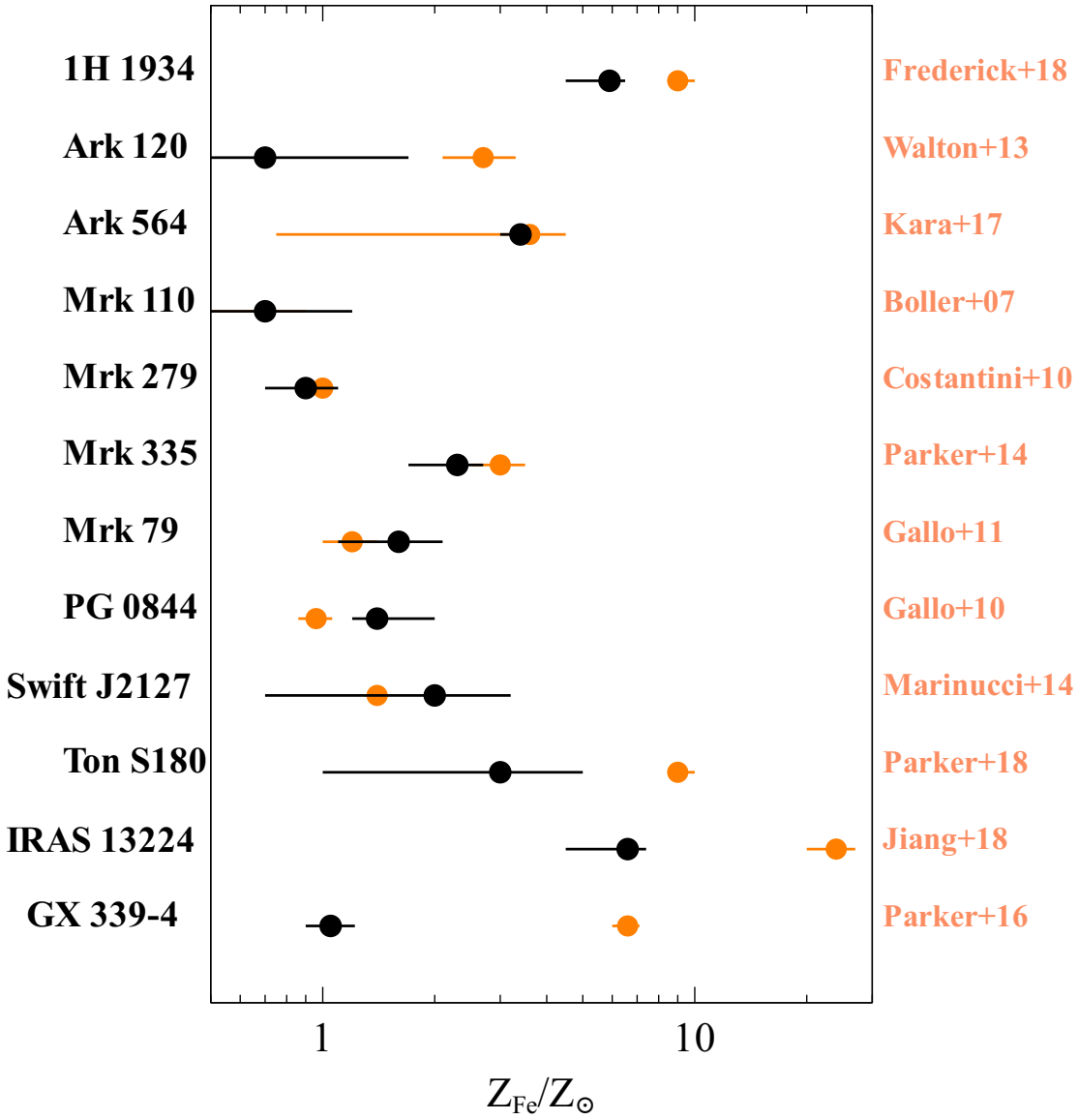

Fig. 6.8 The best-fit disc iron abundances $Z_{\rm Fe}$ measured by modelling with a variable disc density reflection model in black compared with the values obtained in previous work in orange.

orange. Corresponding references are labelled on the right side. Most of the sources require a significantly lower disc iron abundance.

The decrease of the inferred iron abundances is due to the increase of the continuum in the reflection spectrum when a high density model is used. For example, the best-fit reflection fraction for Ton S180 is $f_{\rm refl} = 1.9 \pm 0.7$ when the spectrum is modelled using a variable density disc reflection model. The averaged spectrum of Ton S180 is dominated by the disc reflection component and requires an iron abundance of $Z_{\rm Fe} = 3 \pm 2 Z_{\odot}$. By contrast, we model the soft excess emission in the same spectrum of Ton S180 with an additional simple soft `cutoff` component and a reflection model assuming $\log(n_{\rm e}) = 15$ by following the indication of Parker et al. [228]. Although such a model combination slightly improves the fit by ΔC-stat=7 with 2 more parameters, the disc reflection component with a fixed disc density requires a very high iron abundance of $Z_{\rm Fe} > 8 Z_{\odot}$. A much lower reflection fraction of $f_{\rm refl} = 0.50^{+0.06}_{-0.05}$ is required. In order to model the strong Fe K emission feature in the iron band of Ton S180, a higher iron abundance is required when the continuum flux of the reflection component is relatively lower. Note that the reflection fraction $f_{\rm refl}$ here is not the same reflection fraction used in Dauser et al. [47]. An empirical definition of $F_{\rm refl}/F_{\rm pl}$ in the *XMM-Newton* band is used in order to compare different reflection models, as explained in Section 6.3.1.

Although a high density disc model is able to decrease the inferred iron abundance, some AGN still show a high iron abundance compared to solar [e.g. IRAS 13224−3809, 124]. This is because all the other elements rather than iron are assumed to be solar during our spectral fitting. The increase of metallicity will increase the contribution of the disc reflection component to the total spectrum, and thus decrease the iron abundance. We will improve our high density disc reflection model by taking other element abundances into consideration in future work.

6.6 Discussion

We summarise the disc density measurements in this paper and previous analysis [296, 164, 88, 124, 123] in Fig. 6.9. The results from previous work of AGN are marked by orange points. Blue circles are for GX 339-4 observations in 2015 and blue squares are for observations in 2013. Black points are the measurements for our sample. The orange straight lines are the same as the ones as in Fig. 6.7 and the blue straight line is the solution for $f = 0.01$, $R = 2R_{\rm g}$, and $\xi' = 2$. We can draw the following conclusions from this diagram.

First, a significantly higher disc density is found in stellar-mass BHs than in SMBHs. In the hard state of GX 339-4 and the intermediate state of Cyg X-1, the density of the disc

is at least $\log(n_{\rm e}) > 20.5$. This result matches the MHD simulation for a stellar-mass BH accretion disc [e.g. 213, 271]. In the high flux state of GX 339-4, a disc density of $\log(n_{\rm e}) \approx 19$ is required, similar with the disc density in AGN with $\log(m_{\rm BH}\dot{m}^2) < 7$.

Second, the accretion rate affects the disc density in the same way as the BH mass: a higher disc density is found where the BH accretes at a lower fraction of its Eddington limit. This conclusion has been found previously by studying the different states of the BH XRB GX 339−4 (see Chapter 1). Similarly, we find tentative evidence for a similar conclusion for AGN. For example, Mrk 509 and PG 0804+761 have a similar BH mass of $m_{\rm BH} \approx 10^8$ [21, 88]. However, Mrk 509 has a higher disc density than PG 0804+761. This might be due to the higher accretion rate in PG 0804+761 ($\dot{m} = 1.20^{+1.0}_{-0.4}$) than in Mrk 509 [$\dot{m} = 0.2 - 0.4$, 234].

Third, 65% of SMBHs in our sample show evidence for a disc density significantly higher than $\log(n_{\rm e}) = 15$. This suggests that a high population of BHs, including stellar-mass BHs and SMBHs that accrete at a significant accretion rate (e.g. $\dot{m} > 5\%$), have a thin disc with a high disc density.

Fourth, theoretically most coronal heating mechanisms assume that a large fraction of the disc energy is dissipated in the coronal region [e.g. magnetic coronae model, 76, 43, 284]. Assuming $\xi' = 1$, our analysis suggests at least 10% of the power in the disc is released to the corona in AGN. If a higher value of ξ' [e.g. $\xi' = 2$, 288] is assumed, an even higher f is expected. See the blue and orange solid lines in Fig.6.9.

Fifth, although there is a weak correlation between $\log(n_{\rm e})$ and $\log(m_{\rm BH}\dot{m}^2)$ in our sample, a disc density of $\log(n_{\rm e}) > 16$ is clearly found in AGN with $\log(m_{\rm BH}\dot{m}^2) < 6.5$. The weak correlation could be due to other uncertain effects, such as different f, the vertical structure of the disc density [e.g. 302, 111], or the uncertainties of the BH mass measurements.

Sixth, the disc densities that the reflection model obtains for BH XRBs are significantly lower than the prediction of the radiation pressure-dominated thin disc model [the solid orange line in Fig. 6.9, 277]. Here are the possible reasons: 1) the disc density parameter in the reflection model is the density in the surface of the disc while the thin disc models assume a uniform disc density in the vertical direction; 2) the BH mass and the distance measurements of GX 339−4 are uncertain. However, we note that the disc density of Cyg X-1 is still below the prediction, although the mass and the distance of Cyg X−1 are well constrained [218, 247]; 3) the stellar-mass BH discs during the observations considered in Tomsick et al. [296] and Chapter 2-3 are likely to be dominated by gas pressure instead of radiation pressure. The orange lines in Fig. 6.10 presents the critical accretion rate curves on the $\dot{m}$–$m_{\rm BH}$ parameter plane calculated by Svensson and Zdziarski [288]. The discs corresponding to the regions below the critical accretion rate curves have no radiation pressure-dominated area in the disc. At higher f, this critical accretion rate is higher. The

green dotted lines are the contours of the $\log(m_{\rm BH}\dot{m}^2)$ parameter. Observations that show $\log(m_{\rm BH}\dot{m}^2) < 0$ are in the region for gas pressure-dominated discs. The hard state of GX 339−4 and the intermediate state of Cyg X-1 may have a different disc from the ones in Seyfert 1 galaxies considered in this work. As shown in Fig. 6.10, the SMBH accretion discs in this work are accreting at least $\dot{m} \approx 0.1$. However, the densities measured in XRBs are still lower the density of a gas pressure-dominated disc in Shakura and Sunyaev [e.g. the dashed red line in Fig. 6.9 277]. It suggests that more physics are needed to be considered, such as the vertical structure of a gas pressure-dominated disc [e.g. 302].

In conclusion, we find that the high density disc reflection model can not only decrease the inferred iron abundance but also successfully explains the 0.5–10 keV band spectra of the Seyfert 1 galaxies in our sample with no requirement for additional components for the soft excess emission. The density of the disc is significantly higher than the previous $\log(n_e) = 15$ assumption in AGN with $\log(m_{\rm BH}\dot{m}^2) < 7.5$, as predicted by the standard thin disc model. More future work is needed to complete the high density disc reflection spectroscopy for AGN in following approaches: 1) abundances of other elements in addition to iron need to be considered; 2) simultaneous broad band observations of these Seyfert galaxies are required (e.g. from *NuSTAR*) to test whether the high density model can account for the Compton hump above 10 keV; 3) time-resolved spectral analysis is required to study the short-term variability of the disc density within one observation.

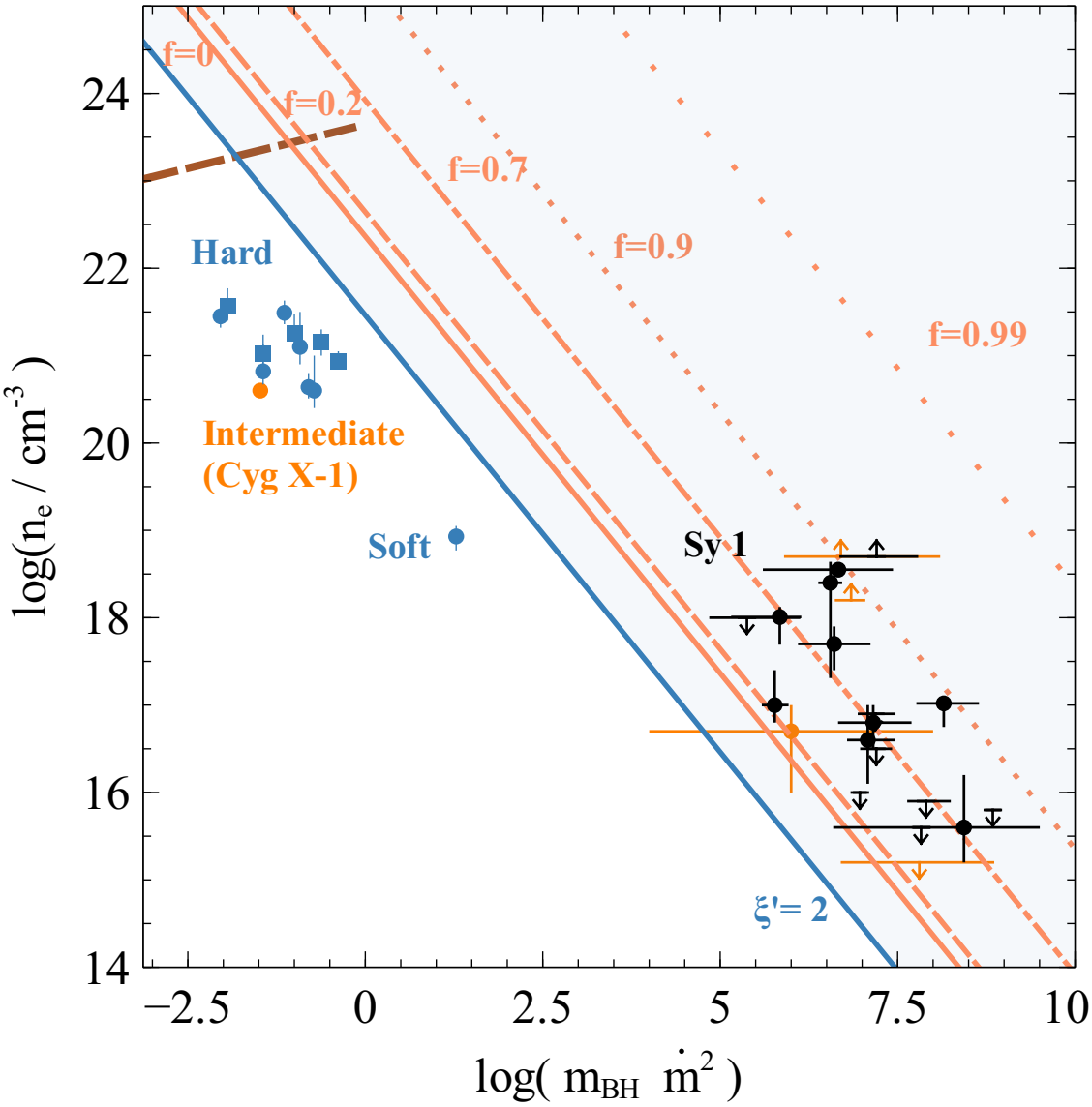

Fig. 6.9 Disc density $\log(n_{\rm e})$ versus $\log(m_{\rm BH}\dot{m}^2)$ for our sample and previous analysis. Previous analysis are marked by orange points (see text for references). Blue circles represent GX 339−4 observations in 2015 and squares represent observations in 2013 that are analysed in Chapter 2. A BH mass of $m_{\rm BH} = 10$ is assumed for GX339−4. Orange lines are the disc solutions for different values of f. Same assumptions are made as in Fig. 6.7. Blue solid line is the solution assuming $f = 0$, $\xi' = 2$, and $r = 2r_{\rm g}$. The red dashed line shows the solution for a gas pressure-dominated disc at $r = 2r_{\rm g}$ assuming $f = 0$. All the disc density curves are calculated by Svensson and Zdziarski [288].

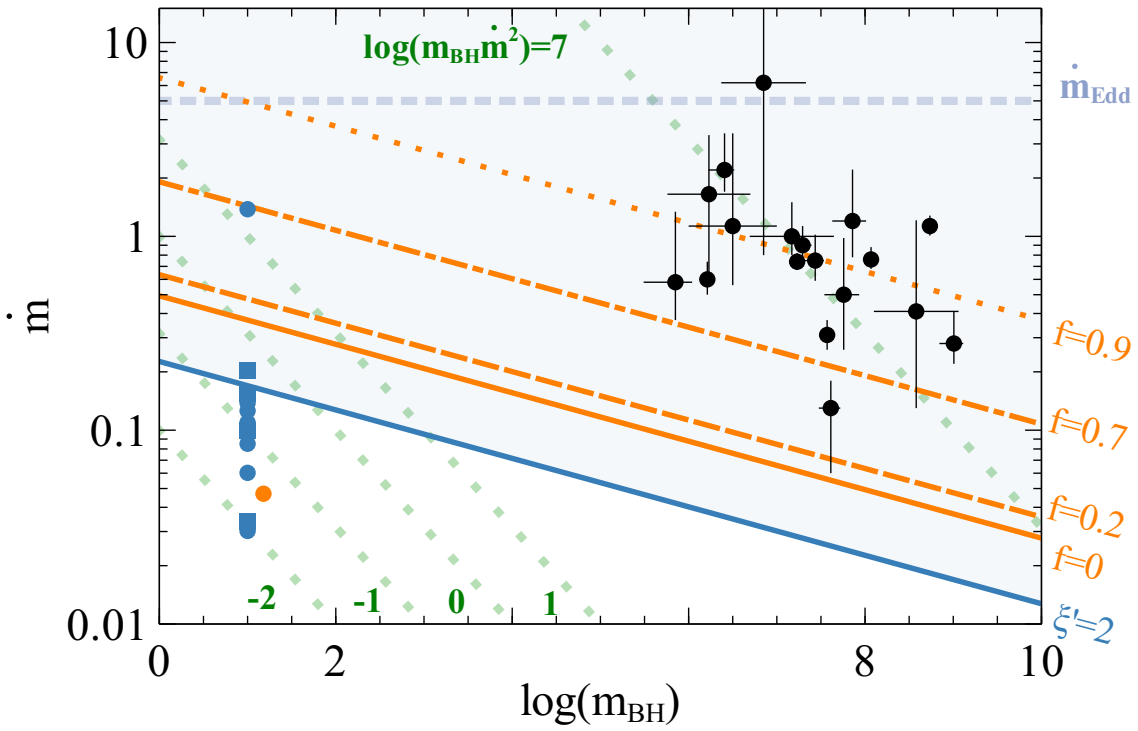

Fig. 6.10 Comparison of the mass accretion rates of Seyfert 1 galaxies in this work with BH XRBs considered in Tomsick et al. [296], Jiang et al. [123]. Blue circles represent GX 339−4 observations in 2015 and squares represent observations in 2013. The orange circle represent Cyg X-1. The dashed horizontal lines mark the mass accretion rate at the Eddington limit assuming an accretion efficiency of 20%. Below the orange and blue lines there is no radiation pressure dominated region in the disc. These curves are calculated by Svensson and Zdziarski [288]. Orange lines assume $\xi' = 1$ and the blue line assumes $\xi' = 2$ and $f = 0$ as in Fig. 6.9. The green dotted curves show the contours of $\log(m_{\rm BH}\dot{m}^2) = -2, -1, 0, 1, 7$ from left to right. Observations that show $\log(m_{\rm BH}\dot{m}^2) < 0$ are in the region for gas pressure-dominated discs.

Chapter 7

Future Work

In this section, I briefly introduce my plan for future X-ray studies of accreting BH systems. Recent X-ray missions and missions in near future are mentioned to demonstrate opportunities for observations.

7.1 Black Hole X-ray Binaries

- The illumination from the disc blackbody component below the slab needs to be considered in the calculation of the rest-frame disc reflection spectra. The inclusion of an additional illuminating spectrum changes the overall shape of the reflection model. This might affect the spectral fitting for the observations where the disc thermal component and the disc reflection component co-exist in the spectrum. An example is the work by Reis et al. [249] where a model that takes the disc illumination into account was applied to the *RXTE* and *XMM-Newton* observations of GX 339−4.

- The hard state of a BH XRB usually shows a blackbody component in the soft band. However the origin of this blackbody component remains uncertain. For example, Wang-Ji et al. [320] analysed *NuSTAR* and *Swift* observations of GX 339−4 and obtained an additional disc blackbody component of $kT > 0.7$ keV in the hard state ($L_{\rm X} < 1\% L_{\rm Edd}$) in addition to the disc reflection component when assuming a fixed disc density of $n_{\rm e} = 10^{15}$ cm^{-3}. By contrast, the soft state ($L_{\rm X} \approx 27\% L_{\rm Edd}$) of GX 339−4 shows a disc temperature of $kT = 0.83$ keV, which is similar with the 'disc temperature' seen in the low-flux hard state despite their very different luminosities/accretion rates. Therefore additional physics rather than the disc thermal component, such as a high density disc reflection, should account for at least a fraction of the soft emission in the hard state. Another supporting evidence for reflection in

the soft band is the reverberation lag between the soft emission and the coronal emission identified in the hard state of MAXI J1820+070 [138]. These soft reverberation lags are similar to the ones found in AGN [e.g. 70].

However, most of the Galactic XRBs locate in the Galactic plane and thus have a modest column density ($N_{\rm H} \approx 4 \times 10^{21}$ cm^{-2}). This might cause some degeneracy between the column density and other parameters (see Chapter 2). Future pile-up–free soft–X-ray observations of XRBs that are away from the Galactic plane might be able to break this degeneracy.

- As discussed in Chapter 2 and 3, the sizes of the coronal regions in BH XRBs are weakly constrained by analysing only the *NuSTAR* and *Swift* spectra. With *NICER*, we will be able to obtain pile-up–free observations of XRBs in the iron band. These observations will enable us to estimate the sizes of the coronal regions by measuring the disc emissivity profiles. An example work is Fabian et al. [69], where the disc emissivity profile was measured for the BH XRB Cyg X-1 by using its *Suzaku* spectra.

- The high density disc reflection model enables us to study the disc properties in more details and look for possible changes of disc physics during the state transition. For example, Reis et al. [251] found that the HFQPO frequency and the disc reflection fraction show positive correlation along the 'Q'-shaped HID diagram. Observations involving *NICER*, *NuSTAR* and the China's first X-ray mission *HXMT* will be able to provide pile-up–free spectra and variability studies of BH XRBs in the 0.5–200 keV band. With these observations, we will be able to look for any possible correlations between QPOs, reflection fractions, and the densities and ionisation states of the discs in XRBs.

7.2 Active Galactic Nuclei

- The high density disc reflection model is able to explain the soft excess and the broad Fe Kα emission line in at least some of the Seyfert 1 galaxies (e.g. see Chapter 6). Simultaneous hard band observations of the reflection Compton humps, such as from *NuSTAR*, are required for future work as well. An example work is Mallick et al. [164], where a high disc density model is able to explain the *XMM-Newton* and *NuSTAR* spectra of the NLS1 Mrk 1044 with no requirement for an additional component.

- Some Seyfert galaxies show very fast X-ray variability on timescales shorter than a kilo-second [e.g. IRAS 13224−3809, 5]. The variability is dominated by the coronal

emission and the disc reflection component changes correspondingly, as introduced in Chapter 4. However this work models the soft excess emission in IRAS 13224−3809 with a combination of disc reflection and a phenomenological blackbody model. A fixed disc density of $n_{\rm e} = 10^{15}$ cm^{-3} was assumed in the flux-resolved and time-resolved spectral analysis. A high density disc reflection model needs to be applied in order to study the short-term variability of the disc and find any possible correlation between the corona and the disc density of IRAS 13224−3809.

- It has been realized for a long time that a high fraction of disc energy has to be dissipated in the corona instead of being radiated away locally in the disc as in the Shakura and Sunyaev [277] model [e.g. 103]. Same conclusions can be found by using a high density model for the spectral fitting of Seyfert galaxies, as shown in Chapter 6. Systematic check of the SEDs of the Sy1 galaxies considered in this work needs to be done in order to see whether the SED fitting is consistent with the X-ray spectral modelling.

- The Einstein Probe (*EP*) [332] is a small mission led by the Chinese Academy of Science and will be launched by 2022. *EP* is designed to monitor the whole X-ray sky in the 0.5–4 keV band with a much higher sensitivity compared to previous missions by using the lobster-eye optics. With *EP*, we will be able to carry out monitoring programmes for AGN that are much fainter than XRBs. These monitoring programmes will be able to provide invaluable information for follow-up observations of AGN. For example, a strong disc reflection is commonly seen in the extremely low flux states of some Sy1 galaxies [e.g. Mrk 335, 231]. We will be able to capture the desirable states of AGN and trigger follow-up observations for further studies with the help of *EP*. Another mission led by NASA, the Imaging X-ray Polarimetry Explorer (*IXPE*) [322], will be launched by 2021. *IXPE* will be able to provide a polarisation view of the inner accretion regions in AGN. With *IXPE*, we might be able to measure the polarisation of the disc reflection component. It has been shown in theoretical studies that the polarisation fraction of the disc reflection component can reach up to 20%, assuming that the disc is illuminated by unpolarised radiation from a simple lamp-post corona [174]

References

[1] Abramowicz, M. A. and Kluźniak, W. (2001). A precise determination of black hole spin in GRO J1655-40. *A&A*, 374:L19–L20.

[2] Agol, E. and Krolik, J. H. (2000). Magnetic Stress at the Marginally Stable Orbit: Altered Disk Structure, Radiation, and Black Hole Spin Evolution. *ApJ*, 528:161–170.

[3] Allen, D. A., Norris, R. P., Meadows, V. S., and Roche, P. F. (1991). A large sample of southern IRAS galaxies - Spectral classes and superclustering. *MNRAS*, 248:528–543.

[4] Alston, W., Fabian, A., Markevičiutė, J., Parker, M., Middleton, M., and Kara, E. (2016). Quasi periodic oscillations in active galactic nuclei. *Astronomische Nachrichten*, 337:417–422.

[5] Alston, W. N., Fabian, A. C., Buisson, D. J. K., Kara, E., Parker, M. L., Lohfink, A. M., Uttley, P., Wilkins, D. R., Pinto, C., De Marco, B., Cackett, E. M., Middleton, M. J., Walton, D. J., Reynolds, C. S., Jiang, J., Gallo, L. C., Zogbhi, A., Miniutti, G., Dovciak, M., and Young, A. J. (2019). The remarkable X-ray variability of IRAS 13224-3809 - I. The variability process. *MNRAS*, 482(2):2088–2106.

[6] Alston, W. N., Parker, M. L., Markevičiūtė, J., Fabian, A. C., Middleton, M., Lohfink, A., Kara, E., and Pinto, C. (2015). Discovery of an 2-h high-frequency X-ray QPO and iron Kα reverberation in the active galaxy MS 2254.9-3712. *MNRAS*, 449:467–476.

[7] Antonucci, R. (1993). Unified models for active galactic nuclei and quasars. *ARA&A*, 31:473–521.

[8] Armas Padilla, M. and Munoz-Darias, T. (2017). GRS 1716-249 is transitioning to the soft state. *The Astronomer's Telegram*, 10236.

[9] Arnaud, K. A. (1996). XSPEC: The First Ten Years.

[10] Bachetti, M., Harrison, F. A., Walton, D. J., Grefenstette, B. W., Chakrabarty, D., Fürst, F., Barret, D., Beloborodov, A., Boggs, S. E., Christensen, F. E., Craig, W. W., Fabian, A. C., Hailey, C. J., Hornschemeier, A., Kaspi, V., Kulkarni, S. R., Maccarone, T., Miller, J. M., Rana, V., Stern, D., Tendulkar, S. P., Tomsick, J., Webb, N. A., and Zhang, W. W. (2014). An ultraluminous X-ray source powered by an accreting neutron star. *Nature*, 514:202–204.

[11] Balick, B. and Brown, R. L. (1974). Intense sub-arcsecond structure in the galactic center. *ApJ*, 194:265–270.

[12] Ballantyne, D. R., Ross, R. R., and Fabian, A. C. (2001). X-ray reflection by photoionized accretion discs. *MNRAS*, 327:10–22.

[13] Ballet, J., Denis, M., Gilfanov, M., Sunyaev, R., Harmon, B. A., Zhang, S. N., Paciesas, W. S., and Fishman, G. J. (1993). GRS 1716-249 = GRO J1719-24. *IAU Circ.*, 5874.

[14] Bałucińska-Church, M. and Church, M. J. (2000). Discovery of a red- and blueshifted iron disc line in the Galactic jet source GROJ1655-40. *MNRAS*, 312:L55–L59.

[15] Balucinska-Church, M. and McCammon, D. (1992). Photoelectric absorption cross sections with variable abundances. *ApJ*, 400:699.

[16] Bardeen, J. M., Press, W. H., and Teukolsky, S. A. (1972). Rotating Black Holes: Locally Nonrotating Frames, Energy Extraction, and Scalar Synchrotron Radiation. *ApJ*, 178:347–370.

[17] Barr, P., White, N. E., and Page, C. G. (1985). The discovery of low-level iron K line emission from CYG X-1. *MNRAS*, 216:65P–70.

[18] Barthelmy, S. D., Barbier, L. M., Cummings, J. R., Fenimore, E. E., Gehrels, N., Hullinger, D., Krimm, H. A., Markwardt, C. B., Palmer, D. M., Parsons, A., Sato, G., Suzuki, M., Takahashi, T., Tashiro, M., and Tueller, J. (2005). The Burst Alert Telescope (BAT) on the SWIFT Midex Mission. *Space Sci. Rev.*, 120:143–164.

[19] Bassi, T., Del Santo, M., D'Aı, A., Motta, S. E., Malzac, J., Segreto, A., Miller-Jones, J. C. A., Atri, P., Plotkin, R. M., Belloni, T. M., Mineo, T., and Tzioumis, A. K. (2019). The long outburst of the black hole transient GRS 1716-249 observed in the X-ray and radio band. *MNRAS*, 482:1587–1601.

[20] Belloni, T. M. and Stella, L. (2014). Fast Variability from Black-Hole Binaries. *Space Sci. Rev.*, 183:43–60.

[21] Bentz, M. C. and Katz, S. (2015). The AGN Black Hole Mass Database. *PASP*, 127:67.

[22] Bianchi, S., Guainazzi, M., Matt, G., Fonseca Bonilla, N., and Ponti, G. (2009). CAIXA: a catalogue of AGN in the XMM-Newton archive. I. Spectral analysis. *A&A*, 495:421–430.

[23] Blandford, R. D. and Znajek, R. L. (1977). Electromagnetic extraction of energy from Kerr black holes. *MNRAS*, 179:433–456.

[24] Boller, T., Balestra, I., and Kollatschny, W. (2007). XMM-Newton observation of Mrk 110. *A&A*, 465:87–93.

[25] Boller, T., Brandt, W. N., Fabian, A. C., and Fink, H. H. (1997). ROSAT monitoring of persistent giant and rapid variability in the narrow-line Seyfert 1 galaxy IRAS 13224-3809. *MNRAS*, 289:393–405.

[26] Boller, T., Fabian, A. C., Sunyaev, R., Trümper, J., Vaughan, S., Ballantyne, D. R., Brandt, W. N., Keil, R., and Iwasawa, K. (2002). XMM-Newton discovery of a sharp spectral feature at ˜ 7 keV in the narrow-line Seyfert 1 galaxy 1H 0707 - 49. *MNRAS*, 329:L1–L5.

[27] Boller, T., Tanaka, Y., Fabian, A., Brandt, W. N., Gallo, L., Anabuki, N., Haba, Y., and Vaughan, S. (2003). XMM-Newton spectral properties of the narrow-line Seyfert 1 galaxy IRAS 13224 - 3809. *MNRAS*, 343:L89–L93.

[28] Bolton, C. T. (1972). Identification of Cygnus X-1 with HDE 226868. *Nature*, 235:271–273.

[29] Bowyer, S., Byram, E. T., Chubb, T. A., and Friedman, H. (1965). Cosmic x-ray sources. *Science*, 147(3656):394–398.

[30] Bradt, H. V. D. and McClintock, J. E. (1983). The optical counterparts of compact galactic X-ray sources. *ARA&A*, 21:13–66.

[31] Braes, L. L. E. and Miley, G. K. (1971). Physical Sciences: Detection of Radio Emission from Cygnus X-1. *Nature*, 232:246.

[32] Brenneman, L. (2013). *Measuring the Angular Momentum of Supermassive Black Holes*.

[33] Brenneman, L. W., Reynolds, C. S., Nowak, M. A., Reis, R. C., Trippe, M., Fabian, A. C., Iwasawa, K., Lee, J. C., Miller, J. M., Mushotzky, R. F., Nandra, K., and Volonteri, M. (2011). The Spin of the Supermassive Black Hole in NGC 3783. *ApJ*, 736:103.

[34] Brightman, M., Silverman, J. D., Mainieri, V., Ueda, Y., Schramm, M., Matsuoka, K., Nagao, T., Steinhardt, C., Kartaltepe, J., Sanders, D. B., Treister, E., Shemmer, O., Brandt, W. N., Brusa, M., Comastri, A., Ho, L. C., Lanzuisi, G., Lusso, E., Nandra, K., Salvato, M., Zamorani, G., Akiyama, M., Alexander, D. M., Bongiorno, A., Capak, P., Civano, F., Del Moro, A., Doi, A., Elvis, M., Hasinger, G., Laird, E. S., Masters, D., Mignoli, M., Ohta, K., Schawinski, K., and Taniguchi, Y. (2013). A statistical relation between the X-ray spectral index and Eddington ratio of active galactic nuclei in deep surveys. *MNRAS*, 433:2485–2496.

[35] Buisson, D. J. K., Lohfink, A. M., Alston, W. N., Cackett, E. M., Chiang, C.-Y., Dauser, T., De Marco, B., Fabian, A. C., Gallo, L. C., García, J. A., Jiang, J., Kara, E., Middleton, M. J., Miniutti, G., Parker, M. L., Pinto, C., Uttley, P., Walton, D. J., and Wilkins, D. R. (2018). Is there a UV/X-ray connection in IRAS 13224-3809? *MNRAS*, 475:2306–2313.

[36] Burrows, D. N., Hill, J. E., Nousek, J. A., Kennea, J. A., Wells, A., Osborne, J. P., Abbey, A. F., Beardmore, A., Mukerjee, K., Short, A. D. T., Chincarini, G., Campana, S., Citterio, O., Moretti, A., Pagani, C., Tagliaferri, G., Giommi, P., Capalbi, M., Tamburelli, F., Angelini, L., Cusumano, G., Bräuninger, H. W., Burkert, W., and Hartner, G. D. (2005). The Swift X-Ray Telescope. *Space Sci. Rev.*, 120:165–195.

[37] Cash, W. (1979). Parameter estimation in astronomy through application of the likelihood ratio. *ApJ*, 228:939–947.

[38] Chainakun, P., Young, A. J., and Kara, E. (2016). Relativistic X-ray reverberation modelling of the combined time-averaged and lag-energy spectra in AGN. *MNRAS*, 460:3076–3088.

[39] Chartas, G., Krawczynski, H., Zalesky, L., Kochanek, C. S., Dai, X., Morgan, C. W., and Mosquera, A. (2017). Measuring the Innermost Stable Circular Orbits of Supermassive Black Holes. *ApJ*, 837:26.

[40] Chaudhary, P., Brusa, M., Hasinger, G., Merloni, A., Comastri, A., and Nandra, K. (2012). Rest-frame stacking of 2XMM catalog sources. Properties of the Fe Kα line. *A&A*, 537:A6.

[41] Chiang, C.-Y., Walton, D. J., Fabian, A. C., Wilkins, D. R., and Gallo, L. C. (2015). Modelling the extreme X-ray spectrum of IRAS 13224-3809. *MNRAS*, 446:759–769.

[42] Connolly, S. D., McHardy, I. M., Skipper, C. J., and Emmanoulopoulos, D. (2016). Long-term X-ray spectral variability in AGN from the Palomar sample observed by Swift. *MNRAS*, 459:3963–3985.

[43] Coroniti, F. V. (1981). On the magnetic viscosity in Keplerian accretion disks. *ApJ*, 244:587–599.

[44] Costantini, E., Kaastra, J. S., Korista, K., Ebrero, J., Arav, N., Kriss, G., and Steenbrugge, K. C. (2010). XMM-Newton unveils the complex iron Kα region of Mrk 279. *A&A*, 512:A25.

[45] Cunningham, C. (1976). Returning radiation in accretion disks around black holes. *ApJ*, 208:534–549.

[46] Dauser, T., Garcia, J., Parker, M. L., Fabian, A. C., and Wilms, J. (2014). The role of the reflection fraction in constraining black hole spin. *MNRAS*, 444:L100–L104.

[47] Dauser, T., García, J., Walton, D. J., Eikmann, W., Kallman, T., McClintock, J., and Wilms, J. (2016a). Normalizing a relativistic model of X-ray reflection. Definition of the reflection fraction and its implementation in relxill. *A&A*, 590:A76.

[48] Dauser, T., García, J., and Wilms, J. (2016b). Relativistic reflection: Review and recent developments in modeling. *Astronomische Nachrichten*, 337:362.

[49] Dauser, T., Garcia, J., Wilms, J., Böck, M., Brenneman, L. W., Falanga, M., Fukumura, K., and Reynolds, C. S. (2013). Irradiation of an accretion disc by a jet: general properties and implications for spin measurements of black holes. *MNRAS*, 430:1694–1708.

[50] Dauser, T., Svoboda, J., Schartel, N., Wilms, J., Dovčiak, M., Ehle, M., Karas, V., Santos-Lleó, M., and Marshall, H. L. (2012). Spectral analysis of 1H 0707-495 with XMM-Newton. *MNRAS*, 422:1914–1921.

[51] De Marco, B., Ponti, G., Cappi, M., Dadina, M., Uttley, P., Cackett, E. M., Fabian, A. C., and Miniutti, G. (2013). Discovery of a relation between black hole mass and soft X-ray time lags in active galactic nuclei. *MNRAS*, 431:2441–2452.

[52] della Valle, M., Mirabel, I. F., and Rodriguez, L. F. (1994). The optical and radio counterpart of the X-ray Nova Ophiuchi 1993. *A&A*, 290:803–806.

[53] Di Gesu, L., Costantini, E., Arav, N., Borguet, B., Detmers, R. G., Ebrero, J., Edmonds, D., Kaastra, J. S., Piconcelli, E., and Verbunt, F. (2013). Simultaneous XMM-Newton and HST-COS observation of 1H0419-577. The absorbing and emitting ionized gas. *A&A*, 556:A94.

[54] Done, C., Davis, S. W., Jin, C., Blaes, O., and Ward, M. (2012). Intrinsic disc emission and the soft X-ray excess in active galactic nuclei. *MNRAS*, 420(3):1848–1860.

[55] Done, C. and Jin, C. (2016). The mass and spin of the extreme Narrow Line Seyfert 1 Galaxy 1H 0707-495 and its implications for the trigger for relativistic jets. *MNRAS*, 460:1716–1724.

[56] Dumont, A. M., Czerny, B., Collin, S., and Zycki, P. T. (2002). Reprocessing of X-rays in AGN. I. Plane parallel geometry - test of pressure equilibrium. *A&A*, 387:63–75.

[57] Einstein, A. (1916). Die Grundlage der allgemeinen Relativitätstheorie. *Annalen der Physik*, 354:769–822.

[58] Elvis, M. (2000). A Structure for Quasars. *ApJ*, 545:63–76.

[59] Esin, A. A., McClintock, J. E., and Narayan, R. (1997). Advection-Dominated Accretion and the Spectral States of Black Hole X-Ray Binaries: Application to Nova Muscae 1991. *ApJ*, 489:865–889.

[60] Event Horizon Telescope Collaboration, e. a. (2019). First M87 Event Horizon Telescope Results. I. The Shadow of the Supermassive Black Hole. *ApJ*, 875(1):L1.

[61] Fabian, A. C. (2009). Black holes at work. *Astronomy and Geophysics*, 50:3.18–3.24.

[62] Fabian, A. C., Kara, E., Walton, D. J., Wilkins, D. R., Ross, R. R., Lozanov, K., Uttley, P., Gallo, L. C., Zoghbi, A., Miniutti, G., Boller, T., Brandt, W. N., Cackett, E. M., Chiang, C.-Y., Dwelly, T., Malzac, J., Miller, J. M., Nardini, E., Ponti, G., Reis, R. C., Reynolds, C. S., Steiner, J. F., Tanaka, Y., and Young, A. J. (2013). Long XMM observation of the narrow-line Seyfert 1 galaxy IRAS 13224-3809: rapid variability, high spin and a soft lag. *MNRAS*, 429:2917–2923.

[63] Fabian, A. C., Lohfink, A., Belmont, R., Malzac, J., and Coppi, P. (2017). Properties of AGN coronae in the NuSTAR era - II. Hybrid plasma. *MNRAS*, 467:2566–2570.

[64] Fabian, A. C., Lohfink, A., Kara, E., Parker, M. L., Vasudevan, R., and Reynolds, C. S. (2015). Properties of AGN coronae in the NuSTAR era. *MNRAS*, 451:4375–4383.

[65] Fabian, A. C., Miniutti, G., Gallo, L., Boller, T., Tanaka, Y., Vaughan, S., and Ross, R. R. (2004). X-ray reflection in the narrow-line Seyfert 1 galaxy 1H 0707-495. *MNRAS*, 353:1071–1077.

[66] Fabian, A. C., Miniutti, G., Iwasawa, K., and Ross, R. R. (2005). X-ray reflection in the Seyfert galaxy 1H 0419-577 revealing strong relativistic effects in the vicinity of a Kerr black hole. *MNRAS*, 361:795–802.

[67] Fabian, A. C., Rees, M. J., Stella, L., and White, N. E. (1989). X-ray fluorescence from the inner disc in Cygnus X-1. *MNRAS*, 238:729–736.

[68] Fabian, A. C. and Vaughan, S. (2003). The iron line in MCG-6-30-15 from XMM-Newton: evidence for gravitational light bending? *MNRAS*, 340:L28–L32.

[69] Fabian, A. C., Wilkins, D. R., Miller, J. M., Reis, R. C., Reynolds, C. S., Cackett, E. M., Nowak, M. A., Pooley, G. G., Pottschmidt, K., Sanders, J. S., Ross, R. R., and Wilms, J. (2012). On the determination of the spin of the black hole in Cyg X-1 from X-ray reflection spectra. *MNRAS*, 424:217–223.

[70] Fabian, A. C., Zoghbi, A., Ross, R. R., Uttley, P., Gallo, L. C., Brandt, W. N., Blustin, A. J., Boller, T., Caballero-Garcia, M. D., Larsson, J., Miller, J. M., Miniutti, G., Ponti, G., Reis, R. C., Reynolds, C. S., Tanaka, Y., and Young, A. J. (2009). Broad line emission from iron K- and L-shell transitions in the active galaxy 1H0707-495. *Nature*, 459:540–542.

[71] Feain, I. J., Ekers, R. D., Murphy, T., Gaensler, B. M., Macquart, J.-P., Norris, R. P., Cornwell, T. J., Johnston-Hollitt, M., Ott, J., and Middelberg, E. (2009). Faraday Rotation Structure on Kiloparsec Scales in the Radio Lobes of Centaurus A. *ApJ*, 707:114–125.

[72] Foreman-Mackey, D., Hogg, D. W., Lang, D., and Goodman, J. (2013). emcee: The MCMC Hammer. *PASP*, 125:306.

[73] Frederick, S., Kara, E., Reynolds, C., Pinto, C., and Fabian, A. (2018). X-Ray Reverberation Mapping and Dramatic Variability of Seyfert 1 Galaxy 1H 1934-063. *ApJ*, 867:67.

[74] Fürst, F., Nowak, M. A., Tomsick, J. A., Miller, J. M., Corbel, S., Bachetti, M., Boggs, S. E., Christensen, F. E., Craig, W. W., Fabian, A. C., Gandhi, P., Grinberg, V., Hailey, C. J., Harrison, F. A., Kara, E., Kennea, J. A., Madsen, K. K., Pottschmidt, K., Stern, D., Walton, D. J., Wilms, J., and Zhang, W. W. (2015). The Complex Accretion Geometry of GX 339-4 as Seen by NuSTAR and Swift. *ApJ*, 808:122.

[75] Fürst, F., Walton, D. J., Harrison, F. A., Stern, D., Barret, D., Brightman, M., Fabian, A. C., Grefenstette, B., Madsen, K. K., Middleton, M. J., Miller, J. M., Pottschmidt, K., Ptak, A., Rana, V., and Webb, N. (2016). Discovery of Coherent Pulsations from the Ultraluminous X-Ray Source NGC 7793 P13. *ApJ*, 831:L14.

[76] Galeev, A. A., Rosner, R., and Vaiana, G. S. (1979). Structured coronae of accretion disks. *ApJ*, 229:318–326.

[77] Gallo, L. C., Boller, T., Tanaka, Y., Fabian, A. C., Brandt, W. N., Welsh, W. F., Anabuki, N., and Haba, Y. (2004). The X-ray variability of the narrow-line type 1 Seyfert galaxy IRAS 13224-3809 from an XMM-Newton observation. *MNRAS*, 347:269–276.

[78] Gallo, L. C. and Fabian, A. C. (2011). How the effects of resonant absorption on black hole reflection spectra can mimic high-velocity outflows. *MNRAS*, 418:L59–L63.

[79] Gallo, L. C. and Fabian, A. C. (2013). The origin of blueshifted absorption features in the X-ray spectrum of PG 1211+143: outflow or disc. *MNRAS*, 434:L66–L69.

[80] Gallo, L. C., Miniutti, G., Miller, J. M., Brenneman, L. W., Fabian, A. C., Guainazzi, M., and Reynolds, C. S. (2011). Multi-epoch X-ray observations of the Seyfert 1.2 galaxy Mrk 79: bulk motion of the illuminating X-ray source. *MNRAS*, 411:607–619.

[81] Gallo, L. C., Wilkins, D. R., Bonson, K., Chiang, C. Y., Grupe, D., Parker, M. L., Zoghbi, A., Fabian, A. C., Komossa, S., and Longinotti, A. L. (2015). Suzaku observations of Mrk 335: confronting partial covering and relativistic reflection. *MNRAS*, 446:633–650.

[82] García, J., Dauser, T., Lohfink, A., Kallman, T. R., Steiner, J. F., McClintock, J. E., Brenneman, L., Wilms, J., Eikmann, W., Reynolds, C. S., and Tombesi, F. (2014). Improved Reflection Models of Black Hole Accretion Disks: Treating the Angular Distribution of X-Rays. *ApJ*, 782:76.

[83] García, J., Dauser, T., Reynolds, C. S., Kallman, T. R., McClintock, J. E., Wilms, J., and Eikmann, W. (2013). X-Ray Reflected Spectra from Accretion Disk Models. III. A Complete Grid of Ionized Reflection Calculations. *ApJ*, 768:146.

[84] García, J. and Kallman, T. R. (2010). X-ray Reflected Spectra from Accretion Disk Models. I. Constant Density Atmospheres. *ApJ*, 718:695–706.

[85] García, J., Kallman, T. R., and Mushotzky, R. F. (2011). X-ray Reflected Spectra from Accretion Disk Models. II. Diagnostic Tools for X-ray Observations. *ApJ*, 731:131.

[86] García, J. A., Fabian, A. C., Kallman, T. R., Dauser, T., Parker, M. L., McClintock, J. E., Steiner, J. F., and Wilms, J. (2016). The effects of high density on the X-ray spectrum reflected from accretion discs around black holes. *MNRAS*, 462:751–760.

[87] García, J. A., Kallman, T. R., Bautista, M., Mendoza, C., Deprince, J., Palmeri, P., and Quinet, P. (2018). The Problem of the High Iron Abundance in Accretion Disks around Black Holes. In *Workshop on Astrophysical Opacities*, volume 515 of *Astronomical Society of the Pacific Conference Series*, page 282.

[88] Garcia, J. A., Kara, E., Walton, D., Beuchert, T., Dauser, T., Gatuzz, E., Balokovic, M., Steiner, J. F., Tombesi, F., Connors, R. M. T., Kallman, T. R., Harrison, F. A., Fabian, A., Wilms, J., Stern, D., Lanz, L., Ricci, C., and Ballantyne, D. R. (2018). The Soft-Excess in Mrk 509: Warm Corona or Relativistic Reflection? *arXiv e-prints*, page arXiv:1812.03194.

[89] García, J. A., Kara, E., Walton, D., Beuchert, T., Dauser, T., Gatuzz, E., Balokovic, M., Steiner, J. F., Tombesi, F., Connors, R. M. T., Kallman, T. R., Harrison, F. A., Fabian, A., Wilms, J., Stern, D., Lanz, L., Ricci, C., and Ballantyne, D. R. (2019). Implications of the Warm Corona and Relativistic Reflection Models for the Soft Excess in Mrk 509. *ApJ*, 871:88.

[90] García, J. A., Steiner, J. F., McClintock, J. E., Remillard, R. A., Grinberg, V., and Dauser, T. (2015). X-Ray Reflection Spectroscopy of the Black Hole GX 339–4: Exploring the Hard State with Unprecedented Sensitivity. *ApJ*, 813:84.

[91] George, I. M. and Fabian, A. C. (1991). X-ray reflection from cold matter in Active Galactic Nuclei and X-ray binaries. *MNRAS*, 249:352.

[92] Goodman, J. and Weare, J. (2010). Ensemble samplers with affine invariance. *Communications in Applied Mathematics and Computational Science, Vol. 5, No. 1, p. 65-80, 2010*, 5:65–80.

[93] Gou, L., McClintock, J. E., Remillard, R. A., Steiner, J. F., Reid, M. J., Orosz, J. A., Narayan, R., Hanke, M., and García, J. (2014). Confirmation via the Continuum-fitting Method that the Spin of the Black Hole in Cygnus X-1 Is Extreme. *ApJ*, 790:29.

[94] Greenstein, J. L. and Schmidt, M. (1964). The Quasi-Stellar Radio Sources 3C 48 and 3C 273. *ApJ*, 140:1.

[95] Grevesse, N., Noels, A., and Sauval, A. J. (1996). Standard Abundances. In Holt, S. S. and Sonneborn, G., editors, *Cosmic Abundances*, volume 99 of *Astronomical Society of the Pacific Conference Series*, page 117.

[96] Grevesse, N. and Sauval, A. J. (1998). Standard Solar Composition. *Space Sci. Rev.*, 85:161–174.

[97] Grinberg, V., Leutenegger, M. A., Hell, N., Pottschmidt, K., Böck, M., García, J. A., Hanke, M., Nowak, M. A., Sundqvist, J. O., Townsend, R. H. D., and Wilms, J. (2015). Long term variability of Cygnus X-1. VII. Orbital variability of the focussed wind in Cyg X-1/HDE 226868 system. *A&A*, 576:A117.

[98] Grupe, D., Komossa, S., and Gallo, L. C. (2007). Discovery of the Narrow-Line Seyfert 1 Galaxy Markarian 335 in a Historical Low X-Ray Flux State. *ApJ*, 668:L111–L114.

[99] Grupe, D., Komossa, S., Gallo, L. C., Longinotti, A. L., Fabian, A. C., Pradhan, A. K., Gruberbauer, M., and Xu, D. (2012). A Remarkable Long-term Light Curve and Deep, Low-state Spectroscopy: Swift and XMM-Newton Monitoring of the NLS1 Galaxy Mkn 335. *The Astrophysical Journal Supplement Series*, 199:28.

[100] Grupe, D., Komossa, S., Leighly, K. M., and Page, K. L. (2010). The Simultaneous Optical-to-X-Ray Spectral Energy Distribution of Soft X-Ray Selected Active Galactic Nuclei Observed by Swift. *ApJS*, 187:64–106.

[101] Guainazzi, M., Comastri, A., Stirpe, G. M., Brandt, W. N., Fiore, F., Leighly, K. M., Matt, G., Molendi, S., Puchnarewicz, E. M., Piro, L., and Siemiginowska, A. (1998). 1H0419-577: a "two-state" soft X-ray Seyfert galaxy. *A&A*, 339:327–336.

[102] Guilbert, P. W. and Rees, M. J. (1988). 'Cold' material in non-thermal sources. *MNRAS*, 233:475–484.

[103] Haardt, F. and Maraschi, L. (1991). A two-phase model for the X-ray emission from Seyfert galaxies. *ApJ*, 380:L51–L54.

[104] Haardt, F. and Maraschi, L. (1993a). X-ray spectra from two-phase accretion disks. *ApJ*, 413:507–517.

[105] Haardt, F. and Maraschi, L. (1993b). X-ray spectra from two-phase accretion disks. *ApJ*, 413:507–517.

[106] Hagino, K., Odaka, H., Done, C., Tomaru, R., Watanabe, S., and Takahashi, T. (2016). A disc wind interpretation of the strong Fe Kα features in 1H 0707-495. *MNRAS*, 461:3954–3963.

[107] Harmon, B. A., Fishman, G. J., Paciesas, W. S., and Zhang, S. N. (1993). X-Ray Nova in Ophiuchus. *International Astronomical Union Circular*, 5900:1.

[108] Harrison, F. A., Craig, W. W., Christensen, F. E., Hailey, C. J., Zhang, W. W., Boggs, S. E., Stern, D., Cook, W. R., Forster, K., Giommi, P., Grefenstette, B. W., Kim, Y., Kitaguchi, T., Koglin, J. E., Madsen, K. K., Mao, P. H., Miyasaka, H., Mori, K., Perri, M., Pivovaroff, M. J., Puccetti, S., Rana, V. R., Westergaard, N. J., Willis, J., Zoglauer, A., An, H., Bachetti, M., Barrière, N. M., Bellm, E. C., Bhalerao, V., Brejnholt, N. F., Fuerst, F., Liebe, C. C., Markwardt, C. B., Nynka, M., Vogel, J. K., Walton, D. J., Wik, D. R., Alexander, D. M., Cominsky, L. R., Hornschemeier, A. E., Hornstrup, A., Kaspi, V. M., Madejski, G. M., Matt, G., Molendi, S., Smith, D. M., Tomsick, J. A., Ajello, M., Ballantyne, D. R.,

Baloković, M., Barret, D., Bauer, F. E., Blandford, R. D., Brandt, W. N., Brenneman, L. W., Chiang, J., Chakrabarty, D., Chenevez, J., Comastri, A., Dufour, F., Elvis, M., Fabian, A. C., Farrah, D., Fryer, C. L., Gotthelf, E. V., Grindlay, J. E., Helfand, D. J., Krivonos, R., Meier, D. L., Miller, J. M., Natalucci, L., Ogle, P., Ofek, E. O., Ptak, A., Reynolds, S. P., Rigby, J. R., Tagliaferri, G., Thorsett, S. E., Treister, E., and Urry, C. M. (2013). The Nuclear Spectroscopic Telescope Array (NuSTAR) High-energy X-Ray Mission. *ApJ*, 770:103.

[109] Hazard, C., Mackey, M. B., and Shimmins, A. J. (1963). Investigation of the Radio Source 3C 273 By The Method of Lunar Occultations. *Nature*, 197:1037–1039.

[110] Heida, M., Jonker, P. G., Torres, M. A. P., and Chiavassa, A. (2017). The Mass Function of GX 339-4 from Spectroscopic Observations of Its Donor Star. *ApJ*, 846:132.

[111] Hirose, S., Krolik, J. H., and Stone, J. M. (2006). Vertical Structure of Gas Pressure-dominated Accretion Disks with Local Dissipation of Turbulence and Radiative Transport. *ApJ*, 640:901–917.

[112] Hjellming, M. R. and Wade, C. (1972). New directions and new frontiers in variable star research. International Astronomical Union, Colloquium No. 15 (5th colloquium on variable stars), Bamberg, 1971, 31 Aug - 3 Sep. *Veroeffentlichungen der Remeis-Sternwarte zu Bamberg*, 100.

[113] Hjellming, R. M., Rupen, M. P., Shrader, C. R., Campbell-Wilson, D., Hunstead, R. W., and McKay, D. J. (1996). Radio and X-Ray Flaring Events in X-Ray Nova Ophiuchi 1993. *ApJ*, 470:L105.

[114] Hönig, S. F., Kishimoto, M., Tristram, K. R. W., Prieto, M. A., Gandhi, P., Asmus, D., Antonucci, R., Burtscher, L., Duschl, W. J., and Weigelt, G. (2013). Dust in the Polar Region as a Major Contributor to the Infrared Emission of Active Galactic Nuclei. *ApJ*, 771:87.

[115] Hoyle, F. and Fowler, W. A. (1963). On the nature of strong radio sources. *MNRAS*, 125:169.

[116] Hynes, R. I., Steeghs, D., Casares, J., Charles, P. A., and O'Brien, K. (2003a). Dynamical Evidence for a Black Hole in GX 339-4. *ApJ*, 583:L95–L98.

[117] Hynes, R. I., Steeghs, D., Casares, J., Charles, P. A., and O'Brien, K. (2003b). Dynamical Evidence for a Black Hole in GX 339-4. *ApJ*, 583:L95–L98.

[118] Israel, G. L., Belfiore, A., Stella, L., Esposito, P., Casella, P., De Luca, A., Marelli, M., Papitto, A., Perri, M., Puccetti, S., Castillo, G. A. R., Salvetti, D., Tiengo, A., Zampieri, L., D'Agostino, D., Greiner, J., Haberl, F., Novara, G., Salvaterra, R., Turolla, R., Watson, M., Wilms, J., and Wolter, A. (2017a). An accreting pulsar with extreme properties drives an ultraluminous x-ray source in NGC 5907. *Science*, 355:817–819.

[119] Israel, G. L., Papitto, A., Esposito, P., Stella, L., Zampieri, L., Belfiore, A., Rodríguez Castillo, G. A., De Luca, A., Tiengo, A., Haberl, F., Greiner, J., Salvaterra, R., Sandrelli, S., and Lisini, G. (2017b). Discovery of a 0.42-s pulsar in the ultraluminous X-ray source NGC 7793 P13. *MNRAS*, 466:L48–L52.

[120] Jacobs, V. L., Davis, J., Kepple, P. C., and Blaha, M. (1977). The influence of autoionization accompanied by excitation on the dielectronic recombination and the ionization equilibrium of silicon ions. *ApJ*, 215:690–699.

[121] Jansen, F., Lumb, D., Altieri, B., Clavel, J., Ehle, M., Erd, C., Gabriel, C., Guainazzi, M., Gondoin, P., Much, R., Munoz, R., Santos, M., Schartel, N., Texier, D., and Vacanti, G. (2001). XMM-Newton observatory. I. The spacecraft and operations. *A&A*, 365:L1–L6.

[122] Jiang, J., Bambi, C., and Steiner, J. F. (2015). Using iron line reverberation and spectroscopy to distinguish Kerr and non-Kerr black holes. *J. Cosmology Astropart. Phys.*, 5:025.

[123] Jiang, J., Fabian, A. C., Wang, J., Walton, D. J., García, J. A., Parker, M. L., Steiner, J. F., and Tomsick, J. A. (2019a). High-density reflection spectroscopy: I. A case study of GX 339-4. *MNRAS*, 484:1972–1982.

[124] Jiang, J., Parker, M. L., Fabian, A. C., Alston, W. N., Buisson, D. J. K., Cackett, E. M., Chiang, C.-Y., Dauser, T., Gallo, L. C., García, J. A., Harrison, F. A., Lohfink, A. M., De Marco, B., Kara, E., Miller, J. M., Miniutti, G., Pinto, C., Walton, D. J., and Wilkins, D. R. (2018). The 1.5 Ms observing campaign on IRAS 13224-3809 - I. X-ray spectral analysis. *MNRAS*, 477:3711–3726.

[125] Jiang, J., Walton, D. J., Fabian, A. C., and Parker, M. L. (2019b). A relativistic disc reflection model for 1H0419-577: Multi-epoch spectral analysis with XMM-Newton and NuSTAR. *MNRAS*, 483:2958–2967.

[126] Jin, C., Done, C., Ward, M., Gierliński, M., and Mullaney, J. (2009). The Seyfert AGN RX J0136.9-3510 and the spectral state of super Eddington accretion flows. *MNRAS*, 398(1):L16–L20.

[127] Johannsen, T. and Psaltis, D. (2010). Testing the No-hair Theorem with Observations in the Electromagnetic Spectrum. I. Properties of a Quasi-Kerr Spacetime. *ApJ*, 716:187–197.

[128] Kaastra, J. S. and Bleeker, J. A. M. (2016). Optimal binning of X-ray spectra and response matrix design. *A&A*, 587:A151.

[129] Kalberla, P. M. W., Burton, W. B., Hartmann, D., Arnal, E. M., Bajaja, E., Morras, R., and Pöppel, W. G. L. (2005a). The Leiden/Argentine/Bonn (LAB) Survey of Galactic HI. Final data release of the combined LDS and IAR surveys with improved stray-radiation corrections. *A&A*, 440:775–782.

[130] Kalberla, P. M. W., Burton, W. B., Hartmann, D., Arnal, E. M., Bajaja, E., Morras, R., and Pöppel, W. G. L. (2005b). The Leiden/Argentine/Bonn (LAB) Survey of Galactic HI. Final data release of the combined LDS and IAR surveys with improved stray-radiation corrections. *A&A*, 440:775–782.

[131] Kallman, T. and Bautista, M. (2001). Photoionization and High-Density Gas. *The Astrophysical Journal Supplement Series*, 133:221–253.

[132] Kara, E., Alston, W. N., Fabian, A. C., Cackett, E. M., Uttley, P., Reynolds, C. S., and Zoghbi, A. (2016). A global look at X-ray time lags in Seyfert galaxies. *MNRAS*, 462:511–531.

[133] Kara, E., Fabian, A. C., Cackett, E. M., Miniutti, G., and Uttley, P. (2013a). Revealing the X-ray source in IRAS 13224-3809 through flux-dependent reverberation lags. *MNRAS*, 430:1408–1413.

[134] Kara, E., Fabian, A. C., Cackett, E. M., Steiner, J. F., Uttley, P., Wilkins, D. R., and Zoghbi, A. (2013b). The closest look at 1H0707-495: X-ray reverberation lags with 1.3 Ms of data. *MNRAS*, 428:2795–2804.

[135] Kara, E., Fabian, A. C., Cackett, E. M., Steiner, J. F., Uttley, P., Wilkins, D. R., and Zoghbi, A. (2013c). The closest look at 1H0707-495: X-ray reverberation lags with 1.3 Ms of data. *MNRAS*, 428:2795–2804.

[136] Kara, E., Fabian, A. C., Lohfink, A. M., Parker, M. L., Walton, D. J., Boggs, S. E., Christensen, F. E., Hailey, C. J., Harrison, F. A., Matt, G., Reynolds, C. S., Stern, D., and Zhang, W. W. (2015). The Compton hump and variable blue wing in the extreme low-flux NuSTAR observations of 1H0707-495. *MNRAS*, 449:234–242.

[137] Kara, E., García, J. A., Lohfink, A., Fabian, A. C., Reynolds, C. S., Tombesi, F., and Wilkins, D. R. (2017). The high-Eddington NLS1 Ark 564 has the coolest corona. *MNRAS*, 468:3489–3498.

[138] Kara, E., Steiner, J. F., Fabian, A. C., Cackett, E. M., Uttley, P., Remillard, R. A., Gendreau, K. C., Arzoumanian, Z., Altamirano, D., Eikenberry, S., Enoto, T., Homan, J., Neilsen, J., and Stevens, A. L. (2019). The corona contracts in a black-hole transient. *Nature*, 565:198–201.

[139] Kaspi, S., Smith, P. S., Netzer, H., Maoz, D., Jannuzi, B. T., and Giveon, U. (2000). Reverberation Measurements for 17 Quasars and the Size-Mass-Luminosity Relations in Active Galactic Nuclei. *ApJ*, 533:631–649.

[140] Kawaguchi, T., Mineshige, S., Machida, M., Matsumoto, R., and Shibata, K. (2000). Temporal 1/f Fluctuations from Fractal Magnetic Fields in Black-Hole Accretion Flow. *PASJ*, 52:L1.

[141] Kerr, R. P. (1963a). Gravitational field of a spinning mass as an example of algebraically special metrics. *Phys. Rev. Lett.*, 11:237–238.

[142] Kerr, R. P. (1963b). Gravitational field of a spinning mass as an example of algebraically special metrics. *Phys. Rev. Lett.*, 11:237–238.

[143] King, A. L., Lohfink, A., and Kara, E. (2017). AGN Coronae through a Jet Perspective. *ApJ*, 835:226.

[144] Kitamoto, S., Takahashi, K., Yamashita, K., Tanaka, Y., and Nagase, F. (1990). X-ray spectrum and iron line emission from Cygnus X-1. *PASJ*, 42:85–97.

[145] Kluzniak, W. and Abramowicz, M. A. (2001). Strong-Field Gravity and Orbital Resonance in Black Holes and Neutron Stars — kHz Quasi-Periodic Oscillations (QPO). *Acta Physica Polonica B*, 32:3605.

[146] Kolehmainen, M. and Done, C. (2010). Limits on spin determination from disc spectral fitting in gx 3394. *Monthly Notices of the Royal Astronomical Society*, 406(4):2206–2212.

[147] Kosec, P., Pinto, C., Fabian, A. C., and Walton, D. J. (2018). Searching for outflows in ultraluminous X-ray sources through high-resolution X-ray spectroscopy. *MNRAS*, 473:5680–5697.

[148] Krawczynski, H., Hughes, S. B., Horan, D., Aharonian, F., Aller, M. F., Aller, H., Boltwood, P., Buckley, J., Coppi, P., Fossati, G., Götting, N., Holder, J., Horns, D., Kurtanidze, O. M., Marscher, A. P., Nikolashvili, M., Remillard, R. A., Sadun, A., and Schröder, M. (2004). Multiwavelength Observations of Strong Flares from the TeV Blazar 1ES 1959+650. *ApJ*, 601:151–164.

[149] Kristian, J., Brucato, R., Visvanathan, N., Lanning, H., and Sandage, A. (1971). On the Optical Identification of Cygnus X-1. *ApJ*, 168:L91.

[150] Laor, A. (1991). Line profiles from a disk around a rotating black hole. *ApJ*, 376:90–94.

[151] Larsson, J., Miniutti, G., Fabian, A. C., Miller, J. M., Reynolds, C. S., and Ponti, G. (2008). Suzaku observations of Markarian 335: evidence for a distributed reflector. *MNRAS*, 384:1316–1326.

[152] Leighly, K. M. (2001). HST STIS Ultraviolet Spectral Evidence for Outflows in Extreme Narrow-Line Seyfert 1 Galaxies. In Peterson, B. M., Pogge, R. W., and Polidan, R. S., editors, *Probing the Physics of Active Galactic Nuclei*, volume 224 of *Astronomical Society of the Pacific Conference Series*, page 293.

[153] Leighly, K. M. and Moore, J. R. (2004). Hubble Space Telescope STIS Ultraviolet Spectral Evidence of Outflow in Extreme Narrow-Line Seyfert 1 Galaxies. I. Data and Analysis. *ApJ*, 611:107–124.

[154] Leighly, K. M., Mushotzky, R. F., Nandra, K., and Forster, K. (1997). Evidence for Relativistic Outflows in Narrow-Line Seyfert 1 Galaxies. *ApJ*, 489:L25–L28.

[155] Li, L.-X., Zimmerman, E. R., Narayan, R., and McClintock, J. E. (2005). Multitemperature Blackbody Spectrum of a Thin Accretion Disk around a Kerr Black Hole: Model Computations and Comparison with Observations. *ApJS*, 157:335–370.

[156] Liang, E. P. and Nolan, P. L. (1984). Cygnus X-1 revisited. *Space Sci. Rev.*, 38:353–384.

[157] LIGO Scientific Collaboration and VIRGO Collaboration (2016). GW151226: Observation of Gravitational Waves from a 22-Solar-Mass Binary Black Hole Coalescence. *Phys. Rev. Lett.*, 116:241103.

[158] LIGO Scientific Collaboration and Virgo Collaboration (2016). Observation of Gravitational Waves from a Binary Black Hole Merger. *Phys. Rev. Lett.*, 116:061102.

[159] Longinotti, A. L., Bianchi, S., Santos-Lleo, M., Rodríguez-Pascual, P., Guainazzi, M., Cardaci, M., and Pollock, A. M. T. (2007). An X-ray look at the Seyfert 1 Galaxy Mrk 590: XMM-Newton and Chandra reveal complexity in circumnuclear gas. *A&A*, 470:73–81.

[160] Longinotti, A. L., Krongold, Y., Kriss, G. A., Ely, J., Gallo, L., Grupe, D., Komossa, S., Mathur, S., and Pradhan, A. (2013). The Rise of an Ionized Wind in the Narrow-line Seyfert 1 Galaxy Mrk 335 Observed by XMM-Newton and HST. *ApJ*, 766:104.

[161] Lynden-Bell, D. (1969). Galactic Nuclei as Collapsed Old Quasars. *Nature*, 223:690–694.

[162] Lynden-Bell, D. and Rees, M. J. (1971). On quasars, dust and the galactic centre. *MNRAS*, 152:461.

[163] Madsen, K. K., Beardmore, A. P., Forster, K., Guainazzi, M., Marshall, H. L., Miller, E. D., Page, K. L., and Stuhlinger, M. (2017). IACHEC Cross-calibration of Chandra, NuSTAR, Swift, Suzaku, XMM-Newton with 3C 273 and PKS 2155-304. *AJ*, 153:2.

[164] Mallick, L., Alston, W. N., Parker, M. L., Fabian, A. C., Pinto, C., Dewangan, G. C., Markowitz, A., Gandhi, P., Kembhavi, A. K., and Misra, R. (2018). A high-density relativistic reflection origin for the soft and hard X-ray excess emission from Mrk 1044. *MNRAS*, 479:615–634.

[165] Marinucci, A., Matt, G., Kara, E., Miniutti, G., Elvis, M., Arevalo, P., Ballantyne, D. R., Baloković, M., Bauer, F., Brenneman, L., Boggs, S. E., Cappi, M., Christensen, F. E., Craig, W. W., Fabian, A. C., Fuerst, F., Hailey, C. J., Harrison, F. A., Risaliti, G., Reynolds, C. S., Stern, D. K., Walton, D. J., and Zhang, W. (2014). Simultaneous NuSTAR and XMM-Newton 0.5-80 keV spectroscopy of the narrow-line Seyfert 1 galaxy SWIFT J2127.4+5654. *MNRAS*, 440:2347–2356.

[166] Martocchia, A., Karas, V., and Matt, G. (2000). Effects of Kerr space-time on spectral features from X-ray illuminated accretion discs. *MNRAS*, 312:817–826.

[167] Martocchia, A. and Matt, G. (1996). Iron Kalpha line intensity from accretion discs around rotating black holes. *MNRAS*, 282:L53–L57.

[168] Martocchia, A., Matt, G., Karas, V., Belloni, T., and Feroci, M. (2002). Evidence for a relativistic iron line in GRS 1915+105. *A&A*, 387:215–221.

[169] Mas-Hesse, J. M., Rodriguez-Pascual, P. M., de Cordoba, L. S. F., and Boller, T. (1994). UV variability of IRAS 13224-3809, a rapidly X-ray variable far-infrared luminous galaxy. *A&A*, 283:L9–L12.

[170] Masetti, N., Bianchini, A., Bonibaker, J., della Valle, M., and Vio, R. (1996). The superhump phenomenon in GRS 1716-249 (=X-Ray Nova Ophiuchi 1993). *A&A*, 314:123–130.

[171] Masumitsu, T., Tanaka, K., Kawase, T., Negoro, H., Serino, M., Iwakiri, W., Ueno, S., Tomida, H., Nakahira, S., Ishikawa, M., Sugawara, Y., Mihara, T., Sugizaki, M., Shidatsu, M., Sugimoto, J., Takagi, T., Matsuoka, M., Kawai, N., Isobe, N., Sugita, S., Yoshii, T., Tachibana, Y., Ono, Y., Fujiwara, T., Harita, S., Muraki, Y., Yoshida, A., Sakamoto, T., Kawakubo, Y., Kitaoka, Y., Tsunemi, H., Shomura, R., Nakajima, M., Ueda, Y., Kawamuro, T., Hori, T., Oda, S., Tanimoto, A., Tsuboi, Y., Nakamura, Y., Sasaki, R., Yamauchi, M., Furuya, K., and Yamaoka, K. (2016). Further MAXI/GSC observations show that GRS 1716-249/GRO J1719-24 is in outburst and currently in the hard state. *The Astronomer's Telegram*, 9895:1.

[172] Matsuoka, M., Kawasaki, K., Ueno, S., Tomida, H., Kohama, M., Suzuki, M., Adachi, Y., Ishikawa, M., Mihara, T., Sugizaki, M., Isobe, N., Nakagawa, Y., Tsunemi, H., Miyata, E., Kawai, N., Kataoka, J., Morii, M., Yoshida, A., Negoro, H., Nakajima, M., Ueda, Y., Chujo, H., Yamaoka, K., Yamazaki, O., Nakahira, S., You, T., Ishiwata, R., Miyoshi, S., Eguchi, S.,

Hiroi, K., Katayama, H., and Ebisawa, K. (2009). The MAXI Mission on the ISS: Science and Instruments for Monitoring All-Sky X-Ray Images. *PASJ*, 61:999–1010.

[173] Matt, G., Marinucci, A., Guainazzi, M., Brenneman, L. W., Elvis, M., Lohfink, A., Arèvalo, P., Boggs, S. E., Cappi, M., Christensen, F. E., Craig, W. W., Fabian, A. C., Fuerst, F., Hailey, C. J., Harrison, F. A., Parker, M., Reynolds, C. S., Stern, D., Walton, D. J., and Zhang, W. W. (2014). The soft-X-ray emission of Ark 120. XMM-Newton, NuSTAR, and the importance of taking the broad view. *MNRAS*, 439:3016–3021.

[174] Matt, G., Perola, G. C., Costa, E., and Piro, L. (1989). X ray polarization of the reprocessed emission from accretion disk in Seyfert galaxies. In Hunt, J. and Battrick, B., editors, *Two Topics in X-Ray Astronomy, Volume 1: X Ray Binaries. Volume 2: AGN and the X Ray Background*, volume 296 of *ESA Special Publication*.

[175] Matzeu, G. A., Reeves, J. N., Braito, V., Nardini, E., McLaughlin, D. E., Lobban, A. P., Tombesi, F., and Costa, M. T. (2017). Evidence for a radiatively driven disc-wind in PDS\,456? *ArXiv e-prints*.

[176] Matzeu, G. A., Reeves, J. N., Nardini, E., Braito, V., Costa, M. T., Tombesi, F., and Gofford, J. (2016). Short-term X-ray spectral variability of the quasar PDS 456 observed in a low-flux state. *MNRAS*, 458:1311–1329.

[177] McClintock, J. E., Narayan, R., and Steiner, J. F. (2014). Black Hole Spin via Continuum Fitting and the Role of Spin in Powering Transient Jets. *Space Sci. Rev.*, 183:295–322.

[178] McHardy, I. M., Koerding, E., Knigge, C., Uttley, P., and Fender, R. P. (2006). Active galactic nuclei as scaled-up Galactic black holes. *Nature*, 444:730–732.

[179] McLure, R. J. and Dunlop, J. S. (2004). The cosmological evolution of quasar black hole masses. *MNRAS*, 352:1390–1404.

[180] Merloni, A. and Fabian, A. C. (2001). Accretion disc coronae as magnetic reservoirs. *MNRAS*, 321:549–552.

[181] Michell, J. (1784). On the Means of Discovering the Distance, Magnitude, c. of the Fixed Stars, in Consequence of the Diminution of the Velocity of Their Light, in Case Such a Diminution Should be Found to Take Place in any of Them, and Such Other Data Should be Procured from Observations, as Would be Farther Necessary for That Purpose. By the Rev. John Michell, B. D. F. R. S. In a Letter to Henry Cavendish, Esq. F. R. S. and A. S. *Philosophical Transactions of the Royal Society of London Series I*, 74:35–57.

[182] Miller, J. M. (2006). A short review of relativistic iron lines from stellar-mass black holes. *Astronomische Nachrichten*, 327:997.

[183] Miller, J. M. (2007). Relativistic X-Ray Lines from the Inner Accretion Disks Around Black Holes. *Annual Review of Astronomy and Astrophysics*, 45:441–479.

[184] Miller, J. M., D'Aì, A., Bautz, M. W., Bhattacharyya, S., Burrows, D. N., Cackett, E. M., Fabian, A. C., Freyberg, M. J., Haberl, F., Kennea, J., Nowak, M. A., Reis, R. C., Strohmayer, T. E., and Tsujimoto, M. (2010). On Relativistic Disk Spectroscopy in Compact Objects with X-ray CCD Cameras. *ApJ*, 724:1441–1455.

[185] Miller, J. M., Fabian, A. C., in't Zand, J. J. M., Reynolds, C. S., Wijnands, R., Nowak, M. A., and Lewin, W. H. G. (2002). A Relativistic Fe Kα Emission Line in the Intermediate-Luminosity BeppoSAX Spectrum of the Galactic Microquasar V4641 Sgr. *ApJ*, 577:L15–L18.

[186] Miller, J. M., Fabian, A. C., Reynolds, C. S., Nowak, M. A., Homan, J., Freyberg, M. J., Ehle, M., Belloni, T., Wijnands, R., van der Klis, M., Charles, P. A., and Lewin, W. H. G. (2004). Evidence of Black Hole Spin in GX 339-4: XMM-Newton/EPIC-pn and RXTE Spectroscopy of the Very High State. *ApJ*, 606:L131–L134.

[187] Miller, J. M., Homan, J., Steeghs, D., Rupen, M., Hunstead, R. W., Wijnands, R., Charles, P. A., and Fabian, A. C. (2006). A Long, Hard Look at the Low/Hard State in Accreting Black Holes. *ApJ*, 653:525–535.

[188] Miller, J. M., Reynolds, C. S., Fabian, A. C., Cackett, E. M., Miniutti, G., Raymond, J., Steeghs, D., Reis, R., and Homan, J. (2008). Initial Measurements of Black Hole Spin in GX 339-4 from Suzaku Spectroscopy. *ApJ*, 679:L113.

[189] Miller, J. M., Reynolds, C. S., Fabian, A. C., Miniutti, G., and Gallo, L. C. (2009). Stellar-Mass Black Hole Spin Constraints from Disk Reflection and Continuum Modeling. *ApJ*, 697:900–912.

[190] Miniutti, G., Fabian, A. C., Goyder, R., and Lasenby, A. N. (2003). The lack of variability of the iron line in MCG-6-30-15: general relativistic effects. *MNRAS*, 344:L22–L26.

[191] Miniutti, G., Fabian, A. C., and Miller, J. M. (2004). The relativistic Fe emission line in XTE J1650-500 with BeppoSAX: evidence for black hole spin and light-bending effects? *MNRAS*, 351:466–472.

[192] Miniutti, G., Panessa, F., de Rosa, A., Fabian, A. C., Malizia, A., Molina, M., Miller, J. M., and Vaughan, S. (2009). An intermediate black hole spin in the NLS1 galaxy SWIFT J2127.4+5654: chaotic accretion or spin energy extraction? *MNRAS*, 398:255–262.

[193] Mizumoto, M., Ebisawa, K., Tsujimoto, M., and Inoue, H. (2016). Origin of the X-ray broad iron spectral feature in GRS 1915+105. *PASJ*, 68:S16.

[194] Moran, E. C., Barth, A. J., Kay, L. E., and Filippenko, A. V. (2000). The Frequency of Polarized Broad Emission Lines in Type 2 Seyfert Galaxies. *ApJ*, 540:L73–L77.

[195] Morgan, C. W., Kochanek, C. S., Dai, X., Morgan, N. D., and Falco, E. E. (2008). X-Ray and Optical Microlensing in the Lensed Quasar PG 1115+080. *ApJ*, 689:755–761.

[196] Morrison, R. and McCammon, D. (1983). Interstellar photoelectric absorption cross sections, 0.03-10 keV. *ApJ*, 270:119–122.

[197] Motta, S. E. (2016). Quasi periodic oscillations in black hole binaries. *Astronomische Nachrichten*, 337:398.

[198] Muñoz-Darias, T., Casares, J., and Martínez-Pais, I. G. (2008). On the masses and evolutionary status of the black hole binary GX 339-4: a twin system of XTE J1550-564? *MNRAS*, 385:2205–2209.

[199] Muñoz-Darias, T., Motta, S., Stiele, H., and Belloni, T. M. (2011). The black hole candidate MAXI J1659-152: spectral and timing analysis during its 2010 outburst. *MNRAS*, 415:292–300.

[200] Murray, N., Chiang, J., Grossman, S. A., and Voit, G. M. (1995). Accretion Disk Winds from Active Galactic Nuclei. *ApJ*, 451:498.

[201] Mushotzky, R. F., Done, C., and Pounds, K. A. (1993). X-ray spectra and time variability of active galactic nuclei. *ARA&A*, 31:717–761.

[202] Nagao, T., Murayama, T., and Taniguchi, Y. (2001). The Narrow-Line Region of Seyfert Galaxies: Narrow-Line Seyfert 1 Galaxies versus Broad-Line Seyfert 1 Galaxies. *ApJ*, 546:744–758.

[203] Nandra, K., O'Neill, P. M., George, I. M., and Reeves, J. N. (2007). An XMM-Newton survey of broad iron lines in Seyfert galaxies. *MNRAS*, 382:194–228.

[204] Nandra, K., Pounds, K. A., and Stewart, G. C. (1990). The X-ray spectrum of MCG-6-30-15 and its temporal variability. *MNRAS*, 242:660–668.

[205] Narayan, R. (2005). Low-Luminosity Accretion in Black Hole X-Ray Binaries and Active Galactic Nuclei. *Ap&SS*, 300:177–188.

[206] Narayan, R. and McClintock, J. E. (2008). Advection-dominated accretion and the black hole event horizon. *New Astron. Rev.*, 51:733–751.

[207] Narayan, R. and Yi, I. (1995). Advection-dominated Accretion: Underfed Black Holes and Neutron Stars. *ApJ*, 452:710.

[208] Narayan, R., Yi, I., and Mahadevan, R. (1995). Explaining the spectrum of Sagittarius A* with a model of an accreting black hole. *Nature*, 374:623–625.

[209] Nardini, E., Fabian, A. C., and Walton, D. J. (2012). Investigating the reflection contribution to the X-ray emission of Ton S180. *MNRAS*, 423:3299–3307.

[210] Nardini, E., Porquet, D., Reeves, J. N., Braito, V., Lobban, A., and Matt, G. (2016). A Deep X-Ray View of the Bare AGN Ark 120. II. Evidence for Fe K Emission Transients. *ApJ*, 832:45.

[211] Nayakshin, S. and Kallman, T. R. (2001). Accretion Disk Models and Their X-Ray Reflection Signatures. I. Local Spectra. *ApJ*, 546:406–418.

[212] Negoro, H., Masumitsu, T., Kawase, T., Tanaka, K., Serino, M., Tanimoto, A., Ueno, S., Tomida, H., Nakahira, S., Ishikawa, M., Sugawara, Y., Mihara, T., Sugizaki, M., Iwakiri, W., Shidatsu, M., Sugimoto, J., Takagi, T., Matsuoka, M., Kawai, N., Isobe, N., Sugita, S., Yoshii, T., Tachibana, Y., Ono, Y., Fujiwara, T., Harita, S., Muraki, Y., Yoshida, A., Sakamoto, T., Kawakubo, Y., Kitaoka, Y., Tsunemi, H., Shomura, R., Nakajima, M., Ueda, Y., Kawamuro, T., Hori, T., Oda, S., Tsuboi, Y., Nakamura, Y., Sasaki, R., Yamauchi, M., Furuya, K., and Yamaoka, K. (2016). MAXI/GSC detection of a new outburst from GRS 1716-249/GRO J1719-24 or a new X-ray transient MAXI J1719-254. *The Astronomer's Telegram*, 9876:1.

[213] Noble, S. C., Krolik, J. H., and Hawley, J. F. (2010). Dependence of Inner Accretion Disk Stress on Parameters: The Schwarzschild Case. *ApJ*, 711:959–973.

[214] Novikov, I. D. and Thorne, K. S. (1973). Astrophysics of black holes. In Dewitt, C. and Dewitt, B. S., editors, *Black Holes (Les Astres Occlus)*, pages 343–450.

[215] Oda, M., Gorenstein, P., Gursky, H., Kellogg, E., Schreier, E., Tananbaum, H., and Giacconi, R. (1971). X-Ray Pulsations from Cygnus X-1 Observed from UHURU. *ApJ*, 166:L1.

[216] Oh, K., Koss, M., Markwardt, C. B., Schawinski, K., Baumgartner, W. H., Barthelmy, S. D., Cenko, S. B., Gehrels, N., Mushotzky, R., Petulante, A., Ricci, C., Lien, A., and Trakhtenbrot, B. (2018). The 105-Month Swift-BAT All-sky Hard X-Ray Survey. *ApJS*, 235:4.

[217] Oke, J. B. (1963). Absolute Energy Distribution in the Optical Spectrum of 3C 273. *Nature*, 197:1040–1041.

[218] Orosz, J. A., McClintock, J. E., Aufdenberg, J. P., Remillard, R. A., Reid, M. J., Narayan, R., and Gou, L. (2011). The Mass of the Black Hole in Cygnus X-1. *ApJ*, 742:84.

[219] Orosz, J. A., McClintock, J. E., Narayan, R., Bailyn, C. D., Hartman, J. D., Macri, L., Liu, J., Pietsch, W., Remillard, R. A., Shporer, A., and Mazeh, T. (2007). A 15.65-solar-mass black hole in an eclipsing binary in the nearby spiral galaxy M 33. *Nature*, 449(7164):872–875.

[220] Osterbrock, D. E. and Phillips, M. M. (1977). Emission-line spectra of seven Arakelian galaxies. *PASP*, 89:251–254.

[221] Page, D. N. and Thorne, K. S. (1974). Disk-Accretion onto a Black Hole. Time-Averaged Structure of Accretion Disk. *ApJ*, 191:499–506.

[222] Page, K. L., Schartel, N., Turner, M. J. L., and O'Brien, P. T. (2004). XMM-Newton observations of seven soft X-ray excess quasi-stellar objects. *MNRAS*, 352:523–534.

[223] Panessa, F. and Bassani, L. (2002). Unabsorbed Seyfert 2 galaxies. *A&A*, 394:435–442.

[224] Pappa, A., Georgantopoulos, I., Stewart, G. C., and Zezas, A. L. (2001). The X-ray spectra of optically selected Seyfert 2 galaxies: are there any Seyfert 2 galaxies with no absorption? *MNRAS*, 326:995–1006.

[225] Parker, M. L., Alston, W. N., Buisson, D. J. K., Fabian, A. C., Jiang, J., Kara, E., Lohfink, A., Pinto, C., and Reynolds, C. S. (2017). Revealing the ultrafast outflow in IRAS 132243809 through spectral variability. *MNRAS*, 469:1553.

[226] Parker, M. L., Buisson, D. J. K., Jiang, J., Gallo, L. C., Kara, E., Matzeu, G. A., and Walton, D. J. (2018a). Constraining the geometry of AGN outflows with reflection spectroscopy. *MNRAS*, 479:L45–L49.

[227] Parker, M. L., Fabian, A. C., Matt, G., Koljonen, K. I. I., Kara, E., Alston, W., Walton, D. J., Marinucci, A., Brenneman, L., and Risaliti, G. (2015). Revealing the X-ray variability of AGN with principal component analysis. *MNRAS*, 447:72–96.

[228] Parker, M. L., Miller, J. M., and Fabian, A. C. (2018b). X-ray reflection from the inner disc of the AGN Ton S180. *MNRAS*, 474:1538–1544.

[229] Parker, M. L., Pinto, C., Fabian, A. C., Lohfink, A., Buisson, D. J. K., Alston, W. N., Kara, E., Cackett, E. M., Chiang, C.-Y., Dauser, T., De Marco, B., Gallo, L. C., Garcia, J., Harrison, F. A., King, A. L., Middleton, M. J., Miller, J. M., Miniutti, G., Reynolds, C. S., Uttley, P., Vasudevan, R., Walton, D. J., Wilkins, D. R., and Zoghbi, A. (2017). The response of relativistic outflowing gas to the inner accretion disk of a black hole. *Nature*, 543:83–86.

[230] Parker, M. L., Tomsick, J. A., Kennea, J. A., Miller, J. M., Harrison, F. A., Barret, D., Boggs, S. E., Christensen, F. E., Craig, W. W., Fabian, A. C., Fürst, F., Grinberg, V., Hailey, C. J., Romano, P., Stern, D., Walton, D. J., and Zhang, W. W. (2016). NuSTAR and Swift Observations of the Very High State in GX 339-4: Weighing the Black Hole with X-Rays. *ApJ*, 821:L6.

[231] Parker, M. L., Wilkins, D. R., Fabian, A. C., Grupe, D., Dauser, T., Matt, G., Harrison, F. A., Brenneman, L., Boggs, S. E., Christensen, F. E., Craig, W. W., Gallo, L. C., Hailey, C. J., Kara, E., Komossa, S., Marinucci, A., Miller, J. M., Risaliti, G., Stern, D., Walton, D. J., and Zhang, W. W. (2014). The NuSTAR spectrum of Mrk 335: extreme relativistic effects within two gravitational radii of the event horizon? *MNRAS*, 443:1723–1732.

[232] Pasham, D. R., Remillard, R. A., Fragile, P. C., Franchini, A., Stone, N. C., Lodato, G., Homan, J., Chakrabarty, D., Baganoff, F. K., Steiner, J. F., Coughlin, E. R., and Pasham, N. R. (2019). A loud quasi-periodic oscillations after a star is disrupted by a massive black hole. *Science*, 363:531–534.

[233] Pei, Y. C. (1992). Interstellar Dust from the Milky Way to the Magellanic Clouds. *ApJ*, 395:130.

[234] Petrucci, P. O., Paltani, S., Malzac, J., Kaastra, J. S., Cappi, M., Ponti, G., De Marco, B., Kriss, G. A., Steenbrugge, K. C., Bianchi, S., Branduardi-Raymont, G., Mehdipour, M., Costantini, E., Dadina, M., and Lubiński, P. (2013). Multiwavelength campaign on Mrk 509. XII. Broad band spectral analysis. *A&A*, 549:A73.

[235] Pinto, C., Alston, W., Parker, M. L., Fabian, A. C., Gallo, L. C., Buisson, D. J. K., Walton, D. J., Kara, E., Jiang, J., Lohfink, A., and Reynolds, C. S. (2017a). Ultrafast outflows disappear in high radiation fields. *ArXiv e-prints*.

[236] Pinto, C., Fabian, A., Middleton, M., and Walton, D. (2017b). Ultrafast outflows in ultraluminous X-ray sources. *Astronomische Nachrichten*, 338:234–240.

[237] Pinto, C., Middleton, M. J., and Fabian, A. C. (2016). Resolved atomic lines reveal outflows in two ultraluminous X-ray sources. *Nature*, 533:64–67.

[238] Plant, D. S., Fender, R. P., Ponti, G., Muñoz-Darias, T., and Coriat, M. (2015). The truncated and evolving inner accretion disc of the black hole gx 339-4. *A&A*, 573:A120.

[239] Ponti, G., Gallo, L. C., Fabian, A. C., Miniutti, G., Zoghbi, A., Uttley, P., Ross, R. R., Vasudevan, R. V., Tanaka, Y., and Brandt, W. N. (2010). Relativistic disc reflection in the extreme NLS1 IRAS13224-3809. *MNRAS*, 406:2591–2604.

[240] Porquet, D., Done, C., Reeves, J. N., Grosso, N., Marinucci, A., Matt, G., Lobban, A., Nardini, E., Braito, V., Marin, F., Kubota, A., Ricci, C., Koss, M., Stern, D., Ballantyne, and Farrah, D. (2019). A deep X-ray view of the bare AGN Ark120. V. Spin determination from disc-Comptonisation efficiency method. *arXiv e-prints*, page arXiv:1901.01812.

[241] Pounds, K. (2005). Exploring X-ray emission and absorption in AGN with XMM-Newton EPIC. In Briel, U. G., Sembay, S., and Read, A., editors, *5 years of Science with XMM-Newton*, pages 65–71.

[242] Pounds, K. A., Nandra, K., Stewart, G. C., George, I. M., and Fabian, A. C. (1990). X-ray reflection from cold matter in the nuclei of active galaxies. *Nature*, 344:132.

[243] Pounds, K. A., Reeves, J. N., Page, K. L., and O'Brien, P. T. (2004a). An XMM-Newton Observation of the Seyfert 1 Galaxy 1H 0419-577 in an Extreme Low State. *ApJ*, 605:670–676.

[244] Pounds, K. A., Reeves, J. N., Page, K. L., and O'Brien, P. T. (2004b). Resolving the Large-Scale Spectral Variability of the Luminous Seyfert 1 Galaxy 1H 0419-577: Evidence for a New Emission Component and Absorption by Cold Dense Matter. *ApJ*, 616:696–706.

[245] Raimundo, S. I., Fabian, A. C., Vasudevan, R. V., Gandhi, P., and Wu, J. (2012). Can we measure the accretion efficiency of active galactic nuclei? *MNRAS*, 419:2529–2544.

[246] Reeves, J. N., Porquet, D., Braito, V., Nardini, E., Lobban, A., and Turner, T. J. (2016). A Deep X-Ray View of the Bare AGN Ark 120. I. Revealing the Soft X-Ray Line Emission. *ApJ*, 828:98.

[247] Reid, M. J., McClintock, J. E., Narayan, R., Gou, L., Remillard, R. A., and Orosz, J. A. (2011). The Trigonometric Parallax of Cygnus X-1. *ApJ*, 742(2):83.

[248] Reis, R. C., Fabian, A. C., Reynolds, C. S., Brenneman, L. W., Walton, D. J., Trippe, M., Miller, J. M., Mushotzky, R. F., and Nowak, M. A. (2012). X-Ray Spectral Variability in NGC 3783. *ApJ*, 745:93.

[249] Reis, R. C., Fabian, A. C., Ross, R. R., Miniutti, G., Miller, J. M., and Reynolds, C. (2008). A systematic look at the very high and low/hard state of GX339-4: constraining the black hole spin with a new reflection model. *MNRAS*, 387:1489–1498.

[250] Reis, R. C. and Miller, J. M. (2013). On the Size and Location of the X-Ray Emitting Coronae around Black Holes. *ApJ*, 769:L7.

[251] Reis, R. C., Miller, J. M., Reynolds, M. T., Fabian, A. C., Walton, D. J., Cackett, E., and Steiner, J. F. (2013). Evidence of Light-bending Effects and Its Implication for Spectral State Transitions. *ApJ*, 763:48.

[252] Remillard, R. A. and McClintock, J. E. (2006). X-Ray Properties of Black-Hole Binaries. *Annual Review of Astronomy and Astrophysics*, 44:49–92.

[253] Reynolds, C. S. (2014). Measuring Black Hole Spin Using X-Ray Reflection Spectroscopy. *Space Sci. Rev.*, 183:277–294.

[254] Reynolds, C. S. (2019). Observing black holes spin. *Nature Astronomy*, 3:41–47.

[255] Reynolds, C. S., Brenneman, L. W., Lohfink, A. M., Trippe, M. L., Miller, J. M., Fabian, A. C., and Nowak, M. A. (2012). A Monte Carlo Markov Chain Based Investigation of Black Hole Spin in the Active Galaxy NGC 3783. *ApJ*, 755:88.

[256] Reynolds, C. S. and Nowak, M. A. (2003). Fluorescent iron lines as a probe of astrophysical black hole systems. *Phys. Rep.*, 377:389–466.

[257] Ricci, C., Tazaki, F., Ueda, Y., Paltani, S., Boissay, R., and Terashima, Y. (2014). Suzaku Observation of IRAS 00521-7054, a Peculiar Type-II AGN with a Very Broad Feature at 6 keV. *ApJ*, 795:147.

[258] Risaliti, G., Harrison, F. A., Madsen, K. K., Walton, D. J., Boggs, S. E., Christensen, F. E., Craig, W. W., Grefenstette, B. W., Hailey, C. J., Nardini, E., Stern, D., and Zhang, W. W. (2013). A rapidly spinning supermassive black hole at the centre of NGC 1365. *Nature*, 494:449–451.

[259] Risaliti, G., Maiolino, R., and Salvati, M. (1999). The Distribution of Absorbing Column Densities among Seyfert 2 Galaxies. *ApJ*, 522:157–164.

[260] Rodriguez-Pascual, P. M., Mas-Hesse, J. M., and Santos-Lleo, M. (1997). The broad line region of narrow-line Seyfert 1 galaxies. *A&A*, 327:72–80.

[261] Roming, P. W. A., Kennedy, T. E., Mason, K. O., Nousek, J. A., Ahr, L., Bingham, R. E., Broos, P. S., Carter, M. J., Hancock, B. K., Huckle, H. E., Hunsberger, S. D., Kawakami, H., Killough, R., Koch, T. S., McLelland, M. K., Smith, K., Smith, P. J., Soto, J. C., Boyd, P. T., Breeveld, A. A., Holland, S. T., Ivanushkina, M., Pryzby, M. S., Still, M. D., and Stock, J. (2005). The Swift Ultra-Violet/Optical Telescope. *Space Sci. Rev.*, 120:95–142.

[262] Ross, R. R. (1979). Spectral formation in compact X-ray sources. *ApJ*, 233:334–343.

[263] Ross, R. R. and Fabian, A. C. (1993). The effects of photoionization on X-ray reflection spectra in active galactic nuclei. *MNRAS*, 261:74–82.

[264] Ross, R. R. and Fabian, A. C. (2005). A comprehensive range of X-ray ionized-reflection models. *MNRAS*, 358:211–216.

[265] Ross, R. R. and Fabian, A. C. (2007). X-ray reflection in accreting stellar-mass black hole systems. *MNRAS*, 381:1697–1701.

[266] Ross, R. R., Weaver, R., and McCray, R. (1978). The Comptonization of iron X-ray features in compact X-ray sources. *ApJ*, 219:292–299.

[267] Rossi, S., Homan, J., Miller, J. M., and Belloni, T. (2005). Iron-line and continuum flux variations in the RXTE spectra of the black hole candidate XTE J1650-500. *MNRAS*, 360:763–768.

[268] Różańska, A., Dumont, A. M., Czerny, B., and Collin, S. (2002). The structure and radiation spectra of illuminated accretion discs in active galactic nuclei - I. Moderate illumination. *MNRAS*, 332:799–813.

[269] Sani, E., Lutz, D., Risaliti, G., Netzer, H., Gallo, L. C., Trakhtenbrot, B., Sturm, E., and Boller, T. (2010). Enhanced star formation in narrow-line Seyfert 1 active galactic nuclei revealed by Spitzer. *MNRAS*, 403:1246–1260.

[270] Schmidt, M. (1963). 3C 273 : A Star-Like Object with Large Red-Shift. *Nature*, 197:1040.

[271] Schnittman, J. D., Krolik, J. H., and Noble, S. C. (2013). X-Ray Spectra from Magnetohydrodynamic Simulations of Accreting Black Holes. *ApJ*, 769:156.

[272] Schödel, R., Ott, T., Genzel, R., Hofmann, R., Lehnert, M., Eckart, A., Mouawad, N., Alexander, T., Reid, M. J., Lenzen, R., Hartung, M., Lacombe, F., Rouan, D., Gendron, E., Rousset, G., Lagrange, A.-M., Brandner, W., Ageorges, N., Lidman, C., Moorwood, A. F. M., Spyromilio, J., Hubin, N., and Menten, K. M. (2002). A star in a 15.2-year orbit around the supermassive black hole at the centre of the Milky Way. *Nature*, 419:694–696.

[273] Schwarzschild, K. (1916). On the Gravitational Field of a Mass Point According to Einstein's Theory. *Abh. Konigl. Preuss. Akad. Wissenschaften Jahre 1906,92, Berlin,1907*, 1916.

[274] Sesana, A., Barausse, E., Dotti, M., and Rossi, E. M. (2014). Linking the Spin Evolution of Massive Black Holes to Galaxy Kinematics. *ApJ*, 794:104.

[275] Seyfert, C. K. (1943). Nuclear Emission in Spiral Nebulae. *ApJ*, 97:28.

[276] Shafee, R., McClintock, J. E., Narayan, R., Davis, S. W., Li, L.-X., and Remillard, R. A. (2006). Estimating the Spin of Stellar-Mass Black Holes by Spectral Fitting of the X-Ray Continuum. *ApJ*, 636:L113–L116.

[277] Shakura, N. I. and Sunyaev, R. A. (1973). Black holes in binary systems. Observational appearance. *A&A*, 24:337–355.

[278] Shemmer, O., Brandt, W. N., Netzer, H., Maiolino, R., and Kaspi, S. (2006). The Hard X-Ray Spectral Slope as an Accretion Rate Indicator in Radio-quiet Active Galactic Nuclei. *ApJ*, 646:L29–L32.

[279] Shi, Y., Rieke, G. H., Smith, P., Rigby, J., Hines, D., Donley, J., Schmidt, G., and Diamond-Stanic, A. M. (2010). Unobscured Type 2 Active Galactic Nuclei. *ApJ*, 714:115–129.

[280] Smith, H. J. and Hoffleit, D. (1963). Light Variations in the Superluminous Radio Galaxy 3C273. *Nature*, 198:650–651.

[281] Soleri, P., Muñoz-Darias, T., Motta, S., Belloni, T., Casella, P., Méndez, M., Altamirano, D., Linares, M., Wijnands, R., Fender, R., and van der Klis, M. (2013). A complex state transition from the black hole candidate Swift J1753.5-0127. *MNRAS*, 429:1244–1257.

[282] Steiner, J. F., McClintock, J. E., Remillard, R. A., Gou, L., Yamada, S., and Narayan, R. (2010). The Constant Inner-disk Radius of LMC X-3: A Basis for Measuring Black Hole Spin. *ApJ*, 718:L117–L121.

[283] Steiner, J. F., Reis, R. C., Fabian, A. C., Remillard, R. A., McClintock, J. E., Gou, L., Cooke, R., Brenneman, L. W., and Sanders, J. S. (2012). A broad iron line in LMC X-1. *MNRAS*, 427:2552–2561.

[284] Stella, L. and Rosner, R. (1984). Magnetic field instabilities in accretion disks. *ApJ*, 277:312–321.

[285] Strüder, L., Briel, U., Dennerl, K., Hartmann, R., Kendziorra, E., Meidinger, N., Pfeffermann, E., Reppin, C., Aschenbach, B., Bornemann, W., Bräuninger, H., Burkert, W., Elender, M., Freyberg, M., Haberl, F., Hartner, G., Heuschmann, F., Hippmann, H., Kastelic, E., Kemmer, S., Kettenring, G., Kink, W., Krause, N., Müller, S., Oppitz, A., Pietsch, W., Popp, M., Predehl, P., Read, A., Stephan, K. H., Stötter, D., Trümper, J., Holl, P., Kemmer, J., Soltau, H., Stötter, R., Weber, U., Weichert, U., von Zanthier, C., Carathanassis, D., Lutz, G., Richter, R. H., Solc, P., Böttcher, H., Kuster, M., Staubert, R., Abbey, A., Holland, A., Turner, M., Balasini, M., Bignami, G. F., La Palombara, N., Villa, G., Buttler, W., Gianini, F., Lainé, R., Lumb, D., and Dhez, P. (2001). The European Photon Imaging Camera on XMM-Newton: The pn-CCD camera. *A&A*, 365:L18–L26.

[286] Summers, H. P. (1974). The ionization equilibrium of hydrogen-like to argon-like ions of elements. *MNRAS*, 169:663–680.

[287] Svensson, R. (1984). Steady mildly relativistic thermal plasmas - Processes and properties. *MNRAS*, 209:175–208.

[288] Svensson, R. and Zdziarski, A. A. (1994). Black hole accretion disks with coronae. *ApJ*, 436:599–606.

[289] Takahashi, H., Hayashida, K., and Anabuki, N. (2010). Suzaku Wide-Band X-Ray Observation of the Narrow-Line Seyfert 1 Galaxy Ton S180. *Publications of the Astronomical Society of Japan*, 62:1483.

[290] Tan, Y., Wang, J. X., Shu, X. W., and Zhou, Y. (2012). A Possible Ultra Strong and Broad Fe Kα Emission Line in Seyfert 2 Galaxy IRAS 00521-7054. *ApJ*, 747:L11.

[291] Tanaka, Y., Nandra, K., Fabian, A. C., Inoue, H., Otani, C., Dotani, T., Hayashida, K., Iwasawa, K., Kii, T., Kunieda, H., Makino, F., and Matsuoka, M. (1995). Gravitationally redshifted emission implying an accretion disk and massive black hole in the active galaxy MCG-6-30-15. *Nature*, 375:659–661.

[292] Tazaki, F., Ueda, Y., Ishino, Y., Eguchi, S., Isobe, N., Terashima, Y., and Mushotzky, R. F. (2010). Suzaku Observation of the Brightest Broad-line Radio Galaxy 4C 50.55 (IGR J21247+5058). *ApJ*, 721:1340–1347.

[293] Thomas, H.-C., Beuermann, K., Reinsch, K., Schwope, A. D., Truemper, J., and Voges, W. (1998). Identification of soft high galactic latitude RASS X-ray sources. I. A complete count-rate limited sample. *A&A*, 335:467–478.

[294] Tombesi, F., Cappi, M., Reeves, J. N., Palumbo, G. G. C., Yaqoob, T., Braito, V., and Dadina, M. (2010). Evidence for ultra-fast outflows in radio-quiet AGNs. I. Detection and statistical incidence of Fe K-shell absorption lines. *A&A*, 521:A57.

[295] Tomsick, J. A., Nowak, M. A., Parker, M., Miller, J. M., Fabian, A. C., Harrison, F. A., Bachetti, M., Barret, D., Boggs, S. E., Christensen, F. E., Craig, W. W., Forster, K., Fürst, F., Grefenstette, B. W., Hailey, C. J., King, A. L., Madsen, K. K., Natalucci, L., Pottschmidt, K., Ross, R. R., Stern, D., Walton, D. J., Wilms, J., and Zhang, W. W. (2014). The Reflection Component from Cygnus X-1 in the Soft State Measured by NuSTAR and Suzaku. *ApJ*, 780:78.

[296] Tomsick, J. A., Parker, M. L., García, J. A., Yamaoka, K., Barret, D., Chiu, J.-L., Clavel, M., Fabian, A., Fürst, F., Gandhi, P., Grinberg, V., Miller, J. M., Pottschmidt, K., and Walton, D. J. (2018). Alternative Explanations for Extreme Supersolar Iron Abundances Inferred from the Energy Spectrum of Cygnus X-1. *ApJ*, 855:3.

[297] Tomsick, J. A., Yamaoka, K., Corbel, S., Kaaret, P., Kalemci, E., and Migliari, S. (2009). Truncation of the Inner Accretion Disk Around a Black Hole at Low Luminosity. *ApJ*, 707:L87–L91.

[298] Tortosa, A., Marinucci, A., Matt, G., Bianchi, S., La Franca, F., Ballantyne, D. R., Boorman, P. G., Fabian, A. C., Farrah, D., Fuerst, F., Gandhi, P., Harrison, F. A., Koss, M. J., Ricci, C., Stern, D., Ursini, F., and Walton, D. J. (2017). Broad-band X-ray spectral analysis of the Seyfert 1 galaxy GRS 1734-292. *MNRAS*, 466:4193–4200.

[299] Tran, H. D., Lyke, J. E., and Mader, J. A. (2011). Indecent Exposure in Seyfert 2 Galaxies: A Close Look. *ApJ*, 726:L21.

[300] Tripathi, A., Yan, J., Yang, Y., Yan, Y., Garnham, M., Yao, Y., Li, S., Ding, Z., Abdikamalov, A. B., Ayzenberg, D., Bambi, C., Dauser, T., García, J. A., Jiang, J., and Nampalliwar, S. (2019). Constraints on the Spacetime Metric around Seven Bare AGNs Using X-Ray Reflection Spectroscopy. *ApJ*, 874:135.

[301] Turner, M. J. L., Abbey, A., Arnaud, M., Balasini, M., Barbera, M., Belsole, E., Bennie, P. J., Bernard, J. P., Bignami, G. F., Boer, M., Briel, U., Butler, I., Cara, C., Chabaud, C., Cole, R., Collura, A., Conte, M., Cros, A., Denby, M., Dhez, P., Di Coco, G., Dowson, J., Ferrando, P., Ghizzardi, S., Gianotti, F., Goodall, C. V., Gretton, L., Griffiths, R. G., Hainaut, O., Hochedez, J. F., Holland, A. D., Jourdain, E., Kendziorra, E., Lagostina, A., Laine, R., La Palombara, N., Lortholary, M., Lumb, D., Marty, P., Molendi, S., Pigot, C., Poindron, E., Pounds, K. A., Reeves, J. N., Reppin, C., Rothenflug, R., Salvetat, P., Sauvageot, J. L., Schmitt, D., Sembay, S., Short, A. D. T., Spragg, J., Stephen, J., Strüder, L., Tiengo, A., Trifoglio, M., Trümper, J., Vercellone, S., Vigroux, L., Villa, G., Ward, M. J., Whitehead, S., and Zonca, E. (2001). The European Photon Imaging Camera on XMM-Newton: The MOS cameras : The MOS cameras. *A&A*, 365:L27–L35.

[302] Turner, N. J. (2004). On the Vertical Structure of Radiation-dominated Accretion Disks. *ApJ*, 605:L45–L48.

[303] Turner, T. J., Miller, L., Kraemer, S. B., Reeves, J. N., and Pounds, K. A. (2009). Suzaku Observation of a Hard Excess in 1H 0419 - 577: Detection of a Compton-Thick Partial-Covering Absorber. *ApJ*, 698:99–105.

[304] Turner, T. J., Reeves, J. N., Braito, V., and Costa, M. (2018). On the nature of the high-energy rollover in 1H 0419-577. *MNRAS*, 476:1258–1270.

[305] Urry, C. M. and Padovani, P. (1995). Unified Schemes for Radio-Loud Active Galactic Nuclei. *PASP*, 107:803.

[306] Vasudevan, R. V. and Fabian, A. C. (2007). Piecing together the X-ray background: bolometric corrections for active galactic nuclei. *MNRAS*, 381:1235–1251.

[307] Vaughan, S., Boller, T., Fabian, A. C., Ballantyne, D. R., Brandt, W. N., and Trümper, J. (2002). An XMM-Newton observation of Ton S180: constraints on the continuum emission in ultrasoft Seyfert galaxies. *MNRAS*, 337:247–255.

[308] Vaughan, S. and Fabian, A. C. (2004). A long hard look at MCG-6-30-15 with XMM-Newton- II. Detailed EPIC analysis and modelling. *MNRAS*, 348:1415–1438.

[309] Véron-Cetty, M. P. and Véron, P. (2006). A catalogue of quasars and active nuclei: 12th edition. *A&A*, 455:773–777.

[310] Volonteri, M. (2012). The Formation and Evolution of Massive Black Holes. *Science*, 337:544.

[311] Walton, D. J., Brightman, M., Risaliti, G., Fabian, A. C., Fürst, F., Harrison, F. A., Lohfink, A., Matt, G., Miniutti, G., Parker, M. L., and Stern, D. (2018). Disentangling the complex broad-band X-ray spectrum of IRAS 13197-1627 with NuSTAR, XMM-Newton and Suzaku. *MNRAS*, 473:4377–4391.

[312] Walton, D. J., Middleton, M. J., Pinto, C., Fabian, A. C., Bachetti, M., Barret, D., Brightman, M., Fuerst, F., Harrison, F. A., Miller, J. M., and Stern, D. (2016). An Iron K Component to the Ultrafast Outflow in NGC 1313 X-1. *ApJ*, 826:L26.

[313] Walton, D. J., Mooley, K., King, A. L., Tomsick, J. A., Miller, J. M., Dauser, T., García, J. A., Bachetti, M., Brightman, M., Fabian, A. C., Forster, K., Fürst, F., Gandhi, P., Grefenstette, B. W., Harrison, F. A., Madsen, K. K., Meier, D. L., Middleton, M. J., Natalucci, L., Rahoui, F., Rana, V., and Stern, D. (2017). Living on a Flare: Relativistic Reflection in V404 Cyg Observed by NuSTAR during Its Summer 2015 Outburst. *ApJ*, 839:110.

[314] Walton, D. J., Nardini, E., Fabian, A. C., Gallo, L. C., and Reis, R. C. (2013). Suzaku observations of 'bare' active galactic nuclei. *MNRAS*, 428:2901–2920.

[315] Walton, D. J., Nardini, E., Gallo, L. C., Reynolds, M. T., Ricci, C., Dauser, T., Fabian, A. C., García, J. A., Harrison, F. A., Risaliti, G., and Stern, D. (2019). A low-flux state in IRAS 00521-7054 seen with NuSTAR and XMM-Newton: relativistic reflection and an ultrafast outflow. *MNRAS*, 484:2544–2555.

[316] Walton, D. J., Reis, R. C., Cackett, E. M., Fabian, A. C., and Miller, J. M. (2012a). The similarity of broad iron lines in X-ray binaries and active galactic nuclei. *MNRAS*, 422:2510–2531.

[317] Walton, D. J., Reis, R. C., Cackett, E. M., Fabian, A. C., and Miller, J. M. (2012b). The similarity of broad iron lines in X-ray binaries and active galactic nuclei. *MNRAS*, 422:2510–2531.

[318] Walton, D. J., Risaliti, G., Harrison, F. A., Fabian, A. C., Miller, J. M., Arevalo, P., Ballantyne, D. R., Boggs, S. E., Brenneman, L. W., Christensen, F. E., Craig, W. W., Elvis, M., Fuerst, F., Gandhi, P., Grefenstette, B. W., Hailey, C. J., Kara, E., Luo, B., Madsen, K. K., Marinucci, A., Matt, G., Parker, M. L., Reynolds, C. S., Rivers, E., Ross, R. R., Stern, D., and Zhang, W. W. (2014). NuSTAR and XMM-NEWTON Observations of NGC 1365: Extreme Absorption Variability and a Constant Inner Accretion Disk. *ApJ*, 788:76.

[319] Wang, H., Zhou, H., Yuan, W., and Wang, T. (2012). Metallicity and Quasar Outflows. *ApJ*, 751:L23.

[320] Wang-Ji, J., García, J. A., Steiner, J. F., Tomsick, J. A., Harrison, F. A., Bambi, C., Petrucci, P.-O., Ferreira, J., Chakravorty, S., and Clavel, M. (2018). The Evolution of GX 339-4 in the Low-hard State as Seen by NuSTAR and Swift. *ApJ*, 855:61.

[321] Webster, B. L. and Murdin, P. (1972). Cygnus X-1-a Spectroscopic Binary with a Heavy Companion ? *Nature*, 235:37–38.

[322] Weisskopf, M. C., Ramsey, B., O'Dell, S. L., Tennant, A., Elsner, R., Soffita, P., Bellazzini, R., Costa, E., Kolodziejczak, J., Kaspi, V., Mulieri, F., Marshall, H., Matt, G., and Romani, R. (2016). The imaging x-ray polarimetry explorer (ixpe). *Results in Physics*, 6:1179 – 1180.

[323] Wilkins, D. R. and Fabian, A. C. (2011). Determination of the X-ray reflection emissivity profile of 1H 0707-495. *MNRAS*, 414:1269–1277.

[324] Wilkins, D. R. and Fabian, A. C. (2012). Understanding X-ray reflection emissivity profiles in AGN: locating the X-ray source. *MNRAS*, 424:1284–1296.

[325] Wilkins, D. R., Gallo, L. C., Grupe, D., Bonson, K., Komossa, S., and Fabian, A. C. (2015). Flaring from the supermassive black hole in Mrk 335 studied with Swift and NuSTAR. *MNRAS*, 454:4440–4451.

[326] Willingale, R., Starling, R. L. C., Beardmore, A. P., Tanvir, N. R., and O'Brien, P. T. (2013). Calibration of X-ray absorption in our Galaxy. *MNRAS*, 431:394–404.

[327] Wilms, J., Allen, A., and McCray, R. (2000). On the Absorption of X-Rays in the Interstellar Medium. *ApJ*, 542:914–924.

[328] Wilms, J., Reynolds, C. S., Begelman, M. C., Reeves, J., Molendi, S., Staubert, R., and Kendziorra, E. (2001). XMM-EPIC observation of MCG-6-30-15: direct evidence for the extraction of energy from a spinning black hole? *MNRAS*, 328:L27–L31.

[329] Xu, Y., Harrison, F. A., García, J. A., Fabian, A. C., Fürst, F., Gandhi, P., Grefenstette, B. W., Madsen, K. K., Miller, J. M., Parker, M. L., Tomsick, J. A., and Walton, D. J. (2018). Reflection Spectra of the Black Hole Binary Candidate MAXI J1535-571 in the Hard State Observed by NuSTAR. *ApJ*, 852:L34.

[330] Yan, M., Sadeghpour, H. R., and Dalgarno, A. (2001). Erratum: "photoionization cross sections of he and h2" (apj, 496, 1044 [1998]). *The Astrophysical Journal*, 559(2):1194.

[331] Young, A. J., Crawford, C. S., Fabian, A. C., Brandt, W. N., and O'Brien, P. T. (1999). The optical variability of the narrow-line Seyfert 1 galaxy IRAS 13224-3809. *MNRAS*, 304:L46–L52.

[332] Yuan, W., Zhang, C., Chen, Y., Sun, S., Zhang, Y., Cui, W., Ling, Z., Huang, M., Zhao, D., Wang, W., Qiu, Y., Liu, Z., Pan, H., Cai, H., Deng, J., Jia, Z., Jin, C., Sun, H., Hu, H., Liu, F., Zhang, M., Song, L., Lu, F., Jia, S., Li, C., Zhao, H., Ge, M., Zhang, J., Cui, W., Wang, Y., Wang, J., Sun, X., Jin, G., Li, L., Chen, F., Cai, Z., Guo, T., Liu, G., Liu, H., Feng, H., Zhang, S., Zhang, B., Dai, Z., Wu, X., and Gou, L. (2018). Einstein Probe: Exploring the ever-changing X-ray Universe. *Scientia Sinica Physica, Mechanica Astronomica*, 48(3):039502.

[333] Zdziarski, A. A. (1985). Power-law X-ray and gamma-ray emission from relativistic thermal plasmas. *ApJ*, 289:514–525.

[334] Zdziarski, A. A., Gierliński, M., Mikołajewska, J., Wardziński, G., Smith, D. M., Harmon, B. A., and Kitamoto, S. (2004). GX 339-4: the distance, state transitions, hysteresis and spectral correlations. *MNRAS*, 351:791–807.

[335] Zdziarski, A. A., Johnson, W. N., and Magdziarz, P. (1996). Broad-band γ-ray and X-ray spectra of NGC 4151 and their implications for physical processes and geometry. *MNRAS*, 283:193–206.

[336] Zel'dovich, Y. B. and Poduret, M. A. (1964). The neutrino radiance of a star during the gravitational collapse in general relativity. *Akademiia Nauk SSSR Doklady*, 156:56–60.

[337] Zhang, Y. H., Treves, A., Maraschi, L., Bai, J. M., and Liu, F. K. (2006). XMM-Newton View of PKS 2155-304: Hardness Ratio and Cross-Correlation Analysis of EPIC pn Observations. *ApJ*, 637:699–710.

[338] Zhou, X.-L. and Wang, J.-M. (2005). Narrow iron k lines in active galactic nuclei: Evolving populations? *The Astrophysical Journal Letters*, 618(2):L83.

[339] Zoghbi, A., Cackett, E. M., Reynolds, C., Kara, E., Harrison, F. A., Fabian, A. C., Lohfink, A., Matt, G., Balokovic, M., Boggs, S. E., Christensen, F. E., Craig, W., Hailey, C. J., Stern, D., and Zhang, W. W. (2014). Observations of MCG-5-23-16 with Suzaku, XMM-Newton and NuSTAR: Disk Tomography and Compton Hump Reverberation. *ApJ*, 789:56.

[340] Zoghbi, A., Fabian, A. C., Reynolds, C. S., and Cackett, E. M. (2012). Relativistic iron K X-ray reverberation in NGC 4151. *MNRAS*, 422:129–134.

[341] Zoghbi, A., Fabian, A. C., Uttley, P., Miniutti, G., Gallo, L. C., Reynolds, C. S., Miller, J. M., and Ponti, G. (2010). Broad iron L line and X-ray reverberation in 1H0707-495. *MNRAS*, 401:2419–2432.

[342] Zoghbi, A., Uttley, P., and Fabian, A. C. (2011). Understanding reverberation lags in 1H0707-495. *MNRAS*, 412:59–64.

[343] Życki, P. T., Done, C., and Smith, D. A. (1999). The 1989 May outburst of the soft X-ray transient GS 2023+338 (V404 Cyg). *MNRAS*, 309:561–575.